

## ABSTRACT

Title of dissertation: DYNAMICS AND AEROELASTICITY OF  
HOVER CAPABLE FLAPPING WINGS:  
EXPERIMENTS AND ANALYSIS

Beerinder Singh, Doctor of Philosophy, 2006

Dissertation directed by: Professor Inderjit Chopra  
Department of Aerospace Engineering

This dissertation addresses the aerodynamics of insect-based, bio-inspired, flapping wings in hover. An experimental apparatus, with a bio-inspired flapping mechanism, was used to measure the thrust generated for a number of wing designs. Bio-Inspired flapping-pitching mechanisms reported in literature, usually operate in oil or water at very low flapping frequencies ( $\sim 0.17$  Hz). In contrast, the mechanism used in this study operates in air, at relatively high frequencies ( $\sim 12$  Hz). All the wings tested showed a decrease in thrust at high frequencies. A novel mechanism with passive pitching of the wing, caused by aeroelastic forces, was also tested. Flow visualization images, which show the salient features of the airflow, were also acquired. At high flapping frequencies, the light-weight and highly flexible wings used in this study exhibited significant aeroelastic effects. For this reason, an aeroelastic analysis for hover-capable, bio-inspired flapping wings was developed. A finite element based structural analysis of the wing was used, along with an unsteady aerodynamic analysis based on indicial functions. The analysis

was validated with experimental data available in literature, and also with experimental tests conducted on the bio-inspired flapping-pitching mechanism. Results for both elastic and rigid wing analyses were compared with the thrust measured on the bio-inspired flapping-pitching mechanism.

DYNAMICS AND AEROELASTICITY OF HOVER-CAPABLE  
FLAPPING WINGS: EXPERIMENTS AND ANALYSIS

by

Beerinder Singh

Dissertation submitted to the Faculty of the Graduate School of the  
University of Maryland, College Park in partial fulfillment  
of the requirements for the degree of  
Doctor of Philosophy  
2006

Advisory Committee:  
Professor Inderjit Chopra, Chair/Advisor  
Professor Darryll Pines  
Professor Norman Wereley  
Professor James Baeder  
Professor Sean Humbert  
Professor Balakumar Balachandran

© Copyright by  
Beerinder Singh  
2006

## **Dedication**

Dedicated in loving memory to Amritpal and Jasnoor.

## ACKNOWLEDGMENTS

I would like to acknowledge the help and support provided by my advisor Dr. Chopra. I am deeply indebted to him for giving me the opportunity to work at the Rotorcraft Center. His constant guidance and encouragement have made this work possible.

I would also like to acknowledge the members of my dissertation committee. I am grateful to Dr. Pines, Dr. Wereley, Dr. Baeder, Dr. Humbert and Dr. Balachandran for their insightful comments and suggestions.

This work would not have been possible without the funding provided by the MURI program led by Dr. Anderson and Dr. Doligalski. The novel mechanism used in the experiments was designed and built by Mr. Matt Tarascio (currently with Sikorsky). Dr. Ramasamy and Dr. Leishman helped with the flow visualization tests.

My years at the Rotorcraft center have been enriched by my interactions with the graduate students and researchers at the center. Karthik, Vinit, Jaina, Marie, Jayant, Felipe, Ashish, Anubhav, Beatrice, Jinsong, Jinwei, Mao, Jaye, Dr. Nagaraj, Anand, Sudarshan, Jason, Atul, Ron, Shreyas, Sandeep, Ben Hein, Eric Parsons and Joe Schmaus have all played an important part in making this work possible.

I have had a lot of ups and downs in my stay at Maryland and my friends have always been by my side, to help me through the bad times and to enjoy the good

times. Anu, Amrit, Vinit, Nivedita, Anand, Saranga, Mathangi and Rashi have all made my stay in College Park very memorable.

I would not be here today without the unwavering support and encouragement of my parents and my brother and sister-in-law. They have supported me through thick and thin, with utmost patience, to help me achieve this important milestone in my life.

# TABLE OF CONTENTS

List of Tables	vii
List of Figures	viii
1 Introduction	1
1.1 Background . . . . .	1
1.2 Existing MAVs . . . . .	3
1.2.1 Fixed wing MAVs . . . . .	5
1.2.2 Rotary wing MAVs . . . . .	6
1.2.3 Flapping wing MAVs . . . . .	7
1.3 Bio-inspired design . . . . .	7
1.3.1 Insect Flight vs Bird Flight . . . . .	8
1.4 Flapping Flight Research . . . . .	11
1.4.1 Experimental studies . . . . .	12
1.4.1.1 Experiments on live animals . . . . .	12
1.4.1.2 Model experiments . . . . .	15
1.4.2 Analyses . . . . .	22
1.5 Need for New Experimental Data . . . . .	25
1.6 Need for Aeroelastic Modeling . . . . .	25
1.7 Objectives and Approach . . . . .	26
2 Experimental Setup	28
2.1 Bio-Inspired Flapping . . . . .	28
2.2 Bi-stable Flapping Wing Mechanism . . . . .	29
2.3 Thrust Measurement . . . . .	31
2.3.1 Force Transducer . . . . .	32
2.4 Motion Transducers . . . . .	37
2.5 Passive Pitch Mechanism . . . . .	39
2.6 Vacuum Chamber . . . . .	40
2.7 Flow Visualization . . . . .	42
3 Experimental Results	45
3.1 Quasi-Steady Analysis . . . . .	45
3.2 Hover Stand Tests . . . . .	49
3.3 Low Frequency Tests . . . . .	54
3.4 Vacuum Chamber Tests . . . . .	63
3.5 High Frequency Tests . . . . .	66
3.6 Pure Flap Tests (Passive Pitch) . . . . .	73
3.7 Passive Pitch Mechanism . . . . .	76
3.8 Flow Visualization . . . . .	82
3.9 Summary . . . . .	85

4	Aeroelastic Model	88
4.1	Structural Model	88
4.1.1	Wing discretization	89
4.1.2	Large overall motion	90
4.1.3	Finite Element Formulation	100
4.2	Aerodynamic Model	108
5	Model Validation	117
5.1	Structural Model	117
5.1.1	Cantilevered plate spin-up	117
5.1.2	Aluminum plate in pure flapping	120
5.2	Aerodynamic Model	125
5.2.1	Wing motion	125
5.2.2	Comparison with Robofly data	127
5.3	Summary	135
6	Results	138
6.1	Wing Grids	138
6.2	Bending moment comparison	139
6.3	Uncoupled Analysis	142
6.3.1	High frequency tests (Wing III)	145
6.3.2	Low frequency tests	148
6.4	High frequency bending moment	152
6.5	Coupled Analysis	160
6.6	Summary	162
7	Concluding Remarks	168
7.1	Conclusions	169
7.1.1	Experimental results	169
7.1.2	Aeroelastic Modeling	170
7.2	Important Contributions	172
7.3	Recommendations for Future Work	173
A	Finite Element Matrices	175
A.1	Shape function matrices	175
A.2	Dynamic stiffening matrices	177
B	Aerodynamic Expressions	186
B.1	Non-circulatory force	186
B.2	Circulation	187
	Bibliography	188

## LIST OF TABLES

3.1	Wing properties. . . . .	69
4.1	5 point Gauss quadrature points and weights. . . . .	106

## LIST OF FIGURES

1.1	Typical “over the hill” reconnaissance mission profile in urban terrain	2
1.2	Scale effects [3]	3
1.3	Existing MAVs (2005 data)	4
1.4	Seagulls in different modes of flight [25]	9
1.5	Insect wing kinematics.	11
1.6	Unsteady lift generating mechanisms in insects.	17
1.7	Artists conception of the MFI (R.J. Wood).	20
1.8	Dragonfly wings.	24
2.1	Flapping wing mechanism (Concept by M.J. Tarascio [3]).)	30
2.2	Components of the pitch assembly.	31
2.3	Flapping wing mechanism mounted on the rotor test stand.	33
2.4	Commercially available sensors.	33
2.5	Load Cell.	34
2.6	Stresses for square and circular cross-sections with a 45° load.	36
2.7	Pitch motion sensor.	38
2.8	Flap motion sensor.	38
2.9	Passive pitch mechanism.	40
2.10	Vacuum Chamber	41
2.11	Flow visualization test setup.	43
2.12	Flow visualization schematic.	44
3.1	Reference frames.	46
3.2	Blade element.	47

3.3	Thrust measured on the hover test stand for a rectangular wing. . . .	50
3.4	Present wing planform compared with a hummingbird wing [97]. . . .	52
3.5	Measured thrust, flapping angle and pitch angle during one flap cycle at 9.07 Hz . . . . .	53
3.6	Scaled-up insect wings . . . . .	56
3.7	Schematic of planform showing root cut-out . . . . .	57
3.8	Effect of change in load cell design on measured thrust . . . . .	57
3.9	Comparison of thrust generated by Wings II and III . . . . .	59
3.10	Effect of wing pitch angle on thrust (Wing II) . . . . .	61
3.11	Effect of wing pitch angle on thrust (Wing III) . . . . .	61
3.12	Effect of early rotation on thrust (Wing III) . . . . .	62
3.13	Effect of early rotation on thrust (Wing II) . . . . .	63
3.14	Airloads obtained by subtracting inertial forces . . . . .	64
3.15	Thrust measured in air and vacuum for Wing II . . . . .	65
3.16	Thrust and power measured for Wing III at high frequency. . . . .	68
3.17	Wing VII. . . . .	70
3.18	Thrust and power measured for lighter wings at high frequency. . . .	71
3.19	Thrust and power measured for lighter wings at high frequency . . . .	72
3.20	Thrust and power measured for pure flapping motion with passive pitching of the wing. . . . .	74
3.21	Minimum and maximum values of pitch variation. . . . .	75
3.22	Thrust and power measured for passive pitch mechanism with stiff and soft torsion spring for Wing VII. . . . .	77
3.23	Minimum and maximum values of pitch variation for stiff and soft spring for Wing VII. . . . .	78
3.24	Thrust and power measured for passive pitch mechanism with various wings. . . . .	79

3.25	Minimum and maximum values of pitch variation for various wings mounted on the passive pitch mechanism. . . . .	80
3.26	Time variation of loads and motion for Wing X at 22.3 Hz . . . . .	81
3.27	Flow visualization image showing the leading edge vortex. . . . .	83
3.28	Flow visualization images acquired at different stroke positions (Ref. 52)	84
4.1	Mesh generation . . . . .	91
4.2	Reference frames . . . . .	94
4.3	Element degrees of freedom . . . . .	101
4.4	Gauss quadrature points (5×5) . . . . .	106
4.5	Wake structure at one station along the span . . . . .	110
4.6	Flow velocities . . . . .	110
4.7	Leading edge suction . . . . .	114
5.1	Rotating cantilever plate. . . . .	118
5.2	Tip deflection for spin-up motion of a rectangular plate. . . . .	119
5.3	RPM variation with time . . . . .	119
5.4	Aluminum plate in pure flapping motion. . . . .	121
5.5	MEMS accelerometer. . . . .	121
5.6	Comparison of measured and predicted bending moment for a slow support motion (flapping shaft shaken by hand). . . . .	122
5.7	Measured acceleration for slow support motion. . . . .	122
5.8	Measured acceleration at a flapping frequency of 2.7 Hz. . . . .	123
5.9	Comparison of measured bending moment with a rigid analysis at 2.7 Hz. . . . .	123
5.10	Comparison of measured bending moment with an elastic analysis at 2.7 Hz. . . . .	124
5.11	Definition of flapping motion. . . . .	127

5.12	Definition of pitching motion. . . . .	128
5.13	Input velocities for Robofly kinematics. . . . .	129
5.14	Total vertical force with ideal $C_l$ . . . . .	129
5.15	Ideal $C_l$ compared with experimental $C_l$ . . . . .	130
5.16	Total vertical force with experimental $C_l$ . . . . .	130
5.17	Components of the total vertical force. $F_v^c$ - circulatory (with Wagner effect), $F_v^{pol}$ - leading edge suction, $F_v^{nc}$ - non-circulatory, $F_v^k$ - Kussner effect. . . . .	132
5.18	Vertical force without non-circulatory effects . . . . .	132
5.19	Actual and idealized stroke planes and the non-circulatory force . . .	133
5.20	Total horizontal force . . . . .	133
5.21	Vertical force compared with the analysis of Zbikowski et. al. [103] . .	135
6.1	Finite element grid for Wing III . . . . .	139
6.2	Finite element grid for Wing II . . . . .	140
6.3	Position, velocity and acceleration used as inputs for the analysis . .	141
6.4	Bending moment variation compared with experimental data at various flapping frequencies . . . . .	143
6.5	Smooth motion vs Fourier series fit . . . . .	144
6.6	Comparison of analysis and experiment at 11.6 Hz with smooth motion	144
6.7	Rigid wing: predicted and measured thrust . . . . .	146
6.8	Elastic wing: predicted and measured thrust . . . . .	146
6.9	Components of total thrust at 10.96 Hz (symbols: v-vertical, c-circulatory, pol-Polhamus, k-Kussner, nc-non-circulatory) . . . . .	147
6.10	Components of total thrust at 11.6 Hz . . . . .	148
6.11	Comparison of experiment and analysis for Wing III at 45° pitch angle	149
6.12	Comparison of experiment and analysis for Wing III at 30° pitch angle	150

6.13	Comparison of experiment and analysis for Wing II at 30° and 45° pitch angles . . . . .	151
6.14	Components of total thrust for Wing II at 30° and 45° pitch angles . . . . .	151
6.15	Comparison of measured and predicted bending moment for Wing III in pure flapping motion. . . . .	154
6.16	Input flap motion showing duration of acceleration . . . . .	155
6.17	Comparison of measured and predicted bending moment for Wing III in pure flapping motion with $\Delta t/T=0.3$ . . . . .	156
6.18	Improved bending moment prediction for Wing III undergoing combined flapping and pitching using $\Delta t/T=0.3$ . . . . .	157
6.19	Improved thrust prediction (with $\Delta t/T = 0.3$ ). . . . .	158
6.20	Effect of linear inflow model on vertical force at 10.58 Hz . . . . .	160
6.21	Effect of parametric variation of the first natural frequency of the wing at 10.58 Hz. . . . .	161
6.22	Loose coupling procedure. . . . .	163
6.23	Bending moment prediction with coupled analysis for Wing III . . . . .	164
6.24	Thrust prediction with coupled analysis for Wing III . . . . .	165
6.25	Comparison of bending moments calculated using coupled and uncoupled analyses . . . . .	165

## List of Symbols

$A_n$	aerodynamic coefficient
$B_n^p$	elastic aerodynamic influence coefficient for mode $p$
$c$	chord
$[C]$	damping matrix
$C_l$	lift coefficient
$D$	drag, per unit span
$\{F\}$	force vector
$F^c$	circulatory force
$F^k$	Force caused by shed wake (Kussner effect)
$F^{nc}$	non-circulatory force
$F_i$	inertial force, per unit span
$F_n$	force normal to wing chord, per unit span
$F_x$	force tangential to wing chord, per unit span
$i, j, k$	unit vectors
$[K]$	stiffness matrix
$L$	lift, per unit span
$m$	mass
$[M]$	Mass matrix
$N_m$	total number of modes
$p$	mode number
$\{q\}$	generalized coordinates
$\{r\}$	position vector
$R$	span
$Re$	Reynolds number, $\frac{V_{tip}c}{\nu}$
$r$	spanwise coordinate
$t$	time
$T$	time period of one flap cycle, total kinetic energy
$[T_{(..)}]$	transformation matrix
$U$	strain energy
$v_i$	induced inflow velocity
$v_n$	velocity normal to wing chord
$v_x$	velocity tangential to wing chord
$V_{(.)}$	flow velocity
$w$	out of plane deformation
$x, y, z$	coordinates in the pitching reference frame

$\alpha$	angle of attack
$\beta$	wing flapping angle
$\gamma$	vorticity strength
$\Gamma$	circulation
$\{\epsilon\}$	strain vector
$\theta$	wing pitch angle
$\{\kappa\}$	vector of curvatures
$\nu$	kinematic viscosity
$\rho$	mass density
$\phi_w$	Wagner function
$\psi_k$	Kussner function

# Chapter 1

## Introduction

### 1.1 Background

Recent advances in micro-technologies, such as Microelectromechanical Systems (MEMS), have led to the development of miniature CCD cameras, tiny infrared sensors and chip-sized hazardous substance detectors. These developments have led to significant interest in miniature flying vehicles called Micro Air Vehicles (MAVs), which can act as highly portable platforms for these miniature sensors [1]. These aerial vehicles were initially envisioned as highly portable reconnaissance platforms which would be indispensable assets at the platoon level or even for an individual soldier, giving the soldier important information about his surroundings. This will lead to greater situational awareness and effectiveness with lower casualties. Figure 1.1 shows a typical mission profile for an MAV in an urban environment. Although reconnaissance and surveillance applications are the primary drivers behind MAV development, they can also be employed for biochemical sensing, tagging and targeting, search and rescue, communications and may eventually be used as weapons. Apart from these military applications, a large number of commercial applications

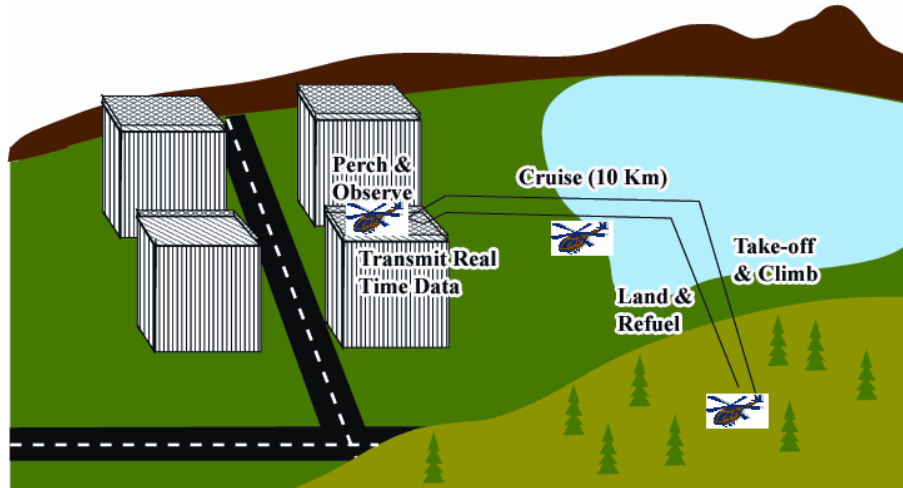


Figure 1.1: Typical “over the hill” reconnaissance mission profile in urban terrain

also exist such as traffic monitoring, fire rescue, border surveillance, power line inspection etc. NASA plans to establish a network of MAVs autonomously exploring the far reaches of the solar system and also for planetary exploration [2]. The low detectability and low noise promised by MAVs, their ability to transmit real-time data from an area of observation, and their ability to maneuver within confined spaces, make them ideal for such military and civilian missions. In 1997, the Defense Advanced Research Projects Agency (DARPA) defined an MAV as an aerial vehicle with a maximum dimension of 15 cm and an all-up weight of 100 grams. These size and weight constraints, derived from both physical and technological considerations, put MAVs in a size class which is at least an order of magnitude smaller than other Unmanned Air Vehicles or UAVs. Figure 1.2 shows the vehicle gross weight vs Reynolds number for a large variety of air vehicles. The Reynolds number can be understood as the ratio of inertial forces to viscous forces in a fluid. Thus, a low Reynolds number signifies higher relative viscous effects. The size limitation

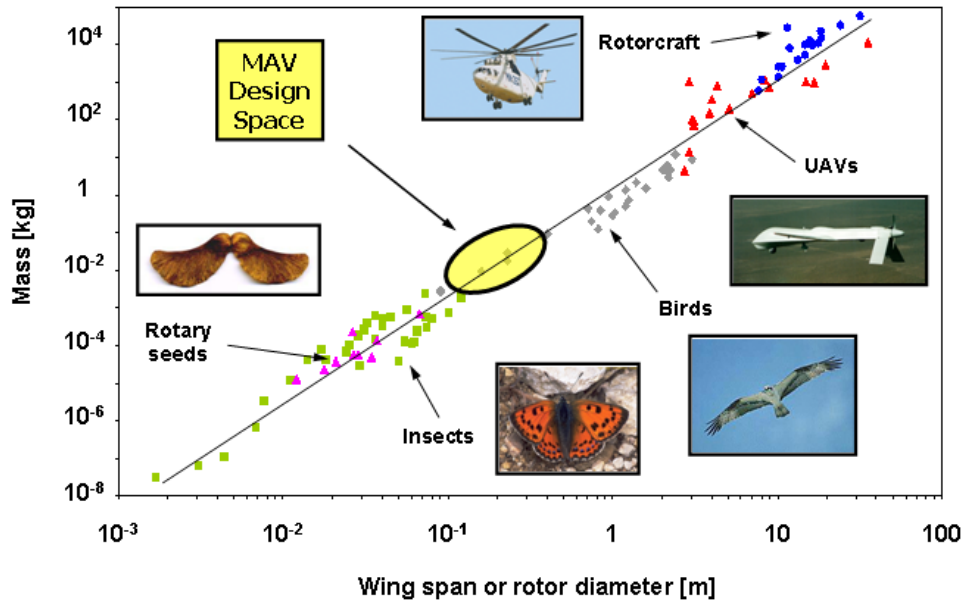


Figure 1.2: Scale effects [3]

puts MAVs in a low Reynolds number aerodynamic regime about which precious little is known. MAVs share this regime with the smallest birds and the largest insects. However, in recent years, the size and weight constraints set by DARPA have become quite flexible, with MAVs ranging from 10 grams to 300 grams in all-up weight.

## 1.2 Existing MAVs

Existing MAVs can be classified into three broad categories based on the aerodynamic mechanisms used to produce lift: fixed wing, rotary wing and flapping wing. In MAV development, an analogy can be drawn with the development of their larger,

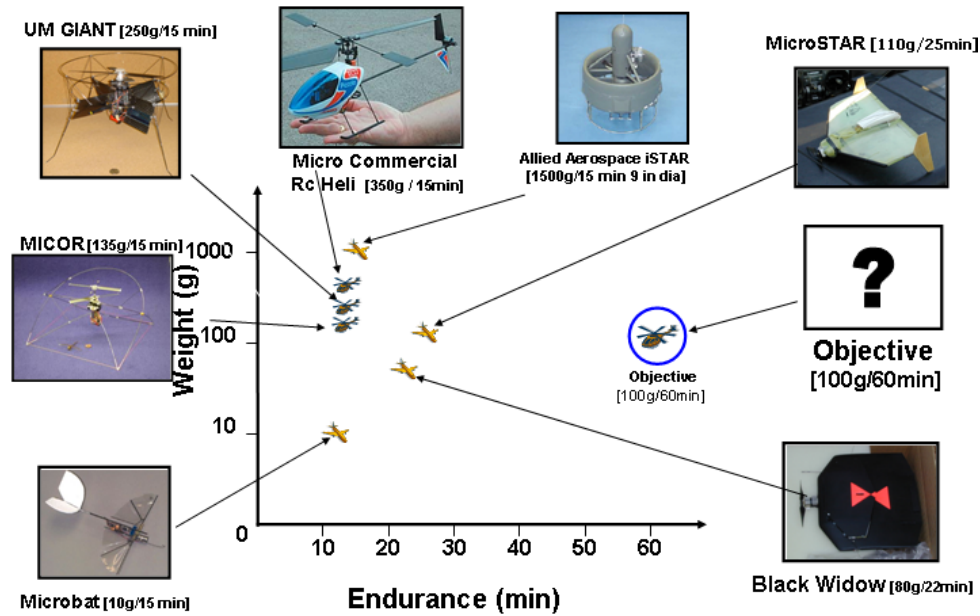


Figure 1.3: Existing MAVs (2005 data)

manned counterparts during the last century. Fixed wing technology was always a step ahead of rotary wing technology because of the additional complexities involved in rotary wing flight. The development of the conventional helicopter took much longer than the fixed wing aircraft. Similarly, among the existing MAVs, fixed-wing MAVs perform better than both rotary and flapping wing MAVs. Flapping wings, with their unsteady wing beating, introduce an additional level of complexity above and beyond rotary wings, and hence their development seems to be the slowest. Figure 1.3 shows the performance of some existing MAVs against the size and weight parameters set by DARPA. In terms of endurance, fixed-wing MAVs outperform rotary and flapping wing MAVs. However, their major shortcoming is the lack of hover capability, which allows an MAV to maneuver in much smaller confined spaces,

and more importantly, to perch and observe while saving valuable stored power. It is evident from Fig. 1.3 that all the hover capable MAVs, such as Micor and Mentor, have low endurance and high weight. Mentor and Microbat are two examples of flapping wing MAVs currently in existence. Mentor uses a phenomenon called “clap-fling”, which is used by a few species of insects to hover. However, because of the clapping of its wings it has an adverse noise signature. The Microbat is a 12 gram vehicle, but it has low endurance and is also incapable of hovering flight.

### **1.2.1 Fixed wing MAVs**

As mentioned above, fixed wing MAVs are the best performers within the size and weight constraints set by DARPA, however they cannot hover and hence cannot maneuver in tight spaces as well as rotary wing MAVs. Perhaps the best example of a fixed wing MAV is the Aerovironment Black Widow [4,5] with a weight of 80 grams and an endurance of about 22 mins. Several such MAVs are now in existence [6–8]. With the problems of flight and basic maneuverability dealt with, researchers are now focusing on optimizing the aerodynamic, aeroelastic and propulsive performance of these MAVs. References [6, 9–12] describe the numerical simulation of the flow around these fixed wing MAVs using CFD. There is a lot of interest in developing these MAVs with lightweight and flexible membrane wings [7, 11, 13–16], leading to the interest in their aeroelastic characteristics. Morphing of these flexible wings to achieve control without the use of conventional control surfaces is also being studied [17].

## 1.2.2 Rotary wing MAVs

The rotary wing MAVs shown in Fig. 1.3 have very low hover endurance. This is because the Figure of Merit (FM), which is a measure of hover efficiency, is very low for rotors at MAV scales. Conventional manned rotorcraft have FM as high as 0.8. However, rotors at MAV scales have a typical FM of 0.45-0.55 [18]. This poor aerodynamic performance is a manifestation of the aerodynamic effects of low operating Reynolds number ( $Re$ ) and higher relative viscous effects. The profile drag for an MAV scale rotor accounted for 50% of the losses as compared to 30% for full-scale helicopters [18]. Surface flow visualization studies conducted on the blades show that only a fraction of the blade surface has attached flow [19]. Flow visualization images also show a large, turbulent hub wake and a slower formation of the tip vortex caused by higher viscous effects [20]. A proper understanding of the wake structure is essential in designing rotors with high efficiency. The validation of a Computational Fluid Dynamics (CFD) analysis for micro hovering rotors is described by Lakshminarayan et. al. [21]. While inviscid phenomena such as thrust and induced velocity are captured well, the CFD analysis shows lower drag and power predictions as compared to experimental data. The design of an efficient rotor system with high endurance requires significant optimization of the airfoil shape, blade planform and twist distribution at low  $Re$ .

Another problem being investigated is that of autonomous control and navigation of rotary wing MAVs [22]. This problem is more challenging for rotary wing MAVs as compared to fixed wing MAVs because of the significant coupling between

lateral and longitudinal motions introduced by the rotor. Also, the measurement and control system must be small and light enough to be viable for MAVs.

### **1.2.3 Flapping wing MAVs**

Taking a cue from nature, wherein, flight at small scales is characterized by flapping wings, researchers are trying to mimic the wing motions of birds and insects to build flapping wing MAVs. With the introduction of a constantly accelerating and decelerating wing, the aerodynamics of such vehicles is highly unsteady in addition to the high relative viscous effects because of low Reynolds number. Ornithopters like the Microbat have been built and flown successfully by both researchers and model airplane enthusiasts. From a biological perspective, these ornithopters are more like birds than insects. This is because of fundamental differences in wing kinematics between insects and birds. Birds primarily utilize wing flapping for propulsion, while lift is generated by a combination of forward speed and wing flapping. This is the reason for the lack of hover capability of these ornithopters. The differences between insect-like and bird-like flapping are discussed further in the next section. A hover capable flapping wing MAV, based on insect wing kinematics, is yet to be designed and tested.

## **1.3 Bio-inspired design**

An argument is often made that nature has almost exclusively resorted to flapping flight because organic materials are not conducive to rotary wing flight.

However, at MAV scales, the reverse argument can also be made that, because of a lack of materials which can mimic biological muscles, rotary wing devices are easier to build and fly. At MAV scales, it is not yet clear whether rotary or flapping wings are more efficient. Thus, at the very least, flapping wing flight needs to be thoroughly investigated to determine its viability for MAVs. Also, since nature has had millions of years to optimize its designs through the process of natural selection, it is important for MAV designers to understand the fundamental physics of flapping flight. Pines and Bohorquez [23] discuss the technical challenges facing future MAV development. Low Reynolds number aerodynamics, light-weight and flexible adaptive wing structures and highly efficient propulsion and power systems need to be investigated thoroughly to build the next generation of MAVs. In flapping flight, a mechanism that can mimic insect wing kinematics is also a major hurdle which requires newer materials such as Electroactive Polymers (EAP) for artificial muscles [24].

### **1.3.1 Insect Flight vs Bird Flight**

In nature, flight has evolved into two different forms – insect flight and bird flight. While both these forms are based on flapping wings, there are important differences among them. Most birds flap their wings in a vertical plane with small changes in the pitch of the wings during a flapping cycle. Figure 1.4 shows a number of seagulls in different modes of flight ranging from take-off to cruise flight. This picture illustrates the range of motion of typical bird wings. Since birds are much



Figure 1.4: Seagulls in different modes of flight [25]

larger than insects, incorporating muscles, feathers and other moving parts into the wings is easier. Birds can control the shape and even the span of their wings to adapt to different flight modes. However, without large changes in pitch, this type of flapping cannot generate sufficient vertical force to support the weight in the absence of any forward speed. As a result, most birds cannot hover. However, the insect world abounds with examples of hovering flight. These insects flap their wings in a nearly horizontal plane, accompanied by large changes in wing pitch angle to produce lift even in the absence of any forward velocity. Among insects, there exist animals that are capable of taking off backwards, flying sideward, and landing upside down. Moreover, birds like the hummingbird, which are capable of hovering, have wing motions very similar to hover-capable insects. Thus, insect-based bio-inspired flight may present a hover-capable and highly maneuverable solution for MAVs.

Even among insects, there exist significant differences between the kinematics of various species. For example butterflies have large wings, which are clapped together without any change in pitch. A number of unsteady and nonlinear phenomena have been used to explain the relatively high lift generated by insects. Weis-Fogh's [26] clap-fling hypothesis is one such lift generating mechanism, but it is limited to a few species of insects such as butterflies and so does not explain the flight of other species. The University of Toronto-SRI Mentor is based on this type of clap-fling mechanism. However, in addition to being noisy, such wings may fatigue easily. Also, the efficiency of such a mechanism is not known. Another flight mechanism is the use of tandem wings, such as those found on dragonflies, which are remarkably agile fliers. Infact, in insects like the housefly or the honeybee, the hind wings have evolved into structures called the Halteres. These serve as tiny gyroscopes helping these insects in stabilizing themselves. Kinematic measurements of a large variety of insects have shown that this type of flapping, with a pair of wings undergoing large amplitude flapping and pitching motion, seems to be more prevalent in nature. Although there is tremendous variation in the wing kinematics of such insects, the basic elements of the kinematics are as shown in Fig. 1.5.

The distinction between bird-like flapping, henceforth referred to as ornithoptic flapping, and insect-based, or hover-capable flapping, is also important for another reason. Ornithoptic flapping requires a much simpler mechanism to replicate in contrast to hover-capable flapping. This is because of the large pitch changes required by hover-capable flapping, in addition to flapping in a single plane like ornithoptic flapping. This distinction has important consequences when one looks

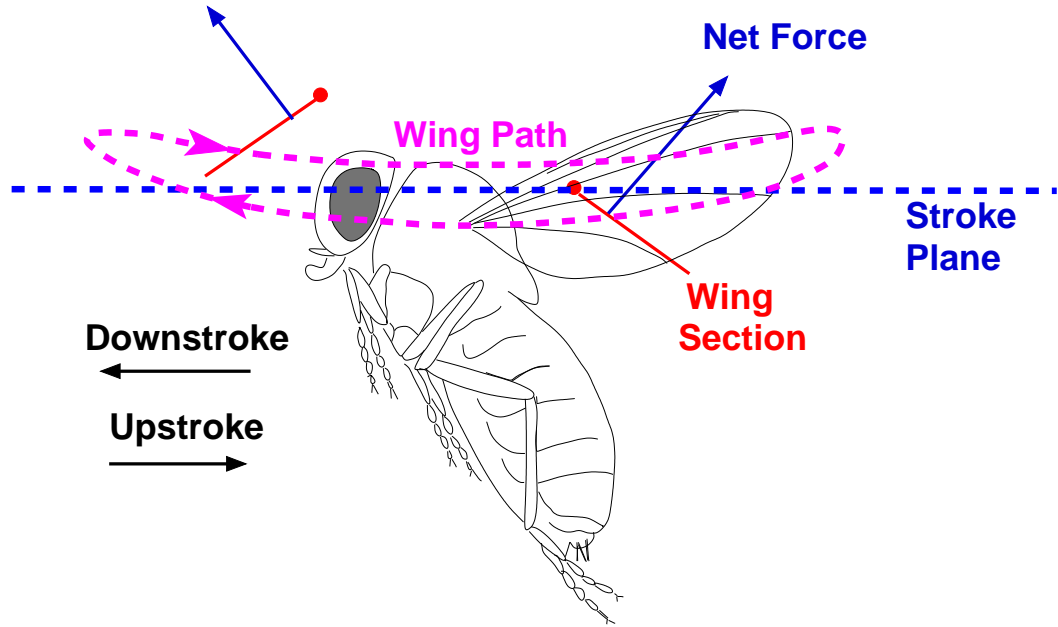


Figure 1.5: Insect wing kinematics.

at the available literature on flapping flight, wherein, ornithoptic flapping has been studied experimentally to a much greater extent. Literature on hover-capable flapping consists of a considerable amount of research by biologists on the wing kinematics and morphology of actual insects and birds [26–30]. For experimental studies, the problems encountered in making a hover-capable mechanism have been circumvented by making large, slow-moving, dynamically scaled models to mimic insect wing kinematics [31–34].

## 1.4 Flapping Flight Research

The flight of insects has intrigued scientists for some time because, at first glance, their flight appears infeasible according to conventional linear, quasi-steady aerodynamic theory. Research on flapping wing flight can be broadly categorized

into experimental studies and analytical studies.

### **1.4.1 Experimental studies**

Experimental studies have been conducted on live animals or by using scaled-up flapping models. Measurement of wing properties and structure can be obtained using dead animals. However, measurement of wing kinematics and flow visualization require the animal to fly in a particular flight state, hovering or forward flight. Needless to say, inducing a fly or a moth to carry out a required task is a difficult proposition.

#### **1.4.1.1 Experiments on live animals**

Measurements of wing kinematics have generally been carried out using a system of high speed cameras to capture the free flight of an insect within an enclosure [27]. Based on calibration grids, the motion of the wings can be deduced from the images captured by the cameras, regardless of the position of the insect. Willmott and Ellington [28] used high speed videography to determine the wing kinematics of a hawkmoth in hover and forward flight. Lift and drag coefficients of hawkmoth wings and bodies were also measured [35]. Wang et. al. [30] measured the kinematics and, torsion and camber deformation of dragonfly wings in flight. Liu [36] measured the wing shape and kinematics of level flying seagulls, cranes and geese. The kinematics were deduced from video of the birds in level flight.

In order to qualitatively and quantitatively understand bird flight several flow

visualization and force measurement studies have been conducted on live birds. Spedding et. al. [37] studied the vortex wakes behind a nightingale trained to fly in a wind tunnel. Usherwood et. al. [38] embedded pressure transducers and accelerometers in the wings of geese to study their take-off. Hedrick et. al. [39] embedded accelerometers in the wings of cockatiels, which were trained to fly in a wind tunnel. Wing kinematics were also measured using a high speed camera. Usherwood et. al. [40] obtained pressure measurements from transducers embedded in the wings of pigeons. However, embedding transducers in live insect wings appears infeasible because of their extremely small sizes.

Several flow visualization studies have also been conducted on live insects. Srygley and Thomas [41] trained Red Admiral butterflies to fly to and from artificial flowers through a wind tunnel. Smoke-wire flow visualization was carried out to obtain a qualitative image of the flow around the wings. A number of unconventional lift generating mechanisms were reported, including leading edge vortices, rotational circulation and the ‘clap-fling’ mechanism. Thomas et. al. [42] carried out flow visualization studies on free-flying and tethered dragonflies. A leading edge vortex of constant diameter, extending from wing-tip to wing-tip, was reported on the fore-wing during free-flight, when the wings were in counterstroke i.e., the fore-wings were leading the hind-wings by a phase angle of  $180^\circ$ . In a high acceleration maneuver, the wings beat in phase with each other with a leading edge vortex extending from the fore-wing to the hind-wing. Bomphrey et. al. [43] conducted flow visualization and force measurements on a tethered hawkmoth in a wind tunnel. The leading edge vortex was found to extend from wing-tip to wing-tip over the insect thorax.

The measured upward force showed a peak near the end of the downstroke, when the leading edge vortex was present on the wing.

Lehmann and Dickinson [44] carried out tests on tethered fruit-flies in which the flight force production was modulated in response to vertically oscillating visual patterns. When the thrust equaled body weight, the variations in stroke amplitude and frequency were found to be respectively,  $2.7^\circ$  and 4.8 Hz around their mean value. However, at peak thrust, the wing kinematics were found to be limited to a unique value of stroke amplitude and frequency. This suggests the existence of an optimum value of stroke amplitude and frequency for maximum thrust production. Also, very small changes in these stroke parameters are utilized by fruit-flies to vary their flight forces. Dillon and Dudley [45] studied vertical force production by tethered bees over a wide range of body mass. Heavier bees were found to produce lower thrust and operated at a lower flapping frequency, although the stroke angle did not change with body mass.

A few studies have been conducted on the material properties and structure of insect wings. Song et. al. [46] studied the dimensions and elastic properties of the forewing of a Cicada. The Young's moduli of the wing membranes and veins were found to be 3.7 GPa and 1.9 GPa, respectively. These values are quite low as compared to metals or composite materials. Combes and Daniel [47, 48] measured the flexural stiffness of insect wings and found that the spanwise flexural stiffness was 1-2 orders of magnitude higher than the chordwise flexural stiffness. A finite element analysis showed that this variation was primarily because of the leading edge veins.

Although these studies provide qualitative and quantitative insight into insect and bird flight, researchers have looked at other means of studying animal flight in a controlled laboratory environment. This is because of the difficulty involved in conducting such experiments on insects and also because tethering an animal or having sensor wires trail from it can alter the performance of the animal.

#### 1.4.1.2 Model experiments

Researchers have studied large, slow-moving models in order to understand the physics of flapping wing flight. Dickinson and Gotz [31] experimentally measured the forces acting on a flat plate, translating and rotating in a sucrose solution at a Reynolds number varying from 75 to 225. Such low Reynolds numbers are characteristic of the Fruit Fly *Drosophila Melanogaster*. Their experiments showed the transient forces acting on a wing which is accelerated from rest to a constant velocity. At high pitch angles, initial values of the lift coefficient were found to be higher than the steady values. The flow pattern was also very unsteady at high pitch angles, with an alternating pattern of leading and trailing edge vortices. Van den Berg and Ellington [32] developed a model 'flapper' using four d.c. servo motors and an elaborate gearbox. This model could accurately mimic the wing motions of a Hawkmoth. The wings were 46.5 cms long and were flapped at a frequency of 0.3 Hz in order to match the operating  $Re$  to that of a real Hawkmoth. A leading edge smoke rake was used to visualize the flow pattern. A leading edge vortex was observed on the wing with a 3D structure, smaller towards the wing root and larger out-

board [33]. Recent experiments conducted on a dynamically scaled model (Robofly) have shown that insects must take advantage of unsteady aerodynamic phenomena to generate thrusts greater than those predicted by quasi-steady analyses [34]. Figure 1.5 shows the typical motion of an insect wing. This motion mainly consists of four parts: a) downstroke, in which the wing translates with a fixed collective pitch angle, b) near the end of the downstroke the wing supinates so that the blade angle of attack is positive on the upstroke, c) upstroke and, d) pronation at the end of the upstroke so that the angle of attack is positive on the downstroke. Figure 1.6 illustrates the unsteady phenomena exploited by insects to generate and control high lift. During the downstroke and upstroke (i.e. the translational phases) high lift is produced because of a leading edge vortex on the wing. Supination and pronation also produce significant lift from rotational circulation, which is also known as Kramer effect. The third effect, wake capture, occurs as the wing passes through its own wake, created during the previous half-stroke [34]. Sane [49] provides a review of the aerodynamics of insect flight based on these experiments.

The Robofly experiments have shown that the leading edge vortex is the key to explaining the high thrust generated by insects at low chord Reynolds numbers ( $Re \sim 150$ ). At high  $Re$ , stable leading edge vortices have been observed on sharp edge delta wings at high angles of attack. On these wings, the leading edge vortex is stabilized by spanwise flow through the vortex core. Based on this analogy, the presence of the attached leading edge vortex on the wing has sometimes been explained by the presence of spanwise flow through the vortex core that transports vorticity from inboard to outboard regions of the wing [50]. However, Birch et al. [51]

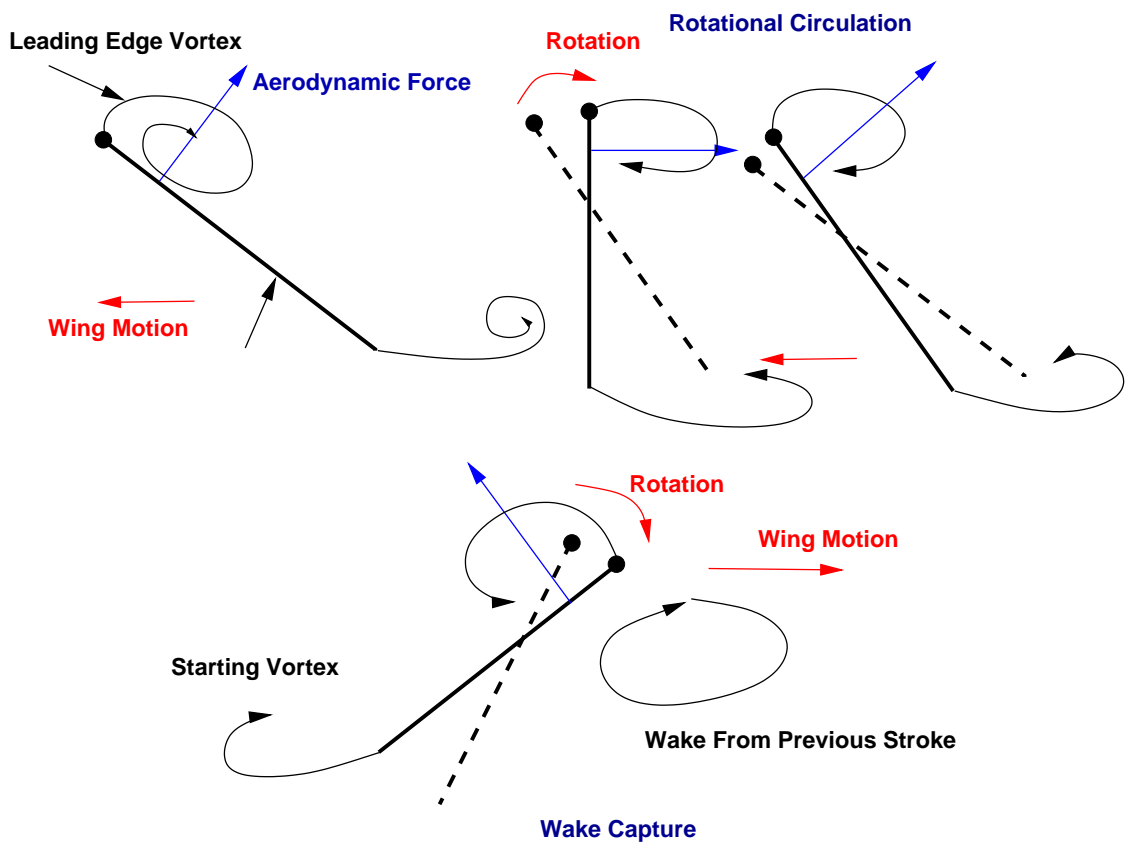


Figure 1.6: Unsteady lift generating mechanisms in insects.

have shown that although spanwise flow does exist on the Robofly wings at an  $Re$  of 1,400, it is absent at a lower  $Re$  of 120. Ellington and Usherwood [50] also showed that in rotary wing experiments conducted at  $Re$  from 10,000 to 50,000, the lift coefficients at high  $Re$  dropped significantly as compared to lower  $Re$ , indicating a weaker leading edge vortex at high  $Re$ . Recent flow visualization studies conducted at a higher  $Re$  ( $\sim 15000$ ) suggest that the vortex is not stable on the wing and that multiple vortices may be generated during the stroke [52]. Thus, the effect of  $Re$  on the leading edge vortex is not clearly understood. This is significant because of the fact that flapping wing MAVs operate in the Reynolds number range  $10^3 - 10^5$ .

In their experiments, Dickinson et. al. [34] decoupled the effects of wing translation and rotation, which could be predicted reasonably well using a quasi-steady model. Using such a quasi-steady model, the effects of translation and rotation were subtracted from the total measured force. The remaining forces were attributed to wake capture caused by the interaction of the wing with its own wake. Birch and Dickinson [53] also showed that a quasi-steady approximation of wake capture was not accurate since this is a truly unsteady effect. Sane and Dickinson [54] carried out a study on the effect of wing kinematics on thrust and drag. With short, symmetrical wing flips, the thrust was highest for a wing stroke of  $180^\circ$  and an angle of attack of  $50^\circ$ . Symmetrical flips were also found to produce high thrust and a quasi-steady model predicted the time averaged thrust accurately although it did not capture the time variation of vertical force. Maybury and Lehmann [55] studied the interactions between scaled up dragonfly wings operating in a liquid medium. Fore-wing performance was found to be unaffected by any changes in the phase

relationship between fore and hind-wing flapping. However, the hind-wing lift production varied by a factor of two depending on the relative phasing of the flapping cycles of the two wings. Lehmann et. al. [56] have also used such a model to study the ‘clap-fling’ mechanism.

Based on the Robofly experiments, an ambitious project was started to build a centimeter sized, 0.1 gram micro-robot called the Micro-mechanical Flying Insect (MFI). Figure 1.7 shows a conceptual design of the MFI. The design target for the MFI is the blowfly *Calliphora*, which has a mass of 100 mg, wing span of 11 mm and a flapping frequency of 150 Hz [57]. Considerable amount of research has been done on the wing actuation mechanism and a prototype MFI exists. The wing transmission consists of two four-bar mechanisms, each actuated by a piezo unimorph, which flap the wing in a horizontal stroke plane [58]. The four-bar mechanism magnifies the relatively small amount of motion of the piezoelectric unimorph actuator to flap the wing spar at a high stroke amplitude. These four-bars actuate the wing root at two points along the chord. When the four-bars are actuated in phase, the wing moves with a constant pitch angle. To change the wing pitch angle the four-bars are actuated out of phase. Sitti et. al. [59] describe the development and characterization of piezoelectric unimorph actuators for the MFI. A stroke amplitude of  $180^\circ$  was achieved at 95 Hz frequency using a PZT-5H unimorph. Wood et. al. [60] used composite materials to construct the MFI body achieving a high strength, low mass structure that was easier to construct. Considerable amount of research has focused on the design of a sensing and control system for the MFI [61–67]. These studies focus on the development of bio-inspired sensors for the MFI using Ocelli for

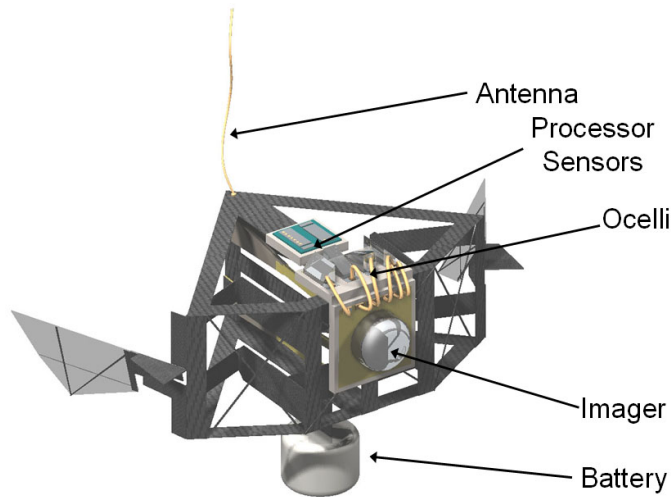


Figure 1.7: Artists conception of the MFI (R.J. Wood).

insect like vision and Halteres for attitude sensing and control. However, all these control studies rely on the Robofly measurements for the aerodynamic characteristics of such flapping wings. The use of such a simplified aerodynamic model to carry out control system design is questionable. The Polyimide wings of the MFI weigh 0.5 mg. There are no available studies on the structural and aerodynamic design of these wings. Flapping at such high frequencies, these light-weight, flexible wings must deform considerably. Thus, aeroelastic design of the wings can improve their aerodynamic efficiency.

Aeroelastic effects in ornithoptic or bird-like flapping have been studied experimentally to a much greater extent. Since the primary function of such flapping wings is propulsion, these experiments tend to focus on the propulsive efficiency of flapping airfoils. Shyy et.al. [25] provide a review of scaling laws, measurement of wing kinematics of birds, low  $Re$  aerodynamics and flexible wing based flapping

flight. The effect of wing flexibility on ornithopter performance is quite well recognized since all flying ornithopter models have very flexible wings. Ho et. al. [68] studied the effect of wing spanwise stiffness on the lift generated by ornithoptic wings in a free-stream flow. A computational fluid dynamics model coupled with an FEM model was used to study the aeroelasticity of ornithoptic wings. Flexible membranes were found to improve lift by minimizing the negative force peaks. Heathcote et. al. [69] studied the effect of chordwise wing flexibility on the propulsive efficiency of a wing undergoing pure heaving motion at zero freestream velocity. The thrust to power ratio was found to be greater for the flexible wings as compared to a rigid wing. Heathcote and Gursul [70] measured the thrust coefficient of plates of different thicknesses, flapping at different frequencies, in freestream Reynolds numbers from 0 to 27000, in a water tunnel. Again, some amount of flexibility was found to be beneficial in generating thrust. Heathcote et. al. [71] studied the effect of spanwise flexibility on thrust of a flapping wing. Some degree of spanwise flexibility was found to be beneficial but, for a highly flexible wing, the tip displacement lagged the flapping motion at the wing base, causing a loss of efficiency. Hong and Altman [72] experimentally measured the lift force of a wing in pure flapping motion at zero free-stream velocity. The generation of lift in the absence of any free-stream velocity was attributed to span-wise flow. A non-planar wing with spanwise camber was found to generate greater lift than a flat plate wing. Beasley and Chopra [73] also found that a non-planar wing, with tip anhedral and a polynomial planform, performed better than planar wings. Jones and Platzer [74] carried out an experimental and numerical study on flapping wing propulsion. Several flapping configurations were

investigated including, a single airfoil flapping in a freestream velocity and two airfoils in opposing plunge similar to ‘clap-fling’. Additional non-moving airfoils were also placed downstream of the flapping airfoils to study interference effects. The thrust was found to be maximum at zero flight speed. Jones et. al. [75] describe the thrust measurements and flow visualization on a flapping wing MAV using two airfoils in opposing plunge to generate thrust. The flexibility of the wing mount was altered to investigate aeroelastic effects. Although the wing itself was quite flexible, the flexible mount showed an increase in thrust upto a frequency of 20 Hz, beyond which, a semi-rigid and rigid mount generated greater thrust. Jones and Platzer [76] describe the development of their MAV based on this concept with a maximum dimension of 23 cm and a mass of 11 grams. These studies clearly indicate that aeroelastic design of flexible wings is very important for flapping flight.

### 1.4.2 Analyses

The development and validation of a comprehensive theory for unsteady force generation by hover-capable flapping wings is partly hindered by a lack of experimental data at the chord Reynolds numbers of interest ( $10^3 - 10^5$ ). Most of the analytical studies on the aerodynamics of flapping wings have examined rigid wings. Some of these studies look at ornithoptic or bird-like flapping, i.e., flapping without the pronation and supination phases of insect-like flapping. Some are restricted to small disturbances while others are computationally intensive CFD simulations. DeLaurier [77] developed an aerodynamic model for ornithoptic flapping, which has

been applied to the aeroelastic analysis of a large-scale ornithopter [78].

Analytical studies on the aerodynamics of hover-capable flapping may be classified as quasi-steady models, reduced order models, unsteady vortex lattice models and Computational Fluid Dynamics (CFD), in order of increasing complexity. Quasi-steady analyses can be used to model the aerodynamics of flapping wings provided experimentally measured lift and drag coefficients are used [79]. However, these analyses do not account for unsteady effects such as the starting vortex or wake capture [53]. Reduced order models utilize indicial functions to quantify the effects of unsteady wing motion on airloads [80]. The unsteady vortex lattice method and vortex particle methods have also been applied to flapping wing systems [81, 82]. Vest and Katz [83] used an unsteady vortex lattice model to study the aerodynamics of bird flight. Eldredge [84] studied a 2-D wing undergoing large amplitude flapping-pitching motion using a vortex particle method. The leading edge vortex and starting vortex were observed from the resulting vorticity distribution.

CFD methods, which solve the incompressible form of the Navier-Stokes equations, are computationally intensive but they provide a clearer picture of the flow [85–87]. Liu et. al. [88] carried out a CFD study of Hawkmoth wings undergoing both flapping and rotational motions using an incompressible solver. Ramamurti and Sandberg [86] used a finite element based flow solver to study the forces on a model fruit-fly wing. The effect of phase difference between the flapping and rotational motions was studied. High thrust was obtained when wing rotation occurred before stroke reversal. Sun and Tang [89, 90] used CFD to predict the forces measured in the RoboBee experiments. Wu and Sun [91] used this analysis to study the effect of

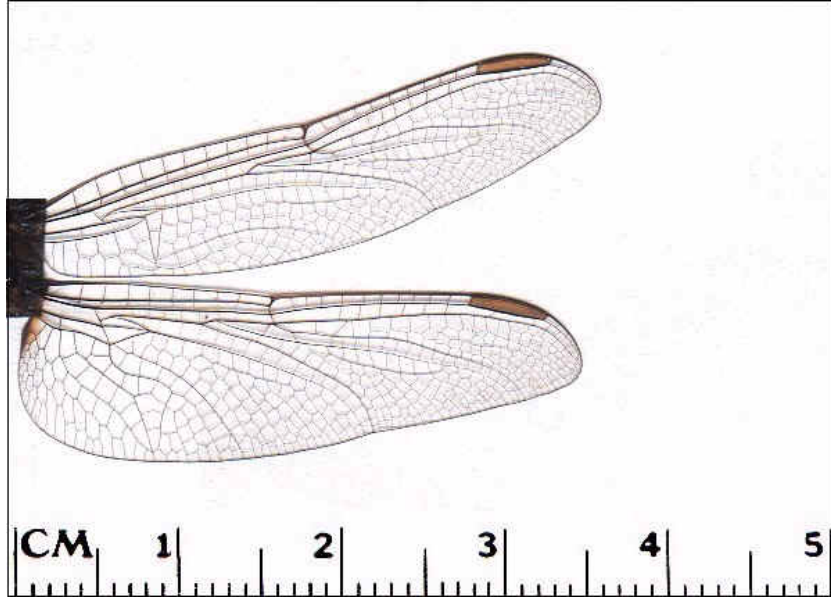


Figure 1.8: Dragonfly wings.

various non-dimensional parameters such as  $Re$ , stroke amplitude and mid-stroke angle of attack on the lift and drag coefficients. Sun and Wu [92] studied power requirements in forward flight using this model. For comparison with experimental data, these studies rely on model experiments conducted at very low frequencies. For this reason, these analytical models do not account for aeroelastic effects caused by wing bending and twisting under inertial and aerodynamic loading.

An important feature of insect wings is that they can elastically deform during flight. Also, unlike birds or bats, insect muscles stop at the wing base so any active control of the wing shape is not likely [93, 94]. Figure 1.8 shows the wings of a dragonfly. These wings consist of veins covered with membranes, and are devoid of any muscle. Passive aeroelastic design is therefore very important for insect wings. The Robofly measurements are based on very low frequencies of motion because the fluid used has a high viscosity. Thus wing bending and passive aeroelastic effects

are likely to be very small in the Robofly experiments.

## 1.5 Need for New Experimental Data

There are two major shortcomings of previous studies on insect-based, hover-capable flapping wings. First, because of the mechanical complexity involved in replicating the wing kinematics, these tests were conducted on scaled-up models in a liquid medium. Thus the operating frequencies of these models is so low that wing flexibility is not expected to play an important role. However, a practically viable flapping wing MAV would require light-weight wings which would be quite flexible. Second, the majority of such tests were conducted at low to very low  $Re$  (100-1000). Based on their size, MAV  $Re$ 's lie between  $10^4$ - $10^5$ . Thus, there is a lack of experimental data and testing in a Reynolds number range suitable for MAVs.

## 1.6 Need for Aeroelastic Modeling

With highly flexible wings operating at high frequencies, wing deformations are expected to be quite significant. The effect of these deformations on wing performance needs to be modeled and quantified. Experiments conducted on insect wings suggest that their deformations are primarily caused by inertial forces, while aerodynamic forces are an order of magnitude smaller and hence, they do not contribute to the wing deformations [95]. If this is infact the case, it would be a double edged sword, because, from a computational point of view, the wing structural and

aerodynamic analyses could be uncoupled. However, from an experimental point of view, the small aerodynamic loads cannot be easily measured, especially in the presence of large inertial forces.

Even though the aerodynamic forces may be small enough to neglect their effect on wing deformations, wing deformations will have an effect on the aerodynamic loads. Thus it is important to have a complete aeroelastic model of the system.

Another point of concern is that the aeroelastic model must be computationally efficient, if wing optimization studies are to be carried out. CFD studies are computationally expensive and doubly so when coupled with a detailed computational structural dynamics model. Thus evaluating different wing designs is quite difficult with such analyses.

## 1.7 Objectives and Approach

The objective of this research work is to measure the thrust generated by wings mounted on a flapping-pitching mechanism, flapping at high frequencies in air. For this objective, a force measurement methodology will be developed to measure the inertial and aerodynamic forces acting on the flapping wing. Comparisons of the measured thrust will be made with simple quasi-steady analyses. A more detailed aeroelastic analysis will then be developed to understand the effects of wing elasticity. As mentioned above, this aeroelastic model must be simple and computationally efficient. A finite element model of the wing will be implemented and systematically validated with experimental data. An unsteady aerodynamic model based on indi-

cial methods will be coupled with the structural model to predict the experimentally measured thrust.

## Chapter 2

# Experimental Setup

In this chapter, the bio-inspired flapping wing mechanism used in this study is described. Also, unique force and motion transducers which were mounted on this mechanism are described. This setup was used to measure the thrust generated by the flapping wing mechanism in the hover mode alongwith the flapping and pitching motions at the wing base. A novel mechanism that utilizes the inertial and aerodynamic forces acting on the wing, to produce a passive pitching motion, is also described. Details of a flow visualization setup used as part of another study [52] are also presented.

## 2.1 Bio-Inspired Flapping

Emulating the kinematics of insect or hummingbird wings at high frequencies is a difficult proposition in terms of the mechanical complexity involved. This is because, the required flap and pitch motions have large amplitudes. For example, in insects, the flapping angle in the stroke plane may be as high as  $160^\circ$  with a pitch change which is typically greater than  $90^\circ$ . To achieve this type of wing kinematics,

with the flapping and pitching angles controlled separately, at least two actuation systems must be used, one for flapping and another for pitching. Furthermore, the pitch actuation mechanism must either be mounted on the flapping shaft or, it must be able to actuate the pitch motion of the shaft through its large amplitude flapping. A pitch actuator mounted on the flapping shaft would make the entire assembly too heavy to flap at high frequencies. This is the reason why studies on insect-based flapping wings have been conducted on models flapping in a liquid medium at very low frequencies. In order to mimic insect wing kinematics a novel mechanism is described by Tarascio and Chopra [3]. This bi-stable flapping mechanism is used in the present work.

## 2.2 Bi-stable Flapping Wing Mechanism

The flapping wing test apparatus is a passive-pitch, bi-stable mechanism capable of emulating insect wing kinematics (Fig. 2.1). The desired flapping and pitching motion is produced by a Hacker B20 26L brushless motor, which is controlled by a Phoenix PHX-10 sensorless speed controller in combination with a GWS microprocessor precision pulse generator. The motor shaft is rigidly attached to a rotating disk, which in turn is attached to a pin that drives a scotch yoke. The scotch yoke houses ball ends, which are attached to shafts that are free to flap with the motion of the yoke. As the shaft is actively flapped, pitch actuators, which are rigidly attached to the shaft, make contact with Delrin ball ends at the end of each half-stroke. This causes the shaft to pitch and, hence, generate the wing flip at the end

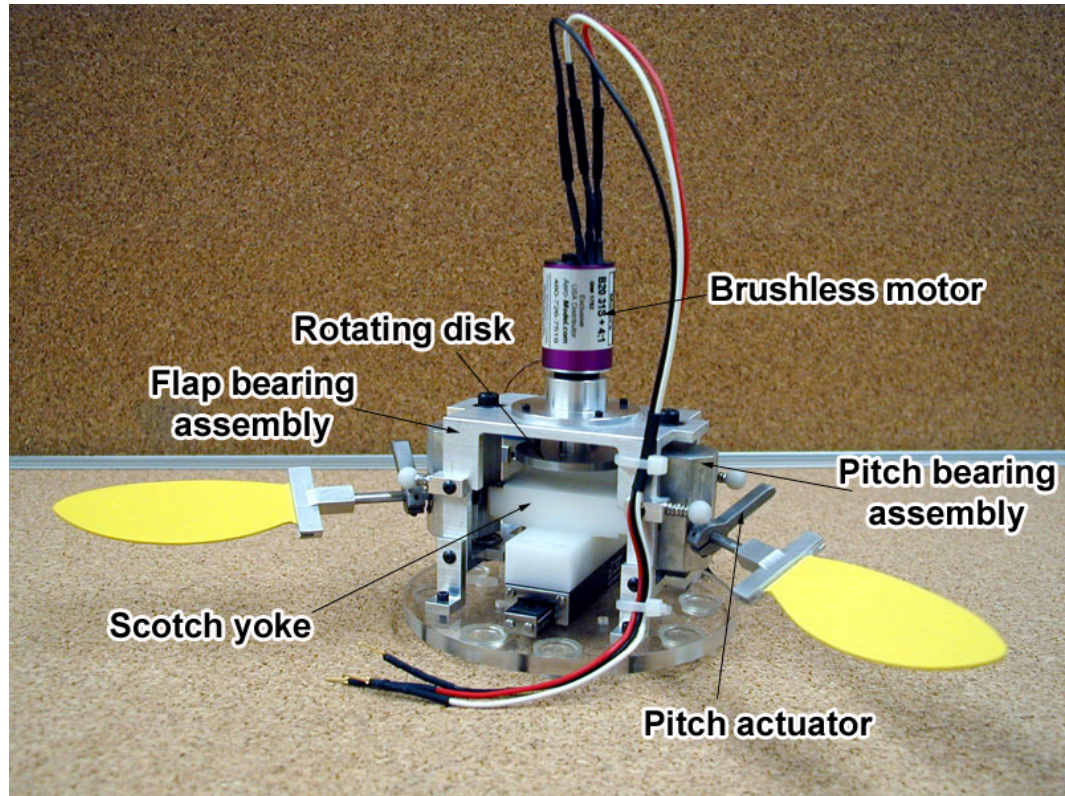


Figure 2.1: Flapping wing mechanism (Concept by M.J. Tarascio [3]).

of the half-stroke.

The rotation of the shaft or “flip” at the end of each half stroke is generated by the pitch assembly, which also serves to fix the pitch angle of the shaft during the translational phases of the wing motion. The pitch assembly consists of the main shaft, which is rigidly attached to a cam, and is, in turn, held in place by a Delrin slider and a compression spring (Fig. 2.2). In combination with the pitch stop, the entire assembly is bi-stable, in that it allows the shaft to rest in only two positions. As the pitch actuator makes contact with the ball stops at the end of each half-stroke, the cam is forced to rock over to the other stable position, with the compression spring holding it in place until the next rotation. This pitch motion

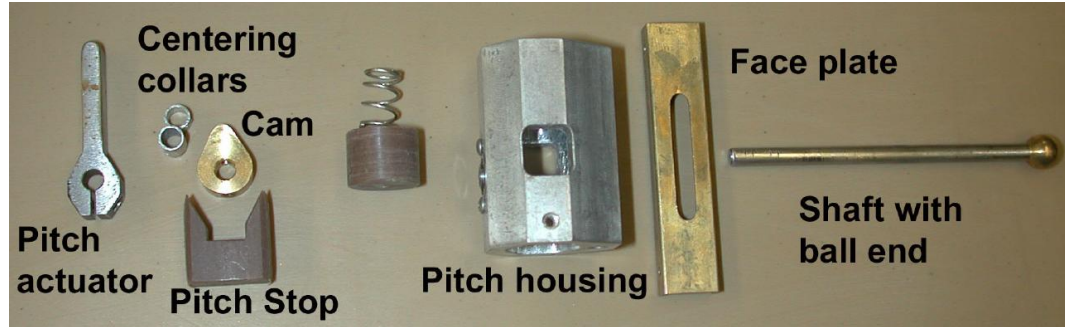


Figure 2.2: Components of the pitch assembly.

is passive, being actuated by the flapping motion of the shaft. The pitch angle of the wing during its translational phases is determined by the shape of the cam and pitch stop shown in Fig. 2.2. Different pitch angles, such as  $30^\circ$  or  $45^\circ$ , can be set using different combinations of cams and pitch stops.

## 2.3 Thrust Measurement

Measurement of the flapping and pitching motions, and the small airloads generated by a wing mounted on the flapping mechanism, poses a significant challenge. The flapping mechanism was initially designed to be mounted on the rotor test stand at the Smart Structures Laboratory at the University of Maryland [3]. Figure 2.3 shows the flapping wing mechanism mounted on this test stand. The test stand consisted of a 1000 gram load cell and a 25 oz-in reaction torque sensor to measure the thrust and torque generated by the mechanism. The vertical force was decoupled from the torque by using a spring-steel diaphragm which did not carry any vertical load and passed only the moment to the torque sensor. A Hall effect sensor mounted on the flapping mechanism, in combination with a magnet mounted

on the rotating disk, was used to determine the flapping frequency. However, tests conducted using this test stand showed significant errors in thrust measurement. Part of the problem was the very low thrust expected from a rectangular wing with a small chord (1.5 cm). This was compounded by the fact that the mechanism itself generated significant vibratory forces when flapping on the test stand. Keeping this in view, it was decided to measure the forces acting on the wing directly at the wing base. However, with this type of measurement, the pitch angle of the wing must also be measured.

Commercially available sensors were found to be either too large or bulky to be used on the flapping mechanism. Figure 2.4 shows some of these sensors. The smallest available force sensors are thin beam load cells. However, these are generally used for uniaxial measurements, whereas, a bi-axial measurement system was needed because of the pitching of the shaft. The smallest potentiometers available for rotary position measurement are too large to be mounted on the flapping shaft. For these reasons, custom built transducers were used to measure the thrust generated by the flapping wings.

### **2.3.1 Force Transducer**

To measure the airloads, a load-cell was designed and built using Entran ESU-025-500 piezoresistive strain gauges. These strain gauges are extremely small, with a length of 1.27 mm and a width of 0.38 mm. The use of piezo-electric elements makes them extremely sensitive, with typical gauge factors of 100 as compared to

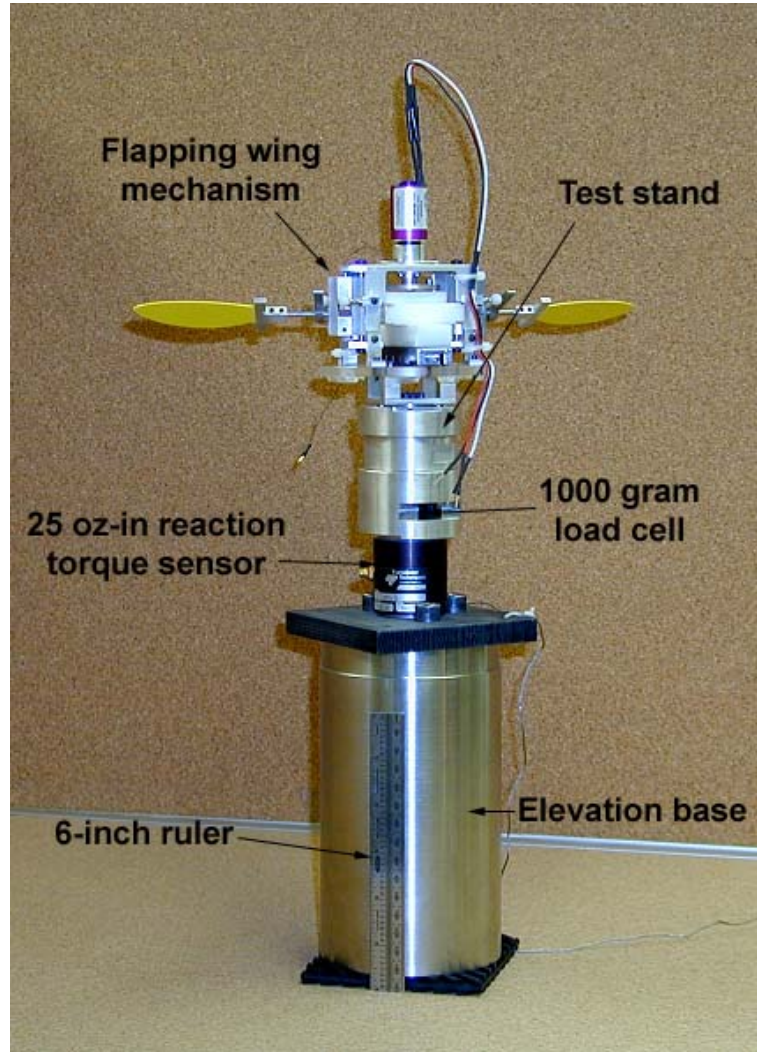


Figure 2.3: Flapping wing mechanism mounted on the rotor test stand.

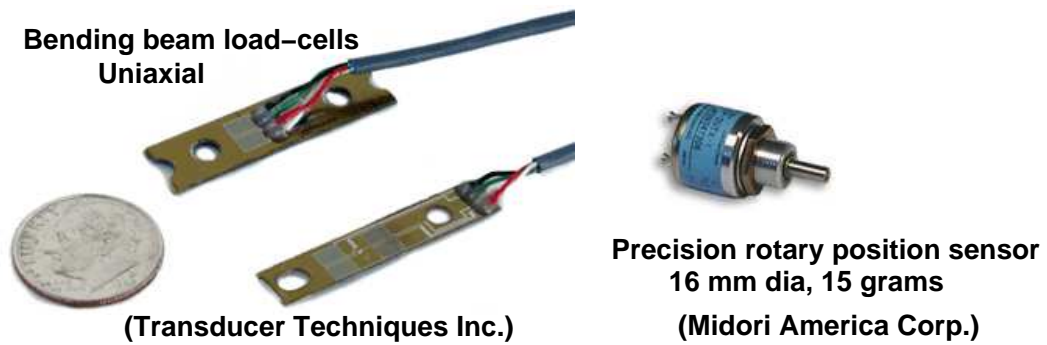


Figure 2.4: Commercially available sensors.

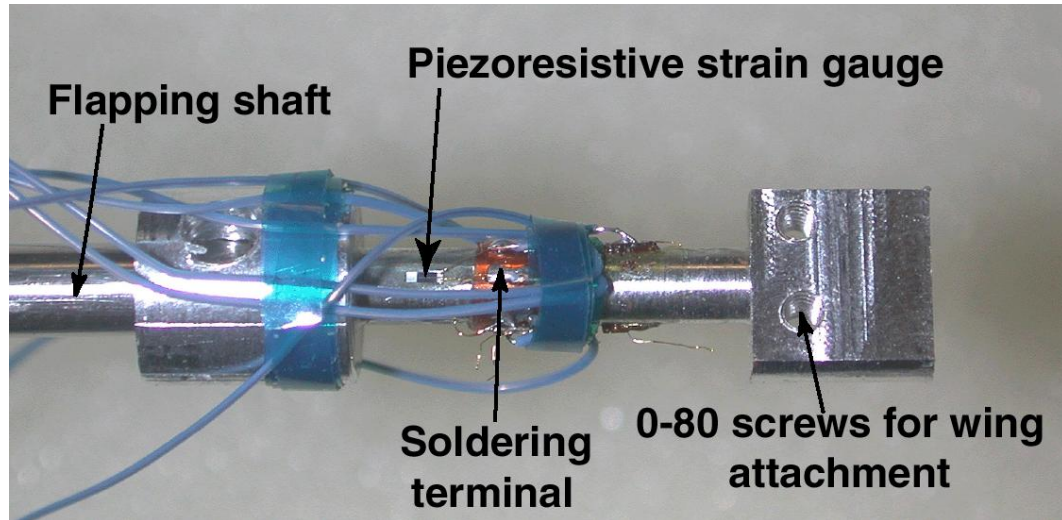


Figure 2.5: Load Cell.

conventional foil gauges which have typical gauge factors of 2. However, piezoresistive gauges have a non-linear response at high strain values. Another disadvantage is their high temperature sensitivity. Keeping these in mind, the load cell was designed and tested to ensure that it operated within the linear range of the strain gauges and temperature effects were minimized.

The load-cell was designed with a narrow beam cross-section (0.1" diameter) on which two strain gauges were mounted to measure the loads in two orthogonal directions (Fig. 2.5). Each strain gauge was connected in a half-bridge configuration with a dummy gauge, which provided temperature compensation. The load-cell was mounted at the end of the flapping shaft, with the wing being mounted at the end of the load-cell.

The initial design of the load cell used a square beam cross-section because it was easier to mount the gauges on a flat surface. Placing, mounting and aligning the miniature gauges by hand was a challenge in itself. Because of gauge alignment

error, the square cross section load cell was found to be unsuitable for testing. This was because, if the gauge was off-center, it introduced couplings between the two orthogonal axes of measurement. Figure 2.6 shows the stresses on square and circular cross-sections with a load at  $45^\circ$  to the horizontal. The strain gauge will show the correct strain only if it is placed accurately at the center of a side of the square. This was difficult to achieve. To minimize this error, a circular cross section was used. On this cross-section, the mid-line of the U-shaped gauges could be aligned with lines marked at  $90^\circ$  intervals on the surface. However, with this cross-section, the gauges did not have a flat surface to bond with. This reduced the useful life of the load cell.

Because strain gauges were used on the load-cell, only the moment acting at the base of the wing was measured. To convert this moment into an equivalent force, the distance from the wing base at which this force acts must be known. The resultant aerodynamic force on the flapping wings was assumed to act at the point defined by the second moment of wing area [27]. This distance,  $r_2$ , was used to determine the forces acting on the wing from the measured moments. These forces were then transformed into vertical and horizontal components using the measured pitch angle. The mean aerodynamic thrust was calculated by taking the ensemble average of the vertical force over a number of flapping cycles.

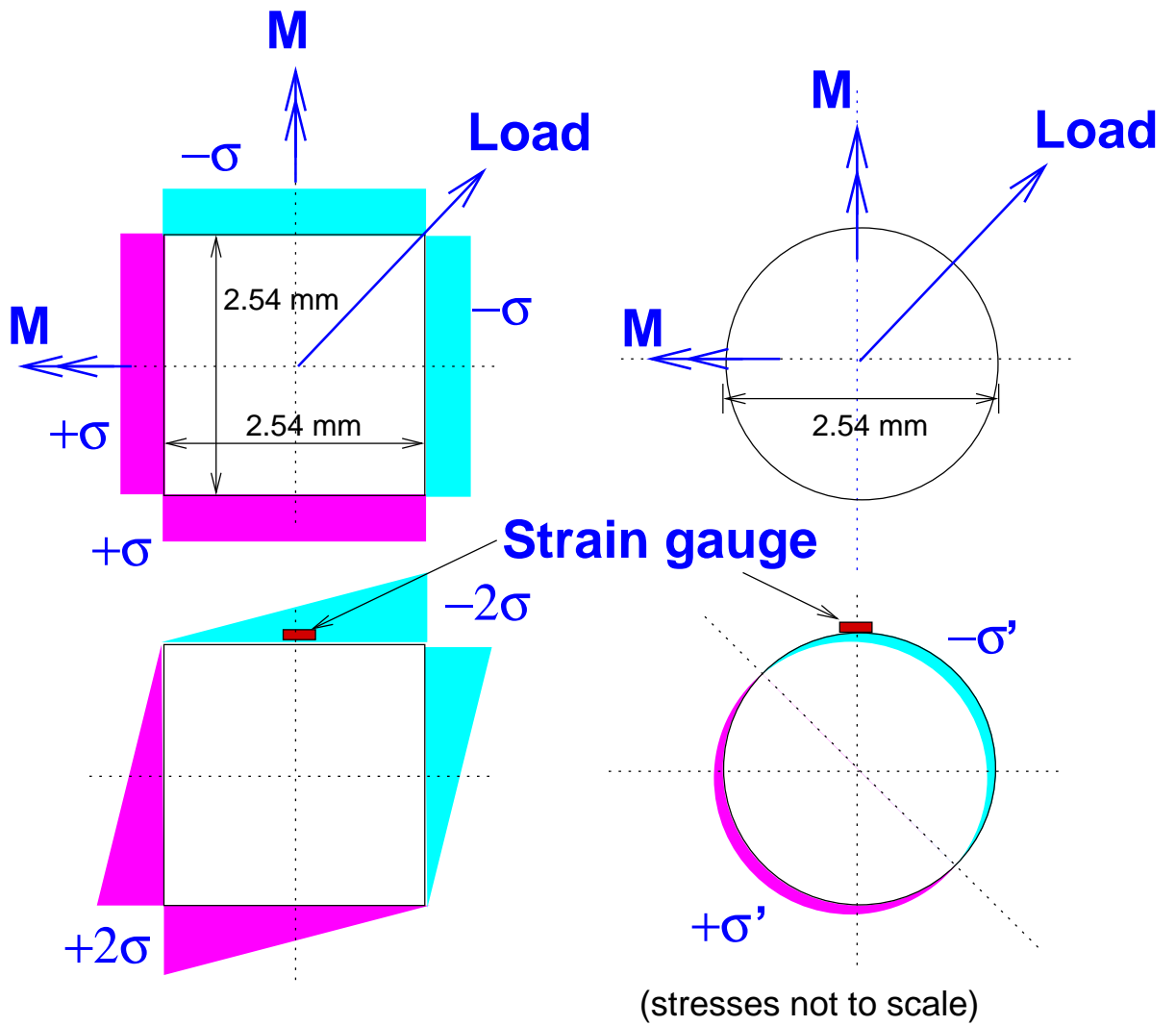


Figure 2.6: Stresses for square and circular cross-sections with a 45° load.

## 2.4 Motion Transducers

The load-cell measured the forces normal and tangential to the wing chord. To obtain the vertical and horizontal components of these forces, the pitch angle of the shaft was measured. This was done by using a Hall effect sensor in combination with a semi-circular disk mounted on the shaft (Fig. 2.7). The disk had a tapered flexible magnet in a semi-circular slot, with the Hall effect sensor mounted on the pitch housing. The pitching motion of the shaft caused the magnet to move in relation to the Hall effect sensor, producing a change in its output. A flexible magnet was used because it could be easily cut to a taper and molded into the semi-circular slot on the disk. In the first generation sensor, ten small magnets were arranged in a semi-circle on the disk, which caused the Hall sensor output to change from its maximum positive value to its maximum negative value every 18 degrees. This required careful manual application of the calibration curve to convert the raw signal into the pitch angle. However, with the tapered magnet, the calibration was simpler because of the monotonic nature of the Hall sensor output.

In addition to a pitch motion sensor, another Hall sensor was used to measure the flapping motion of the mechanism. In this case, another tapered magnet was mounted on the cross-slide of the mechanism, with the Hall sensor fixed to the flap bearing assembly, as shown in Fig. 2.8. Because the taper on the magnet was not very smooth, the calibration was nonlinear for both the motion sensors. The flapping motion was used to determine the flapping velocity, which, when multiplied with the horizontal force on the wing, yielded the total aerodynamic and inertial power.

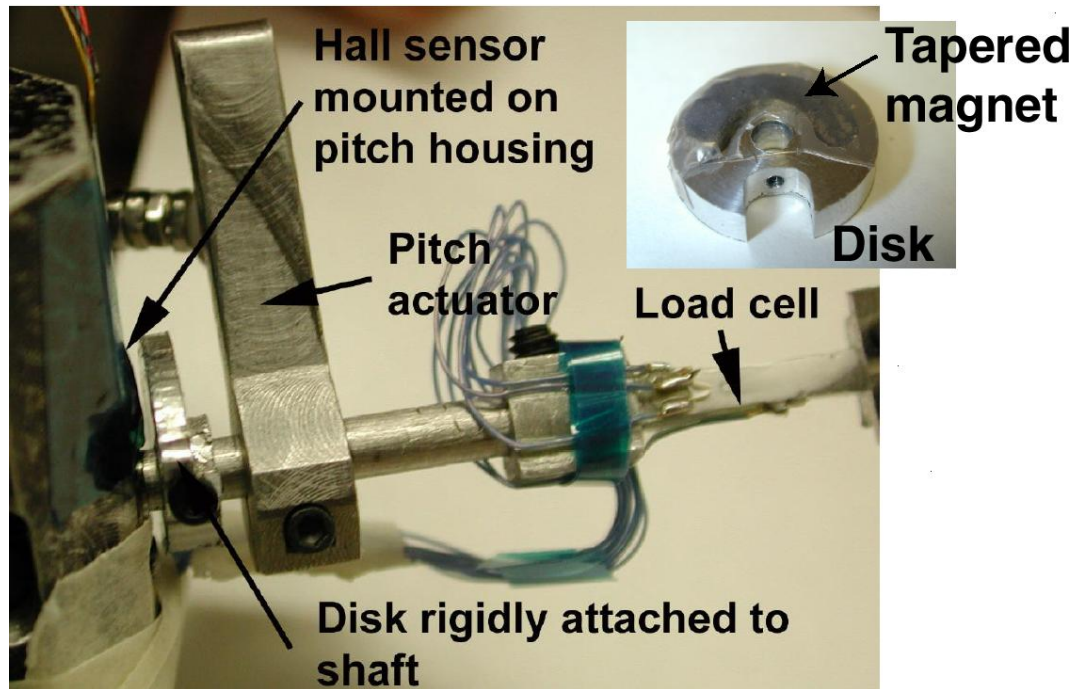


Figure 2.7: Pitch motion sensor.

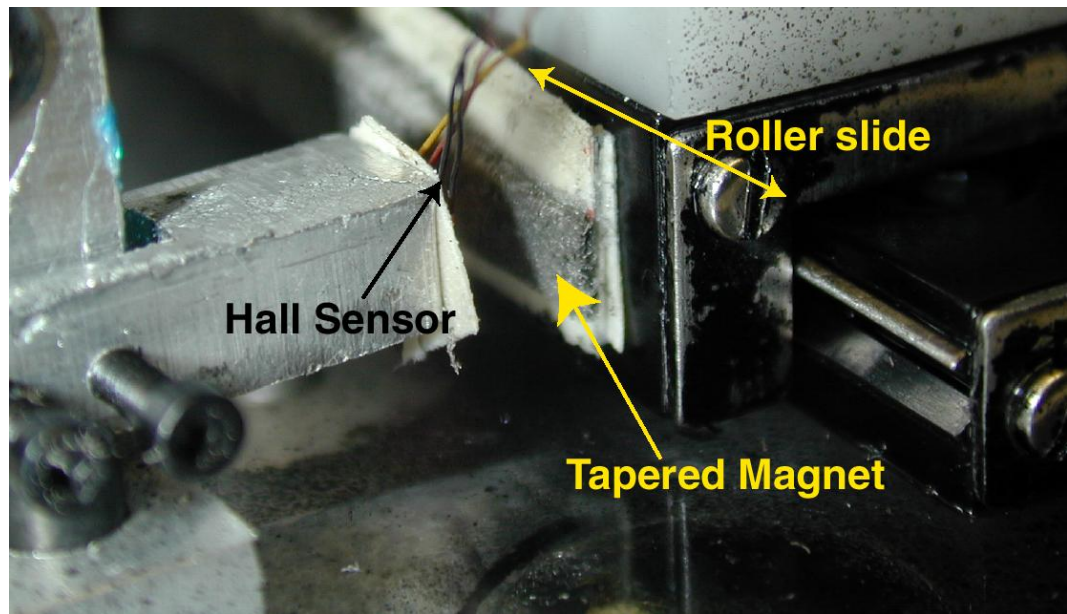


Figure 2.8: Flap motion sensor.

When the flapping motion was differentiated to determine the flapping velocity, it was passed through a low pass filter to eliminate the noise introduced by numerical differentiation.

Two signal conditioning amplifiers (Vishay Measurements, Model 2311) were used to excite the strain gauge circuits and also to amplify the output signal. The Hall sensor outputs were amplified using an instrumentation amplifier (INA 128P). These signals were interfaced with a computer using National Instrumentation (NI) Data Acquisition (DAQ) hardware. The data were acquired using a GUI driven Matlab program to simultaneously acquire and process the signals.

## 2.5 Passive Pitch Mechanism

A major concern with the bio-inspired mechanism described above was the frequency that the wings could be tested at. This frequency was not only limited because of the wing mass but also because of the pitch actuator hitting the ball ends during the wing flip. Initial tests conducted on a pure flap mechanism with the wing chord held vertical showed high thrust. This mechanism could be tested at higher frequencies because there was no active pitching of the wing. Because of this, the flapping wing mechanism was modified to include a torsion spring at the base of the wing. This enabled passive pitching of the wing because of the inertial and aerodynamic forces caused by the flapping motion. Figure 2.9 shows the details of this mechanism. The flapping shaft passed through a set of bearings in the pitch bearing assembly. This enabled the shaft to rotate to any angular position. This

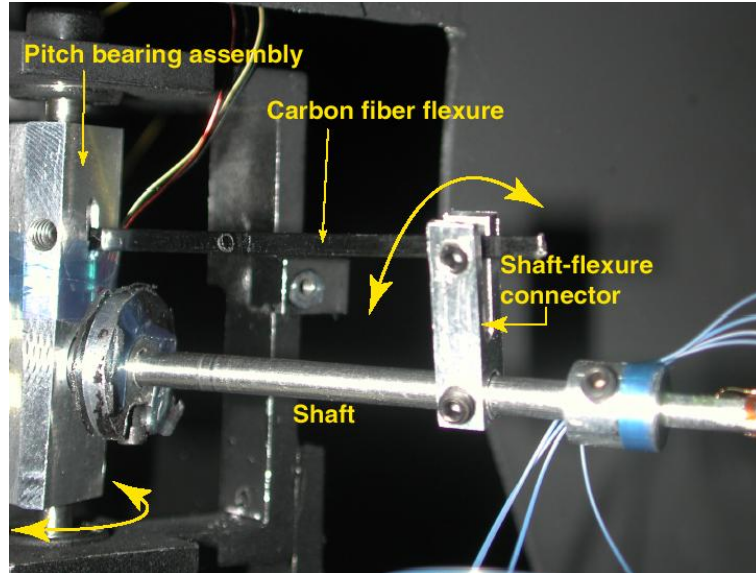


Figure 2.9: Passive pitch mechanism.

rotation was prevented by a torsion spring made from a carbon fiber flexure, which was held rigidly to the shaft. The rotation of the shaft caused the carbon fiber bar to flex, thus providing the torsional stiffness. By moving the shaft-flexure connector further inboard, the torsional stiffness could be increased.

## 2.6 Vacuum Chamber

Initial measurements conducted using the load cell showed that inertial forces contributed significantly to the total measured load. In order to obtain the time variation of airloads during a flapping cycle, the inertial forces had to be determined. A vacuum chamber could provide an air free environment to measure these inertial forces. An existing vacuum chamber, used for testing model rotors, was too large for testing MAVs. Also, in this chamber, the flapping mechanism could not be observed

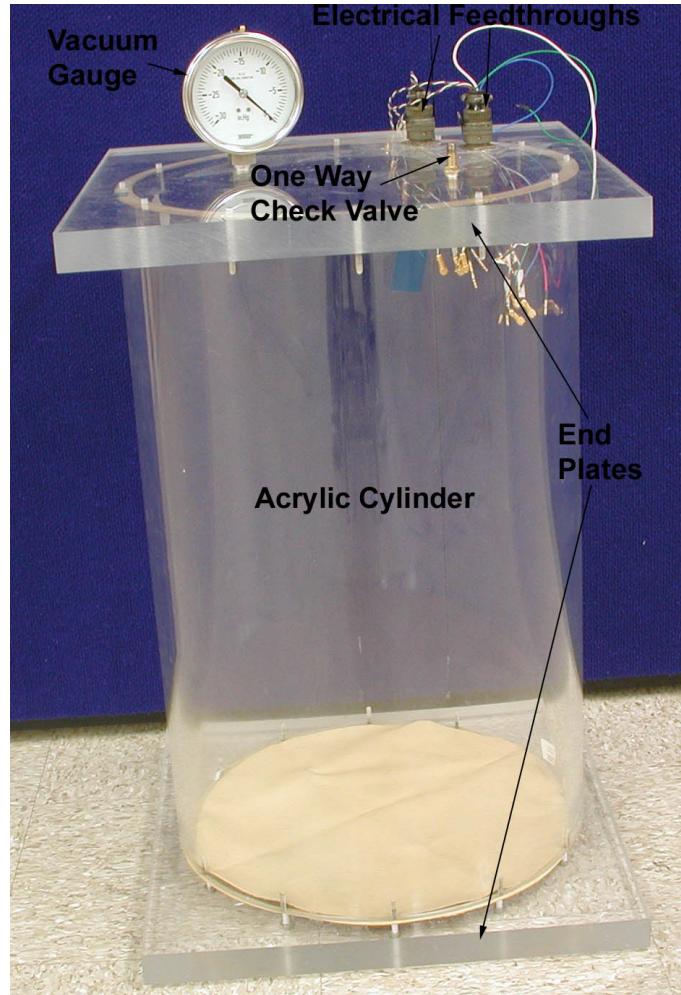


Figure 2.10: Vacuum Chamber

during testing. Because of this, a small vacuum chamber was designed and built using clear acrylic material.

This vacuum chamber was designed and built using a 16" diameter, 1/2" thick acrylic cylinder (Fig. 2.10). At the two ends of this cylinder, holes were drilled and tapped for twelve 10-32 size screws equally spaced around the circumference. Two acrylic plates were tightened on to the ends of the cylinder using these screws, with a rubber gasket in between the end plate and the cylinder. Initial tests with a 0.4" thick acrylic plate showed excessive deformation of the end plate under external

pressure. An axisymmetric finite element analysis of the vacuum chamber was carried out using IDEAS-FEM and 1" thick plates were found to be safe. Initial testing with these thick plates showed that the vacuum chamber could achieve the required vacuum safely and maintain it for at least one hour.

The upper plate of the chamber was fitted with a valve to connect to a vacuum pump. In addition, this plate also had a vacuum gauge and two electrical feedthroughs for connecting the motor, force sensor and motion sensors. All vacuum chamber tests were conducted at a gauge pressure of 27" of mercury, which corresponds to a 90% vacuum.

## 2.7 Flow Visualization

In order to qualitatively understand the unsteady aerodynamic mechanisms involved, a flow visualization study was conducted [52]. The flow visualization test stand consisted of a steel frame bolted to the ground, on which the flapping wing mechanism was mounted approximately 4 ft. above ground level (Fig. 2.11). Aluminum plates extended from ground level to approximately 3 ft. above the mechanism to provide an image plane for the single wing. At the top of the aluminum plates, an aluminum honeycomb extended 2 ft. horizontally. The seed for the flow visualization was produced by vaporizing a mineral oil into a dense fog, which passed through a series of ducts before reaching a diffuser mounted on top of the honeycomb. The diffuser reduced the vertical velocity of the fog, while the honeycomb helped to eliminate any swirl or turbulence in the flow. With the mechanism turned off, the

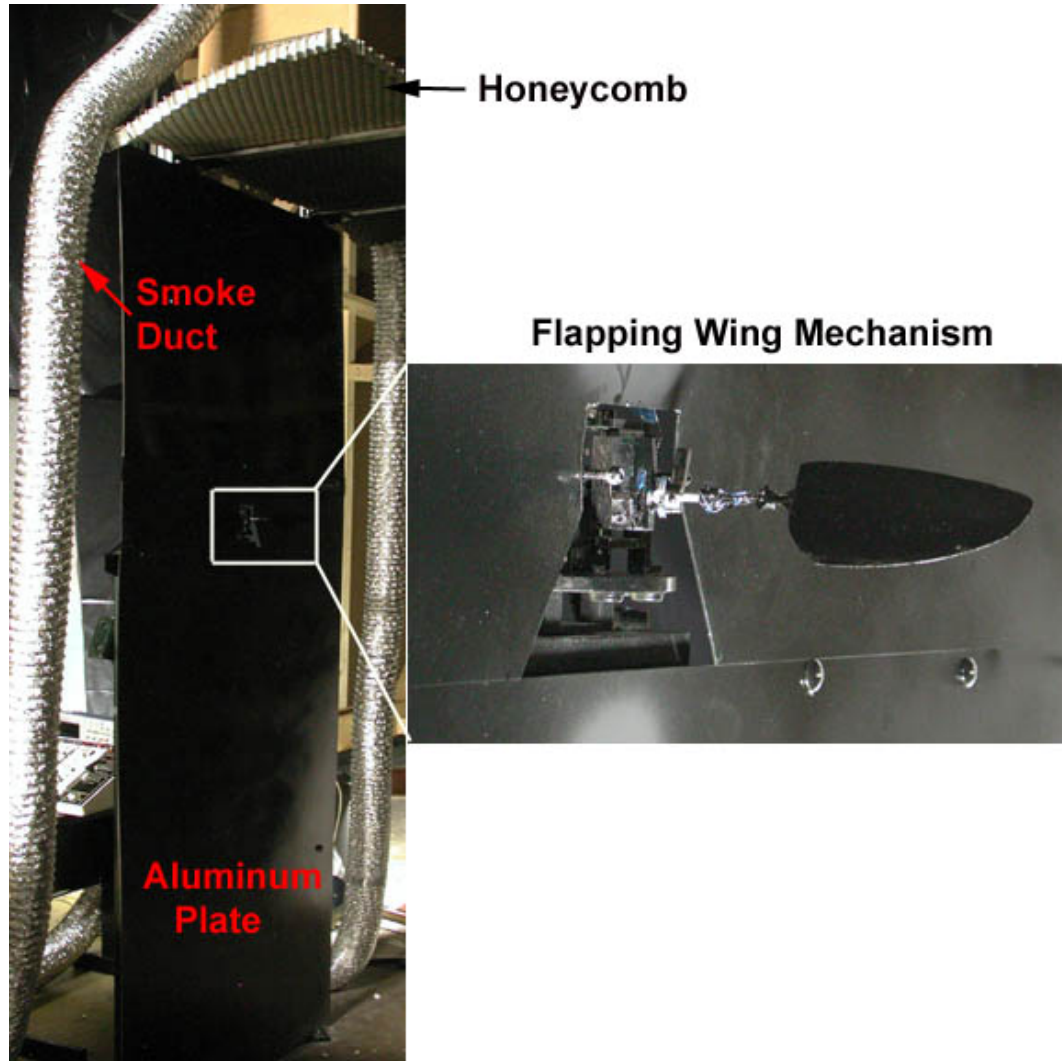


Figure 2.11: Flow visualization test setup.

smoke failed to reach the mechanism. This ensured that the velocity of the smoke itself did not affect observed the flow patterns.

Flow visualization images were acquired by strobing the flow with a laser light sheet generated by a dual Nd:YAG laser, as shown in Fig. 2.12. This laser was triggered once every flapping cycle by a Hall effect switch mounted on the flapping wing mechanism. Images were acquired using a Nikon D-70 6.1 megapixel digital camera that was placed perpendicular to the laser light sheet as shown in Fig. 2.12.

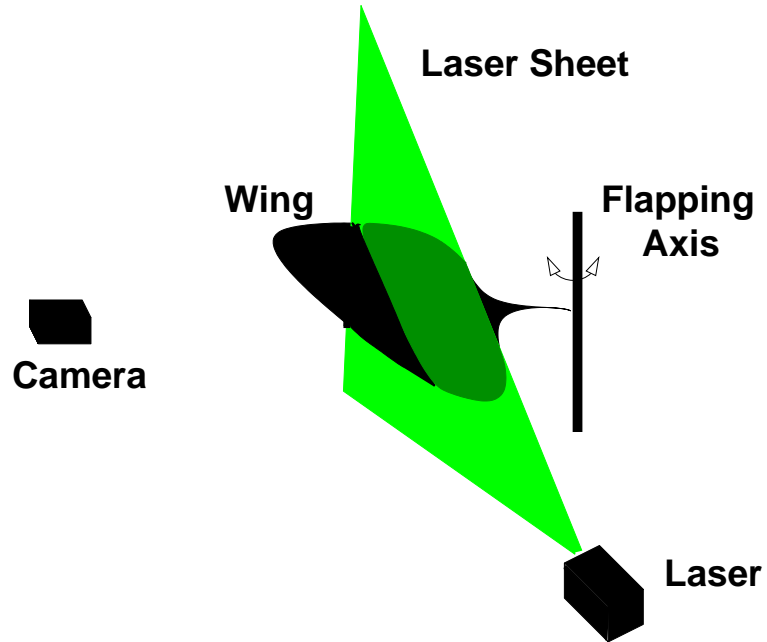


Figure 2.12: Flow visualization schematic.

To produce the seed particles, mineral oil was mixed with nitrogen under pressure and then heated to its boiling point, where it became vaporized. As the vapor emerged from the heat exchanger nozzle, it was mixed with ambient air, rapidly cooled, and condensed into a fog.

## Chapter 3

# Experimental Results

The results of several experimental tests conducted on flapping wing systems are described in this chapter. The following sections describe the thrust measurements carried out on the bio-inspired flapping mechanism using different wings and different stroke parameters. A quasi-steady analysis, implemented using empirical lift and drag data from the Robofly measurements, was used to predict the thrust generated by the wings. High frequency tests carried out on several lightweight wings are also described. Thrust and power were also measured for a novel flapping mechanism with passive pitching caused by aeroelastic forces.

### 3.1 Quasi-Steady Analysis

Experiments have shown that the lift and drag coefficients on flapping wings are higher because of the leading edge vortex [34]. Previous quasi-steady analyses, such as Ellington's [27], did not account for this increased performance and hence could not accurately predict the lift generating capacity of insect wings. However, quasi-steady analyses can explain the lift produced by an insect wing if the effects of

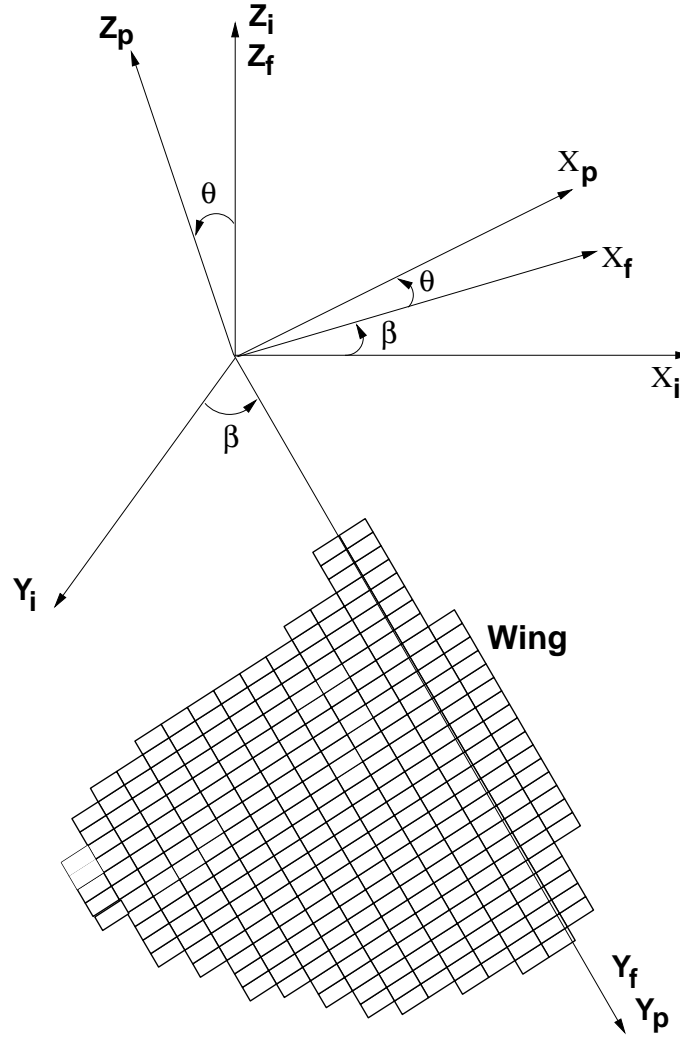


Figure 3.1: Reference frames.

a leading edge vortex, on the lift and drag coefficients, are accounted for. This has led to a revival of quasi-steady models in recent years [49]. However, such models cannot account for the force peaks resulting from the induced inflow and wing wake interactions because these effects are unsteady and three-dimensional in nature [53]. A blade element model similar to the one developed by Walker [79] was used to predict the airloads on the flapping wings. In this analysis, the wing was assumed to be rigid, i.e., the effects of elastic bending and torsion were ignored.

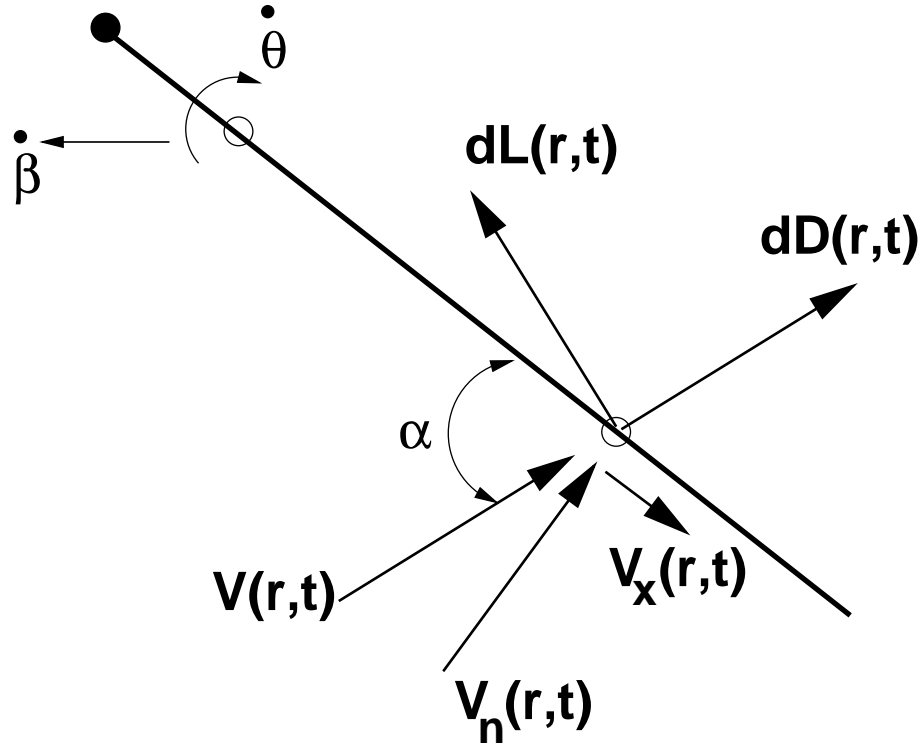


Figure 3.2: Blade element.

The reference frames used to model the motion of the flapping wing are shown in Fig. 3.1. The inertial reference frame  $X_i Y_i Z_i$  has its origin at the center of rotation. The flapping angle  $\beta$  denotes the rotation of the flapping reference frame  $X_f Y_f Z_f$  about the  $Z_i$  axis as shown. The wing pitching reference frame  $X_p Y_p Z_p$  is obtained by rotating the flapping reference frame by the wing pitch angle  $\theta$ , about the  $Y_f$  axis. It must be noted that the reference frames do not follow a right-handed system. However, this allows the x-axis to be along the wing chord, in accordance with thin-airfoil theory.

At a particular instant of time  $t$ , the forces parallel ( $dF_x$ ) and perpendicular ( $dF_n$ ) to the wing chord, at a radial station  $r$ , are given by,

$$dF_n(r, t) = dL(r, t) \cos \alpha + dD(r, t) \sin \alpha \quad (3.1)$$

$$dF_x(r, t) = dL(r, t) \sin \alpha - dD(r, t) \cos \alpha \quad (3.2)$$

where,  $dL(r, t)$  and  $dD(r, t)$  are the circulatory lift and drag which depend on the angle of attack,  $\alpha$ , as given by,

$$\alpha = \tan^{-1} \left( \frac{v_n(r, t)}{v_x(r, t)} \right) \quad (3.3)$$

and where  $v_x(r, t)$  and  $v_n(r, t)$  are the velocities parallel and perpendicular to the wing chord, respectively (Fig. 3.2). Based on thin airfoil theory, these velocities were determined at the 3/4 chord location, which was found to give good agreement with experimental results for the Robofly wings (for lift resulting from translation and rotation). It must be noted that the velocities  $v_x(r, t)$  and  $v_n(r, t)$  were determined based on kinematics alone, i.e., the induced inflow was not included in the analysis. Although this is a serious shortcoming of the analysis, this model was found to give good correlation with experiment [79]. The forces  $dF_n$  and  $dF_x$  were transformed to the flapping reference frame through the pitch angle  $\theta$  to determine the vertical and horizontal circulatory forces.

Non-circulatory forces generated by the acceleration of the wing in a direction perpendicular to the chord were calculated and added to the circulatory forces. The non-circulatory force ( $dF_{nc}$ ), acting perpendicular to the wing chord, is given by,

$$dF_{nc} = \frac{\pi \rho c(r)^2}{4} \dot{v}_n dr \quad (3.4)$$

where,  $\rho$  is the density of the fluid,  $c(r)$  is the chord at radial station  $r$ , and  $v_n$  is the velocity normal to the wing chord, determined at the mid-chord location.

## 3.2 Hover Stand Tests

Initial tests were conducted on the hover test stand used for testing MAV rotors. The wings used had a rectangular planform with 15 mm chord and 80 mm span [3]. These wings, cut from a titanium plate, were quite heavy. This limited the maximum frequency that could be achieved on the flapping mechanism. Figure 3.3 shows the thrust measured on the hover test stand using this wing. Thrust prediction, made using the quasi-steady analysis, is also shown on this plot. Although, the measurement error was quite large, it was surprising that the quasi-steady analysis, with empirical lift and drag data, could at the very least, predict the range of thrust expected from the wing. Three important conclusions were drawn from this test.

1. The mass of the wing caused significant reduction in the frequency at which the mechanism could be operated. With the solid titanium wing, the frequency was limited to nearly 7.5 Hz.
2. The total thrust produced by the rectangular wing was too low to be measured accurately on the hover test stand. The thrust predicted by the analysis was also low.
3. The measurement errors were too large. This was mainly because of the large vibratory loads on the test stand caused by the operation of the mechanism. Infact, the data obtained from the load cell did not show any periodicity and appeared to be white noise.

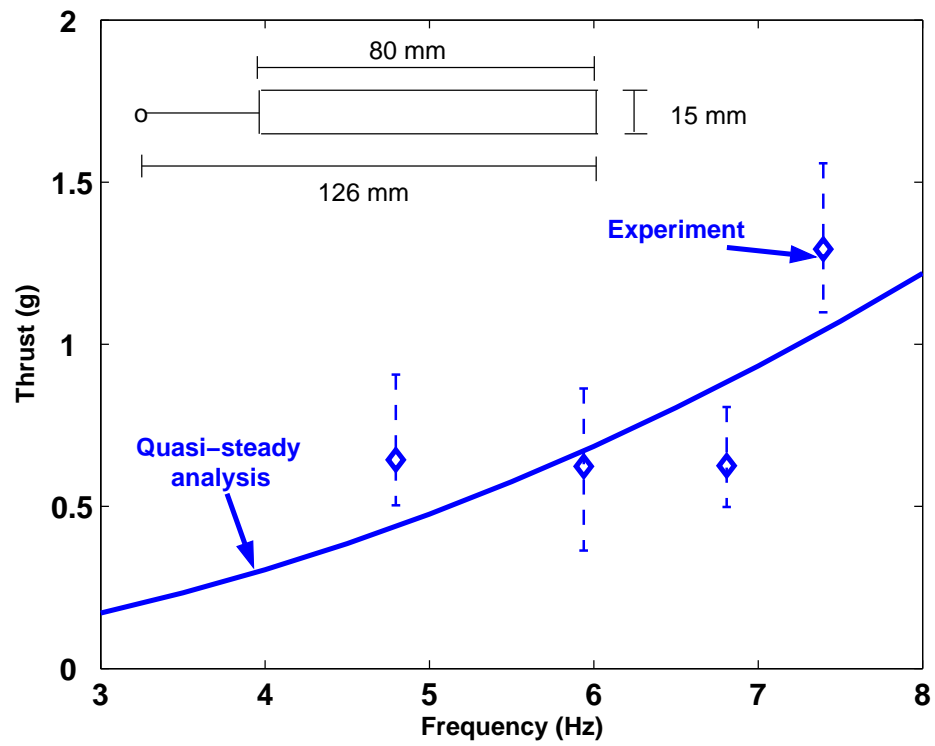


Figure 3.3: Thrust measured on the hover test stand for a rectangular wing.

Because of the large vibratory loads generated by the mechanism, it was decided to measure the forces generated by the wing directly at the wing base. This was accomplished using the load cell described in Chapter 2. Also, the wing planform was modified by increasing the total wing surface area to increase the thrust generated.

## **Wing planform**

Based on the above observations, it was clear that, to achieve high thrust, the wing must be light-weight and have a greater surface area than the rectangular wing. The quasi-steady analysis also showed that a larger chord would increase thrust by increasing the rotational circulation. The detailed structural and planform design of a flapping wing was beyond the scope of the present work. Also, no guidelines were in existence for the design of such wings. Figure 3.4 shows the wing planform chosen along with a typical hummingbird wing. Comparison with a hummingbird wing was made because hummingbirds are closest in terms of Reynolds number range to a typical flapping wing MAV. The current wing planform retains the gradual taper of a hummingbird's wing, albeit with a larger chord towards the root, which may help in generating higher thrust from rotational effects. Photographs of wing cross-sections of insects do not show any well defined cross sectional shape [96]. For this reason, a flat plate cross-section was used in the present study. However, during flapping, the wing cross-sectional shape was dependent on the aeroelastic deformations of the wing.

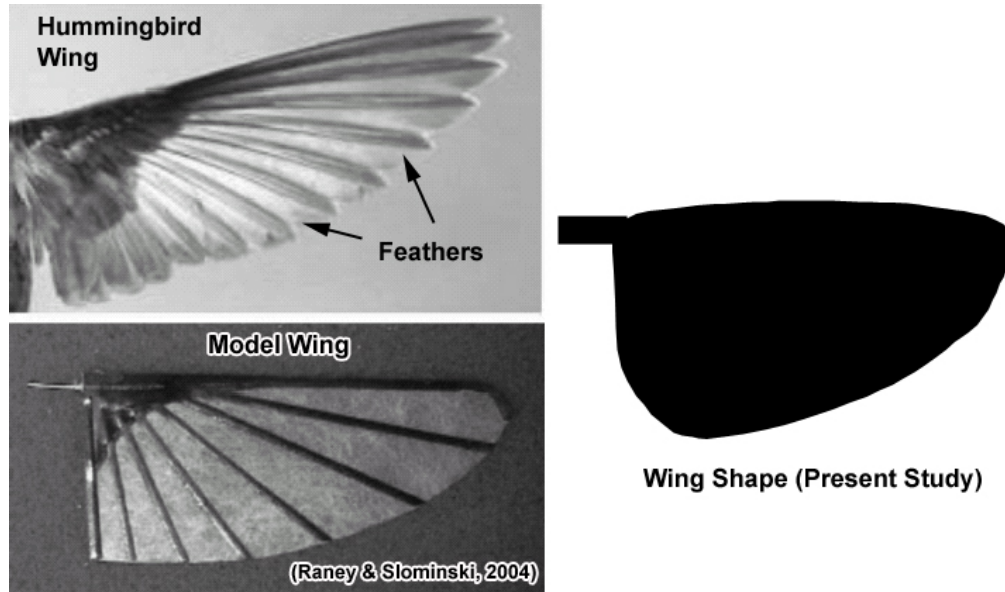


Figure 3.4: Present wing planform compared with a hummingbird wing [97].

It must be noted that most hummingbirds have a mass less than 10 grams with wingbeat frequencies varying between 20-40 Hz. The largest hummingbird, the *Patagona gigas*, has a mass of nearly 22 grams and a wingbeat frequency close to 17 Hz [29]. Thus, with respect to the all-up weight of 100 grams required for an MAV, there are no hover capable examples that exist in nature. Keeping this in view, the first challenge was to experimentally measure the thrust generating ability of the flapping wing mechanism described in Chapter 2.

### Measured forces and angles

Figure 3.5 shows a sample of the forces and shaft positions measured using the load cell and motion transducers described in Chapter 2. These results show the measured quantities as a function of non-dimensional time during one flapping period. The wing pitch position is also plotted in the figure. Unlike the rotor stand

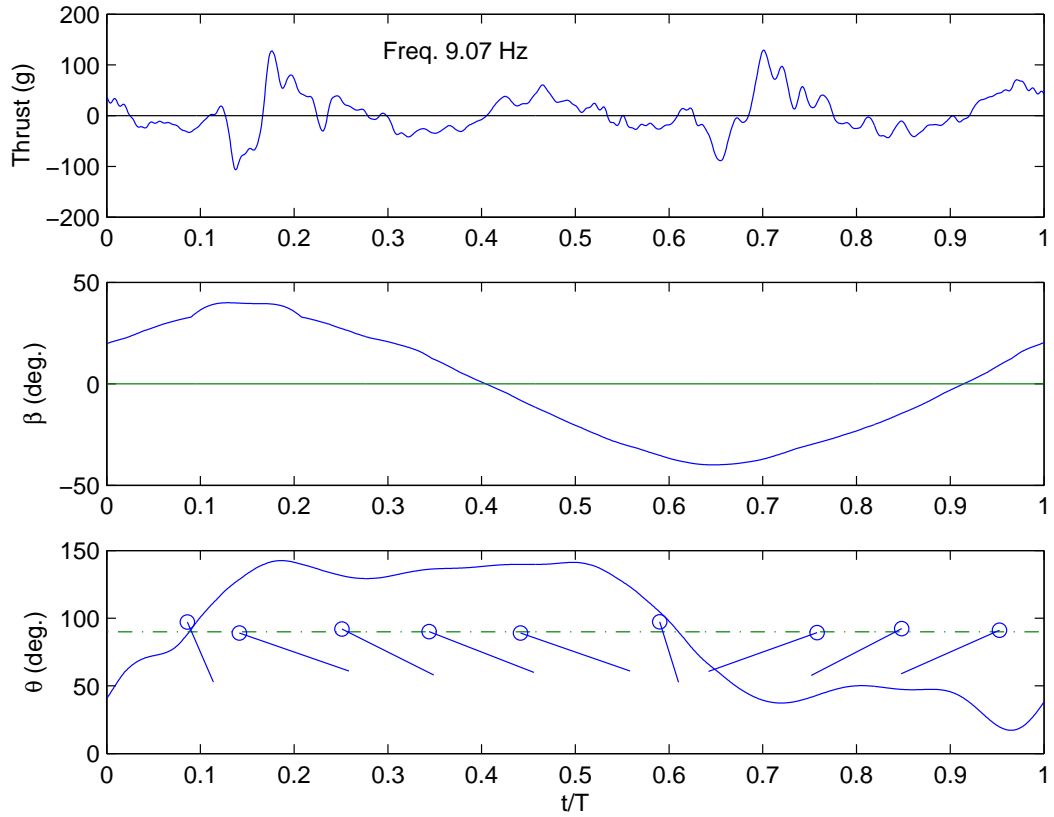


Figure 3.5: Measured thrust, flapping angle and pitch angle during one flap cycle at 9.07 Hz

measurements, the measurements carried out using the load cell showed periodic force measurements, as expected. However, from the magnitude of thrust variation during a flapping cycle, it was clear that inertial loads contributed significantly to the total measured loads. This meant that the time variation of the airloads could not be determined without recourse to vacuum chamber tests. However, the time averaged vertical force must provide the aerodynamic thrust, since no thrust was expected from the inertial forces.

Another concern with the bi-stable mechanism was the abrupt nature of the

pitching motion caused by the pitch actuator hitting the ball ends. Insects and hummingbirds use biological muscles to accomplish such pitch changes in a smooth manner. It is not known whether the type of pitching motion used in this study would significantly effect the thrust generation capability of hover capable flapping wings. However, Fig. 3.5 did not show any abrupt changes in the pitching motion of the wing. It must be noted that the pitch angle was not fixed during the translational motion of the wing, but varied by 10-15°. This variation was caused by the flexibility inherent in the pitch mechanism including the pitch stop and the spring loaded cam. It was assumed that these factors would not significantly effect the thrust generation capability of the mechanism. Furthermore, this working mechanism could fill a serious gap in the availability of experimental data for hover capable flapping wings at typical MAV Reynolds numbers.

### **3.3 Low Frequency Tests**

Several tests were conducted at frequencies up to 10.5 Hz, with different wings set at different pitch angles. In these tests, the first generation pitch motion sensor was used and the flap motion was not measured. The following sections describe the results of these tests. It may be noted that, the flapping mechanism used in the present study was operated in air at frequencies as high as 12 Hz. The operating Reynolds number based on the mean chord at a flapping frequency of 10 Hz was approximately 17,000. This implies that the mean chord based Reynolds number was higher than the transition Reynolds number of 10,000 for all frequencies higher

than approximately 5.8 Hz. Since the majority of tests in the present study were conducted at frequencies higher than 5.8 Hz, the flow was not expected to be in the transition regime.

## **Wings**

The thrust generated by aluminum-mylar wings was measured for a number of stroke and wing parameters. These wings, made from 0.508 mm thick aluminum frames, are shown in Fig. 3.6. The only difference between Wings I and II was the membrane material which made Wing II much lighter. It was found that Wings I and II produced the same amount of thrust but Wing II could attain higher frequencies on the flapping wing mechanism because of its lower mass. For this reason, results are presented for Wings II and III only. All the results were based on a flapping stroke angle of  $80^\circ$ , i.e. the angle  $\beta$  varied from  $-40^\circ$  to  $+40^\circ$ . Each wing was tested at two pitch angles of  $30^\circ$  and  $45^\circ$ . A pitch angle of  $30^\circ$  implies that the pitch was  $30^\circ$  during the downstroke and then changed to  $-30^\circ(150^\circ)$  during the upstroke. Similarly for the  $45^\circ$  case, the pitch angle was  $45^\circ$  during the downstroke and changed to  $-45^\circ(135^\circ)$  during the upstroke. Figure 3.7 shows the dimensions of the wings and the root cut-out.

## **Load cell design**

As described in Chapter 2, the initial design of the load cell used a square cross-section because of the ease of mounting the miniature strain gauges on a flat

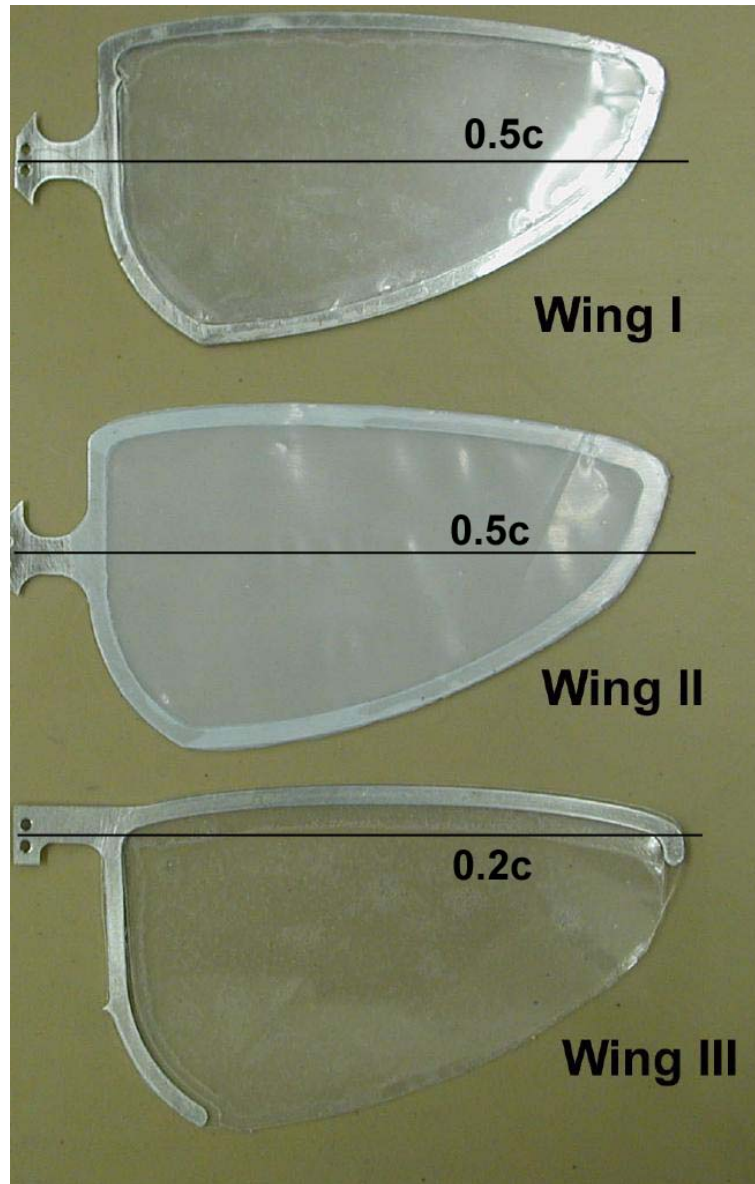


Figure 3.6: Scaled-up insect wings

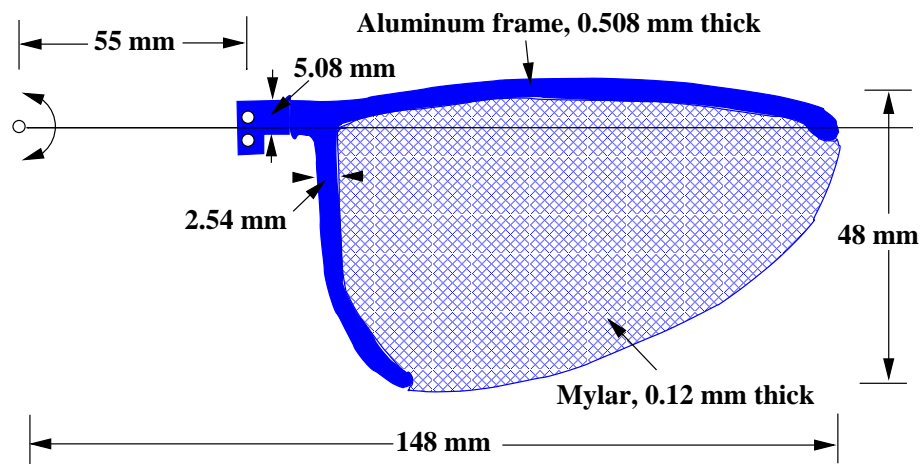


Figure 3.7: Schematic of planform showing root cut-out

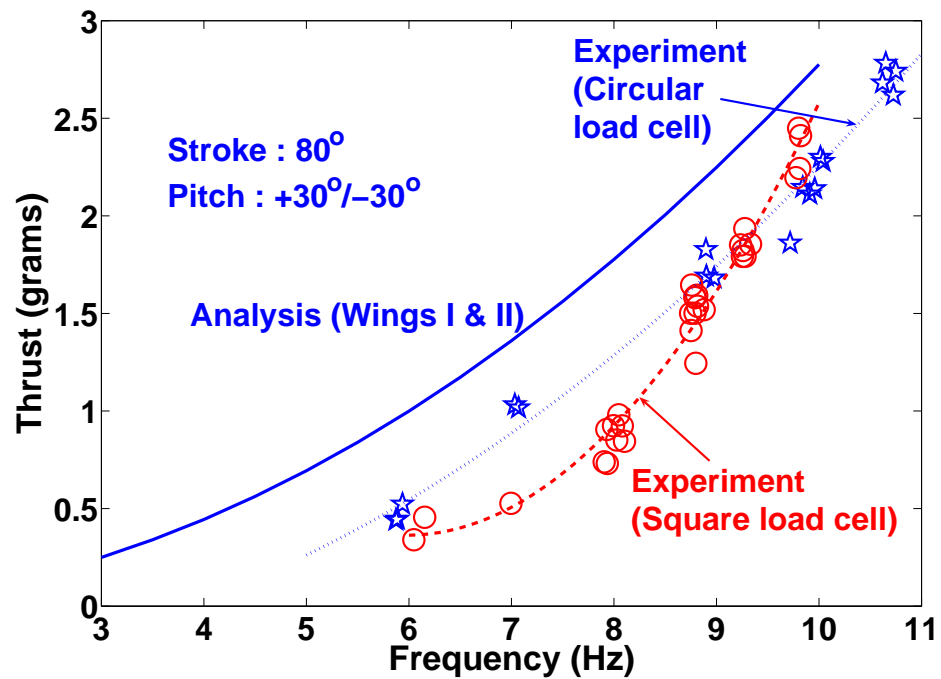


Figure 3.8: Effect of change in load cell design on measured thrust

surface. This load cell had small cross-couplings between the two orthogonal axes of measurement. Figure 3.8 shows the thrust generated by Wing II, when measured with this square cross-section load cell. Also shown in the figure is the thrust predicted using the quasi-steady blade element analysis. The thrust measured using this load cell showed a higher-order variation as opposed to the quadratic variation shown by the analysis. To check whether this discrepancy was caused by the cross-coupling present in the load cell, a circular cross section load cell was designed and built. On a square cross-section load cell, the strain gauges had to be mounted with great precision if spurious surface strains were to be avoided. If the gauge was off-center, it could pick up unwanted surface strains that caused the calibration constants to change as the pitch angle of the load cell was varied. On a circular cross-section, these spurious strains were minimized. Figure 3.8 shows the thrust measured using this redesigned load cell. Although the discrepancy between the analysis and experiment was still present, the circular load cell showed a quadratic increase in thrust as the frequency increased. All remaining thrust measurements were made using the circular cross-section load cell. Although this cross-section provided good results, it suffered from the drawback that the strain gauges did not have a flat surface to bond with. This led to a short useful life of these load cells before the strain gauges had to be replaced, thus increasing the overall testing time. It must be noted that, in Fig. 3.8, all the available data was plotted to show the scatter in the data, and no error bars are shown. This was done because the frequency that the mechanism operated at varied slightly for each test run.

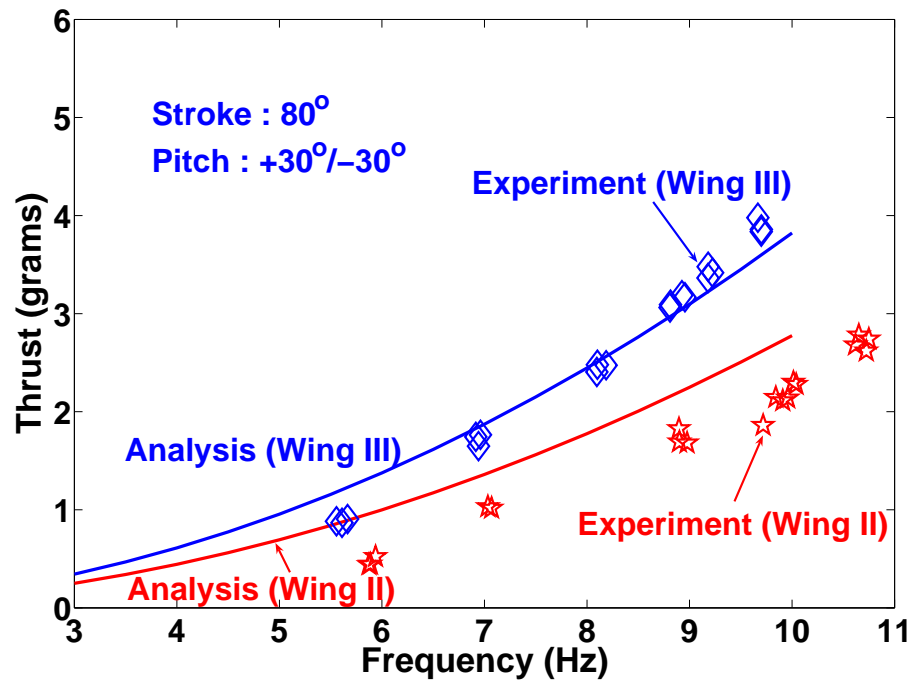


Figure 3.9: Comparison of thrust generated by Wings II and III

### Effect of pitching axis location

Figure 3.9 shows a comparison of the experimental measurements and analytical thrust predictions for the two wings at a pitch angle of  $30^\circ$ . Wing III pitched about the 20% chord location, compared to Wing II, which pitched about the 50% chord location. This change in pitching axis increased the thrust produced by Wing III because it produced more lift from rotational circulation during the pronation and supination phases, as indicated by the analysis. It may be noted that even though the analysis was quasi-steady, the thrust was not severely underpredicted because of the experimental lift and drag data used in the analysis. The analysis over predicted the thrust for Wing II. However, thrust prediction for Wing III was quite good.

## Effect of pitch angle

Figure 3.10 shows the thrust generated by Wing II at a pitch angle of  $45^\circ$  along with the thrust generated at a pitch angle of  $30^\circ$ . At a higher pitch angle, the thrust was expected to increase. However, the experimental results show that the thrust did not change when the pitch angle was increased for Wing II. The quasi-steady analysis over-predicted the results, at both pitch angles, for Wing II.

Figure 3.11 shows the effect of change in pitch angle on the thrust generated by Wing III. In this case, the experimentally measured thrust did show an increase when the pitch angle was increased to  $45^\circ$ . On the other hand, the predictions did not show any significant change with pitch angle. This was because, when the pitch angle for Wing III was increased, the total change in pitch was reduced. At  $45^\circ$  pitch angle, the wing flipped from  $45^\circ$  to  $135^\circ$ , producing a total change of  $90^\circ$ . However, when the pitch angle was  $30^\circ$ , the total change in pitch was  $120^\circ$  as the wing flipped from  $30^\circ$  to  $150^\circ$ . The reduced flip angle at  $45^\circ$  pitch, reduced the rotational circulation for Wing III. Because Wing III generated a significant amount of lift from rotational circulation, the net increase in thrust was very small at  $45^\circ$  pitch angle.

## Effect of pitch phase

Figure 3.12 shows the effect of a slight change in pitch phase on the thrust generated by Wing III at a pitch angle of  $45^\circ$ . To change the pitch phase, the ball ends shown in Fig. 2.1 were moved slightly toward each other, thus causing the

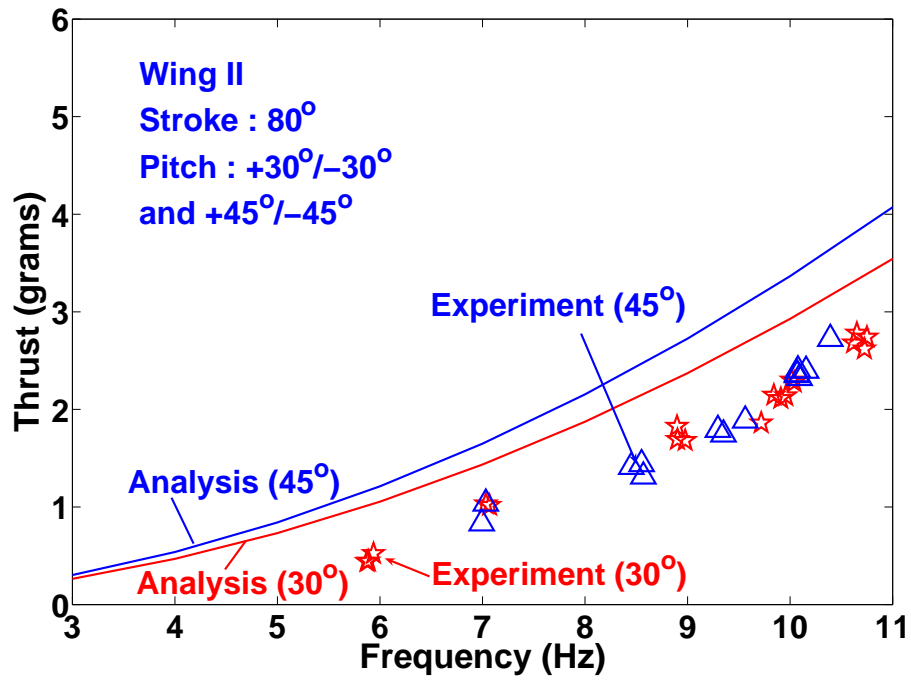


Figure 3.10: Effect of wing pitch angle on thrust (Wing II)

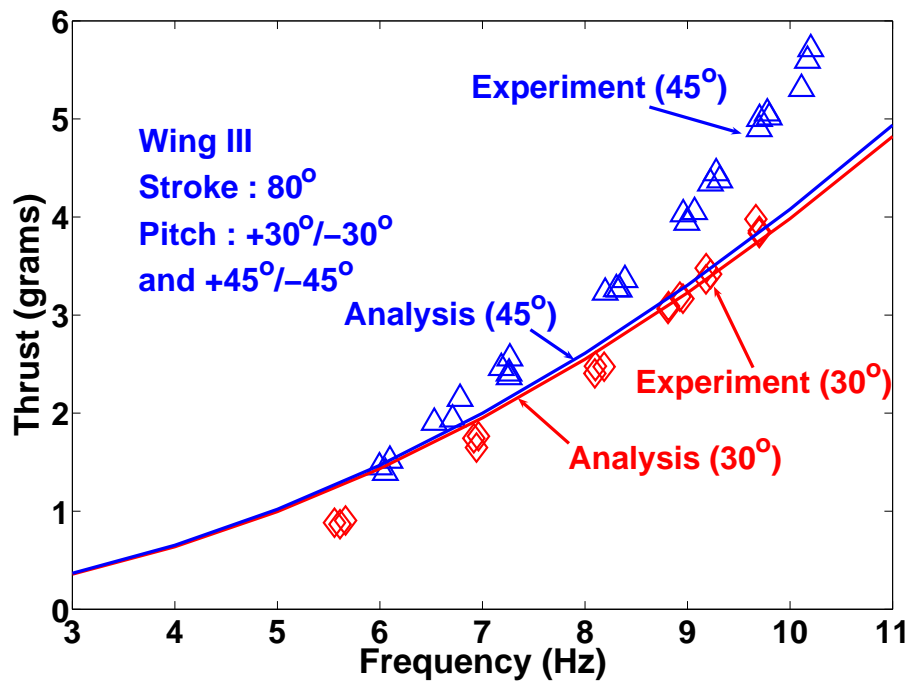


Figure 3.11: Effect of wing pitch angle on thrust (Wing III)

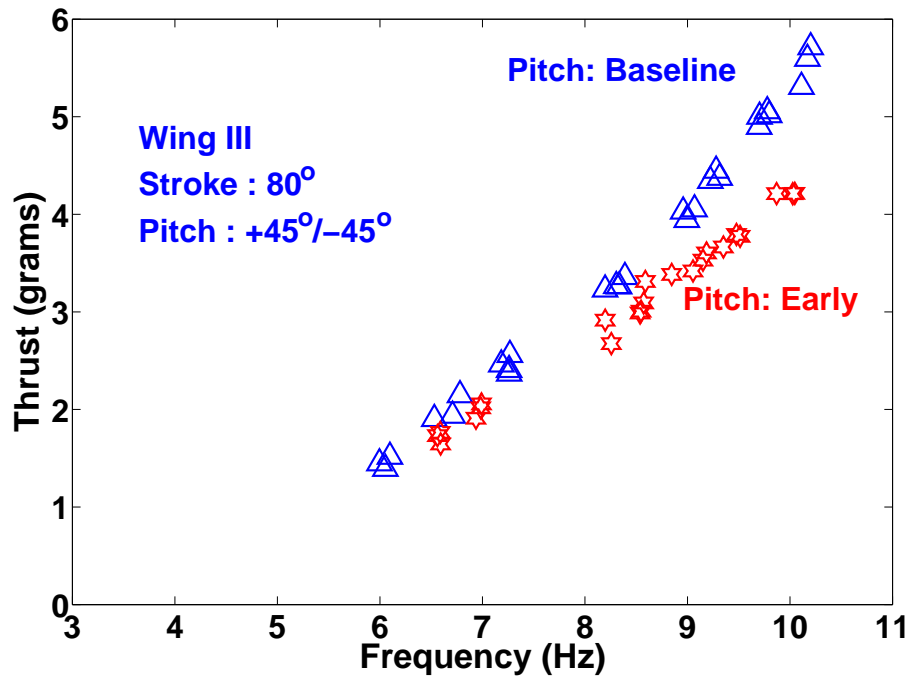


Figure 3.12: Effect of early rotation on thrust (Wing III)

pitch actuator to hit them early, producing an early pitch, (i.e. the wing flips over earlier in the flapping cycle as compared to the baseline case). For this case, the wing starts pitching 0.04T earlier than the pitch starting point for the baseline case, where T is the time period of one flapping cycle. A delayed pitch case could not be tested because of the limitations of the mechanism. Moving the ball ends away from each other would lead to the pitch actuator hitting them late. However, in this case, the wing flapping motion reversed direction before the pitching motion was complete, i.e, before the wing had flipped over. Insects use changes in pitch phase to change the lift generated by their wings. Figure 3.13 shows that the thrust remains unchanged when Wing II pitches early. An interesting observation is the nearly linear variation of thrust with frequency for the case of early pitching of

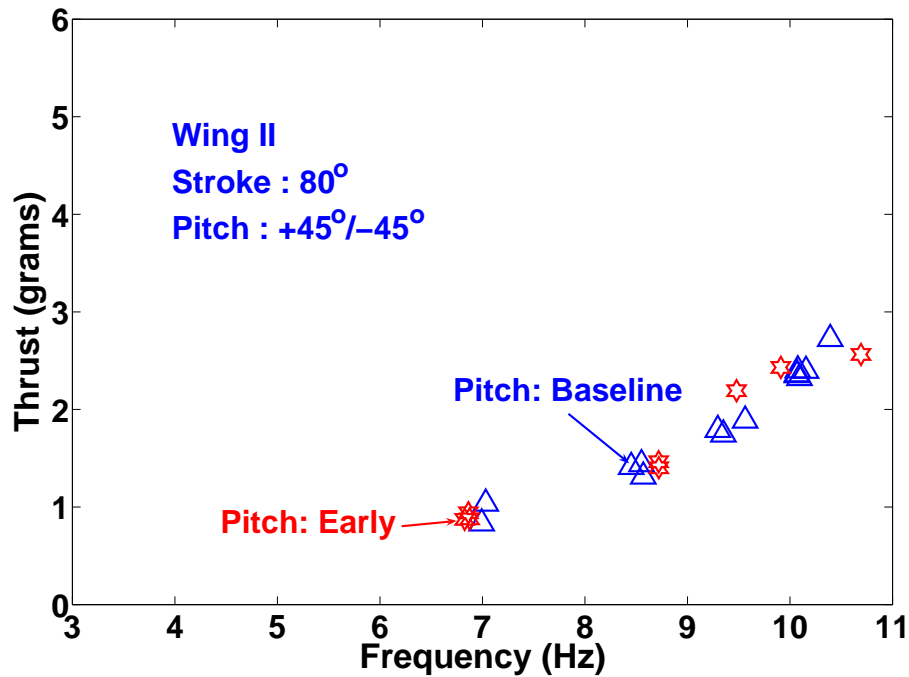


Figure 3.13: Effect of early rotation on thrust (Wing II)

Wing III (Fig. 3.12). The reduction in lift is unexpected since it has been reported elsewhere [34] that early pitching may produce a positive wake capture, i.e., when the wing flips early in the flapping cycle, its interaction with the wake created during the previous cycle increases the total thrust. Figure 3.13 shows the effect of early pitching on the thrust generated by Wing II. Although a limited amount of data was available for this case, the thrust was nearly unchanged when compared to the baseline case.

### 3.4 Vacuum Chamber Tests

Inertial forces constituted a large part of the total forces measured using the load cell. To eliminate these inertial loads from the total measured loads, vacuum

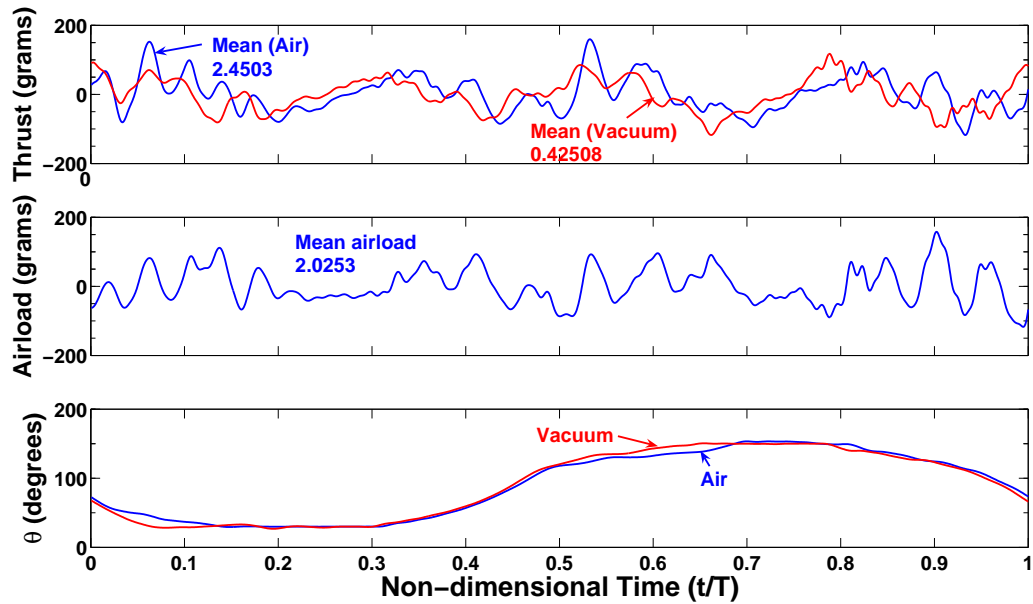


Figure 3.14: Airloads obtained by subtracting inertial forces

chamber tests were conducted. When the wing was tested in vacuum, the frequency attained by the mechanism was not the same as the frequency in air at the same motor supply voltage. However, to subtract the inertial forces from the total loads, the test frequencies in air and vacuum must match closely. This was achieved by adjusting the motor supply voltage during the vacuum chamber tests to change the frequency. Figure 3.14 shows the thrust generated in one flapping cycle by Wing II, in air and in vacuum at a frequency close to 10.7 Hz. The frequency for the vacuum test was 10.71 Hz, while the frequency in air was 10.65 Hz. Because these frequencies were slightly different, the results were plotted against non-dimensional time in the flapping cycle. Figure 3.14 also shows the airloads obtained after subtracting the inertial forces from the total forces, and the pitch angle  $\theta$ , measured both in air and in vacuum. It is evident from this figure that the pitch angle varied slightly

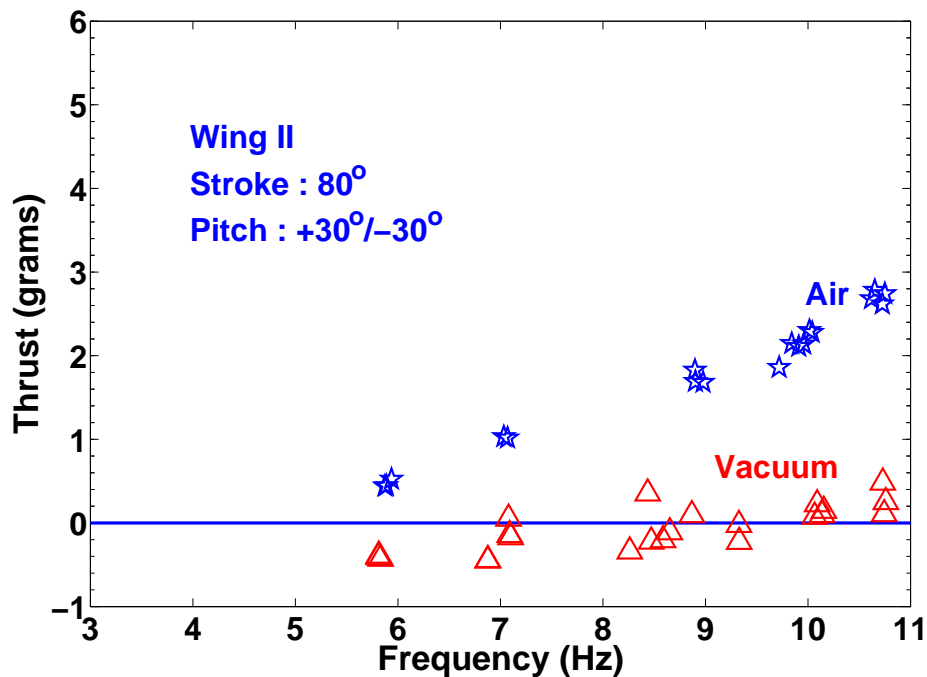


Figure 3.15: Thrust measured in air and vacuum for Wing II

in vacuum because of a change in the dynamics of the drive mechanism. Also, the temporal variation of airloads contained frequencies higher than the flapping frequency, which may be caused by the elastic bending and twisting of the wing. The variation in the airloads was expected to be an order of magnitude smaller than the inertial loads. However, the results showed this variation to be of the same order as the combined loads. This may be caused by the variation in the dynamics of the mechanism itself. However, the average thrust measured in vacuum showed that, as expected, Wing II generated a very small thrust at a pitch angle of  $30^\circ$  (Fig. 3.15). The measurement error in the vacuum chamber data was larger as compared to the measurement error in air. Although the vacuum chamber data did not provide a reliable temporal variation of the airloads, it did increase the confidence level in the

thrust measurement methodology using the load-cell.

## 3.5 High Frequency Tests

### Wing III

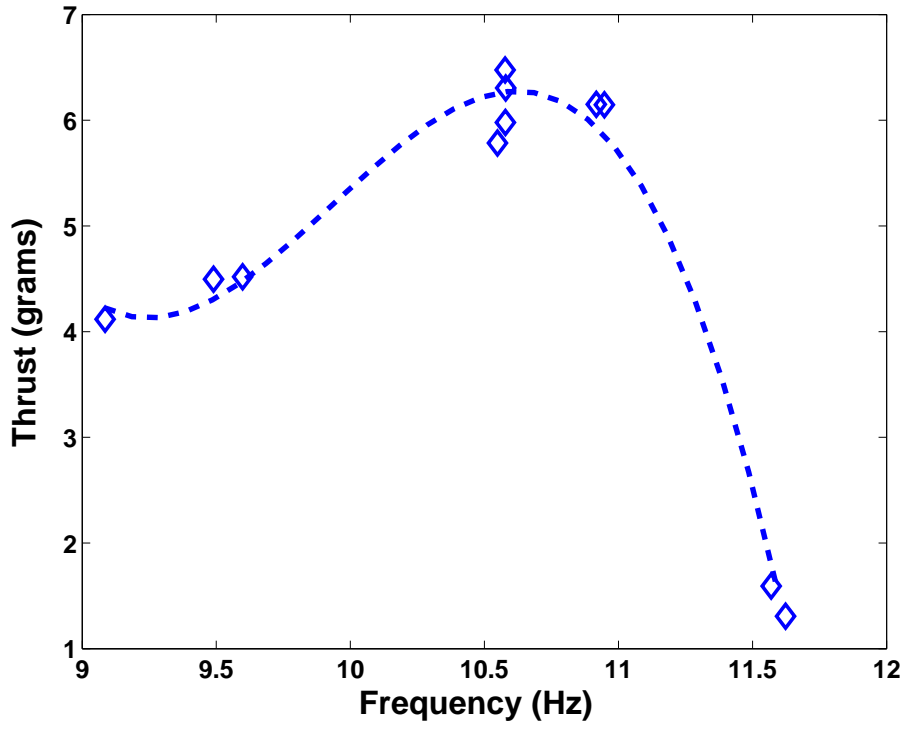
The low frequency tests were carried out to a maximum frequency of  $\sim 10.5$  Hz. In this section, results are presented for some high frequency tests carried out on Wing III. The wing was tested at a pitch angle of  $45^\circ$  because the combination of Wing III with  $45^\circ$  pitch was found to produce the maximum thrust in the low frequency tests. Also, for these tests, the flap position was measured in order to calculate the total inertial and aerodynamic power. Figure 3.16 shows the measured thrust and power for Wing III up to a frequency of  $\sim 11.6$  Hz. The dashed lines show curve fits through the data points. The thrust showed an increase up to a frequency of 10.6 Hz, and then decreased sharply. The frequency range for which these tests were carried out was very small because Wing III weighed 1.3 grams, which required a lot of power input to the mechanism. It must be noted that the power shown in Fig. 3.16 was computed from the measured stroke velocity and the measured forces at the base of the wing. Therefore, this power includes the aerodynamic and inertial power needed to move the wing at a particular frequency, but does not give any information about the power required by the mechanism as a whole. Without the wing, the mechanism could be run at almost 20 Hz. This indicated that the mass of the wing was preventing the mechanism from moving at

high frequency. Also, only a limited amount of data could be acquired because, when the frequency was increased further, the pitch stop (shown in Fig. 2.2) failed because of the high forces. It must also be noted that, although the thrust dropped at high frequency, the measured power showed a continuous increase as the frequency was increased.

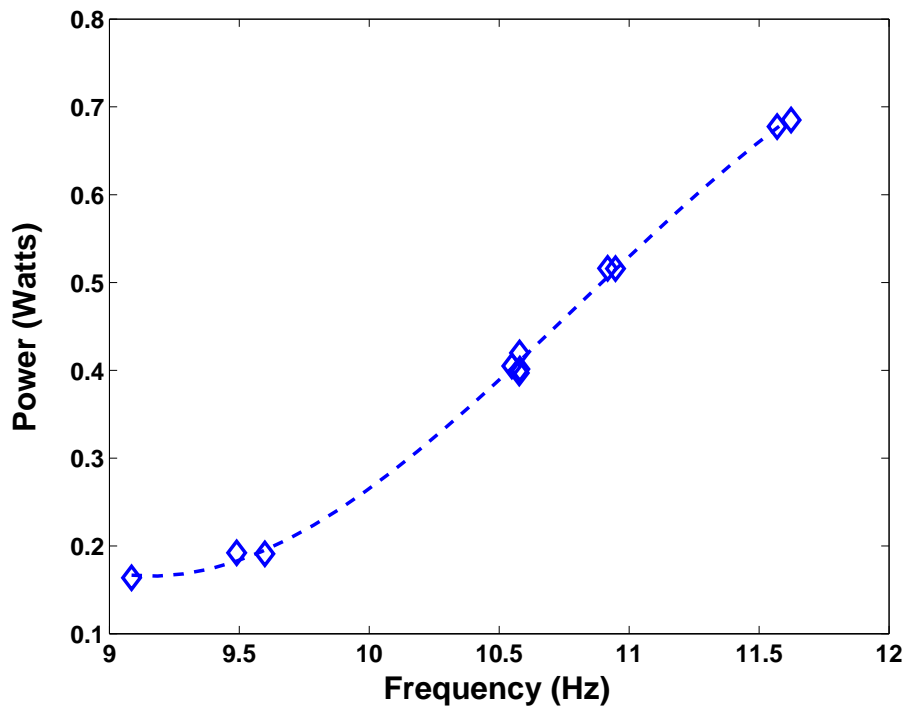
## **Light composite wings**

Because of the large effect of wing mass on flapping frequency, several lightweight wings were built with composite frames instead of aluminum. Figure 3.17 shows one such wing with a carbon composite frame covered with a Mylar sheet. Table 3.1 shows the properties of these wings. All wings with a rectangular planform had the same mean chord as Wings II and III. Wings IV, V and VI were covered with a lightweight film called RC Microlite, which is similar to Monokote widely used by model airplane enthusiasts. Wings VII and VIII used the same frames as Wings V and VI, respectively, covered with a mylar sheet which is stronger and heavier than RC Microlite. All the composite wings were made of rectangular planform because it was easier to cut these shapes out. The first flap frequencies shown in Table 3.1 were determined from the impulse response of the wings, when mounted on the load cell.

Figure 3.18 shows the measured thrust and power for Wings IV and V. The thrust and power measured for Wing III are also shown on these plots. It is evident from the range of frequencies for each wing that a lower wing mass helped in at-



(a) Thrust



(b) Power

Figure 3.16: Thrust and power measured for Wing III at high frequency.

Wing	Planform	Pitching axis	Frame material	Covering material	Mass (g)	First flap freq. (Hz)
II	tapered	0.5c	Aluminum	Mylar	1.3	35.1
III	tapered	0.2c	Aluminum	Mylar	1.3	36.1
IV	rectangular	0.1c	Carbon composite	RC Microlite	0.49	24.4
V	rectangular	0.1c	Carbon composite	RC Microlite	0.65	34.9
VI	rectangular	0.1c	Fiberglass	RC Microlite	0.39	13.0
VII	rectangular	0.1c	Carbon composite	Mylar	0.86	34.2
VIII	rectangular	0.1c	Fiberglass	Mylar	0.61	-
IX	tapered	0.2c	Fiberglass	mylar	0.58	15.03
X	rectangular	0.1c	Carbon composite	mylar	0.68	-

Table 3.1: Wing properties.

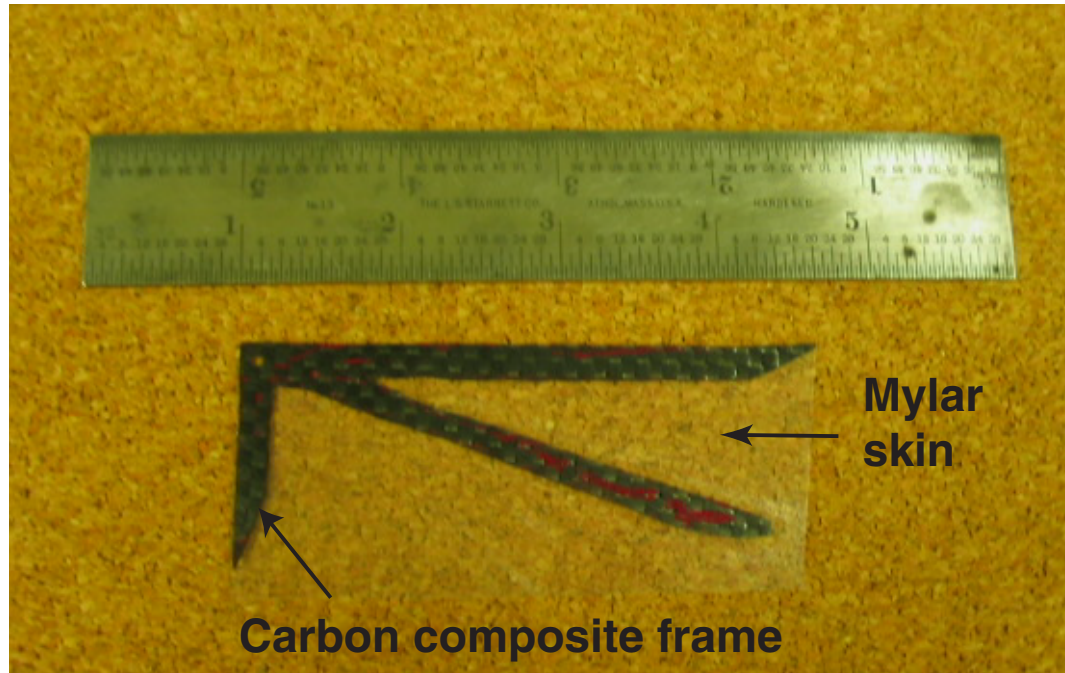
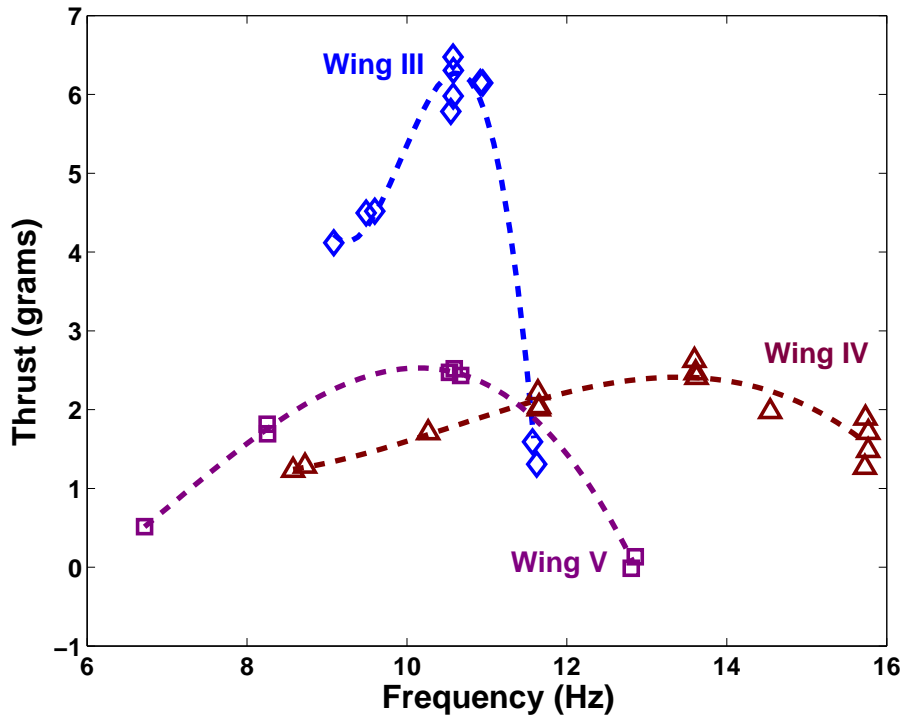


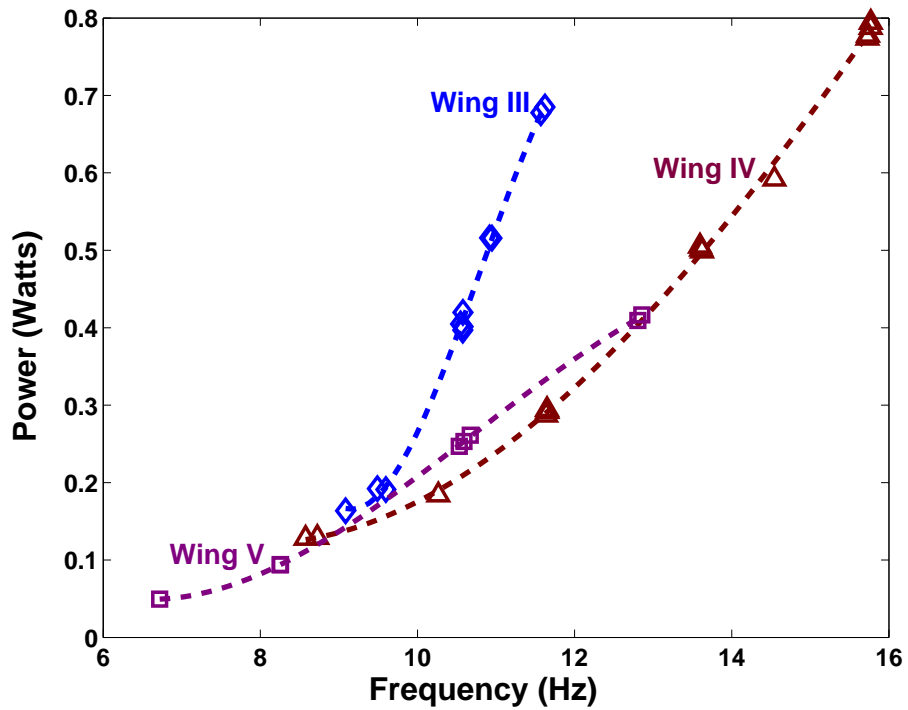
Figure 3.17: Wing VII.

taining high frequencies on the mechanism. The lower wing mass also led to lower power as compared to Wing III. However, the thrust generated by Wings IV and V was much lower than Wing III. Also, like Wing III, the thrust attained a maximum value and then decreased with increasing frequency.

Figure 3.19 shows the thrust and power measured for Wings VI and VII. Again, thrust and power for Wing III are also plotted for reference. Wing VI was the lightest wing tested but it was also highly flexible. This is why the thrust generated by this wing was very low. Wing VII was built to determine the effect of the skin material on thrust. Wings IV and V used RC Microlite, which although lighter than the Mylar sheet, had many wrinkles on it in addition to being very pliable. In comparison, the Mylar sheet provided a relatively stiff, smooth membrane. Using the Mylar instead of RC Microlite increased the thrust for Wing VII by a small

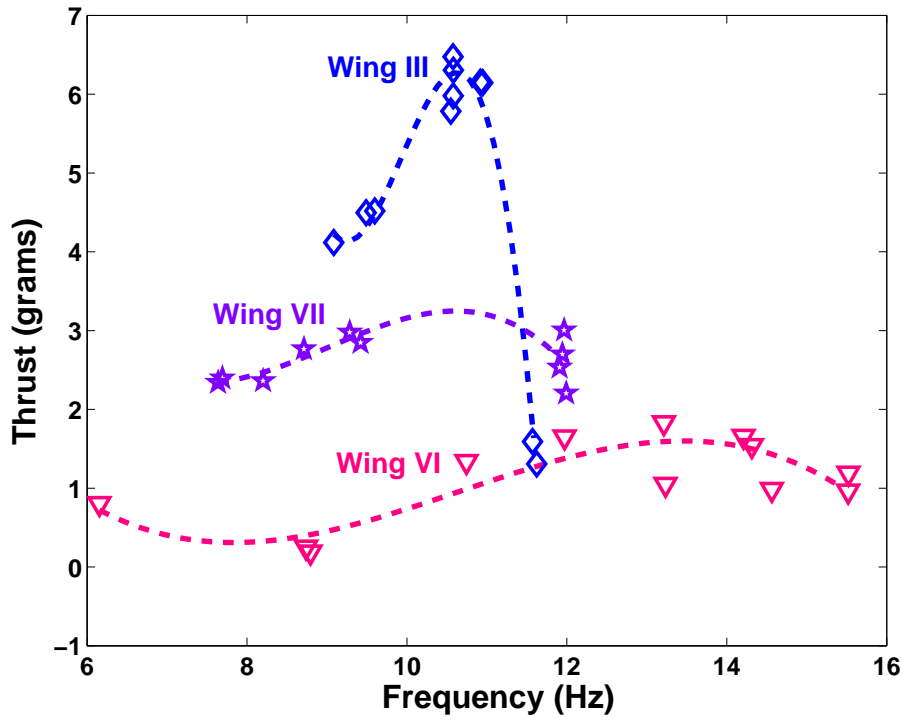


(a) Thrust

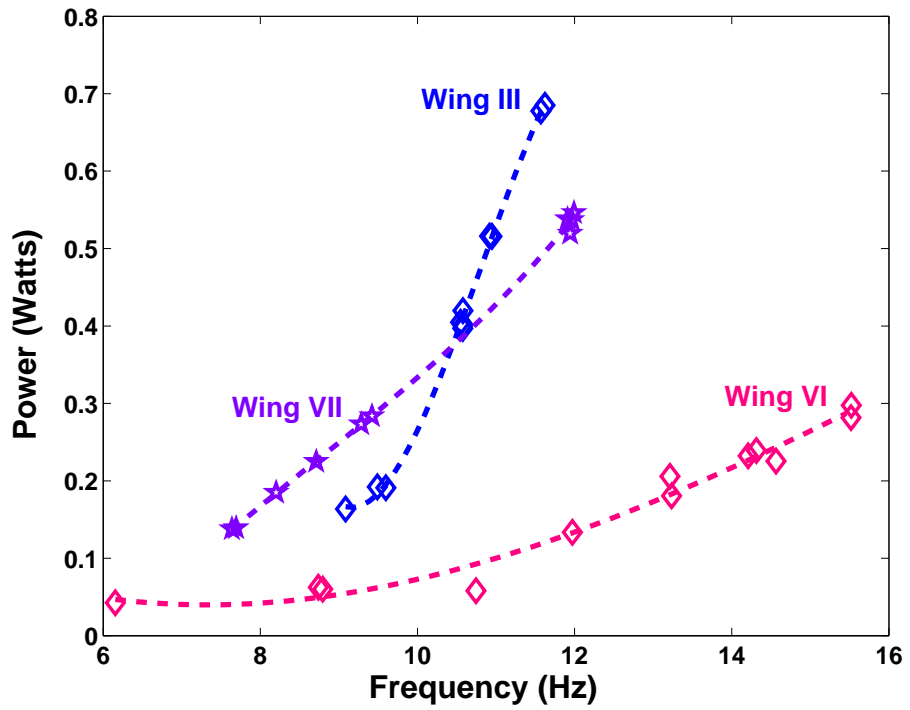


(b) Power

Figure 3.18: Thrust and power measured for lighter wings at high frequency.



(a) Thrust



(b) Power

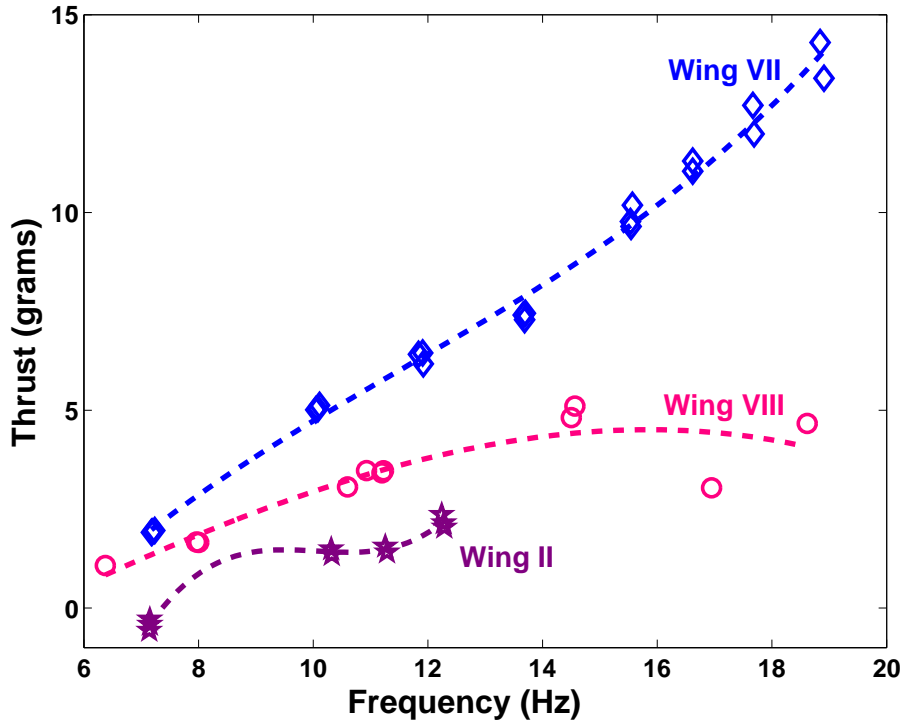
Figure 3.19: Thrust and power measured for lighter wings at high frequency

amount, although the frequency range was reduced because of the higher mass of the Mylar sheet. A significant increase in the power was also noted. For both wings, the thrust increased and then decreased with increasing frequency. Also, the scatter in thrust measurements increased at high frequency for Wing IV and Wing VII.

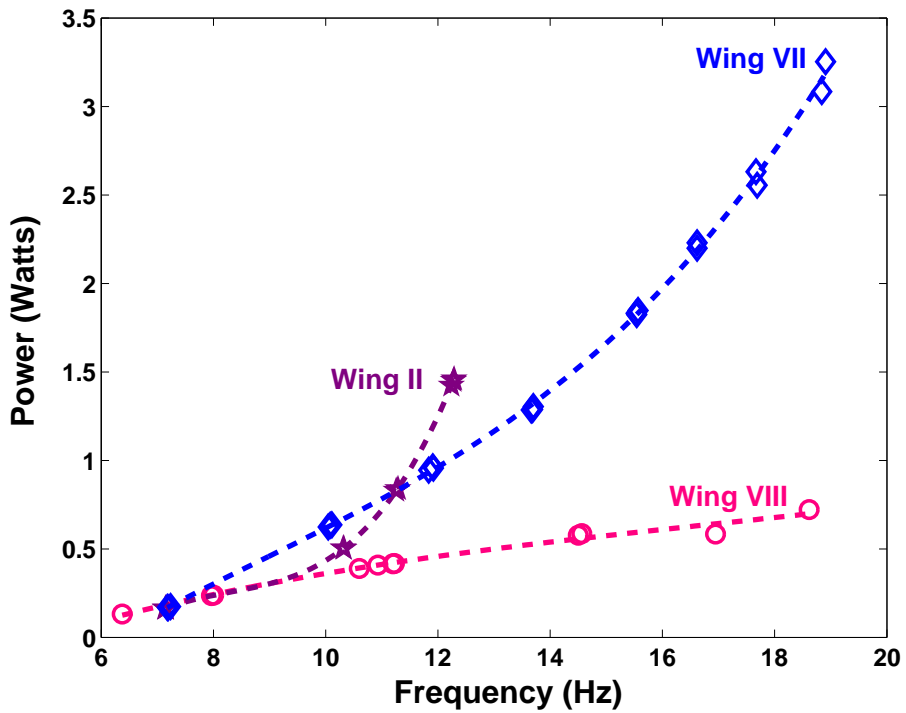
### **3.6 Pure Flap Tests (Passive Pitch)**

Frequency limitations of the mechanism did not allow the testing of heavier wings at high frequencies. Part of this limitation stemmed from the large amount of energy required to actively pitch the flapping shaft when the pitch actuator hit the ball ends. To determine the thrust generated by the wings in a pure flapping motion, the ball ends were removed so that there was no flipping of the shaft at the ends of the stroke. However, there was some pitch flexibility in the mechanism because of the spring loaded cam. For these tests, the wing was held on the shaft at a pitch angle of  $90^\circ$ . When the mechanism was turned on, the wing moved in a horizontal stroke plane and pitched passively because of the inertial and aerodynamic forces acting on the wing.

Figure 3.20 shows the thrust and power measured for Wings II, VII and VIII at various flapping frequencies. Because the wing was held at  $90^\circ$  to the flow, like a bluff body, the aerodynamic and inertial power was higher compared to the bio-inspired flapping case. However, the surprising result was the thrust produced by Wing VII, which was nearly 14 grams at a frequency of 19 Hz. Wing VIII could generate nearly 5 grams of thrust, but Wing II produced very low thrust and also



(a) Thrust



(b) Power

Figure 3.20: Thrust and power measured for pure flapping motion with passive pitching of the wing.

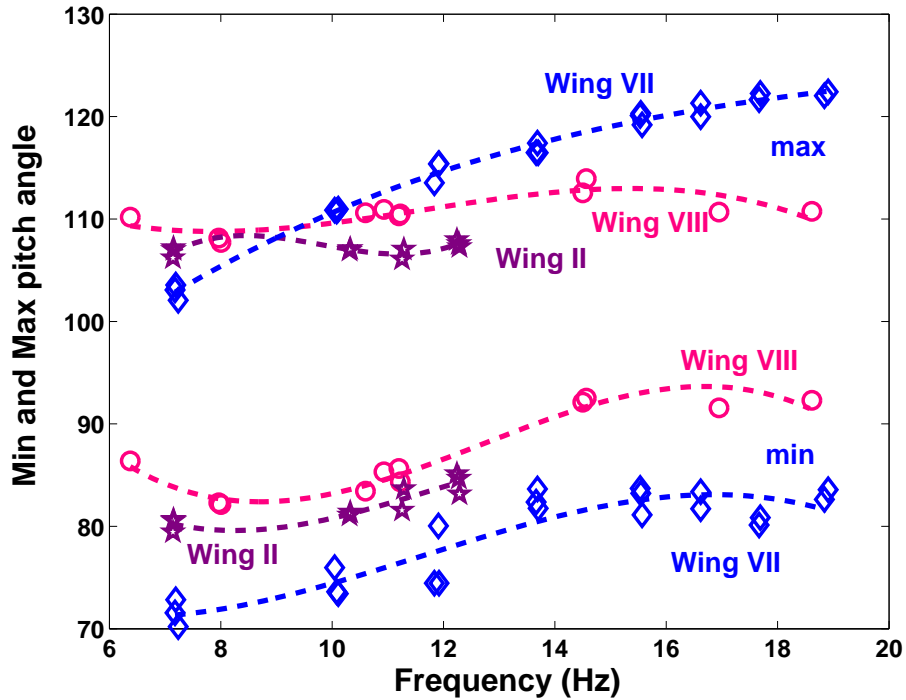


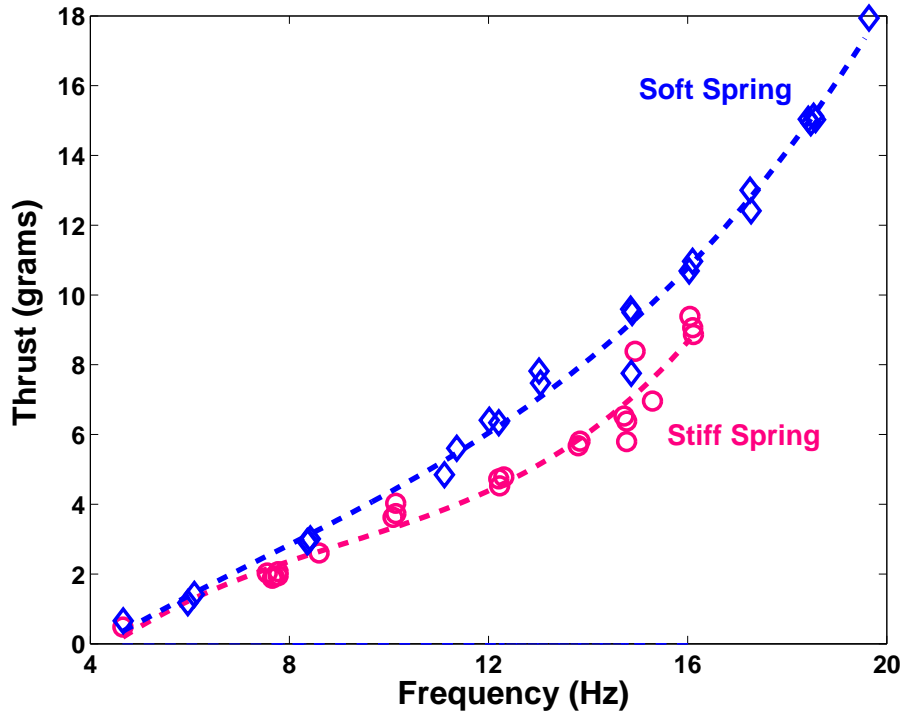
Figure 3.21: Minimum and maximum values of pitch variation.

required more power because of its higher mass. Figure 3.21 shows the minimum and maximum values of the pitch angle variation for the three wings. The lower set of dashed lines show curve fits through the minimum pitch angle values, while the upper set show curve fits through the maximum pitch angle values. For Wing VII, which produced the maximum thrust, the pitch angle changed from  $-10^\circ$  to  $20^\circ$  about the  $90^\circ$  position, at the maximum frequency. Wings II and VIII generated lower thrust with a smaller pitch angle variation. Based on these results, a passive pitch mechanism was built, as described in Chapter 2.

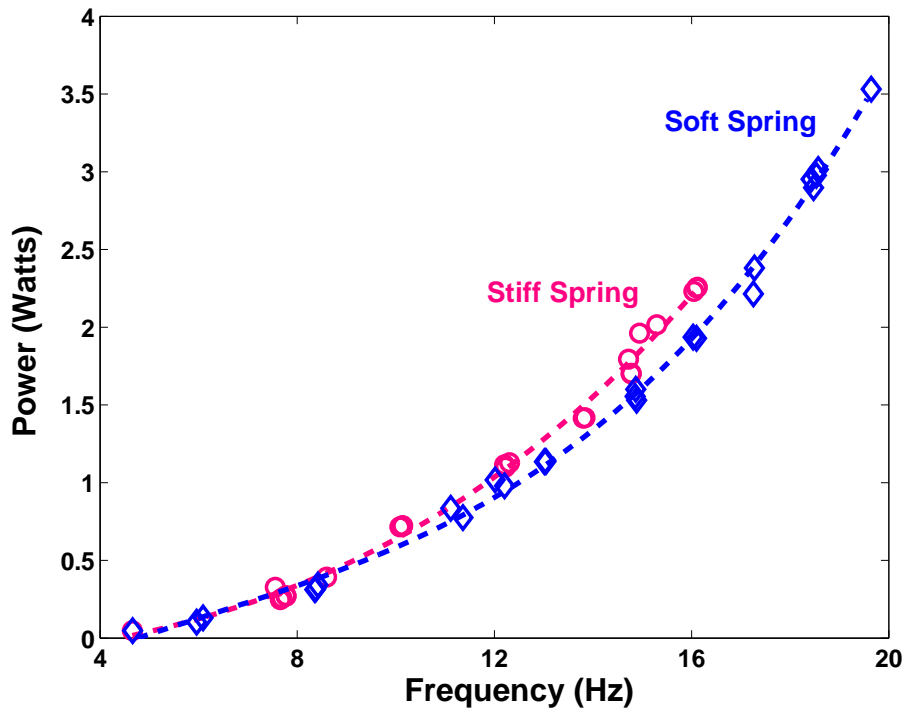
### 3.7 Passive Pitch Mechanism

In this section, thrust and power measurements, made using the passive pitch mechanism, are described. Figure 3.22 shows the measured thrust and power for two positions of the shaft-flexure connector, one providing a stiff spring and the other a soft spring. Wing VII was used for both tests. Figure 3.23 shows the minimum and maximum values of the pitch angle variation for both cases. It is evident that the soft torsion spring allowed a larger pitch variation and produced more thrust at a slightly lower power than the stiff spring case. However, even with the spring in the stiff position, the wing could generate approximately 9 grams of thrust with a pitch variation of just  $\pm 10^\circ$ . This may be caused by the flexibility of the wing itself. To achieve high frequency, and hence high thrust, the wing had to be made light weight. However, a light wing also became very flexible. This made it very difficult to separate the effect of the pitching of the shaft from the torsion of the wing caused by its own flexibility.

Figure 3.24 shows the measured thrust and power for Wings III, VII and X for various flapping frequencies. Figure 3.25 shows the corresponding values of minimum and maximum pitch angle. The difference between Wing VII and Wing X was that Wing X was machined rather than being cut with a blade like Wing VII. Thus Wing X was lighter than Wing VII, and it could attain a higher frequency on the flapping wing mechanism. However, at the same frequency, the pitch angle variation for Wing X was smaller than Wing VII. This was reflected in the lower thrust generated by Wing X as compared to Wing VII. The smaller pitch variation



(a) Thrust



(b) Power

Figure 3.22: Thrust and power measured for passive pitch mechanism with stiff and soft torsion spring for Wing VII.

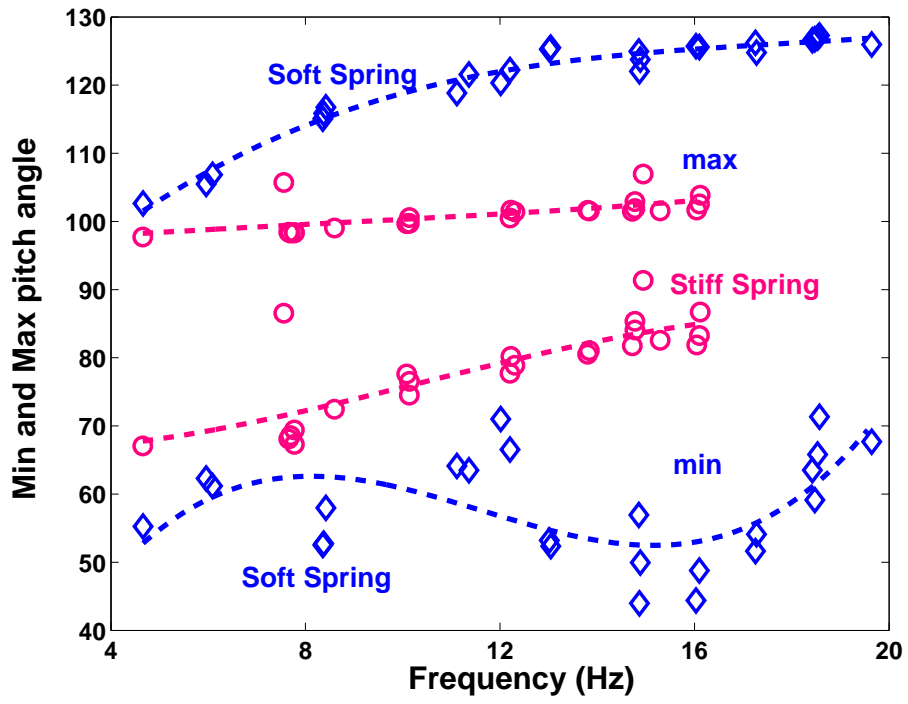
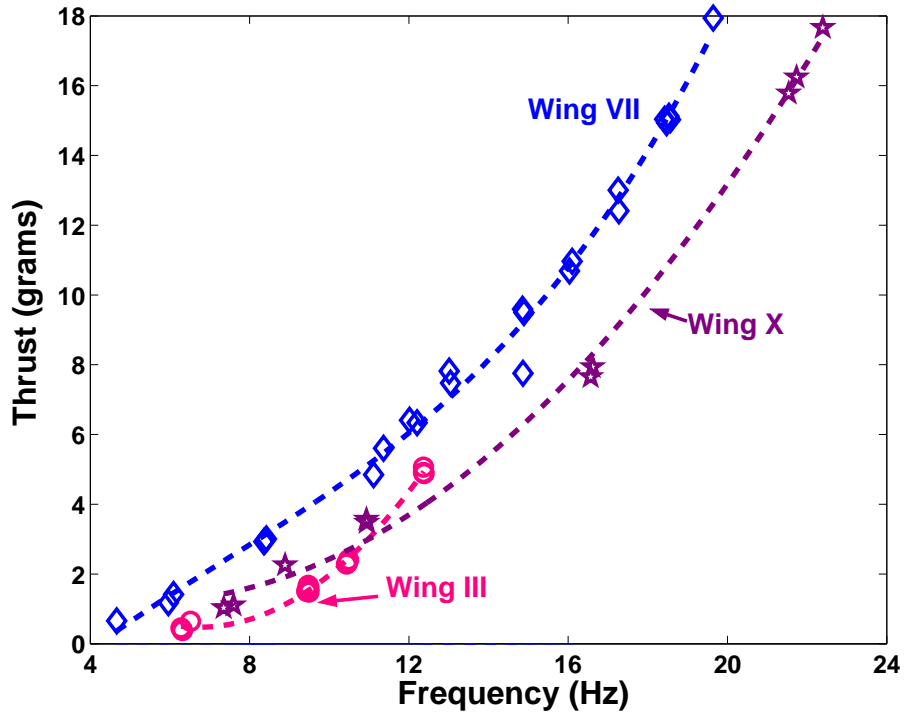
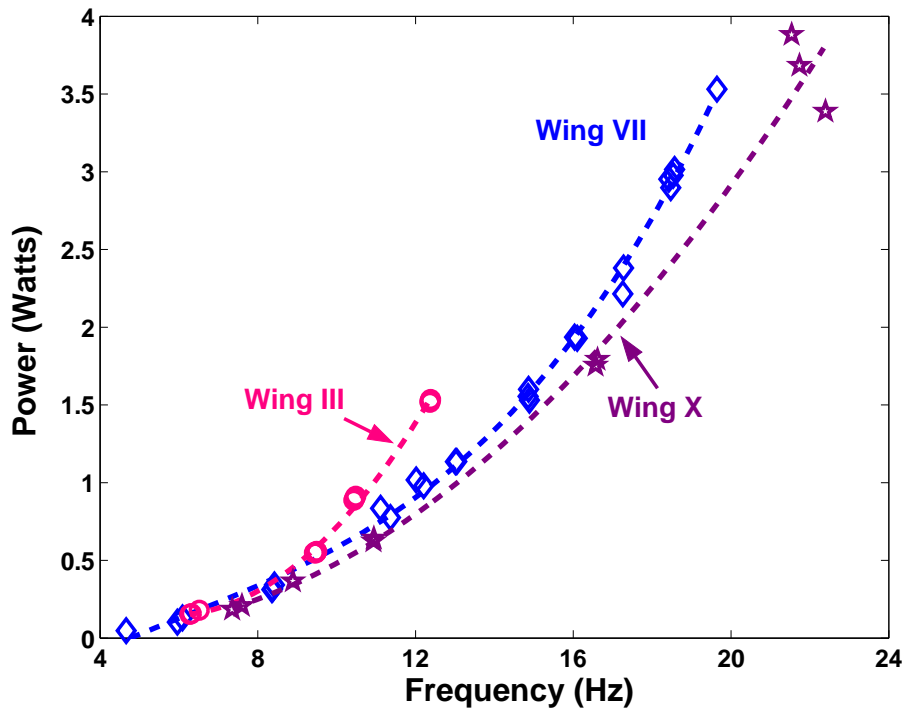


Figure 3.23: Minimum and maximum values of pitch variation for stiff and soft spring for Wing VII.



(a) Thrust



(b) Power

Figure 3.24: Thrust and power measured for passive pitch mechanism with various wings.

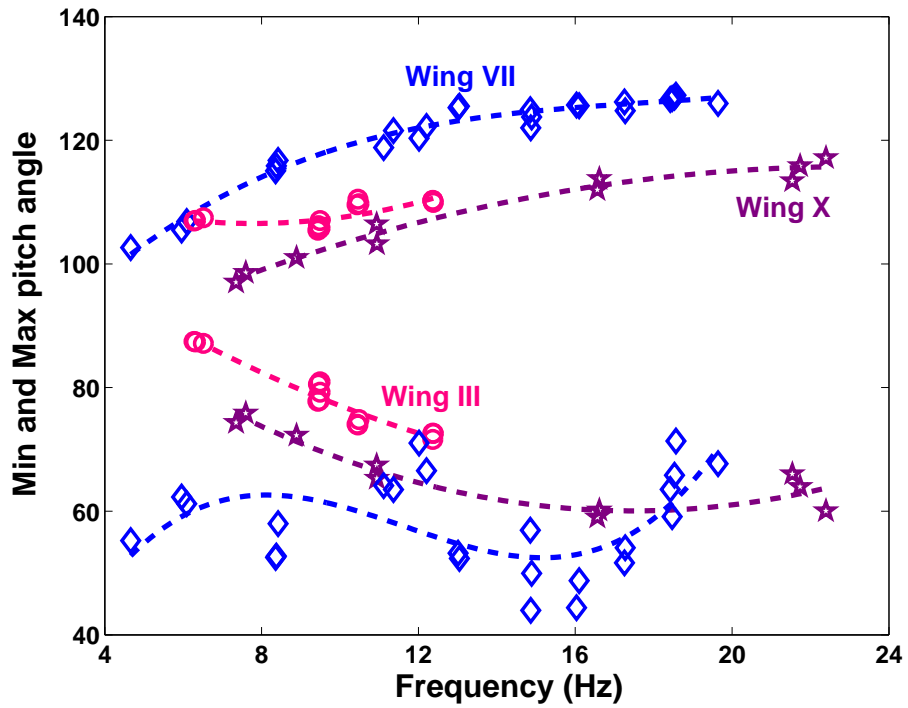


Figure 3.25: Minimum and maximum values of pitch variation for various wings mounted on the passive pitch mechanism.

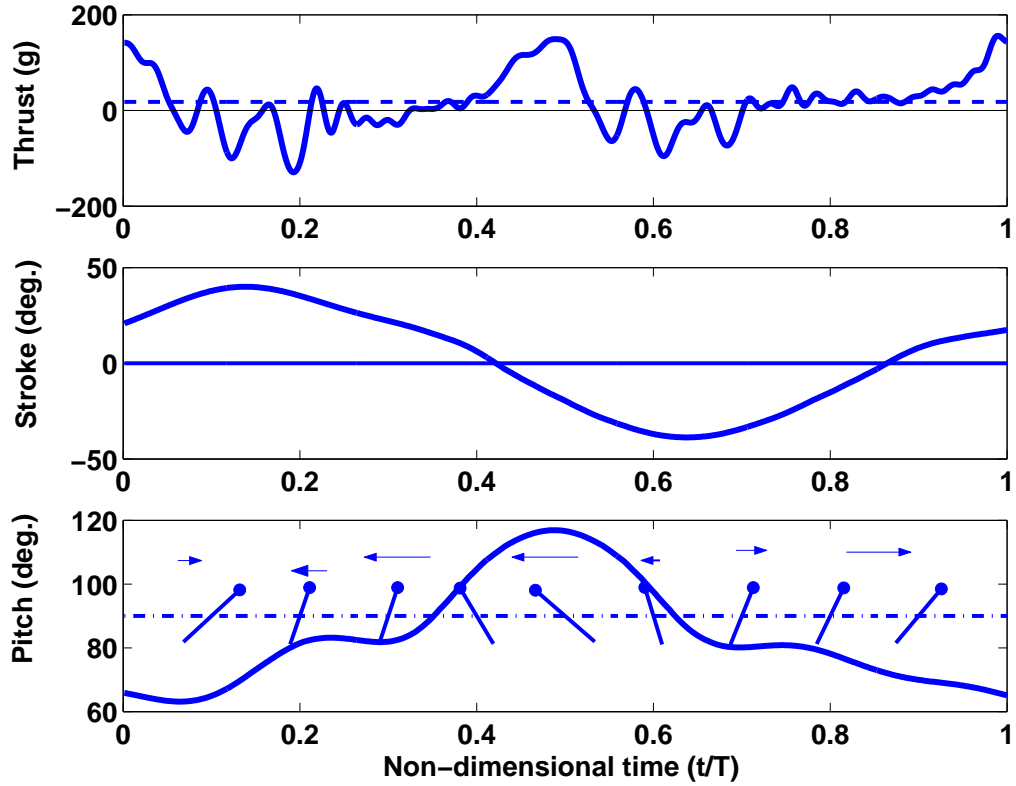


Figure 3.26: Time variation of loads and motion for Wing X at 22.3 Hz

for Wing X may be related to its lower mass and altered center of gravity location. The location of the center of gravity behind the wing elastic axis is important to generate a greater pitching motion because of the inertial forces acting on the wing.

Figure 3.26 shows the time variation of the thrust for Wing X, at high frequency, during one flapping cycle along with the stroke position and shaft pitch angle. The top figure also shows the mean thrust, and the pitch angle is plotted on the bottom figure along with arrows showing the direction of motion of the wing. The results are plotted against non-dimensional time in the flapping cycle. When the wing motion was such that the pitch angle was less than  $90^\circ$  with respect to the direction of motion, the thrust was positive. This was especially evident for

non-dimensional times between 0.7 and 0.9, where the thrust was nearly equal to its mean value. It is also evident that the pitch angle variation was not in phase with the flapping motion. This implies that with proper design and tuning of the torsion spring it may be possible to further increase the thrust generated by the wings.

### 3.8 Flow Visualization

Detailed results of the flow visualization study conducted on the flapping wings have been reported in Ref. 52. Flow features which are key to the aerodynamic modeling of the flapping wings are described in this section. In the flow visualization pictures, the laser sheet was at mid-span of the wing, and the camera was placed perpendicular to the laser sheet, as shown in Fig. 2.12. The Reynolds number for these tests was  $\sim 15,000$ . Figure 3.27 shows a chordwise flow visualization picture at mid-span, which clearly shows a leading edge vortex on the wing. The leading edge vortex helps the wing generate thrust, even at the extremely high pitch angles, without stalling. This is the first instance of a leading edge vortex being observed on a flapping wing at  $Re \sim 15,000$ . Also, strobing the wing with the laser sheet revealed the large amount of deformations that the wing was undergoing during flapping.

Figure 3.28 shows a series of images acquired at different positions in the flapping cycle starting from (b) the mid-point of supination to (l) the end of pronation. Figure 3.28(c) shows the wing during supination. A number of vortical structures were observed near the trailing edge during this rotational phase. As the wing



Figure 3.27: Flow visualization image showing the leading edge vortex.

started its translational motion, a powerful starting vortex formed and grew larger throughout the downstroke (Fig. 3.28(d),(e),(f)). Figure 3.28(f) shows the wing at the mid-point of the downstroke. One of the reasons for the high lift generating capability of insects, even at large pitch angles, is the presence of an attached leading edge vortex on top of the wing. Such a leading edge vortex was observed on top of the wing (Fig. 3.28(f)). Because of this vortex, the wing was able to generate thrust even at a very high pitch angle. Figure 3.28(f)–(j) show the evolution of the leading edge vortex during the latter half of the downstroke. Multiple leading edge vortices were seen forming and shedding off the wing as shown in Fig. 3.28(h)–(j).

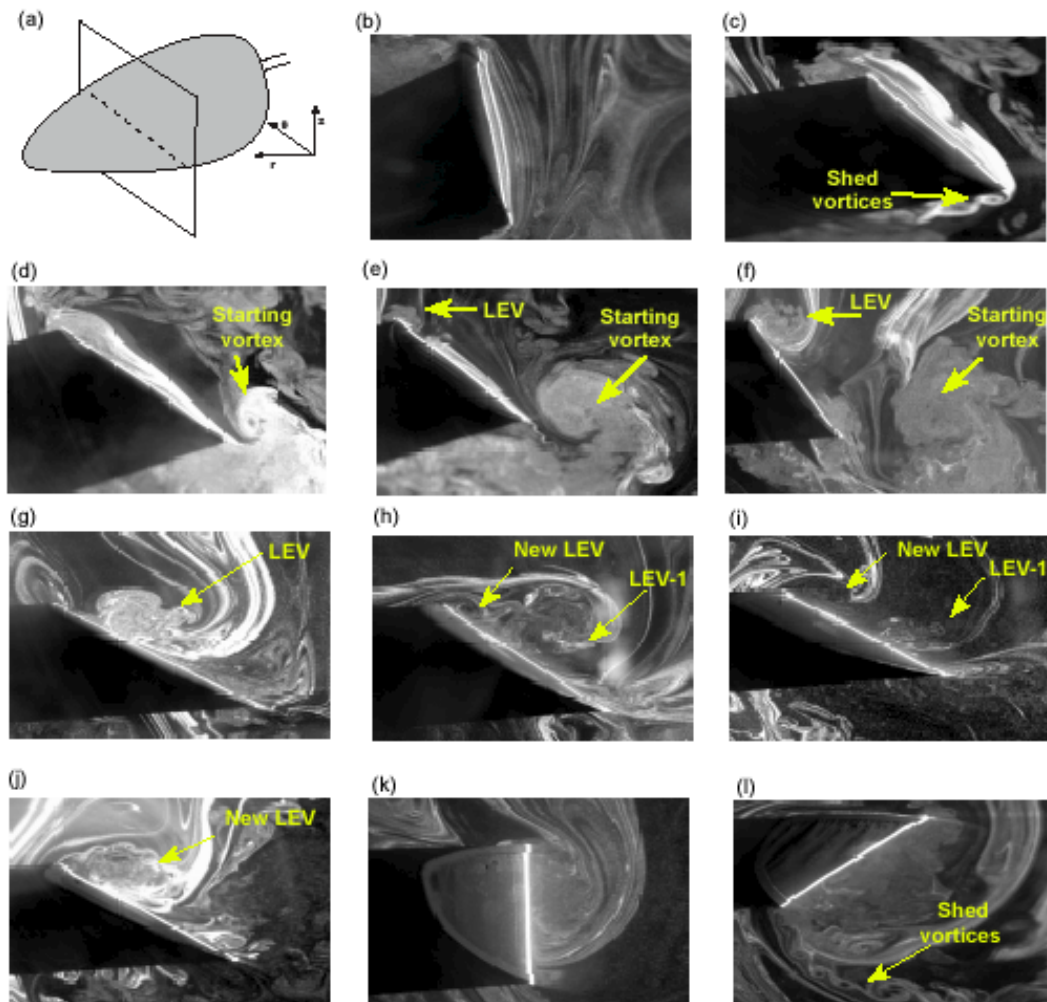


Figure 3.28: Flow visualization images acquired at different stroke positions (Ref. 52)

### 3.9 Summary

The thrust generated by wings, mounted on a flapping-pitching mechanism, was measured for a number of wing and stroke parameters. The two wings tested had the same planform shape. One wing pitched about the 50% chord location (Wing II), while the other pitched about the 20% chord location (Wing III). The latter produced more lift because of higher rotational circulation during the pronation and supination phases. However, when the pitch angle of the wings was increased from  $30^\circ$  to  $45^\circ$ , the thrust produced by Wing III increased but the thrust for Wing II remained the same. A slight change in pitch phase, so that pronation and supination occur early in the flapping cycle, reduced the thrust produced by Wing III. Again, the thrust produced by Wing II remained unchanged from the baseline case.

The inertial forces produced by Wing II were measured by testing it in vacuum. These forces were then subtracted from the total measured loads to obtain the aerodynamic forces on the wings. Although the accuracy of the time varying airloads obtained was questionable, the vacuum chamber tests showed nearly zero thrust produced by the mechanism, as expected.

Wing III, which produced the maximum thrust, was also tested at higher frequencies. However, the thrust showed a sudden drop at high frequency. The mass of the wing significantly reduced the maximum frequency which could be attained on the mechanism. Several light-weight composite wings were tested in order to overcome this limitation of the mechanism. However, all these wings showed a drop

in thrust at high frequency. By measuring the stroke position of the wings, the total aerodynamic and inertial power was computed at the base of the wing using the measured loads. The effect of wing mass on power required was also evident from the power curves.

Preliminary tests for a pure flapping motion with passive pitching of the shaft because of the inertial and aerodynamic forces acting on the wing, showed significant thrust generation by one of the wings tested. In this case the wing was held at a  $90^\circ$  angle and flapped in a horizontal plane. Because of the pitch flexibility of the shaft, the inertial and aerodynamic forces caused the shaft to pitch in a passive manner.

To further explore the lift generation capability of a passive pitch flapping wing mechanism, the bio-inspired flapping-pitching mechanism was modified to include a torsion spring on the flapping shaft. The torsional stiffness of the spring could be easily adjusted from a stiff condition to a soft one. When the spring was kept in the soft position, the pitch variation was larger than the pitch variation for a stiff spring. Also, the larger pitch variation for the soft spring helped generate greater thrust at a slightly smaller power consumption than the stiff spring. The time variation of thrust combined with the flapping and pitching motion of the shaft showed that the pitching motion was not in phase with the flapping motion, leading to a reduction in total thrust since the wing had an adverse angle of attack during part of the flapping cycle.

The flow visualization images acquired, revealed the presence a leading edge vortex on the wing. A large starting vortex was also observed. Multiple leading edge vortices were noticed on the wing, with one vortex shedding towards the trailing

edge while another formed at the leading edge. An important observation from this study was the large amount of wing deformations which were seen when the wing was strobed using the laser light sheet.

## Chapter 4

# Aeroelastic Model

In this chapter the structural and aerodynamic analyses used to model the aeroelastic behavior of hover-capable flapping wings are described. Since most insect wings, and the wings used in experiments, are low aspect ratio wings, plate finite elements were used to model these structures. The approaches available for aerodynamic modeling range from indicial methods based on Wagner and Kussner functions to the computationally intensive Unsteady Vortex Lattice Method (UVLM) and CFD analyses. In the present study, for coupling with the structural model, an unsteady aerodynamic model based on indicial functions was used, since this is the least complex and computationally efficient.

## 4.1 Structural Model

Figure 3.6 shows the aluminum-mylar wings used in the present study. A beam model would not be adequate to represent such low aspect ratio wings. Beam elements can only be used to model the aluminum frame, while plate elements must be used to model the mylar. To avoid complications because of the use of dissimilar

elements, the entire wing structure was modeled using plate elements. However, the use of plate elements introduces added complexity because a grid must be defined. For rectangular wings, this would not be too difficult. However, with the irregular planform of the wings, wing discretization becomes important.

#### **4.1.1 Wing discretization**

The process of discretizing the wing consists of defining nodes and elements on the wing surface. This is usually accomplished by meshing the part to be modeled using a structured or unstructured mesh. A structured mesh consists of a repeating geometric and topological structure. Unstructured grids on the other hand have no underlying structure. An important consideration in grid generation is the requirements of the finite element formulation. For example, certain quadrilateral plate elements perform better if the elements are regular rectangles instead of quadrilaterals. Performance degrades if the opposing sides of the element are not parallel to each other, i.e., if the element is not a rectangle. This is because, in the formulation of these elements, the number of degrees of freedom do not allow the use of a complete polynomial for interpolating the deformations within the element.

Based on the wing planform, an unstructured mesh would be most suited to the current problem. However, available unstructured mesh generation algorithms widely use triangular elements and not quadrilateral elements. The triangular elements which were available did not perform as well as the rectangular elements. Keeping in view the performance degradation of quadrilateral elements, a mesh us-

ing rectangular elements, with an irregular boundary, was chosen to discretize the wing. To begin with, the wing domain was divided into a rectangular mesh as shown in Fig. 4.1. The number of elements along each side of the rectangle could be varied arbitrarily to refine the mesh. Based on the input wing geometry, the algorithm accepted elements with at least a certain portion of their total area within the wing domain, all other elements being rejected. The preprocessor then outputs ordered sets of elements and nodes along with the element connectivity matrix.

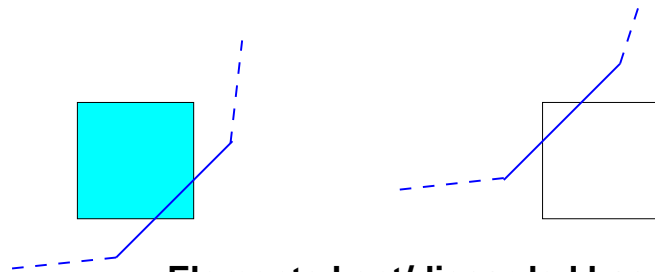
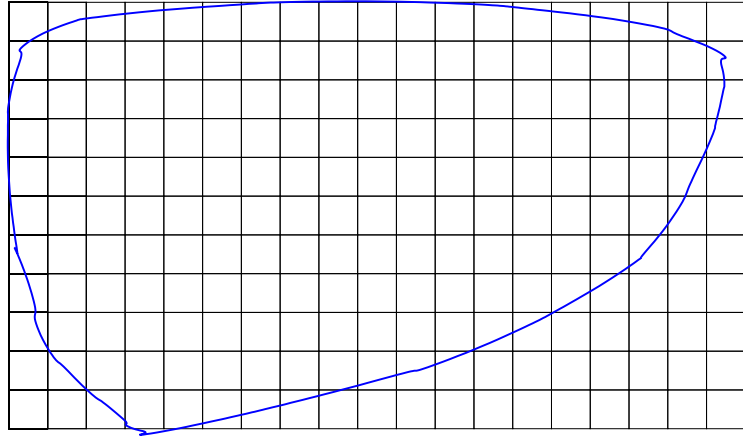
### **4.1.2 Large overall motion**

The structural model needs to account for the large overall motions of the wing, which is discretized using plate finite elements, as shown in Fig. 4.2. The problem of plates as well as arbitrary flexible bodies undergoing large overall motions has been studied before [98–100], although, the method has not been applied to the dynamics of flapping-pitching wings. In order to obtain accurate predictions of the dynamics of a flexible body undergoing large overall motions, dynamic stiffening must be accounted for in the formulation of the total kinetic energy. The equations of motion were derived using Hamilton’s principle using the variation of the strain energy and kinetic energy.

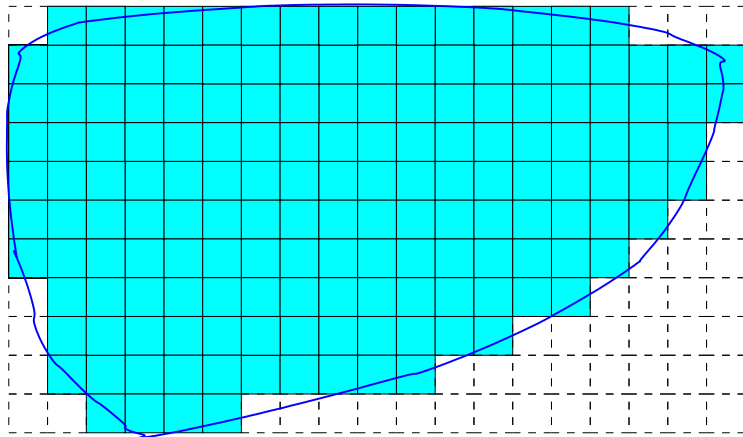
### **Strain Energy**

Since the wings were quite thin, the effects of shear deformation were neglected. Classical Laminated Plate Theory (CLPT) [101] was used so that the analysis would

### Initial Mesh



**Elements kept/discarded based on area within domain**



### Final Mesh

Figure 4.1: Mesh generation

be applicable to both metals and composite materials. With the assumption of small deformations, the linear strains for a plate can be written as,

$$\epsilon_{xx} = \frac{\partial u}{\partial x} - z \frac{\partial^2 w}{\partial x^2} \quad (4.1)$$

$$\epsilon_{yy} = \frac{\partial v}{\partial y} - z \frac{\partial^2 w}{\partial y^2} \quad (4.2)$$

$$\gamma_{xy} = \frac{\partial u}{\partial y} + \frac{\partial v}{\partial x} - 2z \frac{\partial^2 w}{\partial x \partial y} \quad (4.3)$$

where, u, v and w are the deformations along the x, y and z directions, respectively.

In vector notation,

$$\{\epsilon\} = \{\epsilon^0\} + z\{\kappa\} \quad (4.4)$$

where,  $\{\epsilon^0\}$  is the vector of membrane strains,  $\{\kappa\}$  is the vector of curvatures and  $z$  is the coordinate perpendicular to the plane of the plate. Using the material constitutive relation,  $\sigma = [Q]\epsilon$ , the variation of strain energy can be written as,

$$\delta U = \int \int \int_V \{\delta\epsilon\}^T [Q] \{\epsilon\} dx dy dz \quad (4.5)$$

Substituting Eq. 4.4 in the above equation, and integrating across the thickness  $h$ , the strain energy variation can be written as,

$$\delta U = \int \int_S (\{\delta\epsilon^0\}^T [A] \{\epsilon^0\} + \{\delta\epsilon^0\}^T [B] \{\kappa\} + \{\delta\kappa\}^T [B] \{\epsilon^0\} + \{\delta\kappa\}^T [D] \{\kappa\}) dx dy \quad (4.6)$$

where, the matrices A, B and D are given by,

$$[A] = \int_{-h/2}^{h/2} [Q] dz \quad (4.7)$$

$$[B] = \int_{-h/2}^{h/2} z [Q] dz \quad (4.8)$$

$$[D] = \int_{-h/2}^{h/2} z^2 [Q] dz \quad (4.9)$$

The matrix  $[B]$  represents the coupling between bending and extensional strains and is zero for isotropic materials and also for composites with symmetric ply layup. It must be noted that, as far as the analysis is concerned, the only difference between an isotropic material or a composite is in the definition of the matrix  $[Q]$ .

## Kinetic Energy

Figure 4.2 shows the reference frames used to describe the overall motion of the wing. The inertial reference frame  $X_i, Y_i, Z_i$  has its origin at the center of rotation. The flapping angle  $\beta$  denotes the rotation of the flapping reference frame  $X_f, Y_f, Z_f$  about the  $Z_i$  axis as shown. The wing pitching reference frame  $X_p, Y_p, Z_p$  is obtained by rotating the flapping reference frame by the wing pitch angle  $\theta$ , about the  $Y_f$  axis. The relevant orthonormal transformation matrices are,

$$\begin{Bmatrix} i_p \\ j_p \\ k_p \end{Bmatrix} = \begin{bmatrix} \cos \theta & 0 & \sin \theta \\ 0 & 1 & 0 \\ -\sin \theta & 0 & \cos \theta \end{bmatrix} \begin{Bmatrix} i_f \\ j_f \\ k_f \end{Bmatrix} = [T_{pf}] \begin{Bmatrix} i_f \\ j_f \\ k_f \end{Bmatrix} \quad (4.10)$$

$$\begin{Bmatrix} i_f \\ j_f \\ k_f \end{Bmatrix} = \begin{bmatrix} \cos \beta & -\sin \beta & 0 \\ \sin \beta & \cos \beta & 0 \\ 0 & 0 & 1 \end{bmatrix} \begin{Bmatrix} i_i \\ j_i \\ k_i \end{Bmatrix} = [T_{fi}] \begin{Bmatrix} i_i \\ j_i \\ k_i \end{Bmatrix} \quad (4.11)$$

The position vector of a point on the wing in the pitching frame is given by

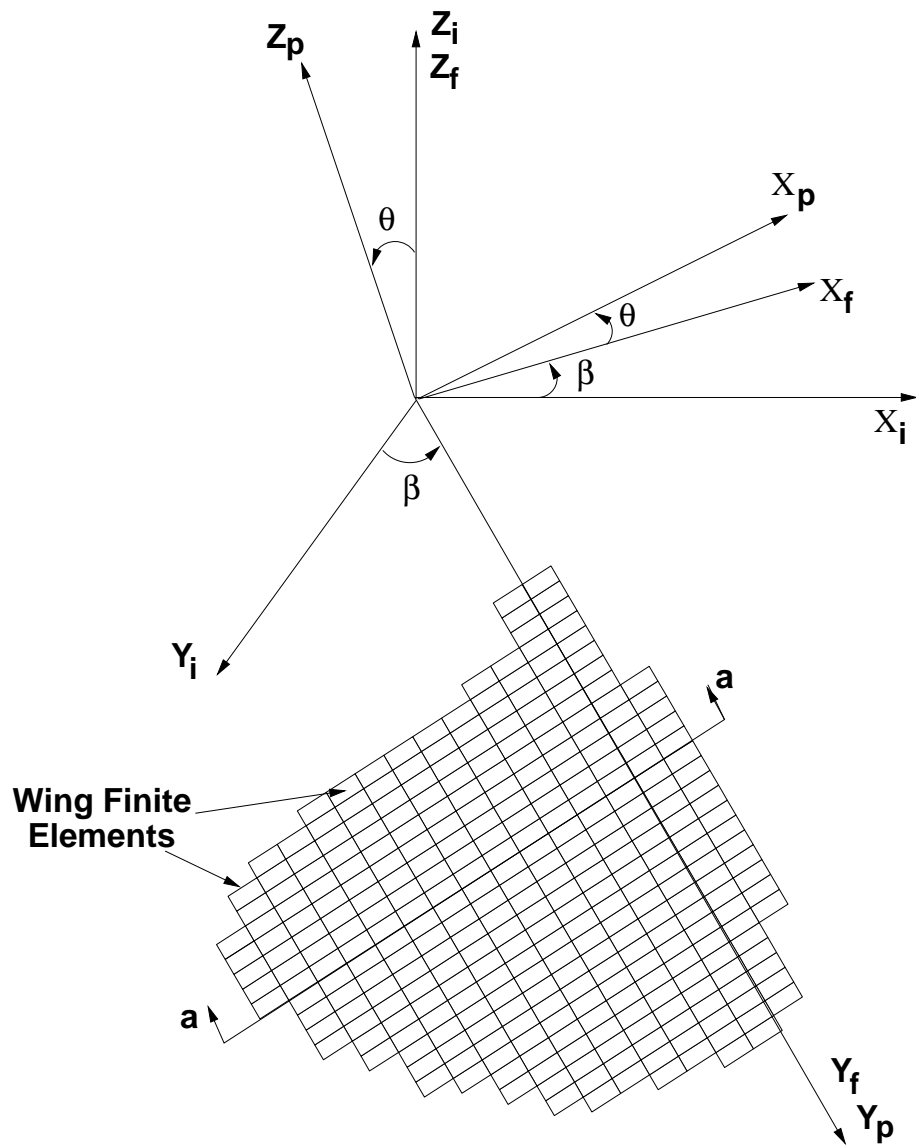


Figure 4.2: Reference frames

(Ref. [98]),

$$\vec{r}_p = \left\{ x_1 + u - \int_0^{x_1} \frac{1}{2} \left( \frac{\partial w}{\partial x} \right)^2 dx \quad y_1 + v - \int_0^{y_1} \frac{1}{2} \left( \frac{\partial w}{\partial y} \right)^2 dy \quad w \right\} \begin{Bmatrix} i_p \\ j_p \\ k_p \end{Bmatrix} \quad (4.12)$$

The integral terms in the above equation represent the foreshortening effect in the in-plane directions of the wing. These terms must be included to account for the dynamic stiffening of the wing under centrifugal forces. Using the transformation matrices described above, the position vector of a point on the wing can be written in the inertial reference frame, as,

$$\begin{aligned} \vec{r}_i &= \left\{ x_1 - \int_0^{x_1} \frac{1}{2} \left( \frac{\partial w}{\partial x} \right)^2 dx \quad y_1 - \int_0^{y_1} \frac{1}{2} \left( \frac{\partial w}{\partial y} \right)^2 dy \quad w \right\} [T_{pf}] [T_{fi}] \begin{Bmatrix} i_i \\ j_i \\ k_i \end{Bmatrix} \\ &= r_{i1} i_i + r_{i2} j_i + r_{i3} k_i \end{aligned} \quad (4.13)$$

The components of the position vector are given by,

$$\begin{aligned} r_{i1} &= \left( x_1 + u - \int_0^{x_1} \frac{1}{2} \left( \frac{\partial w}{\partial x} \right)^2 dx \right) \cos \theta \cos \beta \\ &\quad + \left( y_1 + v - \int_0^{y_1} \frac{1}{2} \left( \frac{\partial w}{\partial y} \right)^2 dy \right) \sin \beta \\ &\quad - w \sin(\theta(t)) \cos \beta \end{aligned} \quad (4.14)$$

$$\begin{aligned} r_{i2} &= - \left( x_1 + u - \int_0^{x_1} \frac{1}{2} \left( \frac{\partial w}{\partial x} \right)^2 dx \right) \cos \theta \sin \beta \\ &\quad + \left( y_1 + v - \int_0^{y_1} \frac{1}{2} \left( \frac{\partial w}{\partial y} \right)^2 dy \right) \cos \beta \\ &\quad + w \sin \theta \sin \beta \end{aligned} \quad (4.15)$$

$$r_{i3} = \left( x_1 + u - \int_0^{x_1} 1/2 \left( \frac{\partial}{\partial x} w \right)^2 dx \right) \sin \theta + w \cos \theta \quad (4.16)$$

In the above equations, the dependence of the deformations  $u$ ,  $v$  and  $w$  on  $(x, y, t)$  is implied. Also, the overall motions  $\theta$  and  $\beta$  are functions of time  $t$ . The velocity of a point on the wing can be found using the following equation,

$$\begin{aligned} \vec{v}_i &= \frac{d\vec{r}_i}{dt} \\ &= v_{i1}i_i + v_{i2}j_i + v_{i3}k_i \end{aligned} \quad (4.17)$$

The velocity components are given by,

$$\begin{aligned} v_{i1} &= \left( \frac{\partial u}{\partial t} - \int_0^{x_1} \left( \frac{\partial w}{\partial x} \right) \frac{\partial^2 w}{\partial t \partial x} dx \right) \cos \theta \cos \beta \\ &\quad - \left( x_1 + u - \int_0^{x_1} \frac{1}{2} \left( \frac{\partial w}{\partial x} \right)^2 dx \right) \\ &\quad \left( \sin \theta \frac{d\theta}{dt} \cos \beta + \cos \theta \sin \beta \frac{d\beta}{dt} \right) \\ &\quad + \left( \frac{\partial v}{\partial t} - \int_0^{y_1} \left( \frac{\partial w}{\partial y} \right) \frac{\partial^2 w}{\partial t \partial y} dy \right) \sin \beta \\ &\quad + \left( y_1 + v - \int_0^{y_1} \frac{1}{2} \left( \frac{\partial w}{\partial y} \right)^2 dy \right) \cos \beta \frac{d\beta}{dt} \\ &\quad - \frac{\partial w}{\partial t} \sin \theta \cos \beta - w \cos \theta \frac{d\theta}{dt} \cos \beta \\ &\quad + w \sin \theta \sin \beta \frac{d\beta}{dt} \end{aligned} \quad (4.18)$$

$$\begin{aligned} v_{i2} &= - \left( \frac{\partial u}{\partial t} - \int_0^{x_1} \left( \frac{\partial w}{\partial x} \right) \frac{\partial^2 w}{\partial t \partial x} dx \right) \cos \theta \sin \beta \\ &\quad + \left( x_1 + u - \int_0^{x_1} 1/2 \left( \frac{\partial w}{\partial x} \right)^2 dx \right) \sin \theta \frac{d\theta}{dt} \sin \beta \end{aligned}$$

$$\begin{aligned}
& - \left( x_1 + u - \int_0^{x_1} 1/2 \left( \frac{\partial w}{\partial x} \right)^2 dx \right) \cos \theta \cos \beta \frac{d\beta}{dt} \\
& + \left( \frac{\partial v}{\partial t} - \int_0^{y_1} \left( \frac{\partial w}{\partial y} \right) \frac{\partial^2 w}{\partial t \partial y} dy \right) \cos \beta \\
& - \left( y_1 + v - \int_0^{y_1} 1/2 \left( \frac{\partial w}{\partial y} \right)^2 dy \right) \sin \beta \frac{d\beta}{dt} \\
& + \frac{\partial w}{\partial t} \sin \theta \sin \beta + w \cos \theta \frac{d\theta}{dt} \sin \beta \\
& + w \sin \theta \cos \beta \frac{d\beta}{dt}
\end{aligned} \tag{4.19}$$

$$\begin{aligned}
v_{i3} & = \left( \frac{\partial u}{\partial t} - \int_0^{x_1} \left( \frac{\partial w}{\partial x} \right) \frac{\partial^2 w}{\partial t \partial x} dx \right) \sin \theta \\
& + \left( x_1 + u - \int_0^{x_1} 1/2 \left( \frac{\partial w}{\partial x} \right)^2 dx \right) \cos \theta \frac{d\theta}{dt} \\
& + \frac{\partial w}{\partial t} \cos \theta - w \sin \theta \frac{d\theta}{dt}
\end{aligned} \tag{4.20}$$

The variations of these velocity components are given by,

$$\begin{aligned}
\delta v_{i1} & = \left( \delta \left( \frac{\partial u}{\partial t} \right) - \int_0^{x_1} \left[ \delta \left( \frac{\partial w}{\partial x} \right) \frac{\partial^2 w}{\partial t \partial x} + \frac{\partial w}{\partial x} \delta \left( \frac{\partial^2 w}{\partial t \partial x} \right) \right] dx \right) \\
& \cos \theta \cos \beta - \left( \delta u - \int_0^{x_1} \frac{\partial w}{\partial x} \delta \left( \frac{\partial w}{\partial x} \right) dx \right) \sin \theta \frac{d\theta}{dt} \\
& \cos \beta - \left( \delta u - \int_0^{x_1} \frac{\partial w}{\partial x} \delta \left( \frac{\partial w}{\partial x} \right) dx \right) \cos \theta \sin \beta \frac{d\beta}{dt} \\
& + \left( \delta \left( \frac{\partial v}{\partial t} \right) - \int_0^{y_1} \left[ \delta \left( \frac{\partial w}{\partial y} \right) \frac{\partial^2 w}{\partial t \partial y} + \frac{\partial w}{\partial y} \delta \left( \frac{\partial^2 w}{\partial t \partial y} \right) \right] dy \right) \sin \beta \\
& + \left( \delta v - \int_0^{y_1} \frac{\partial w}{\partial y} \delta \left( \frac{\partial w}{\partial y} \right) dy \right) \cos \beta \frac{d\beta}{dt} \\
& - \delta \left( \frac{\partial w}{\partial t} \right) \sin \theta \cos \beta - \delta w \cos \theta \frac{d\theta}{dt} \cos \beta \\
& + \delta w \sin \theta \sin \beta \frac{d\beta}{dt}
\end{aligned} \tag{4.21}$$

$$\delta v_{i2} = - \left( \delta \left( \frac{\partial u}{\partial t} \right) - \int_0^{x_1} \left[ \delta \left( \frac{\partial w}{\partial x} \right) \frac{\partial^2 w}{\partial t \partial x} + \frac{\partial w}{\partial x} \delta \left( \frac{\partial^2 w}{\partial t \partial x} \right) \right] dx \right)$$

$$\begin{aligned}
& \cos \theta \sin \beta + \left( \delta u - \int_0^{x_1} \frac{\partial w}{\partial x} \delta \left( \frac{\partial w}{\partial x} \right) dx \right) \sin \theta \frac{d\theta}{dt} \sin \beta \\
& - \left( \delta u - \int_0^{x_1} \frac{\partial w}{\partial x} \delta \left( \frac{\partial w}{\partial x} \right) dx \right) \cos \theta \cos \beta \frac{d\beta}{dt} \\
& + \left( \delta \left( \frac{\partial v}{\partial t} \right) - \int_0^{y_1} \left[ \delta \left( \frac{\partial w}{\partial y} \right) \frac{\partial^2 w}{\partial t \partial y} + \frac{\partial w}{\partial y} \delta \left( \frac{\partial^2 w}{\partial t \partial y} \right) \right] dy \right) \cos \beta \\
& - \left( \delta v - \int_0^{y_1} \frac{\partial w}{\partial y} \delta \left( \frac{\partial w}{\partial y} \right) dy \right) \sin \beta \frac{d\beta}{dt} \\
& + \delta \left( \frac{\partial w}{\partial t} \right) \sin \theta \sin \beta + \delta w \cos \theta \frac{d\theta}{dt} \sin \beta \\
& + \delta w \sin \theta \cos \beta \frac{d\beta}{dt}
\end{aligned} \tag{4.22}$$

$$\begin{aligned}
\delta v_{i3} &= \left( \delta \left( \frac{\partial u}{\partial t} \right) - \int_0^{x_1} \left[ \delta \left( \frac{\partial w}{\partial x} \right) \frac{\partial^2 w}{\partial t \partial x} + \frac{\partial w}{\partial x} \delta \left( \frac{\partial^2 w}{\partial t \partial x} \right) \right] dx \right) \sin \theta \\
& + \left( \delta u - \int_0^{x_1} \frac{\partial w}{\partial x} \delta \left( \frac{\partial w}{\partial x} \right) dx \right) \cos \theta \frac{d\theta}{dt} + \delta \left( \frac{\partial w}{\partial t} \right) \cos \theta \\
& - \delta w \sin \theta \frac{d\theta}{dt}
\end{aligned} \tag{4.23}$$

The variation of the kinetic energy is then obtained from the following relation,

$$\delta T = \int \int \int_V \rho \vec{v}_i \cdot \delta \vec{v}_i dx dy dz \tag{4.24}$$

where,  $\rho$  is the material density. Using Hamilton's principle we have,

$$\int_{t_1}^{t_2} (\delta U - \delta T) dt = 0 \tag{4.25}$$

Substituting Eqs. 4.6 and 4.24 in the above equation, we obtain the equations of motion. Assuming the wing deformations  $u$ ,  $v$  and  $w$  to be small, the higher order non-linear terms may be neglected from the expansion of Eq. 4.24. The remaining terms with orders of magnitude  $O(1)$  and  $O(\epsilon)$  are given by,

$$\begin{aligned}
\int_{t_1}^{t_2} \delta T^1 dt &= \int_{t_1}^{t_2} \int \int \int_V \rho \left( \left[ - \left( \frac{d^2 \beta}{dt^2} \right) y_1 \cos \theta + \cos^2 \theta \left( \frac{d\beta}{dt} \right)^2 x_1 \right. \right. \\
&\quad \left. \left. + \left( \frac{d\theta}{dt} \right)^2 x_1 \right] \delta u + \left[ \left( \frac{d\beta}{dt} \right)^2 y_1 - 2 \sin \theta \left( \frac{d\theta}{dt} \right) \left( \frac{d\beta}{dt} \right) x_1 \right. \right. \\
&\quad \left. \left. + \cos \theta \left( \frac{d^2 \beta}{dt^2} \right) x_1 \right] \delta v + \left[ \sin \theta \left( \frac{d^2 \beta}{dt^2} \right) y_1 - \cos \theta \right. \right. \\
&\quad \left. \left. \left( \frac{d\beta}{dt} \right)^2 x_1 \sin \theta - \left( \frac{d^2 \theta}{dt^2} \right) x_1 \right] \delta w \right) dx dy dz dt \quad (4.26)
\end{aligned}$$

$$\begin{aligned}
\int_{t_1}^{t_2} \delta T^\epsilon dt &= \int_{t_1}^{t_2} \int \int \int_V \rho \left( \left[ - \left( \frac{d^2 \beta}{dt^2} \right) v \cos \theta - w \sin \theta \left( \frac{d\beta}{dt} \right)^2 \cos \theta \right. \right. \\
&\quad \left. \left. + 2 \frac{\partial w}{\partial t} \frac{d\theta}{dt} + \left( \frac{d\theta}{dt} \right)^2 u + w \frac{d^2 \theta}{dt^2} + \cos^2 \theta \left( \frac{d\beta}{dt} \right)^2 u \right. \right. \\
&\quad \left. \left. - 2 \left( \frac{d\beta}{dt} \right) \frac{\partial v}{\partial t} \cos \theta - \frac{\partial^2 u}{\partial t^2} \right] \delta u + \left[ - \frac{\partial^2 v}{\partial t^2} + \left( \frac{d\beta}{dt} \right)^2 v \right. \right. \\
&\quad \left. \left. + 2 \cos \theta \frac{\partial u}{\partial t} \frac{d\beta}{dt} - 2 \sin \theta \frac{\partial w}{\partial t} \frac{d\beta}{dt} - w \sin \theta \frac{d^2 \beta}{dt^2} \right. \right. \\
&\quad \left. \left. + \cos \theta \left( \frac{d^2 \beta}{dt^2} \right) u - 2 \sin \theta \left( \frac{d\theta}{dt} \right) \frac{d\beta}{dt} u \right. \right. \\
&\quad \left. \left. - 2 w \cos \theta \left( \frac{d\theta}{dt} \right) \frac{d\beta}{dt} \right] \delta v + \left[ - \frac{\partial^2 w}{\partial t^2} + w \left( \frac{d\beta}{dt} \right)^2 \right. \right. \\
&\quad \left. \left. - 2 \left( \frac{d\theta}{dt} \right) \frac{\partial u}{\partial t} + w \left( \frac{d\theta}{dt} \right)^2 - \left( \frac{d^2 \theta}{dt^2} \right) u + 2 \frac{\partial v}{\partial t} \sin \theta \frac{d\beta}{dt} \right. \right. \\
&\quad \left. \left. - w \left( \frac{d\beta}{dt} \right)^2 \cos^2 \theta - \cos \theta \left( \frac{d\beta}{dt} \right)^2 u \sin \theta \right. \right. \\
&\quad \left. \left. + \sin \theta \left( \frac{d^2 \beta}{dt^2} \right) v \right] \delta w + x_1 \cos \theta \left( \frac{d^2 \beta}{dt^2} \right) \int_0^{y_1} \frac{\partial w}{\partial y} \delta \left( \frac{\partial w}{\partial y} \right) dy \right. \\
&\quad \left. + \cos^2 \theta \left( \frac{d\beta}{dt} \right)^2 x_1 \int_0^{x_1} \frac{\partial w}{\partial x} \delta \left( \frac{\partial w}{\partial x} \right) dx - \right. \\
&\quad \left. y_1 \left( \frac{d^2 \beta}{dt^2} \right) \cos \theta \int_0^{x_1} \frac{\partial w}{\partial x} \delta \left( \frac{\partial w}{\partial x} \right) dx \right. \\
&\quad \left. + \left( \frac{d\beta}{dt} \right)^2 y_1 \int_0^{y_1} \frac{\partial w}{\partial y} \delta \left( \frac{\partial w}{\partial y} \right) dy + \left( \frac{d\theta}{dt} \right)^2 x_1 \int_0^{x_1} \frac{\partial w}{\partial x} \delta \left( \frac{\partial w}{\partial x} \right) dx \right. \\
&\quad \left. - 2 \sin \theta \left( \frac{d\theta}{dt} \right) x_1 \left( \frac{d\beta}{dt} \right) \int_0^{y_1} \frac{\partial w}{\partial y} \delta \left( \frac{\partial w}{\partial y} \right) dy \right) dx dy dz dt \quad (4.27)
\end{aligned}$$

It must be noted that, in the above equation, terms containing the variation of velocities were eliminated by partially integrating them w.r.t time.

### 4.1.3 Finite Element Formulation

The expressions for strain and kinetic energy were discretized in space by dividing the wing into finite elements. Figure 4.3 shows the degrees of freedom (dof's) of the plate element used. This element was first developed by Bogner, Fox and Schmidt and is referred to as the BFS element [101]. It is one of the most commonly used rectangular thin plate elements. The vector of elemental degrees of freedom is given by,

$$\{q^e\} = \begin{matrix} u_1 & u_2 & u_3 & u_4 & v_1 & v_2 & v_3 & v_4 & w_1 \\ \left(\frac{\partial w}{\partial x}\right)_1 & \left(\frac{\partial w}{\partial y}\right)_1 & \left(\frac{\partial^2 w}{\partial x \partial y}\right)_1 & w_2 & \left(\frac{\partial w}{\partial x}\right)_2 & \left(\frac{\partial w}{\partial y}\right)_2 & \left(\frac{\partial^2 w}{\partial x \partial y}\right)_2 & w_3 & \left(\frac{\partial w}{\partial x}\right)_3 \\ \left(\frac{\partial w}{\partial y}\right)_3 & \left(\frac{\partial^2 w}{\partial x \partial y}\right)_3 & w_4 & \left(\frac{\partial w}{\partial x}\right)_4 & \left(\frac{\partial w}{\partial y}\right)_4 & \left(\frac{\partial^2 w}{\partial x \partial y}\right)_4 \end{matrix}^T \quad (4.28)$$

Within each element, the in-plane deformations  $u$  and  $v$  can be interpolated using the element shape functions as,

$$u^e(x, y, t) = \sum_1^4 N_{1i} u_i \quad (4.29)$$

$$v^e(x, y, t) = \sum_1^4 N_{2i} v_i \quad (4.30)$$

For the BFS element, the bending deformation  $w$  is expressed as,

$$w^e(x, y, t) = c_0 + c_1 x + c_2 y + c_3 x^2 + c_4 xy + c_5 y^2 + c_6 x^3 + c_7 x^2 y + c_8 xy^2$$

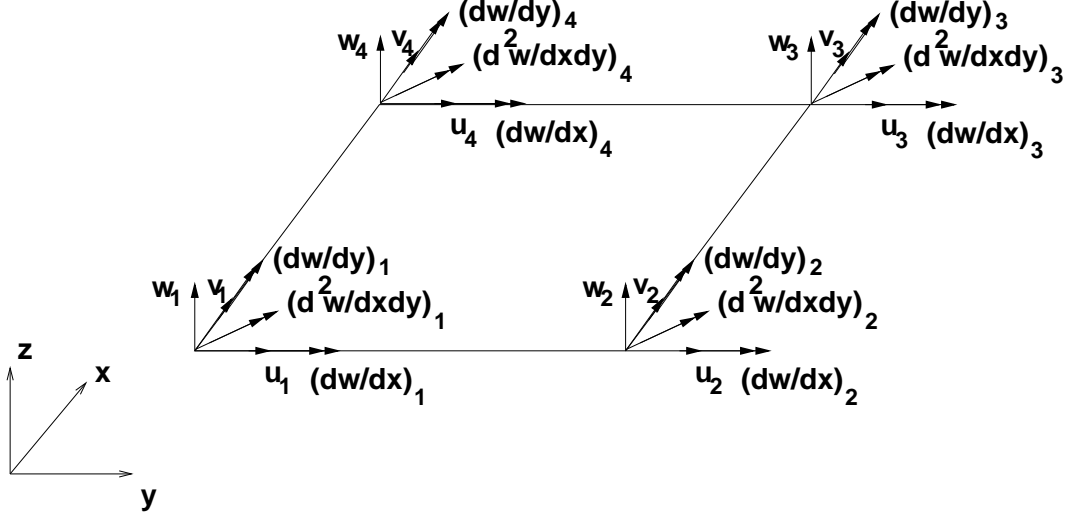


Figure 4.3: Element degrees of freedom

$$\begin{aligned}
 &+c_9y^3 + c_{10}x^3y + c_{11}x^2y^2 + c_{12}xy^3 + c_{13}x^3y^2 \\
 &+c_{14}x^2y^3 + c_{15}x^3y^3
 \end{aligned} \tag{4.31}$$

It must be noted that this polynomial is not complete. This is an issue with most plate elements which require extra nodes and dof's within the element to obtain a complete polynomial. However, this element showed good convergence characteristics for both static and dynamic problems. Substituting the 16 known nodal deformations in Eq. 4.31, we obtain a set of equations for the unknown constants  $c_i$ , which can be solved to obtain the shape functions for the bending deformation. The matrices  $N_1$ ,  $N_2$  and  $N_3$  are defined in Appendix A. In matrix form,

$$\begin{aligned}
 \begin{Bmatrix} u \\ v \\ w \end{Bmatrix}_{3 \times 1} &= \begin{bmatrix} N_1 \\ N_2 \\ N_3 \end{bmatrix}_{3 \times 24} \{q^e\}_{24 \times 1} \\
 &= [N]\{q^e\}
 \end{aligned} \tag{4.32}$$

The  $1 \times 24$  vectors  $N_1, N_2$  and  $N_3$  contain the shape functions for the u, v and w deformations, respectively.

## Strain displacement relation

The membrane strains and curvatures may be written as,

$$\begin{aligned} \{\epsilon^0\} &= \begin{bmatrix} \frac{\partial}{\partial x} & 0 & 0 \\ 0 & \frac{\partial}{\partial y} & 0 \\ \frac{\partial}{\partial y} & \frac{\partial}{\partial x} & 0 \end{bmatrix} \begin{Bmatrix} u \\ v \\ w \end{Bmatrix} \\ &= [\Gamma_1]\{\Delta\} \end{aligned} \quad (4.33)$$

$$\begin{aligned} \{\kappa\} &= \begin{bmatrix} 0 & 0 & -\frac{\partial^2}{\partial x^2} \\ 0 & 0 & -\frac{\partial^2}{\partial y^2} \\ 0 & 0 & -2\frac{\partial^2}{\partial x \partial y} \end{bmatrix} \begin{Bmatrix} u \\ v \\ w \end{Bmatrix} \\ &= [\Gamma_2]\{\Delta\} \end{aligned} \quad (4.34)$$

where,  $[\Gamma_1]$  and  $[\Gamma_2]$  are operator matrices. Substituting Eq. 4.32 in the above equations we get,

$$\{\epsilon^0\} = [\Gamma_1][N]\{q^e\} = [H_1]\{q^e\} \quad (4.35)$$

$$\{\kappa\} = [\Gamma_2][N]\{q^e\} = [H_2]\{q^e\} \quad (4.36)$$

The matrices  $[H_1]$  and  $[H_2]$  are functions of x and y within each element and, relate the elemental deformations to the strain field within the element.

## Static stiffness matrix

Substituting the above equations in Eq. 4.6, the elemental strain energy can be written as,

$$\delta U^e = \{\delta q^e\}^T \left( \int \int_e \left[ [H_1]^T [A] [H_1] + [H_1]^T [B] [H_2] + [H_2]^T [B] [H_1] + [H_2]^T [D] [H_2] \right] dx dy \right) \{q^e\} \quad (4.37)$$

where, the term within brackets defines the static stiffness matrix for one element.

$$K^e = \int \int_e \left[ [H_1]^T [A] [H_1] + [H_1]^T [B] [H_2] + [H_2]^T [B] [H_1] + [H_2]^T [D] [H_2] \right] dx dy \quad (4.38)$$

## Mass matrix and dynamic stiffness matrices

Using Eq. 4.32 the kinetic energy variation given by Eqs. 4.26 and 4.27 can be written for a single element,

$$\begin{aligned} \delta T^e = & \{\delta q^e\}^T \left( \int \int_A \rho t \left[ -(\dot{\theta}^2 + \dot{\beta}^2 \sin^2 \theta) [N_3]^T [N_3] \{q^e\} - [N_3]^T [N_3] \{\ddot{q}^e\} \right. \right. \\ & - (\dot{\beta}^2 \sin \theta \cos \theta + \ddot{\theta}) x_1 [N_3]^T + \sin \theta \ddot{\beta} y_1 [N_3]^T + (\sin \theta \dot{\beta} \dot{\theta} x_1 - \dot{\beta}^2 y_1) [H_y] \{q^e\} \\ & + (\sin \theta \dot{\beta} \dot{\theta} y_1 - (\cos^2 \theta \dot{\beta}^2 + \dot{\theta}^2) x_1) [H_x] \{q^e\} - (\ddot{\theta} + \cos \theta \sin \theta \dot{\beta}^2) \\ & [N_3]^T [N_1] \{q^e\} - 2\dot{\theta} [N_3]^T [N_1] \{\dot{q}^e\} + \sin \theta \ddot{\beta} [N_3]^T [N_2] \{q^e\} \\ & + 2 \sin \theta \dot{\beta} [N_3]^T [N_2] \{\dot{q}^e\} + (\ddot{\theta} - \cos \theta \sin \theta \dot{\beta}^2) [N_1]^T [N_3] \{q^e\} \\ & + 2\dot{\theta} [N_1]^T [N_3] \{\dot{q}^e\} - \cos \theta \ddot{\beta} [N_1]^T [N_2] \{q^e\} - 2 \cos \theta \dot{\zeta} [N_1]^T [N_2] \{\dot{q}^e\} \\ & \left. \left. + (\dot{\theta}^2 + \dot{\beta}^2 \cos^2 \theta) [N_1]^T [N_1] \{q^e\} - [N_1]^T [N_1] \{\ddot{q}^e\} + (\dot{\theta}^2 + \dot{\beta}^2 \cos^2 \theta) x_1 [N_1]^T \right] \right) \end{aligned}$$

$$\begin{aligned}
& -\cos\theta\ddot{\beta}y_1[N_1]^T - \sin\theta\ddot{\beta}[N_2]^T[N_3]\{q^e\} - 2\sin\theta\dot{\beta}[N_2]^T[N_3]\{\dot{q}^e\} \\
& +\dot{\beta}^2[N_2]^T[N_2]\{q^e\} - [N_2]^T[N_2]\{\ddot{q}^e\} + (\cos\theta\ddot{\beta} - 2\sin\theta\dot{\theta}\dot{\beta})[N_2]^T[N_1]\{q^e\} \\
& +2\cos\theta\dot{\beta}[N_2]^T[N_1]\{\dot{q}^e\} + (\cos\theta\ddot{\beta} - 2\sin\theta\dot{\theta}\dot{\beta})x_1[N_2]^T \\
& +\dot{\beta}^2y_1[N_2]^T \Big] dx dy \Big) \tag{4.39}
\end{aligned}$$

where, the matrices  $[H_x]$  and  $[H_y]$  represent dynamic stiffening because of foreshortening, and are given by,

$$[H_x] = \int_0^{x_1} [N_{3,x}]^T [N_{3,x}] dx \tag{4.40}$$

$$[H_y] = \int_0^{y_1} [N_{3,y}]^T [N_{3,y}] dy \tag{4.41}$$

where, the subscripts  $x$  and  $y$ , denote differentiation w.r.t  $x$  and  $y$ , respectively.

From Eq. 4.39, the elemental mass matrix, dynamic stiffness matrix and the elemental force vector may be identified.

$$[M^e] = \int \int_e \rho t \left( [N_1]^T [N_1] + [N_2]^T [N_2] + [N_3]^T [N_3] \right) dx dy \tag{4.42}$$

$$\begin{aligned}
[K_D^e] &= \int \int_e \rho t \left( (\dot{\beta}^2 y_1 - \sin\theta\dot{\beta}\dot{\theta}x_1)[H_y] + ((\cos^2\theta\dot{\beta}^2 + \dot{\theta}^2)x_1 \right. \\
& \quad \left. - \sin\theta\dot{\beta}\dot{\theta}y_1)[H_x] + (\dot{\theta}^2 + \dot{\beta}^2 \sin^2\theta)[N_3]^T [N_3] - (\dot{\theta}^2 \right. \\
& \quad \left. + \dot{\beta}^2 \cos^2\theta)[N_1]^T [N_1] - \dot{\beta}^2 [N_2]^T [N_2] \right) dx dy \tag{4.43}
\end{aligned}$$

$$\{F^e\} = \int \int_e \rho t \left( \sin\theta\ddot{\beta}y_1[N_3]^T - (\dot{\beta}^2 \sin\theta \cos\theta + \ddot{\theta})x_1[N_3]^T \right)$$

$$\begin{aligned}
&+(\dot{\theta}^2 + \dot{\beta}^2 \cos^2 \theta x_1 [N_1]^T - \cos \theta \ddot{\beta} y_1 [N_1]^T + (\cos \theta \ddot{\beta} \\
&-2 \sin \theta \dot{\theta} \dot{\beta}) x_1 [N_2]^T + \dot{\beta}^2 y_1 [N_2]^T) dx dy
\end{aligned} \tag{4.44}$$

Using the element connectivity matrix, the elemental matrices and force vectors were assembled to obtain the global mass matrix  $[M]$ , the global stiffness matrix  $[K]$ , the global dynamic stiffness matrix  $[K_D(t)]$  and the global force vector  $[F]$ . The stiffness matrix is time dependent because of the dynamic stiffness matrix  $[K_D(t)]$ . A cantilever boundary condition at the wing root was then applied to these matrices by eliminating the dof's corresponding to the fixed nodes.

## Numerical integration: Gauss quadrature

The area integrals in the above equations were evaluated using two-dimensional Gauss quadrature. The integral of a generic function  $f(x, y)$  can be approximated as,

$$\int \int_A f(x, y) dx dy \approx \sum_{i=1}^m \sum_{j=1}^n f(\xi_i a, \eta_j b) W_i W_j \tag{4.45}$$

where,  $m$  and  $n$  denote the number of gauss quadrature points in the x and y directions, respectively, and  $W_i$  and  $W_j$  denote the corresponding Gauss weights. Figure 4.4 illustrates the five point Gauss quadrature used in the present study. Table 4.1.3 gives the coordinates and weights of the points.

In order to compute the dynamic stiffening matrices  $[H_x]$  and  $[H_y]$ , the following integrals were determined in closed form for each element,

$$\int_{-a}^{\bar{x}} [N_{3,x}]^T [N_{3,x}] dx$$

Points $\xi_i, \eta_j$	Weights $W_i, W_j$
0.0000000000	0.5688888889
$\pm 0.5384693101$	0.4786286705
$\pm 0.9061798459$	0.2369268850

Table 4.1: 5 point Gauss quadrature points and weights.

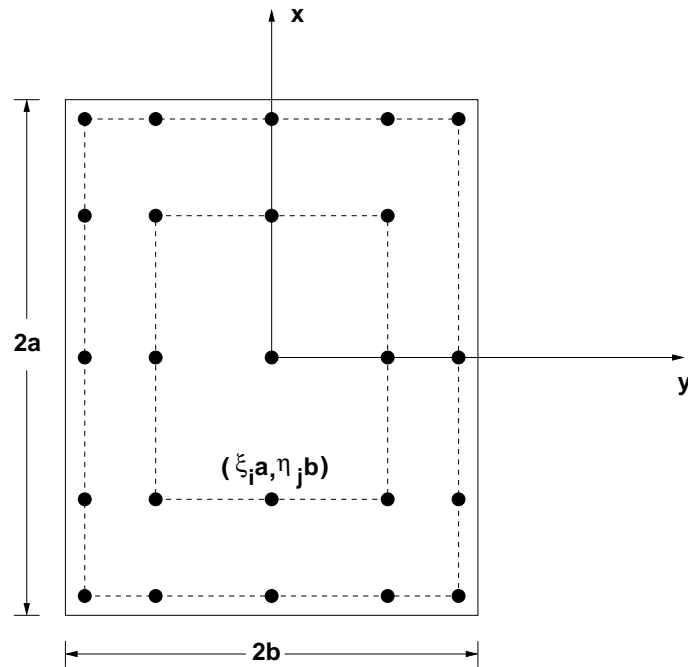


Figure 4.4: Gauss quadrature points ( $5 \times 5$ )

$$\int_{-b}^{\bar{y}} [N_{3,y}]^T [N_{3,y}] dy$$

These matrices are defined in Appendix A.

## Equation of motion

Using the kinetic energy variation, along with the wing strain energy functional and using Hamilton's principle, the equations of motion for a plate undergoing large flapping and pitching motions were obtained. The dynamic response of a static wing is governed by the following equation,

$$[M]\{\ddot{q}\} + [K]\{q\} = 0 \quad (4.46)$$

The eigenvalues and eigenvectors of this system are denoted by  $\Lambda$  and  $\Phi$ . When the wing motion is prescribed, i.e.  $\theta(t)$  and  $\beta(t)$  are known as a function of time, the equations of motion can be written as,

$$[M]\{\ddot{q}\} + ([K] + [K_D(t)])\{q\} = \{F(t)\} \quad (4.47)$$

where, the stiffness matrix is now a function of the prescribed overall base motions. The modal matrix  $\Phi$  for the static case was used to reduce the size of the above system, by retaining the first 'm' modes in the analysis. All results were obtained with the first five modes retained in the analysis. The nodal deformations can be expressed in modal coordinates as,

$$\{q\} = [\Phi_m]\{\bar{q}\} \quad (4.48)$$

where,  $[\Phi_m]$  has  $m$  columns, with each column containing the eigenvector corresponding to one mode. Substituting this equation in Eq. 4.47, the modal equations can be obtained,

$$[\Phi_m]^T [M] [\Phi_m] \{\ddot{\bar{q}}\} + [\Phi_m]^T ([K] + [K_D(t)]) [\Phi_m] \{\bar{q}\} = [\Phi_m]^T \{F(t)\} \quad (4.49)$$

$$[\bar{M}] \{\ddot{\bar{q}}\} + [\bar{K}(t)] \{\bar{q}\} = \{\bar{F}(t)\} \quad (4.50)$$

Modal damping was included in the equations to account for the structural damping of the wing. The resulting system of equations was integrated to obtain the motion of the wing. Once the motion of the wing was known, the bending moment at the base of the wing was obtained by a surface integral of the inertial loads acting on the wing.

## 4.2 Aerodynamic Model

The aerodynamic analysis is a blade element formulation, based on the assumption that the aerodynamic forces acting on a flapping-pitching wing can be broken down into a number of components which are accounted for separately and then added to obtain the total force. The effects of wing elastic deformations have also been accounted for. The following components contribute to the total aerodynamic force,

1. The translational and rotational circulation based on thin airfoil theory, with wing elasticity effects included.

2. The effect of a leading edge vortex on the wing, determined by using Polhamus' leading edge suction analogy for delta wings at high angles of attack [80, 102, 103].
3. Non-circulatory forces based on thin airfoil theory [104].
4. The effect of the starting vortex on the translational and rotational circulation. This was accounted for by using the Wagner function.
5. The effect of the shed wake and a tip vortex, accounted for by using the Kussner function. The induced inflow velocity was determined based on momentum considerations.

Figure 4.5 shows the leading edge vortex and the structure of the wake at one radial location along the wing. Figure 4.6 shows the flow velocities at this radial location. In thin airfoil theory, the problem reduces to the determination of a circulation distribution  $\gamma$  along the chord, as governed by the following integral equation,

$$\frac{1}{2\pi} \int_0^c \frac{\gamma(\xi)}{(x - \xi)} d\xi = V_n + \dot{\theta}(x - ac) - \dot{w}(x) - V_p \frac{\partial w}{\partial x} \quad (4.51)$$

It must be noted that, since the normal and parallel velocities were used in the above equation, there was no small angle assumption involved. The velocities normal and parallel to the wing chord are given by,

$$V_n = V_H \sin \theta + V_v \cos \theta \quad (4.52)$$

$$V_p = V_H \cos \theta - V_v \sin \theta \quad (4.53)$$

The circulation distribution  $\gamma$  can be determined by using the transformation  $\xi = c/2(1 - \cos \phi)$  and expressing  $\gamma(\xi)$  in terms of a Fourier series in  $\phi$  [104],

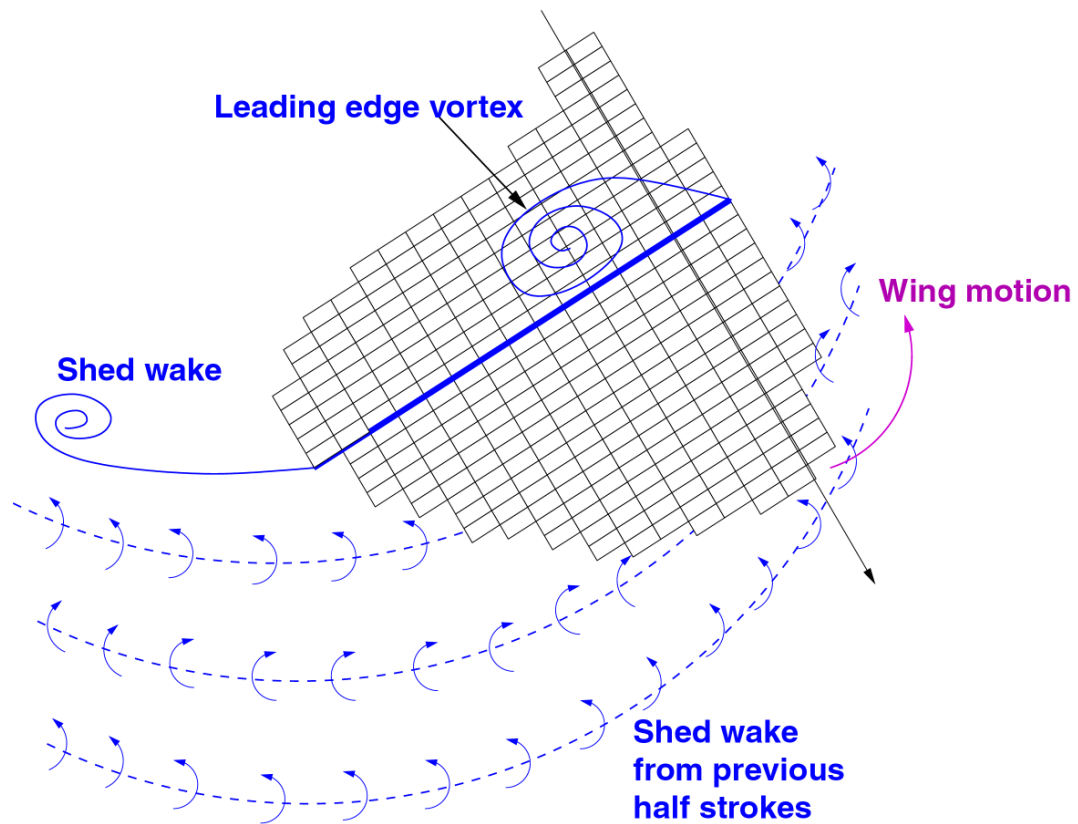


Figure 4.5: Wake structure at one station along the span

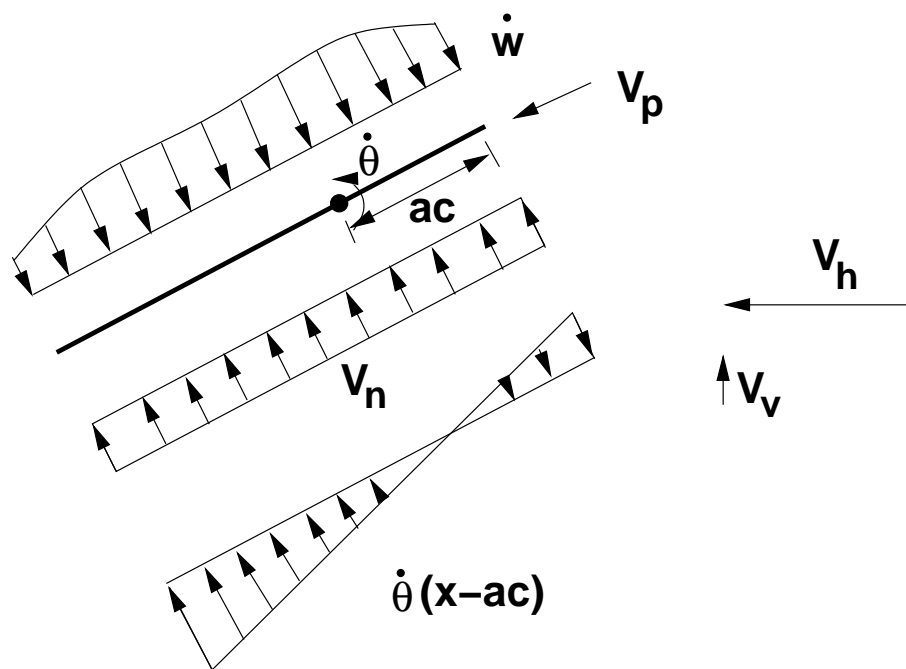


Figure 4.6: Flow velocities

$$\gamma(\phi) = 2V \left( A_0 \frac{1 + \cos \phi}{\sin \phi} + \sum_{n=1}^{\infty} A_n \sin n\phi \right) \quad (4.54)$$

where,  $V$  is the total resultant velocity given by,

$$V = \sqrt{V_H^2 + V_v^2} \quad (4.55)$$

Substituting eq. 4.54 in eq. 4.51, the Fourier series coefficients can be determined as,

$$A_0 = \underbrace{\frac{V_n}{V} + \frac{c\dot{\theta}}{V} \left( \frac{1}{2} - a \right)}_{Rigid} - \underbrace{\frac{1}{\pi V} \int_0^\pi \dot{w} d\phi - \frac{V_p}{\pi V} \int_0^\pi \frac{\partial w}{\partial x} d\phi}_{Elastic} \quad (4.56)$$

$$A_1 = \underbrace{\frac{1}{2} \frac{c\dot{\theta}}{V}}_{Rigid} + \underbrace{\frac{2}{\pi V} \int_0^\pi \dot{w} \cos \phi d\phi - \frac{2V_p}{\pi V} \int_0^\pi \frac{\partial w}{\partial x} \cos \phi d\phi}_{Elastic} \quad (4.57)$$

$$A_n = \underbrace{\frac{2}{\pi V} \int_0^\pi \dot{w} \cos n\phi d\phi - \frac{2V_p}{\pi V} \int_0^\pi \frac{\partial w}{\partial x} \cos n\phi d\phi}_{Elastic} \quad (4.58)$$

The total circulation can be obtained by integrating  $\gamma(\phi)$  along the chord,

$$\Gamma(t) = \pi V c \left( A_0(t) + \frac{A_1(t)}{2} \right) \quad (4.59)$$

Thus the horizontal and vertical circulatory forces, without any unsteady effects, can be determined as,

$$F_v^c(t) = \rho V_h(t) \Gamma(t) \quad (4.60)$$

$$F_h^c(t) = \rho V_v(t) \Gamma(t) \quad (4.61)$$

## Elastic effects

In this section, the procedure to account for the elastic terms in eqs. 4.58 is described. To illustrate this, consider the elastic part of the coefficient  $A_0$ ,

$$A_0^{el} = -\frac{1}{\pi V} \int_0^\pi \dot{w} d\phi - \frac{V_p}{\pi V} \int_0^\pi \frac{\partial w}{\partial x} d\phi \quad (4.62)$$

Let  $b^p(x)$  be the vector of modal deflections for the  $p^{th}$  structural mode at the cross-section shown in Fig. 4.6. Similarly, let  $b'^p(x)$  be the vector of modal slopes with respect to  $x$ . The structural deformations across the chord at this station can then be written as,

$$\dot{w}(x, t) = \sum_{p=1}^{N_m} \dot{q}_p(t) b^p(x) \quad (4.63)$$

$$\frac{\partial w}{\partial x}(x, t) = \sum_{p=1}^{N_m} q_p(t) b'^p(x) \quad (4.64)$$

where,  $q_p(t)$  represents the generalized coordinates and  $N_m$  is the number of structural modes retained in the analysis. Substituting the above equations into eq. 4.62 we get,

$$A_0^{el} = -\frac{1}{\pi V} \sum_{p=1}^{N_m} \dot{q}_p(t) B_0^p - \frac{V_p}{\pi V} \sum_{p=1}^{N_m} \dot{q}_p(t) B_0'^p \quad (4.65)$$

where,  $B_0^p$  and  $B_0'^p$  are given by,

$$B_n^p = \int_0^\pi b^p(x) \cos n\phi d\phi \quad (4.66)$$

$$B_n'^p = \int_0^\pi b'^p(x) \cos n\phi d\phi \quad (4.67)$$

with  $n = 0$ . Thus the dependence of the Fourier coefficients on the chordwise deformation is accounted for by the aerodynamic coefficients  $B_n^p$  and  $B_n'^p$ , which can be determined from the wing mode shapes *a priori*. Similarly, the other Fourier coefficients can be written as,

$$A_1 = \frac{2}{\pi V} \sum_{p=1}^{N_m} \dot{q}_p(t) B_1^p - \frac{2V_p}{\pi V} \sum_{p=1}^{N_m} q_p(t) B_1'^p \quad (4.68)$$

$$A_n = \frac{2}{\pi V} \sum_{p=1}^{N_m} \dot{q}_p(t) B_n^p - \frac{2V_p}{\pi V} \sum_{p=1}^{N_m} q_p(t) B_n'^p \quad (4.69)$$

## Apparent Mass

For a flapping-pitching wing, the forces exerted by the fluid because of its acceleration and deceleration must also be accounted for. Using the unsteady Bernoulli equation, the pressure difference along the chord, caused by this added mass effect, can be written as [104],

$$\Delta p^{nc} = \frac{\partial}{\partial t} \int_0^x \gamma(\xi, t) d\xi = \frac{\partial}{\partial t} \Gamma(x, t) \quad (4.70)$$

Thus, the force normal to the wing caused by the added mass or non-circulatory effect is,

$$F_n^{nc} = \rho \int_0^c \frac{\partial}{\partial t} \Gamma(x, t) dx = \frac{\rho c^2}{2} \left[ \frac{3}{2} \pi \frac{\partial}{\partial t} (A_0(t)V(t)) + \frac{\pi}{2} \frac{\partial}{\partial t} (A_1(t)V(t)) \frac{\pi}{4} \frac{\partial}{\partial t} (A_2(t)V(t)) \right] \quad (4.71)$$

Substituting the expressions for the aerodynamic coefficients in the above equation, the non-circulatory force can be obtained. The expression for  $F_n^{nc}$  is provided in Appendix B. It may be noted that with the assumption of incompressibility the non-circulatory forces act instantaneously at the moment of acceleration or deceleration.

## Leading Edge Suction

The suction force generated by the presence of a leading edge vortex on top of the wing was modeled using an approach similar to that used for modeling the vortices that occur on delta wings at high angles of attack [102, 105, 106]. This method assumes that, at high angles of attack, the leading edge suction force on an

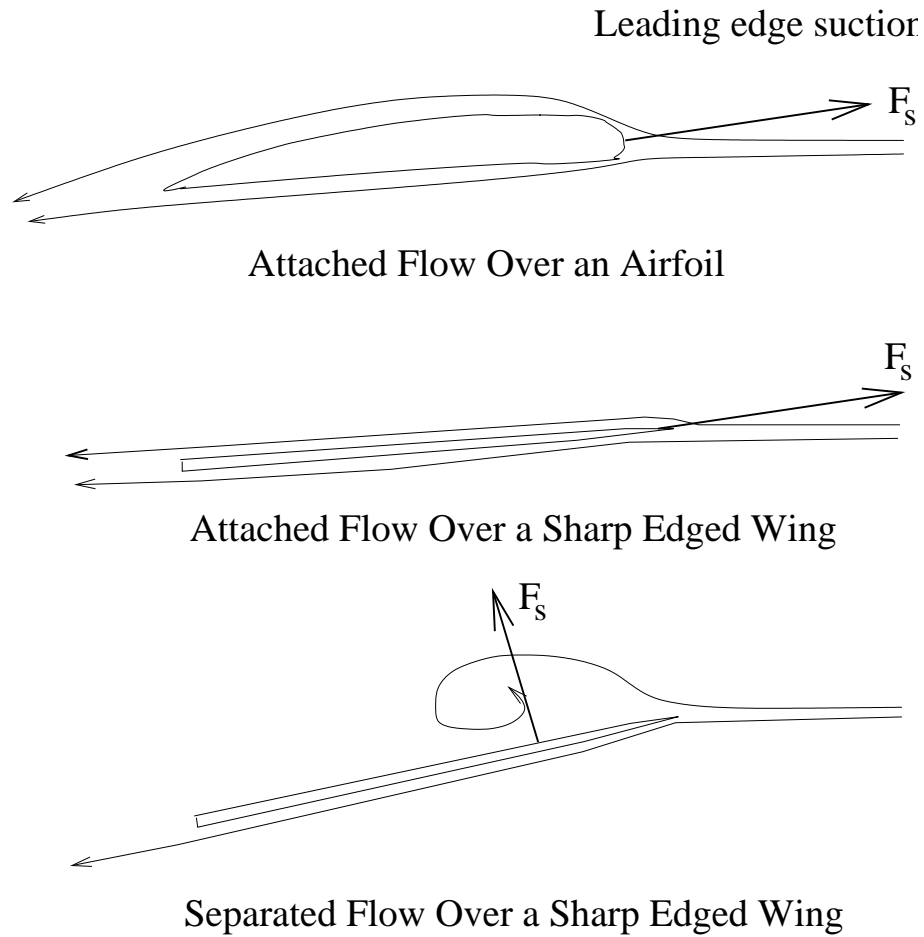


Figure 4.7: Leading edge suction

airfoil is rotated by  $90^\circ$  and acts in the same way as the suction force that would be generated by the presence of a vortex on top of the wing, as shown in Fig. 4.7.

The normal force is thus given by,

$$F_n^{pol}(t) = \rho \Gamma(t) V_h(t) \sin \theta \quad (4.72)$$

where,  $\Gamma(t)$  is given by eq. 4.59.

## Unsteady Effects

The effect of the starting vortex on the build up of circulation was accounted for by using the Wagner function  $\phi_w$ . Using this function, the effect of the starting vortex on the forces given by eqs. 4.61, can be written using the Duhamel integral as,

$$F_v^c(t) = \rho V_h(0)\Gamma(0)\phi_w(t) + \rho V_h(t) \int_0^t \frac{d\Gamma}{d\sigma} \phi_w(t - \sigma) d\sigma \quad (4.73)$$

$$F_h^c(t) = \rho V_v(0)\Gamma(0)\phi_w(t) + \rho V_v(t) \int_0^t \frac{d\Gamma}{d\sigma} \phi_w(t - \sigma) d\sigma \quad (4.74)$$

The expression for  $d\Gamma(t)/dt$  obtained from Eq. 4.59 is provided in Appendix B. Garrick's algebraic approximation to the Wagner function [107] was used in the above equation,

$$\phi_w(s) \approx \frac{s + 2}{s + 4} \quad (4.75)$$

where,  $s$  is the non-dimensional distance traveled by the airfoil in semi-chords. The effect of the shed wake from the previous flapping strokes was accounted for by using the Kussner gust response function  $\psi_k$ . The shed vorticity strength was computed using the following equation,

$$\gamma_w(x, t) = -\frac{1}{V(t)} \frac{d\Gamma(t)}{dt} \quad (4.76)$$

At the end of each stroke, this vorticity distribution was assumed to convect below the wing by a distance  $\frac{v_i T}{2}$ , where,  $v_i$  is the induced inflow velocity and  $T$  is the time for one flapping cycle. With the vorticity distribution below the wing determined, the gust velocity  $w_g$  generated by this distribution can be found and used in a

Duhamel integral to determine its effect on the forces acting on the wing,

$$F_v^k = \rho V_h(t) \int_0^t \frac{d\Gamma}{dw_g} \frac{dw_g}{d\sigma} \psi_k(t - \sigma) d\sigma \quad (4.77)$$

$$F_h^k = \rho V_v(t) \int_0^t \frac{d\Gamma}{dw_g} \frac{dw_g}{d\sigma} \psi_k(t - \sigma) d\sigma \quad (4.78)$$

where, the Kussner function was approximated as,

$$\psi(s) = \frac{s^2 + s}{s^2 + 2.82s + 0.8} \quad (4.79)$$

A tip vortex was also modeled based on the assumption that all the vorticity beyond the point of maximum circulation, along the wing span, rolls up into a tip vortex (Ref. [107]). This tip vortex also convects downward based on the induced inflow velocity and affects the gust velocity seen by the wing.

## Induced Inflow Velocity

In order to determine the induced inflow velocity,  $v_i$ , an iterative scheme was employed. The total thrust produced by the flapping-pitching wing was computed as the sum of all the above components. The inflow velocity was obtained from the following equation which is based on momentum considerations,

$$v_i = \sqrt{\frac{T_{total}}{\rho \Phi R^2}} \quad (4.80)$$

where,  $R$  is the total wing span and  $\Phi$  is the wing stroke angle. The inflow was assumed to be constant in space and time. The computation of forces and inflow velocity was repeated until the inflow converged.

## Chapter 5

# Model Validation

The structural and aerodynamic models described in the previous chapter were validated with data available in literature. The structural model was also validated with experiments conducted on an aluminum plate undergoing pure flapping motion. The aerodynamic model was validated with data available for the Robofly [34]. Since these tests were conducted in oil at very low flapping frequencies, aeroelastic effects were likely to be negligible. This makes these tests ideal for validating the rigid part of the aerodynamic model.

## 5.1 Structural Model

### 5.1.1 Cantilevered plate spin-up

To validate the structural model, the spin-up motion of a cantilevered plate was studied, as shown in Fig. 5.1. The rotational speed of the plate is given by,

$$\omega = \begin{cases} \omega_s \left( \frac{t}{t_s} - \frac{1}{2\pi} \sin \frac{2\pi t}{t_s} \right) & 0 \leq t \leq t_s \\ \omega_s & t > t_s \end{cases} \quad (5.1)$$

The geometric and material properties of the plate are,

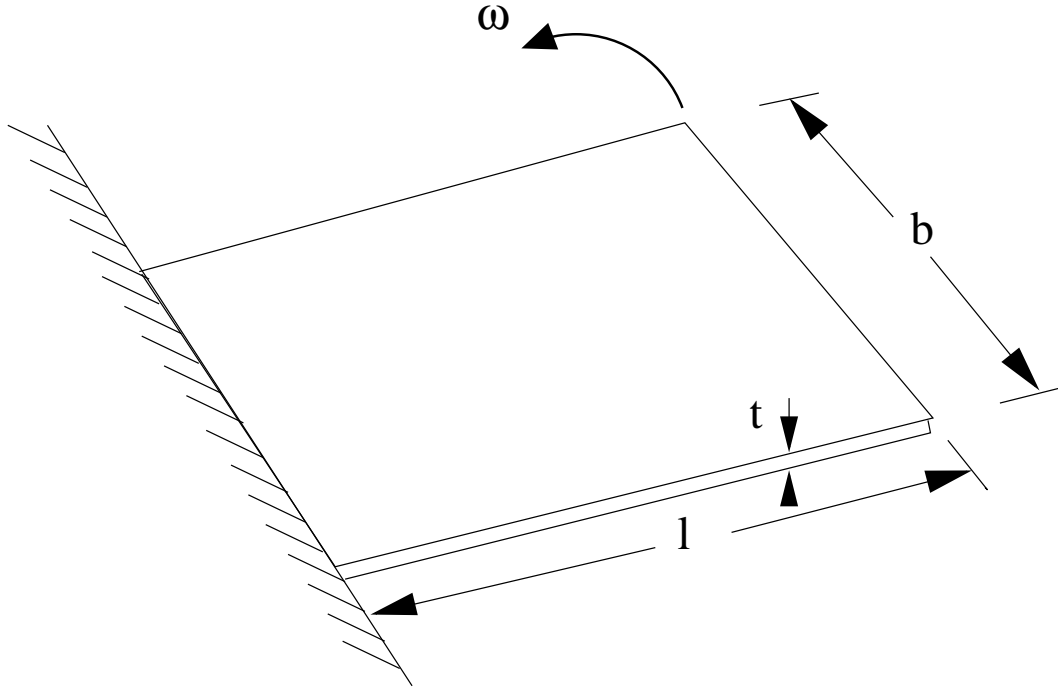


Figure 5.1: Rotating cantilever plate.

$$E = 70 \text{ GPa}, \quad \rho = 3000 \text{ Kg/m}^3, \quad l = 1.0 \text{ m},$$

$$b = 0.5 \text{ m}, \quad t = 0.0025 \text{ m}, \quad \nu = 0.3$$

Figure 5.2 shows the tip deflection with respect to time and Fig. 5.3 shows the RPM variation with time when  $\omega_s = 10 \text{ rad/s}$  and  $t_s = 5 \text{ s}$ . The wing tip deflection showed very good correlation with the results of Ref. 100, with and without dynamic stiffening effects. The results also underscore the importance of including dynamic stiffening effects to correctly model the response of the plate. Further results in this study were obtained including dynamic stiffening in the analysis.

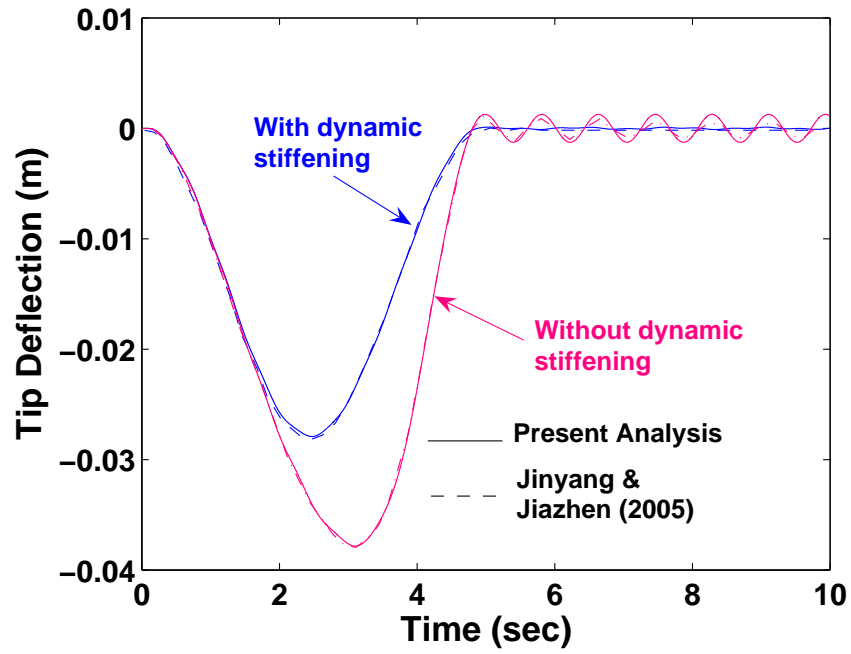


Figure 5.2: Tip deflection for spin-up motion of a rectangular plate.

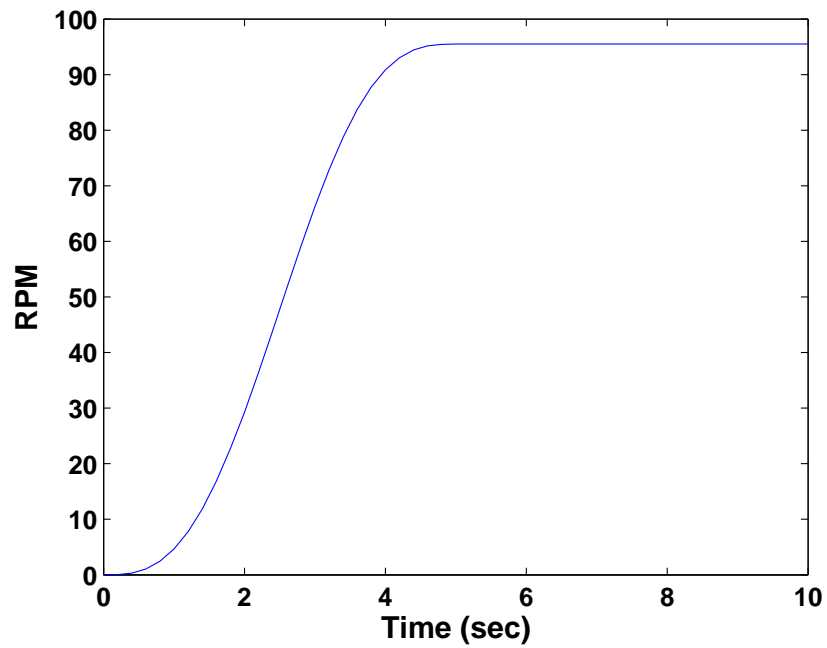


Figure 5.3: RPM variation with time

### 5.1.2 Aluminum plate in pure flapping

The structural model was also validated experimentally for a rectangular aluminum plate undergoing pure flapping motion, as shown in Fig. 5.4. The geometric and material properties of the plate were,

$$E = 70 \text{ GPa}, \quad \rho = 2750 \text{ Kg/m}^3, \quad l = 0.089 \text{ m},$$
$$b = 0.0381 \text{ m}, \quad t = 5.08 \times 10^{-4} \text{ m}, \quad \nu = 0.3$$

In order to accurately predict the bending moment at the base of the wing, an accurate measurement of the flapping acceleration was of prime importance. This was because the bending moment was primarily dependent on the inertial forces which in turn depend on the wing acceleration. With the flap position sensor described in Chapter 2, only the flap position data was available. Numerical differentiation of this data introduced large errors in the acceleration which, when given as input to the analysis, caused large amplitude oscillations in the wing response. For this reason, a miniature MEMS accelerometer (Fig. 5.5) was used to measure the wing flap acceleration and a systematic validation of the analysis was carried out using the test data. Figure 5.6 shows a comparison of the measured and predicted bending moment at the base of the wing when the wing was moved arbitrarily at a slow rate. Figure 5.7 shows the corresponding acceleration input to the analysis. In this case, both the rigid and elastic analyses showed good agreement with experimental data.

Figure 5.8 shows the measured flap acceleration when the plate was flapped at a frequency of 2.7 Hz. With this acceleration input, a rigid analysis failed to

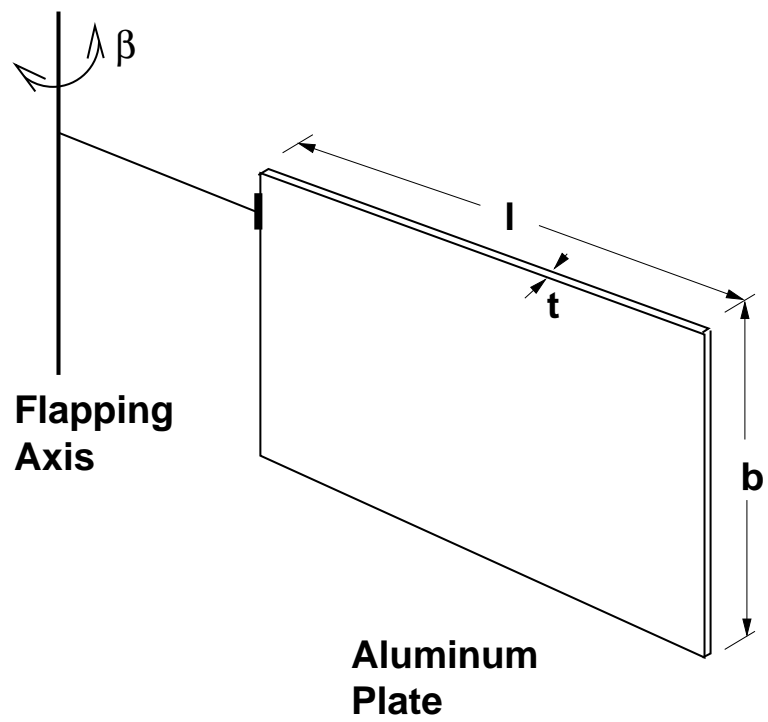


Figure 5.4: Aluminum plate in pure flapping motion.

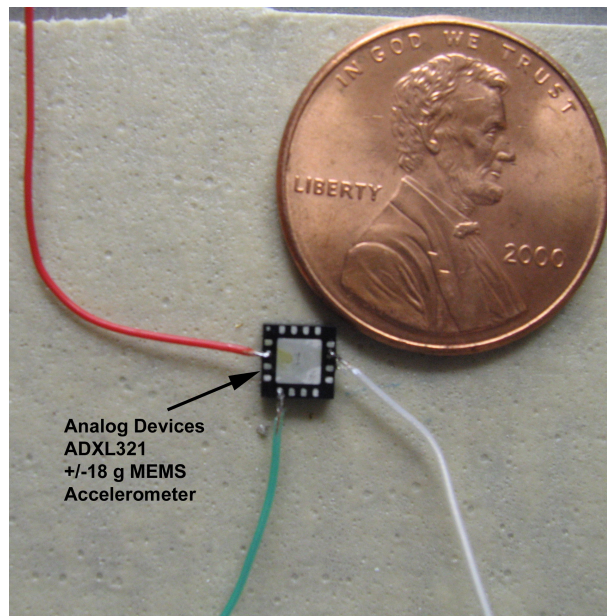


Figure 5.5: MEMS accelerometer.

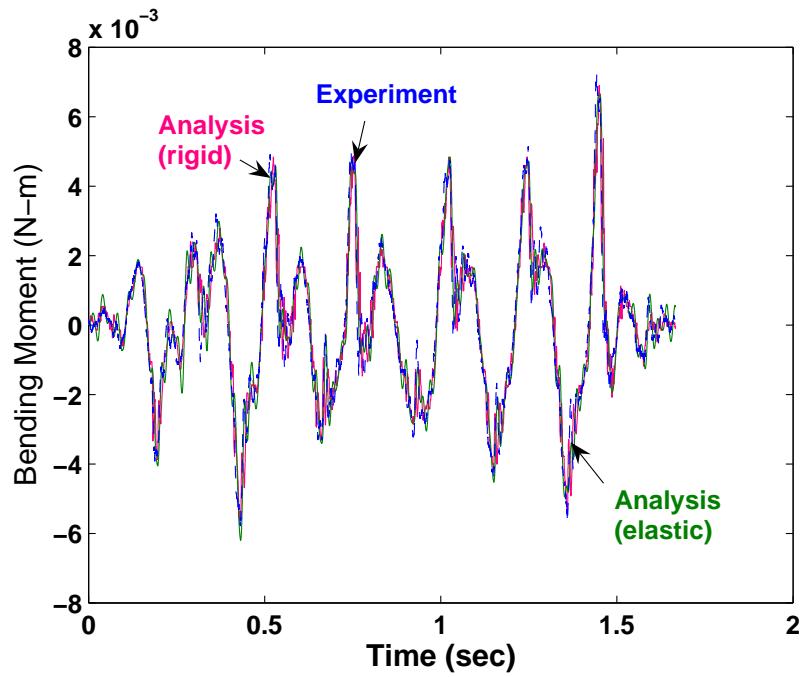


Figure 5.6: Comparison of measured and predicted bending moment for a slow support motion (flapping shaft shaken by hand).

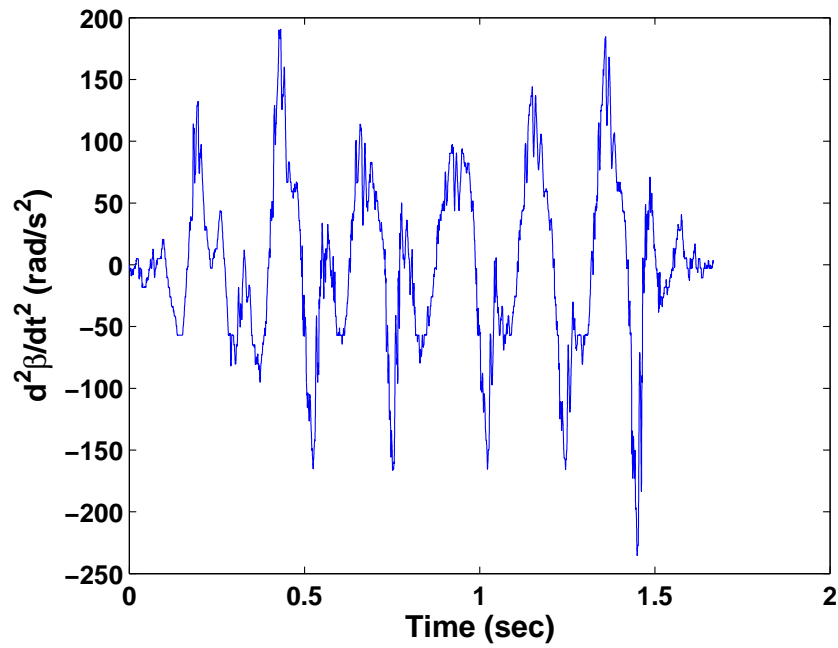


Figure 5.7: Measured acceleration for slow support motion.

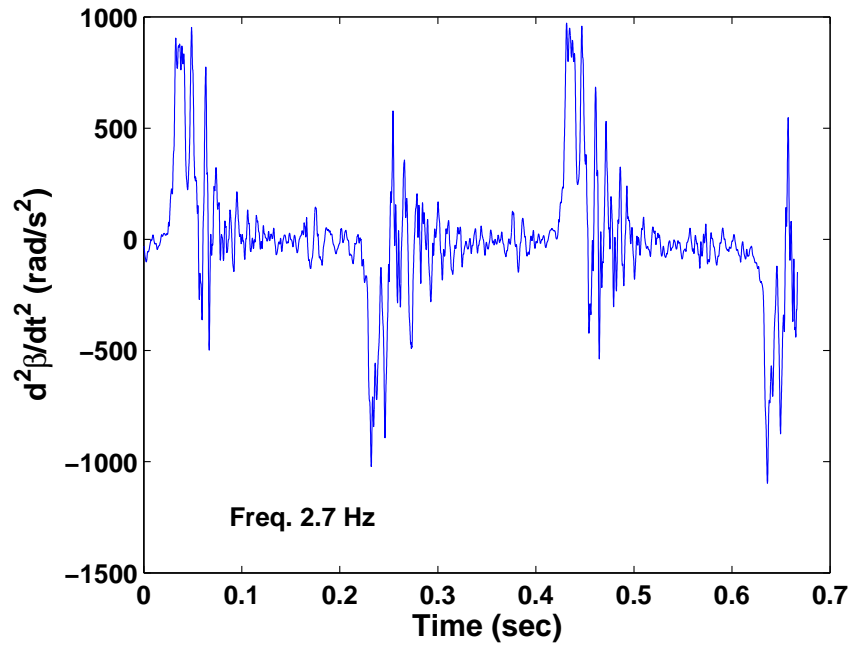


Figure 5.8: Measured acceleration at a flapping frequency of 2.7 Hz.

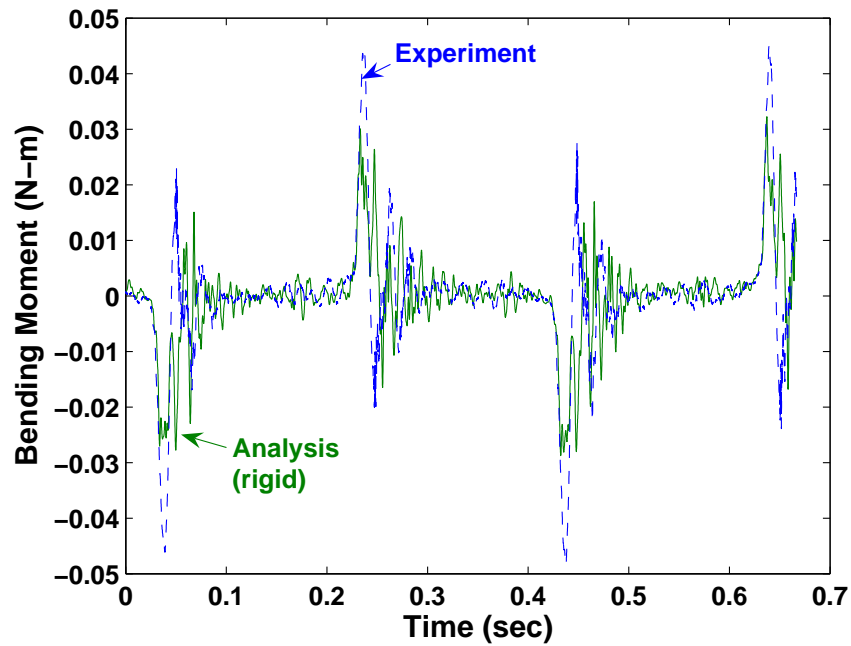


Figure 5.9: Comparison of measured bending moment with a rigid analysis at 2.7 Hz.

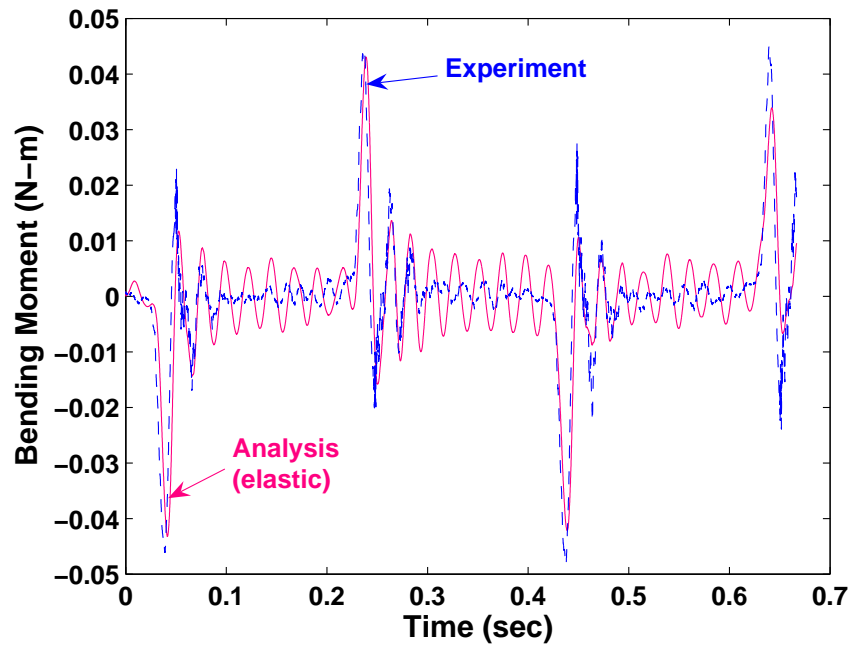


Figure 5.10: Comparison of measured bending moment with an elastic analysis at 2.7 Hz.

capture the measured bending moment variation, as shown in Fig. 5.9. On the other hand, the elastic analysis captured the bending moment variation, especially at the peaks, although, there was some residual oscillation which was not present in the experimental data. This was caused by the error in the measured acceleration. Since the linear acceleration was measured, it had to be divided by the distance of the accelerometer from the flapping axis, in order to obtain the angular acceleration. Since this distance was limited by constraints of the mechanism, it amplified any measurement error in the linear acceleration. The validation of the structural model for an aluminum-mylar wing undergoing combined flapping and pitching is described in the next chapter.

## 5.2 Aerodynamic Model

To validate the aerodynamic model, results were compared with experimental data for the Robofly [53]. In these experiments, the wing was flapped with a stroke of  $160^\circ$  and the flapping frequency was 0.168 Hz. The wing pitch angle was  $45^\circ$  during both the upstroke and the downstroke. The wing rotation was advanced by 12% of the stroke period with respect to stroke reversal. The forces were measured for four flapping cycles, with the wing starting from rest in the first cycle. For validating the aerodynamic analysis results were compared with the forces measured during the fourth cycle, when the wake below the wing is expected to be well established. Since the Robofly operates at very low frequencies, elastic deformations of its wings were expected to be small. This made it ideal for validating the aerodynamic model without any elastic effects.

### 5.2.1 Wing motion

The wing motions  $\beta(t)$  and  $\theta(t)$  were defined using piecewise continuous functions, as shown in Figs. 5.11 and 5.12. During each half-stroke, the wing accelerates, then moves with constant velocity  $\dot{\beta}_0$  and thereafter decelerates. The wing acceleration and deceleration phases last for a time period of  $\Delta t/2$ . During these phases the flapping velocity is given by,

$$\dot{\beta} = -\dot{\beta}_0 \cos \pi \frac{t - t_s}{\Delta t} \quad (5.2)$$

where,  $t_s$  is the time at the start of the acceleration or deceleration phase. This equation can be integrated to obtain the angular position of the wing. When the

wing moves with constant velocity, its position in the stroke plane is given by,

$$\beta = \dot{\beta}_0(t - t_s) \quad (5.3)$$

During the acceleration and deceleration phases, the following integral may be used to determine the wing position,

$$\int_{\tau_1}^{\tau_2} \dot{\beta} dt = \frac{\dot{\beta}_0 \Delta t}{\pi} \left[ \sin \frac{\pi(t_s - \tau_2)}{\Delta t} - \sin \frac{\pi(t_s - \tau_1)}{\Delta t} \right] \quad (5.4)$$

During the acceleration and deceleration phases, the wing acceleration is given by,

$$\ddot{\beta} = \frac{\pi \dot{\zeta}_0}{\Delta t} \sin \frac{\pi(t - t_s)}{\Delta t} \quad (5.5)$$

Since it is usually the stroke amplitude which is specified and not the maximum stroke velocity, the maximum stroke velocity can be determined as,

$$\dot{\beta}_0 = \frac{\beta_0}{\left( \frac{2\Delta t}{\pi} + t_0 \right)} \quad (5.6)$$

where,  $\beta_0$  is the amplitude of motion in the stroke plane.

As shown in Fig. 5.12, the wing pitch velocity is zero for time  $t_0$ , and then varies according to the following equation for time  $\Delta t$ ,

$$\dot{\theta} = \frac{1}{2} \dot{\theta}_0 \left( 1 - \cos \frac{2\pi(t - t_s)}{\Delta t} \right) \quad (5.7)$$

where,  $\dot{\theta}_0$  is the maximum pitching velocity and  $t_s$  is the time at which pitching is initiated. The following integral can be used to determine the pitch of the wing at a given instant of time,

$$\int_{\tau_1}^{\tau_2} \dot{\theta} dt = \frac{\dot{\theta}_0}{4\pi} \left[ 2\pi(\tau_2 - \tau_1) + \Delta t \left( \sin \frac{2\pi(t_s - \tau_2)}{\Delta t} - \sin \frac{2\pi(t_s - \tau_1)}{\Delta t} \right) \right] \quad (5.8)$$



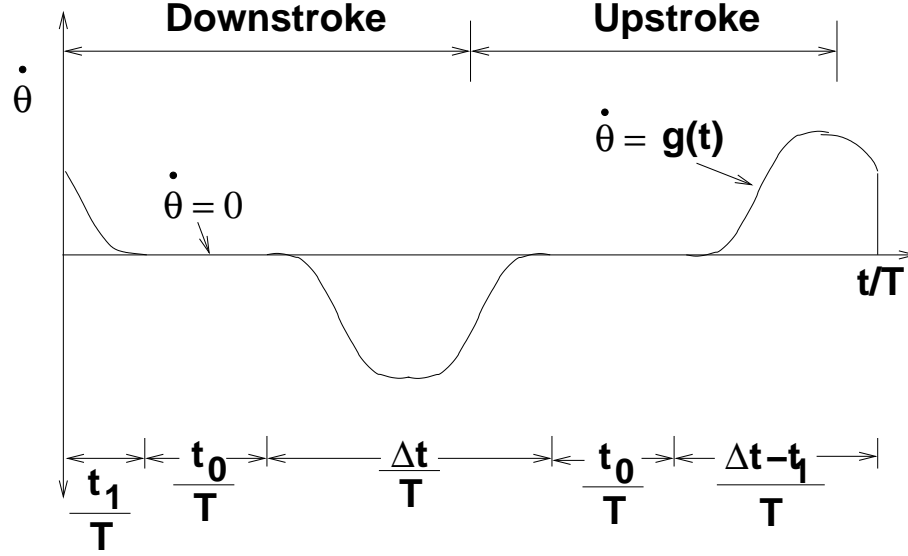


Figure 5.12: Definition of pitching motion.

significant contribution came from the translatory circulation, even though the pitch angle was much larger than  $45^\circ$  at this point. The reason for this lies in the ideal translatory lift coefficient from eqs. 4.59 and 4.61. This coefficient is given by,

$$C_l^{ideal} = 2\pi \sin \alpha \quad (5.11)$$

Figure 5.15 shows this ideal  $C_l$  plotted against the experimental values reported in Ref. 34. It is clear from this figure that, unlike the experimental  $C_l$ , the ideal  $C_l$  does not show any stall as the pitch angle increases beyond  $45^\circ$ . This leads to the overprediction of thrust near the end of the downstroke and upstroke, as seen in Fig. 5.14. To account for this, the aerodynamic model was modified by using the experimental  $C_l$  and  $C_d$  values to determine the circulation generated by the translational motion of the wing. Figure 5.16 shows the vertical force computed using this modified model. It is evident that the model with experimental  $C_l$  can predict the aerodynamic forces better than the model with ideal  $C_l$ .

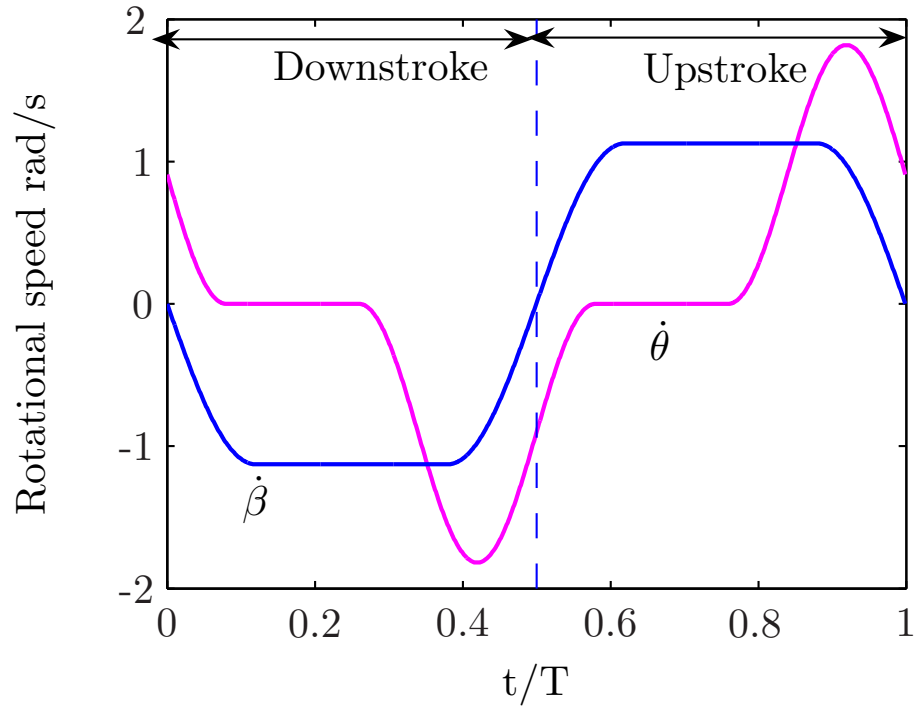


Figure 5.13: Input velocities for Robofly kinematics.

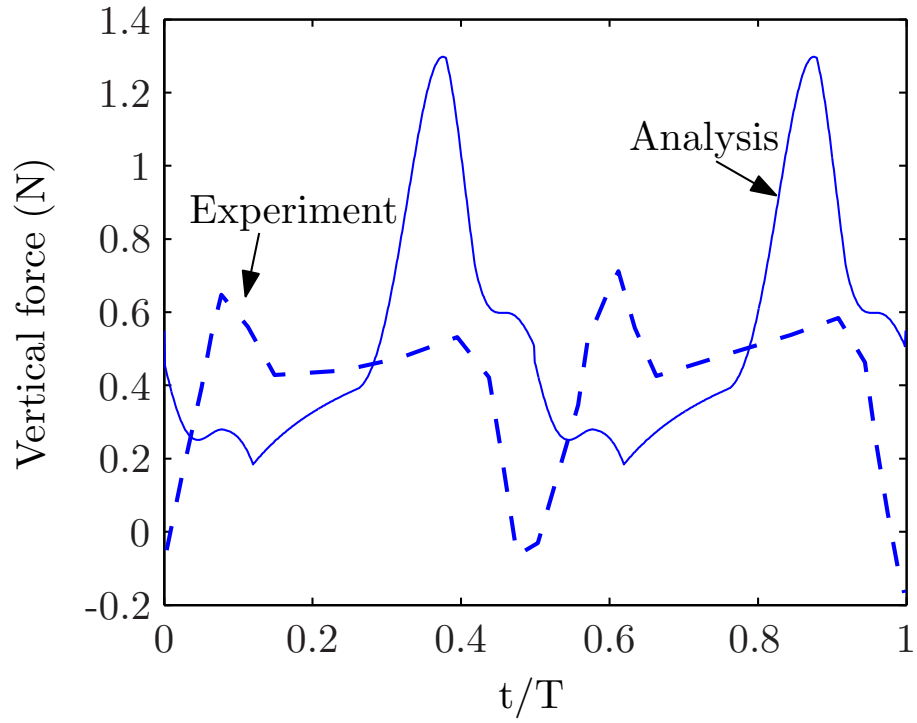


Figure 5.14: Total vertical force with ideal  $C_l$

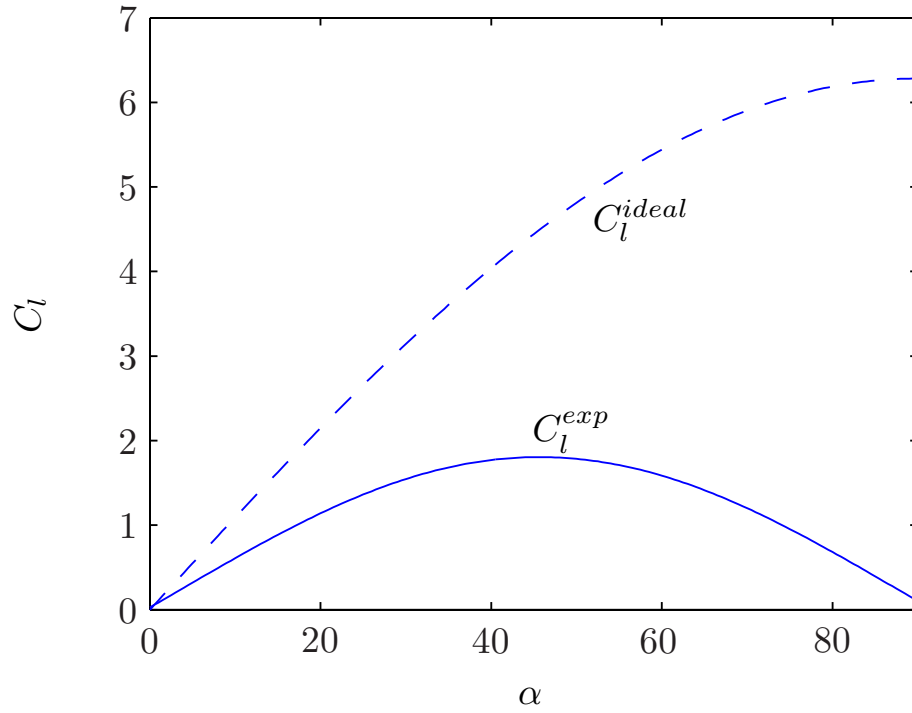


Figure 5.15: Ideal  $C_l$  compared with experimental  $C_l$ .

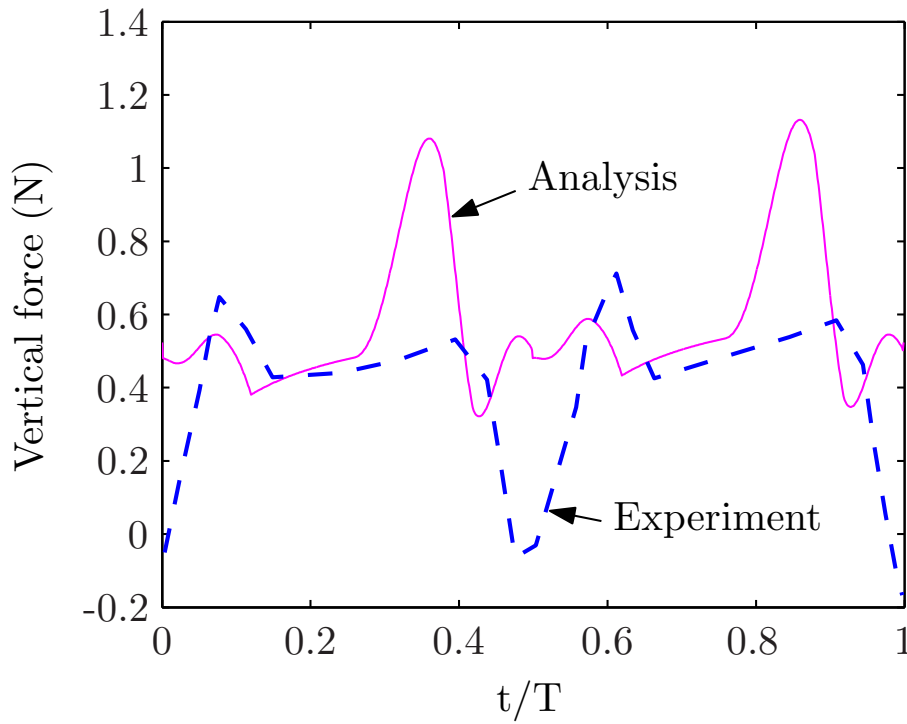


Figure 5.16: Total vertical force with experimental  $C_l$ .

Figure 5.17 shows the breakup of the total vertical force into its individual components. There are several interesting features evident from this figure. First, the force peak at the beginning of each half-stroke is because of non-circulatory effects. Secondly, the slow rise in the force during the middle of each half stroke is caused by a delayed build-up of circulation which is captured by the Wagner effect. Thirdly, the leading edge vortex adds to the total thrust during the translatory part of each half-stroke, although this effect is negated to some extent by the shed wake from previous half-strokes, which is accounted for by the Kussner function. The small peak in the circulatory force near the end of each half-stroke is caused by an increase in rotational circulation. It is evident that the discrepancy between experiment and analysis at the end of each half-stroke is caused by the non-circulatory force. Figure 5.18 shows the comparison between experiment and analysis without the non-circulatory effect. This shows an improvement in the agreement between the analysis and experiment.

At this point, it is pertinent to mention that, in the experiments conducted on the Robofly, the contribution of wing mass acceleration and gravity were removed by using a dummy inertial wing (Ref. 34, pp.1960). What is unclear is the way in which this subtraction of inertial effects, using a dummy inertial wing, effected the non-circulatory forces measured on the real wing. Reference 34 states that the experiments were repeated for a kinematic pattern with and without a flat stroke plane as shown in Fig. 5.19. In both cases, the force peak at the beginning of the half stroke was present. However, the authors use this fact to eliminate non-circulatory forces as the cause of this force peak, by stating that, for a flat stroke plane, non-

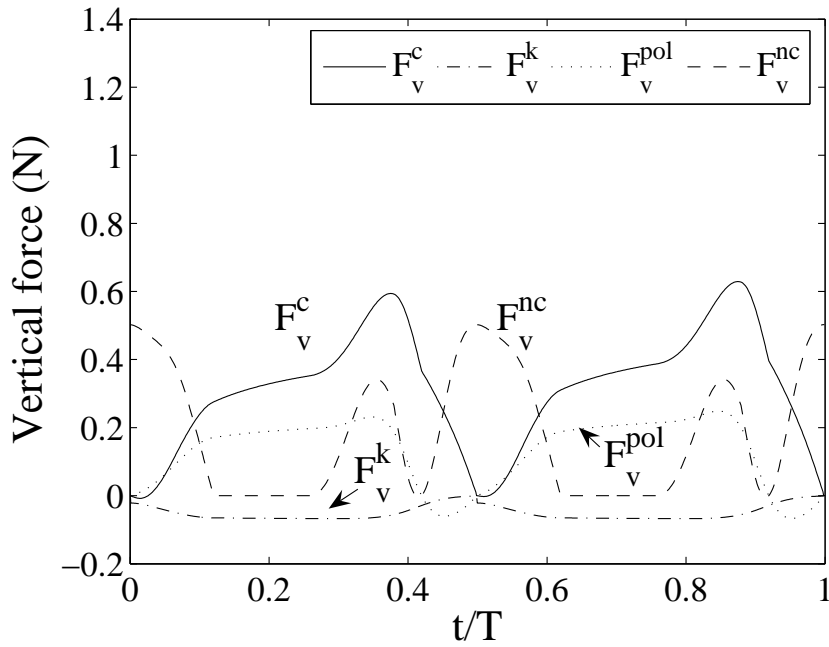


Figure 5.17: Components of the total vertical force.  $F_v^c$  - circulatory (with Wagner effect),  $F_v^{pol}$  - leading edge suction,  $F_v^{nc}$  - non-circulatory,  $F_v^k$  - Kussner effect.

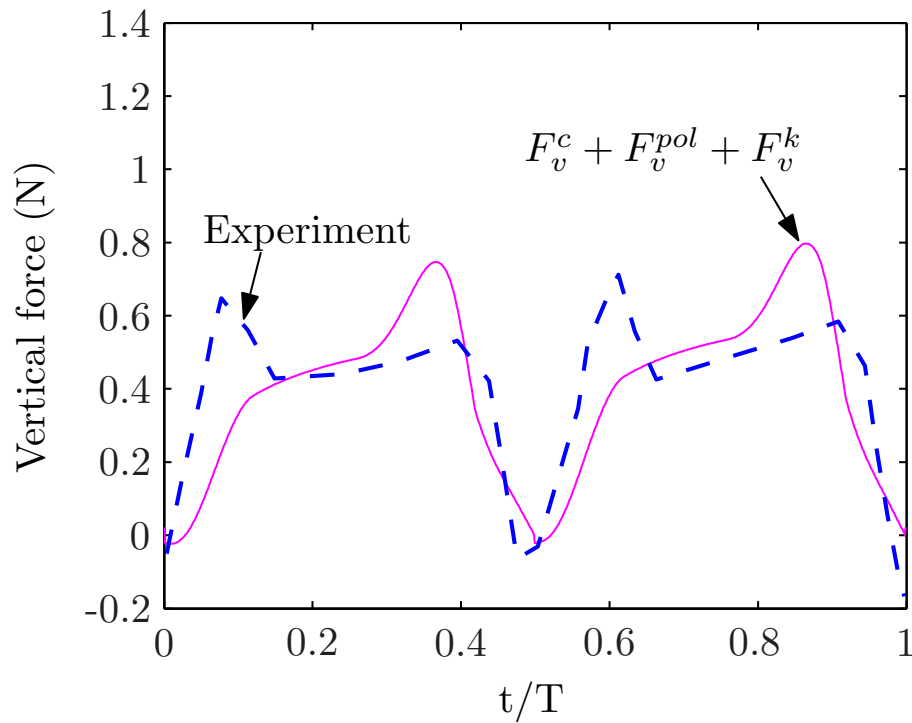


Figure 5.18: Vertical force without non-circulatory effects

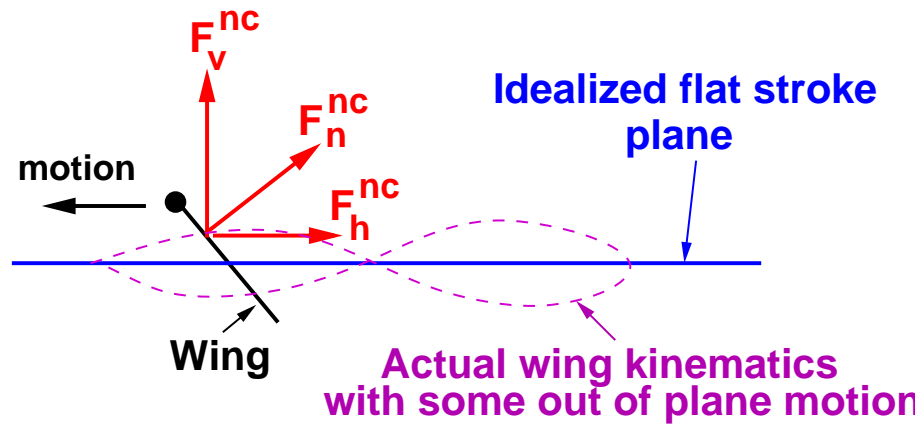


Figure 5.19: Actual and idealized stroke planes and the non-circulatory force

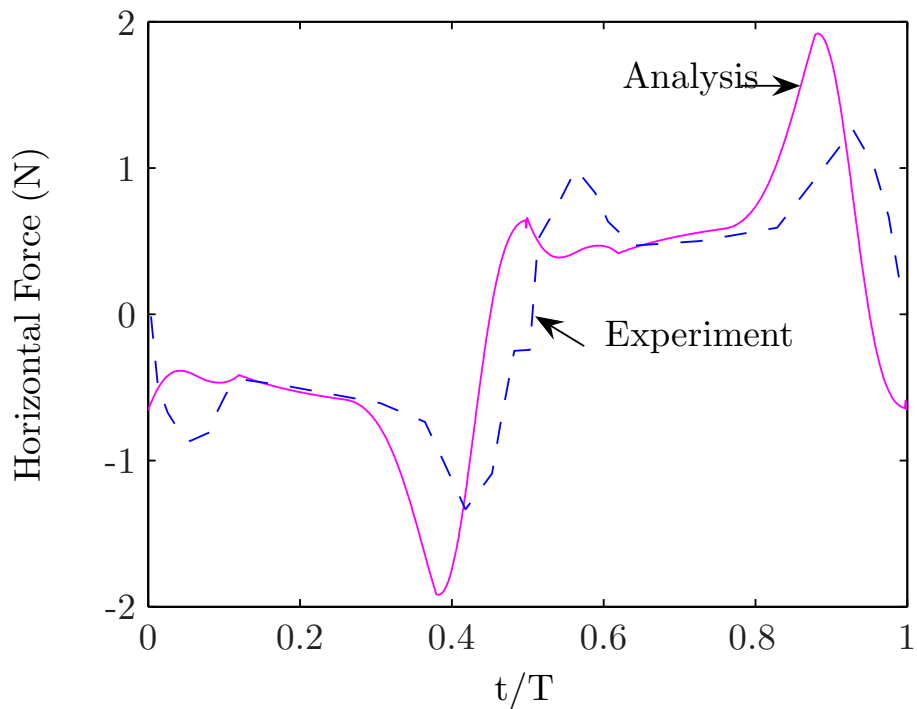


Figure 5.20: Total horizontal force

circulatory forces cannot contaminate the measurement of the vertical force. This is an erroneous assumption because the non-circulatory force acts perpendicular to the wing, and thus, for a wing held at a large pitch angle, it would effect both the horizontal and vertical forces. Based on this assumption, the force peak at the start of each half-stroke has been entirely attributed to wake capture, with no contribution from non-circulatory effects. However, our predictions indicate that this force peak can be explained, at least in part, by the non-circulatory forces.

Figure 5.20 shows a comparison of the computed horizontal force (i.e. drag) with the horizontal force measured on the Robofly. During the translatory phase of the motion, the analysis agreed closely with experiment. However, the force peaks at the beginning and end of each half-stroke were not captured very well. These peaks were also caused by non-circulatory effects. Figure 5.16 shows an instantaneous rise in the vertical force when the wing began its acceleration. Figure 5.20 shows that the measured increase in drag, near the end of each half-stroke, was slower than that predicted by the analysis. This indicated that compressibility effects may need to be included in the the computation of the non-circulatory forces.

Figure 5.21 shows a comparison of the present analysis with that of Ref. [103], along with the experimental data. It is evident from this figure that non-circulatory forces also caused large errors in the analysis developed by Zbikowski et. al. The difference between the present analysis and that of Ref. [103], lies in the derivation of the non-circulatory forces. In Ref. [103], the non-circulatory forces were derived for the entire wing using wing shape factors. However, in the present analysis, the non-circulatory forces were determined from thin airfoil theory for each blade

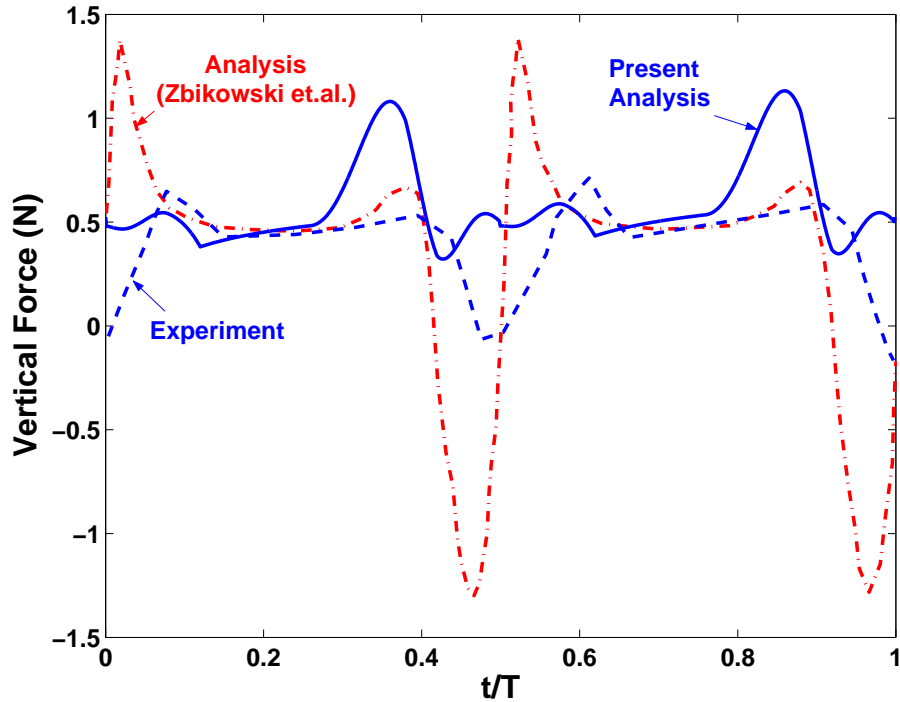


Figure 5.21: Vertical force compared with the analysis of Zbikowski et. al. [103] element. Another observation from Fig. 5.21 is that the analysis of Ref. [103] does not capture the slow rise in vertical force during the translatory part of the stroke, which is captured by the present analysis. This slow rise in vertical force is a manifestation of the starting vortex.

### 5.3 Summary

The structural model developed for a plate undergoing large overall motion was validated with data available in literature and also with experiments conducted on a rectangular aluminum plate in pure flapping motion. The input acceleration provided to the analysis was a key factor in obtaining good correlation with experimental data. However, currently available MEMS accelerometers measure linear

acceleration and not angular acceleration. Calculating the angular acceleration amplifies the measurement error in the linear acceleration.

A validation of the aerodynamic analysis was carried out by comparing the analytical prediction of thrust with experimental data available in literature. These experiments, conducted on wings moving at very low frequency in oil [34], are ideal for validating the aerodynamic analysis without elastic effects. Some key observations of this validation study are summarized here,

1. The ideal translatory lift coefficient, obtained from thin airfoil theory was inadequate to capture the aerodynamic forces. This is because, this coefficient did not capture the lift stall shown by experimental data at angles of attack greater than  $45^\circ$ .
2. The predictions improved when the experimental lift and drag coefficients were used in the analysis. However, there were discrepancies between the analysis and experiment at the beginning and end of each half-stroke.
3. At the beginning of each half-stroke, a force peak was observed in the analysis. This peak was primarily caused by non-circulatory forces. This force peak explained, at least in part, the force peak observed in the experiment. However, in Ref. 34 this peak was attributed to wake capture alone, based on the improper assumption that, for a flat stroke plane non-circulatory forces could not affect the vertical force.
4. In Ref. 34, the forces caused by wing acceleration were removed by using a dummy inertial wing. However, the effect of this subtraction, on the non-

circulatory forces, is unclear. With the non-circulatory forces removed from the total thrust, the analysis showed a significant improvement in predicting the measured thrust.

## Chapter 6

### Results

The thrust generated by a number of highly flexible and light-weight wings, undergoing a bio-inspired flapping-pitching motion, was measured as reported in Chapter 3. The high flexibility of these wings makes them ideal candidates for comparison with the analysis developed in this study. In this chapter, the aerodynamic and structural analyses validated separately in the previous chapter were used to predict the mean thrust measured on the bio-inspired flapping-pitching wings.

#### 6.1 Wing Grids

Figures 6.1 and 6.2 show the finite element grids used to discretize two of the light-weight wings tested on the bio-inspired mechanism. The frames of the wing was made from aluminum. This frame was then covered with a light-weight but sturdy mylar sheet. From an aerodynamic standpoint, Wing II and Wing III were different because of the location of their pitching axes. This axis is defined by the line  $x_p = 0$  in Figs. 6.1 and 6.2. Wing III pitched about its 20% chord location while Wing II pitched about its 50% chord location. The following material

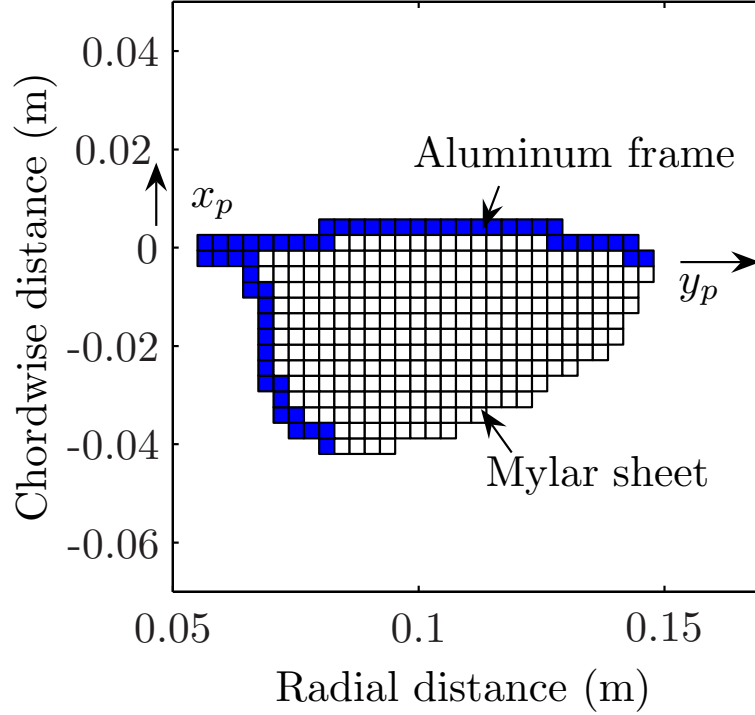


Figure 6.1: Finite element grid for Wing III

properties were used for aluminum: Young's modulus,  $E = 60 \text{ GPa}$ , mass density,  $\rho = 2400 \text{ Kg/m}^3$ , Poisson's ratio,  $\nu = 0.33$  and thickness,  $t = 5.08 \times 10^{-4} \text{ m}$ . The material properties used for Mylar were:  $E = 7 \text{ GPa}$ ,  $\rho = 1250 \text{ Kg/m}^3$ ,  $\nu = 0.25$  and  $t = 1.04 \times 10^{-4} \text{ m}$ .

## 6.2 Bending moment comparison

The bending moment measured from a combined flapping-pitching motion of Wings II and III was compared with the bending moment predicted by the analysis. An important observation from our validation of the structural model was the need for an accurate measurement of the flapping acceleration. This is because the accelerations directly effect the inertial loads acting on the wing, which, in turn, effect the

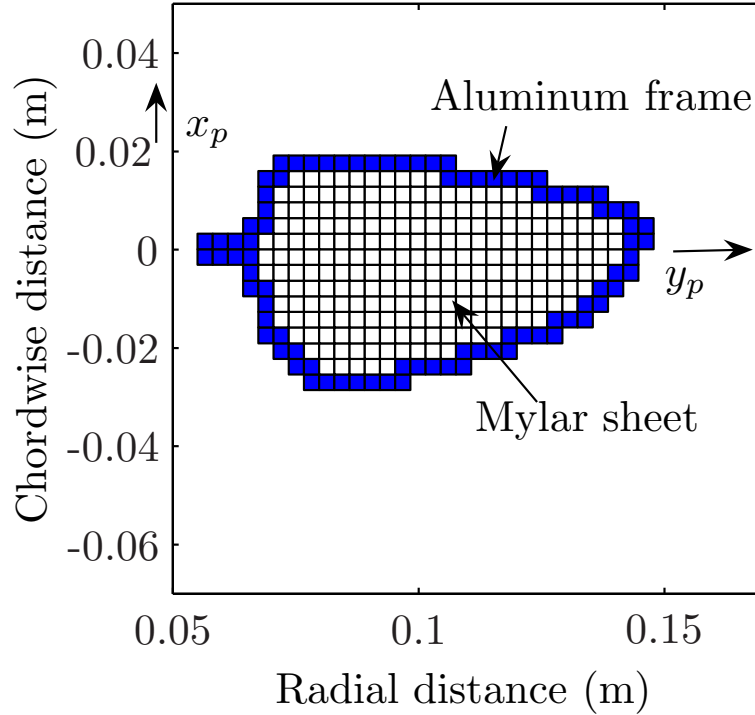


Figure 6.2: Finite element grid for Wing II

measured bending moment. However, in the experiments conducted on the flapping mechanism, only the pitch position was measured. For later tests, a flap position sensor was also introduced. But the analysis required position, velocity and acceleration, for the flapping and pitching motions, as inputs. Numerical differentiation of the measured position introduced significant errors in the computed velocities and accelerations. To alleviate this problem, a Fourier series was fit to the measured flapping and pitch positions, as shown in Fig. 6.3. The coefficients of this Fourier series were then used to determine the approximate velocity and acceleration. This type of motion is henceforth referred to as approximated motion. Figure 6.4 shows comparisons between the measured and predicted bending moments for Wing III at various frequencies. These frequencies represent the higher range of all frequencies

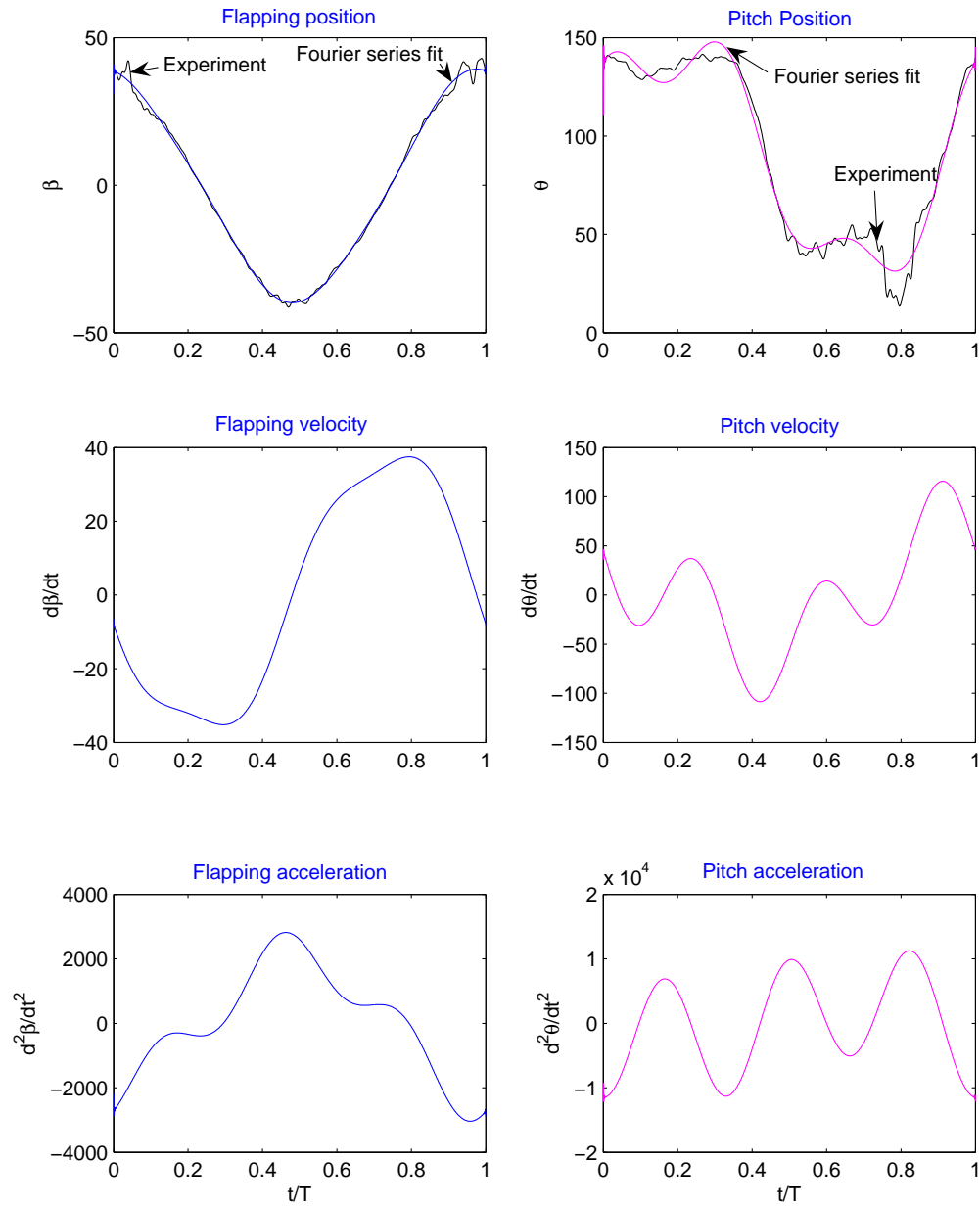


Figure 6.3: Position, velocity and acceleration used as inputs for the analysis

at which test data was available. The input motions for the analysis were approximated from the measured flapping and pitch positions as described above. It can be seen from this figure that, even with approximate flapping and pitching accelerations, the analysis could predict the bending moment satisfactorily at the lower frequencies. At 10.96 Hz, there was some overprediction of the bending moment. However, at 11.6 Hz, the analysis significantly overpredicted the bending moment. Since a geometrically linear structural model was used, this may be part of the reason for the overprediction. However, the approximation of the accelerations also played a significant role. To illustrate this, the bending moment was recomputed at a frequency of 11.6 Hz with a smooth motion used as an input to the analysis. This smooth motion is compared with the approximated motion in Fig. 6.5. The bending moment predicted by the analysis at a flapping frequency of 11.6 Hz, using this smooth motion, is shown in Fig. 6.6. Although there was a significant error, especially in phase, between the measured and predicted values, the peak to peak variation showed significant improvement over the prediction using the approximate motion. This underscores the need for an accurate measurement of the flapping and pitching accelerations. The discrepancy in bending moment prediction at high frequency is discussed further in a subsequent section.

### 6.3 Uncoupled Analysis

There is some experimental evidence to suggest that wing bending in hovering insects is predominantly caused by inertial forces alone [108], with aerodynamic

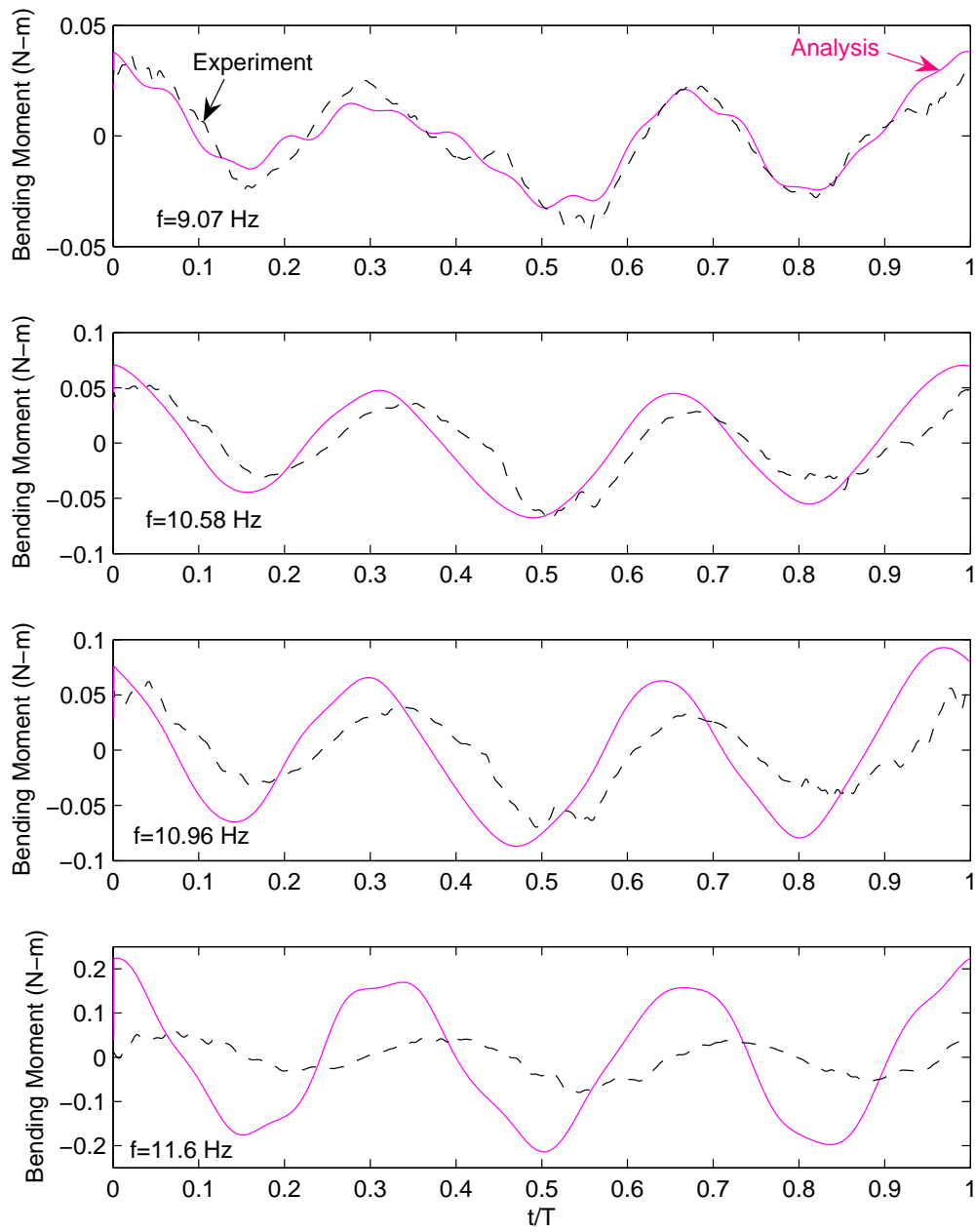


Figure 6.4: Bending moment variation compared with experimental data at various flapping frequencies

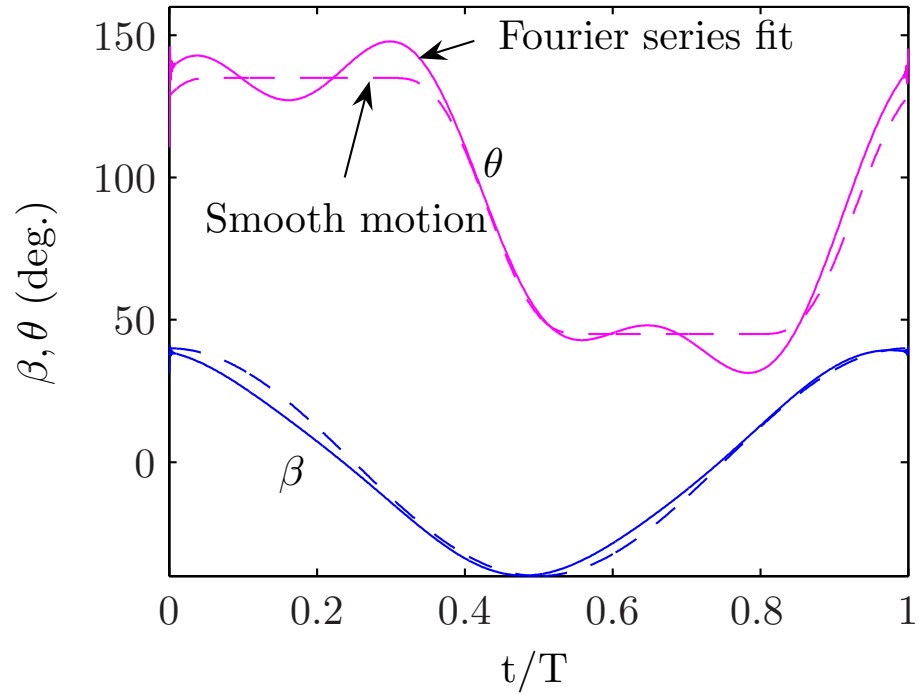


Figure 6.5: Smooth motion vs Fourier series fit

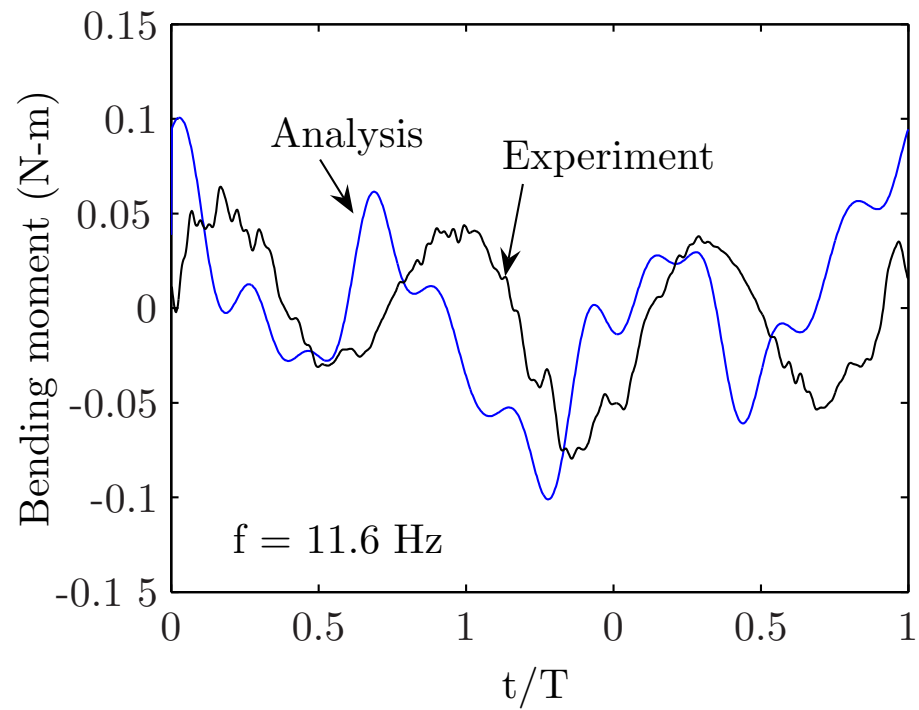


Figure 6.6: Comparison of analysis and experiment at 11.6 Hz with smooth motion

forces being an order of magnitude smaller than the inertial loads. Based on this assumption, an uncoupled analysis was carried out. In this analysis, the wing deformations were computed under inertial loading alone. These deformations were then used in the aerodynamic analysis to determine the thrust generated by the wing.

### **6.3.1 High frequency tests (Wing III)**

As discussed in Chapter 3, Wing III produced a maximum thrust of approximately 6.5 grams at a frequency of 11 Hz and a pitch angle of  $45^\circ$ . This was the highest thrust generated among all the wings tested on the bio-inspired flapping-pitching mechanism. However, this thrust dropped suddenly as the frequency was increased to 11.6 Hz. For this reason, this wing was used to ascertain the predictive capability of the present analysis. Figures 6.7 and 6.8 show the comparisons between experiment and analysis for the high frequency tests conducted on Wing III. These figures show results for both, a rigid wing and an elastic wing. Also, the results were computed using both types of input motions for the analysis, i.e, the approximated motion and the smooth motion.

It is evident from Fig. 6.7 that the approximated motion caused a significant reduction in the thrust generated by the mechanism as compared to the smooth motion. Also, the thrust predicted by the analysis using an approximated motion agreed closely with the measured thrust, except at the highest frequency of 11.6 Hz. Using the approximated motion, an elastic wing analysis showed close agreement with the experimental results, although there was a slight overprediction of thrust

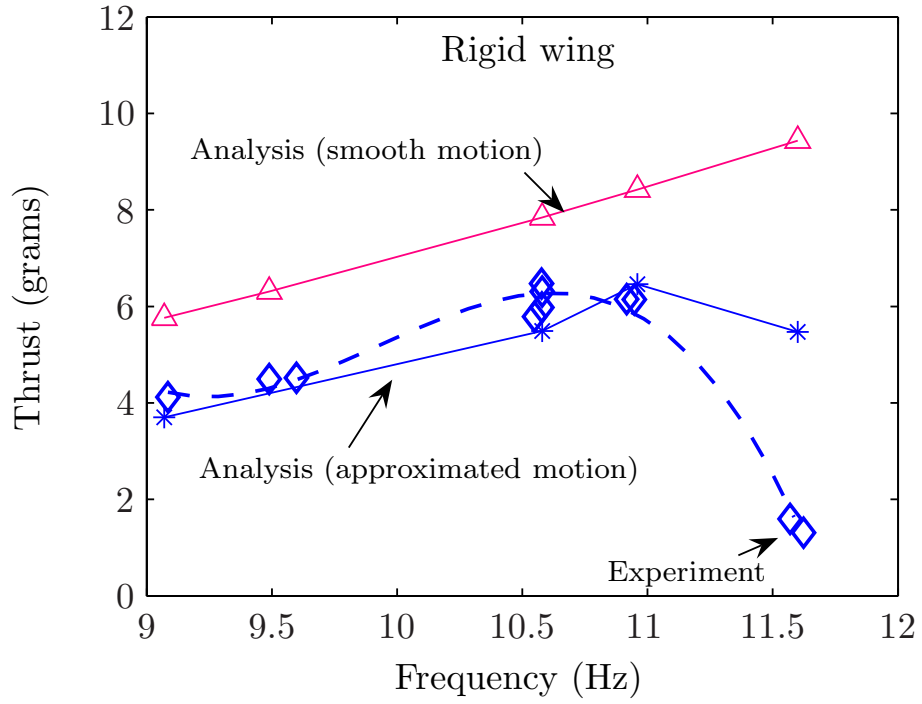


Figure 6.7: Rigid wing: predicted and measured thrust

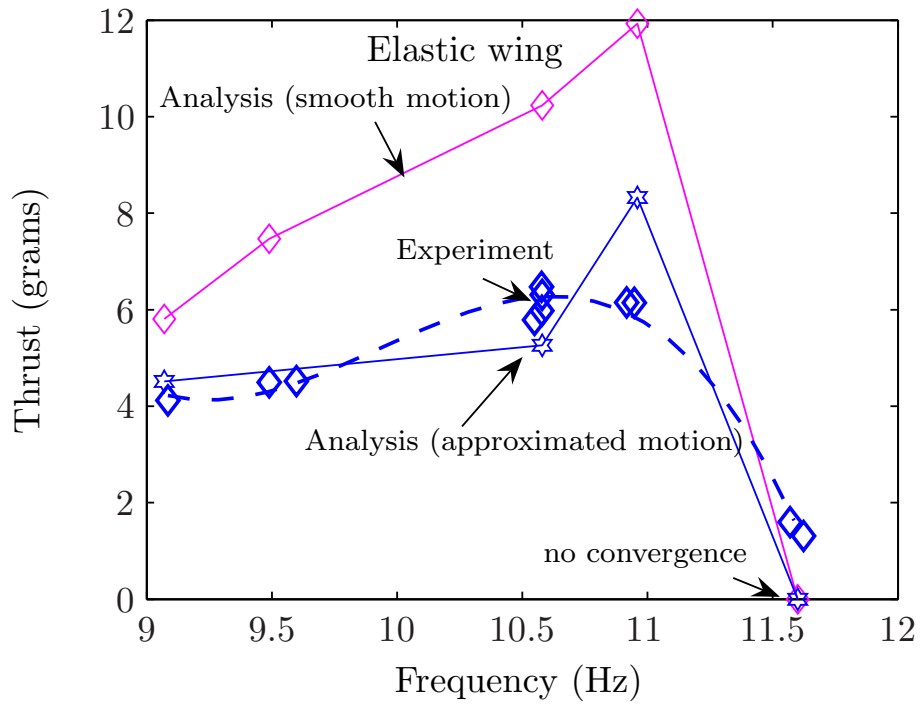


Figure 6.8: Elastic wing: predicted and measured thrust

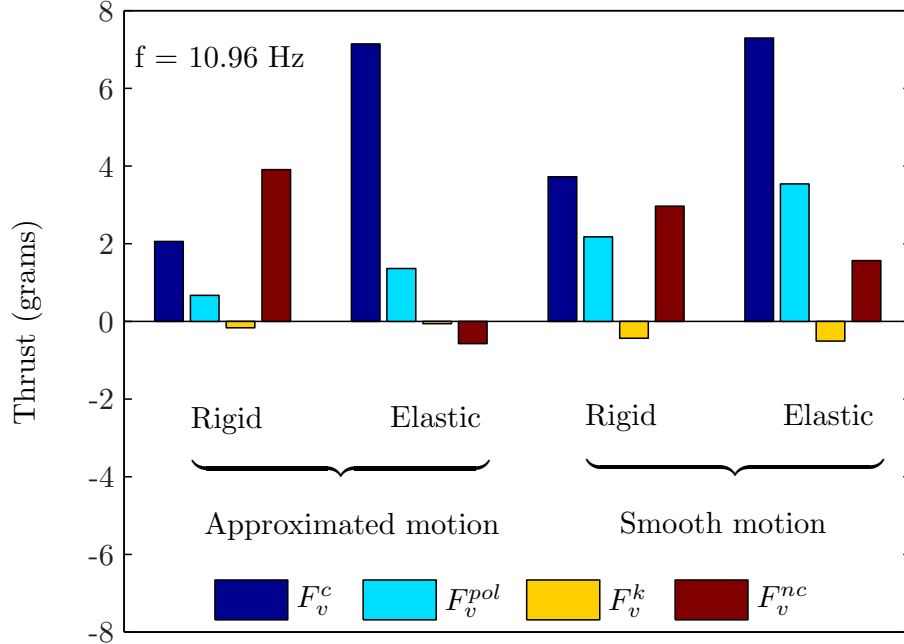


Figure 6.9: Components of total thrust at 10.96 Hz (symbols: v-vertical, c-circulatory, pol-Polhamus, k-Kussner, nc-non-circulatory)

at 10.96 Hz (Fig. 6.8). However, the most important result is that, for both the elastic cases, the analysis showed a drop in thrust at a frequency of 11.6 Hz. For these cases, the inflow did not converge because of the effect of the shed wake.

Figures 6.9 and 6.10 show the contribution of various components of the analysis to the predicted thrust at the two highest frequencies. Figure 6.9 shows that wing elastic deformations significantly increased the circulatory lift because of an increase in the effective wing velocities. However, the large accelerations introduced by wing elasticity, significantly reduced the non-circulatory contribution to the thrust. The reason for a drop in wing thrust at 11.6 Hz can be understood from Fig. 6.10. For an elastic wing, this figure shows the components after the first iteration only, since the inflow did not converge. The non-circulatory forces introduced by wing elasticity

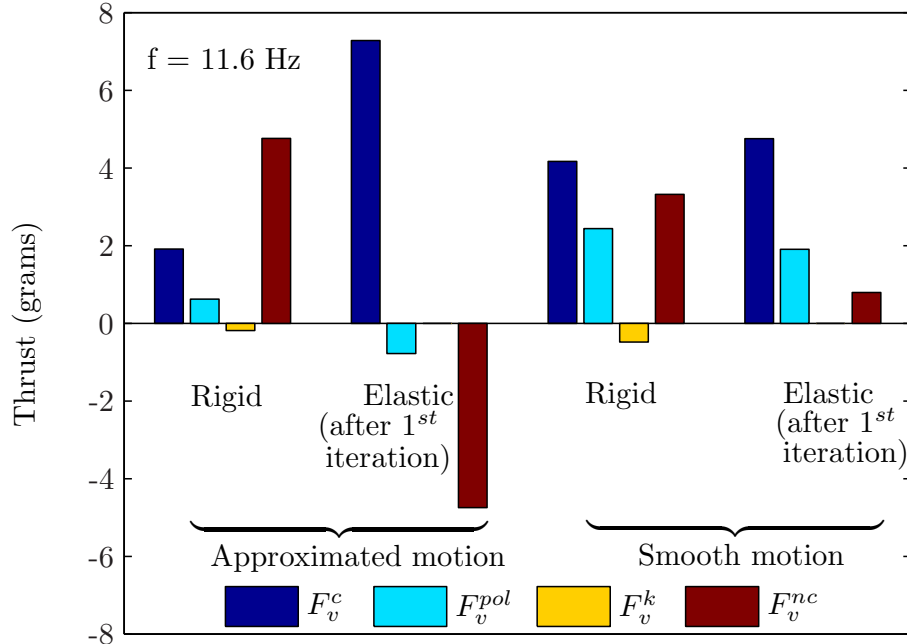


Figure 6.10: Components of total thrust at 11.6 Hz

at this frequency, caused a significant reduction in the total thrust. This led to a reduced inflow, which brought the shed wake closer to the wing plane. The vorticity in the shed wake was quite strong because of the significant circulatory forces. The close proximity of this vorticity to the wing plane was the primary cause for non-convergence of the inflow.

### 6.3.2 Low frequency tests

Figure 6.11 shows a comparison between the analysis and experiment, for low frequency tests carried out on Wing III at a pitch angle of  $45^\circ$ . For reference, the high frequency results are also shown in this figure. For the low frequency tests, only the pitch motion was measured, hence, flapping position data was unavailable. For these cases, the flap motion was assumed to be similar to the high frequency

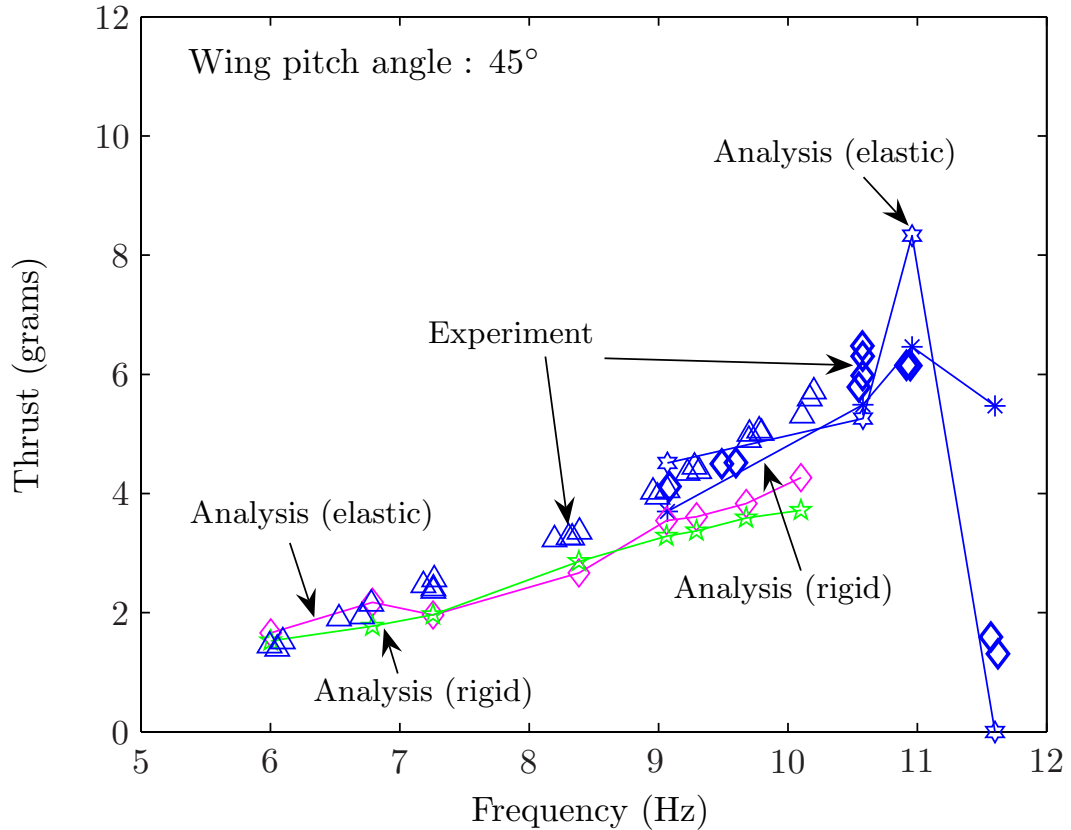


Figure 6.11: Comparison of experiment and analysis for Wing III at  $45^\circ$  pitch angle tests. Figure 6.11 shows good agreement between experiment and analysis at low frequencies, but there is some underprediction of thrust at the higher frequencies. For these frequencies, an elastic analysis improved prediction. Figure 6.12 shows a comparison between experiment and analysis for Wing III at a pitch angle of  $30^\circ$ . For this case, good agreement is seen with experimental data, for both rigid and elastic analyses.

Figure 6.13 shows a comparison of experiment and analysis for the thrust produced by Wing II at  $30^\circ$  and  $45^\circ$  pitch angles. This wing was characterized by its pitching axis, which was located at the 50% chord location as compared to the 20% chord location for Wing III. For both pitch angles, the rigid analysis slightly

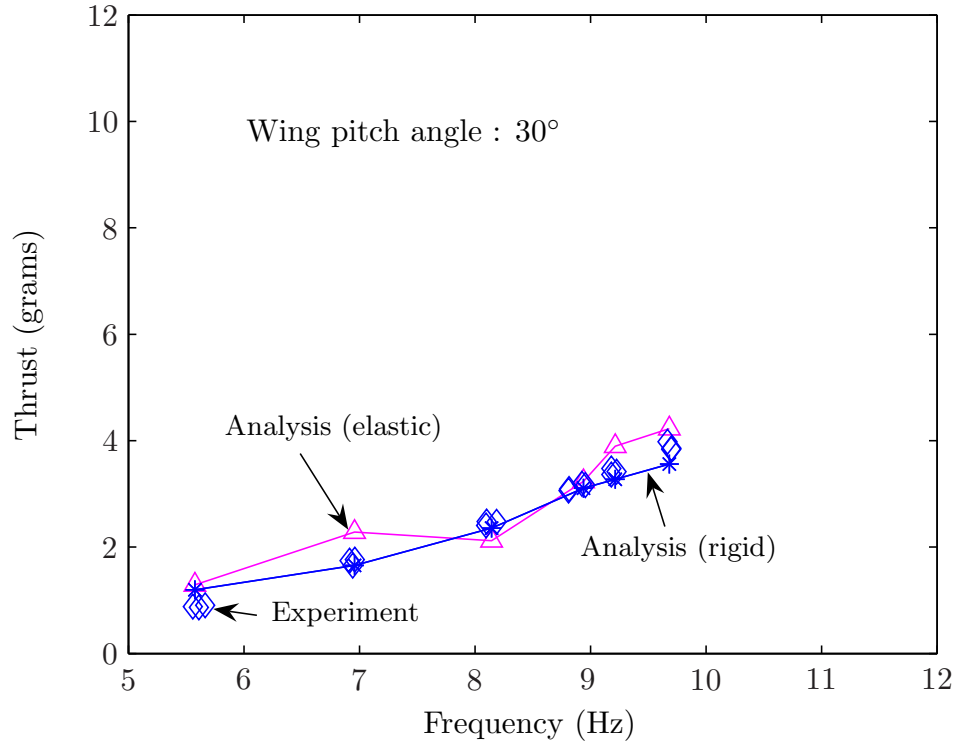


Figure 6.12: Comparison of experiment and analysis for Wing III at 30° pitch angle overpredicted the thrust. The elastic analysis also overpredicted the thrust at 30° pitch angle, but prediction improved at 45° pitch angle. However, an interesting observation from these results is that, unlike Wing III, an increase in pitch angle did not result in an increase in thrust. This effect was captured by the analysis. To examine this closely, Fig. 6.14 shows the components of the total thrust, as predicted by the analysis, at the two pitch angles. For the rigid case, the circulatory force increased with the wing pitch angle, as expected. However, the non-circulatory force reduced with an increase in pitch angle, keeping the total thrust nearly constant. For the elastic case, both the circulatory and non-circulatory forces showed a reduction with increasing pitch angle, leading to a lower overall thrust at the higher pitch angle.

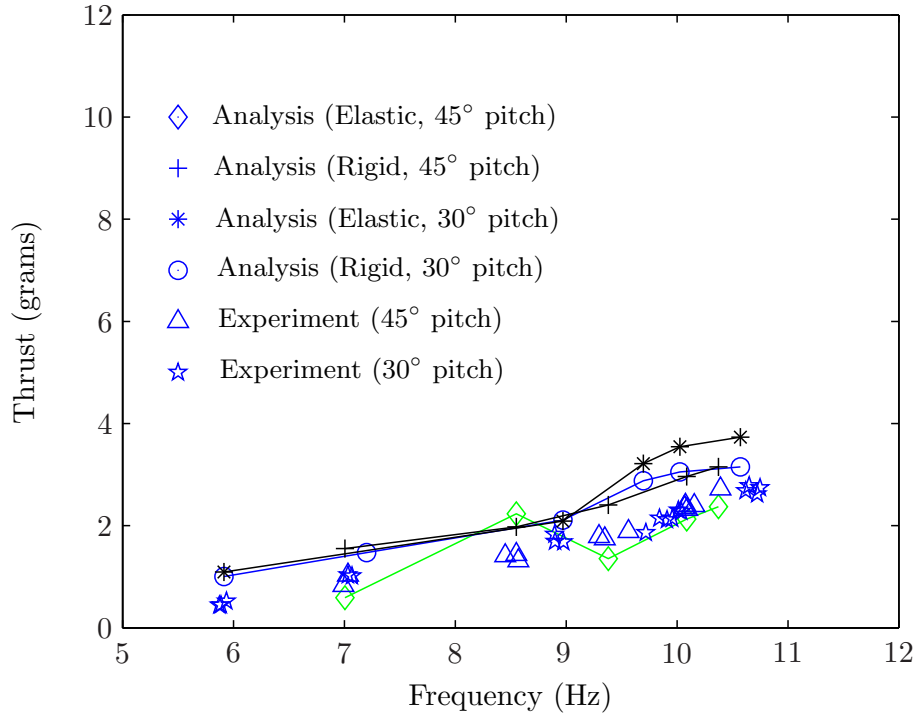


Figure 6.13: Comparison of experiment and analysis for Wing II at 30° and 45° pitch angles

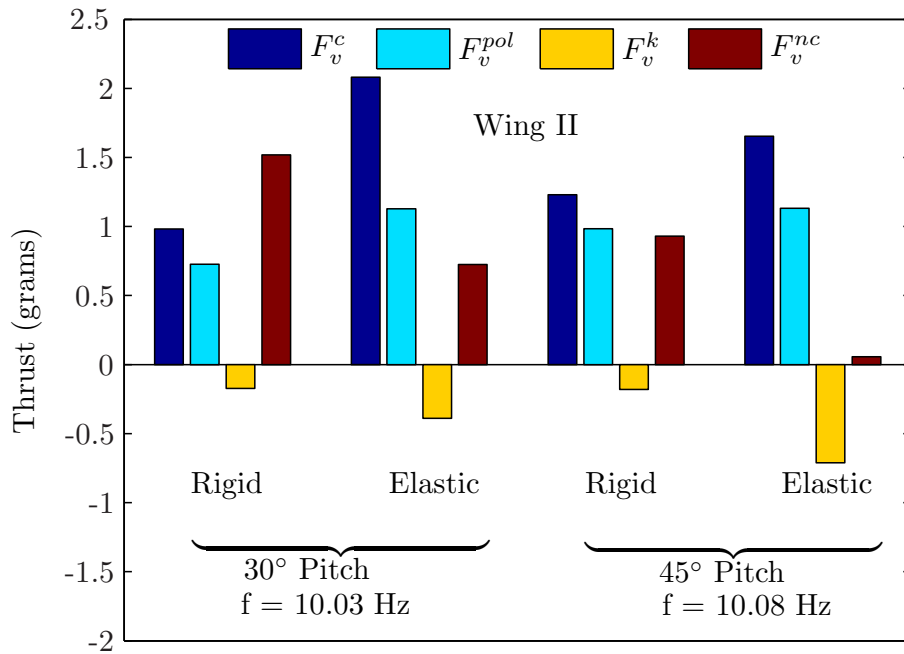


Figure 6.14: Components of total thrust for Wing II at 30° and 45° pitch angles

## 6.4 High frequency bending moment

In order to investigate the error in the bending moment prediction at a high frequency, several tests were conducted with the wing in pure flapping motion, as shown in Fig. 5.4. Because of the absence of active pitching, these tests could be conducted at higher frequencies (up to 17 Hz). A similar bending moment discrepancy was noticed in these tests. Figure 6.15 shows a comparison between the measured and predicted bending moments at different flapping frequencies. It is evident from this figure that the bending moment discrepancy was present in a narrow band of frequency ( $\sim 10.5 - 13.2$  Hz). At higher frequencies (15.0 Hz and 17.3 Hz), the predictions improved considerably, although some high frequency oscillations were not captured.

Figure 6.16 shows the smooth motion input used in the analysis. A systematic evaluation of the problem was carried out using this type of motion input, with only one mode retained in the analysis. The equation of motion was then simplified to the Mathieu equation [109] with a forcing term. Numerical solutions of this equation showed that the wing response was greatly influenced by small changes in the duration of wing acceleration  $\Delta t$  (Fig. 6.16). Small changes in this duration do not show any significant change in the wing position, as shown in Fig. 6.16. Based on this, the input motion for the flapping wing was modified slightly by increasing  $\frac{\Delta t}{T}$  to 0.3. Figure 6.17 shows the bending moments obtained using this modification of the input data. This figure shows considerably improved prediction of the bending moment. Figure 6.18 shows the improved bending moment prediction at high

frequency for the case of combined flapping and pitching of Wing III. Figure 6.19 shows the thrust computed using this improved analysis. The overprediction of thrust, caused by the error in wing response, was considerably improved at a frequency of 10.96 Hz. It may be noted that the parameter  $\Delta t$  was found to have the maximum influence on the response based on a numerical study of a simplified problem. This does not imply that it would be the sole factor of importance in more complex representations of the flapping wing problem.

## Lift and drag coefficients

It must be noted that the lift and drag coefficients used in the analysis were obtained from experimental measurements conducted on the Robofly at  $Re \sim 150$ . However, the experiments in the present study, were conducted at a much higher Reynolds number ( $\sim 17,000$ ). Data from the Robofly experiments was used primarily because there is a lack of reliable experimental data at higher Reynolds numbers. The primary effect of an increase in Reynolds number is the decrease in the minimum drag coefficient as the flow becomes turbulent. Reducing the minimum drag coefficient by a factor of two in the present analysis showed negligible effect on the thrust generated, although it effected the horizontal force significantly. This was because, in the present analysis, the circulatory thrust was mainly dependent on the lift coefficient and the drag curve slope  $C_{d\alpha}$  but not on the minimum drag coefficient.

Another point of concern with the Robofly data is that it includes 3D effects. This is because the data was obtained by accelerating a low aspect ratio wing in a

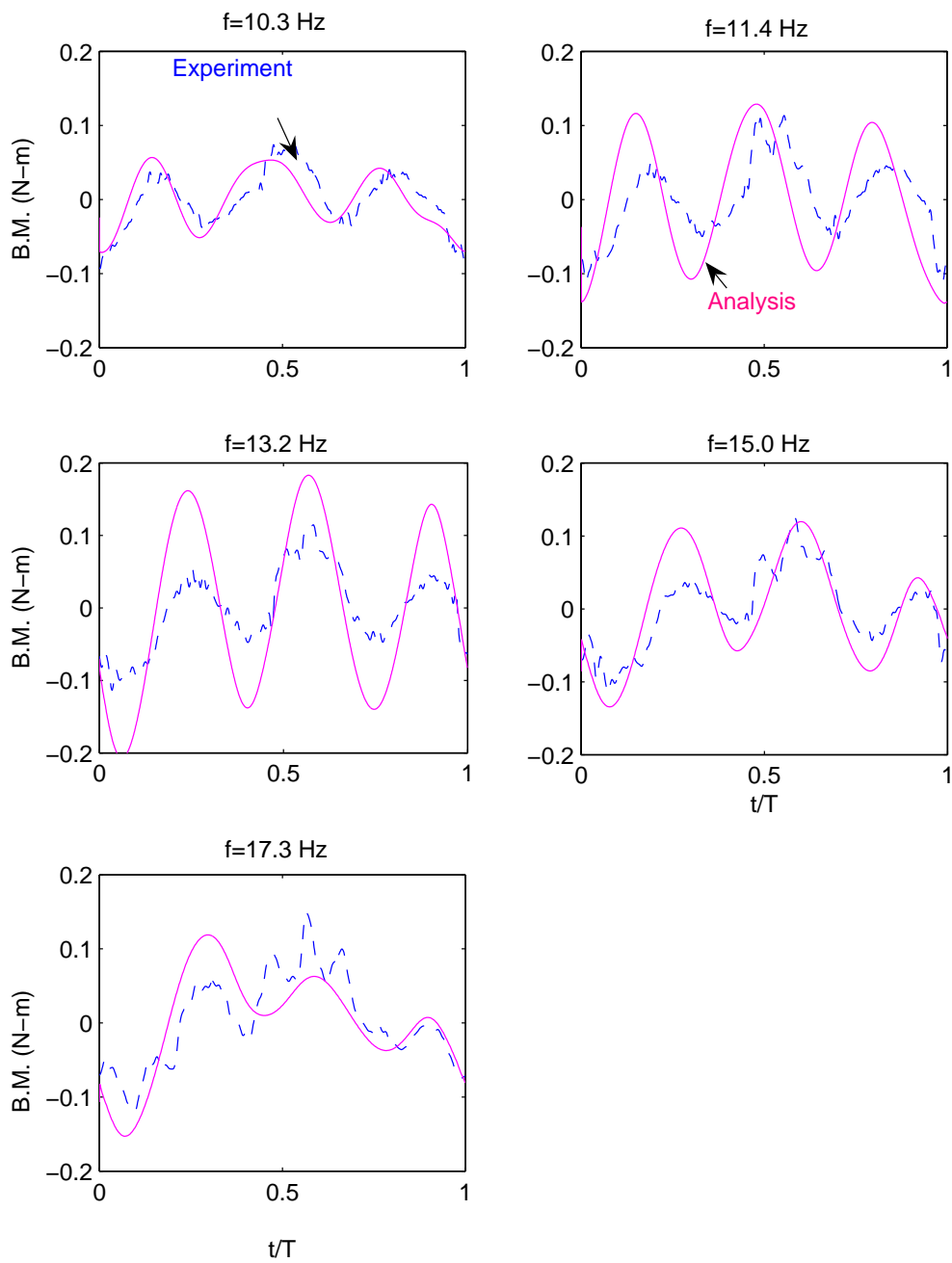


Figure 6.15: Comparison of measured and predicted bending moment for Wing III in pure flapping motion.

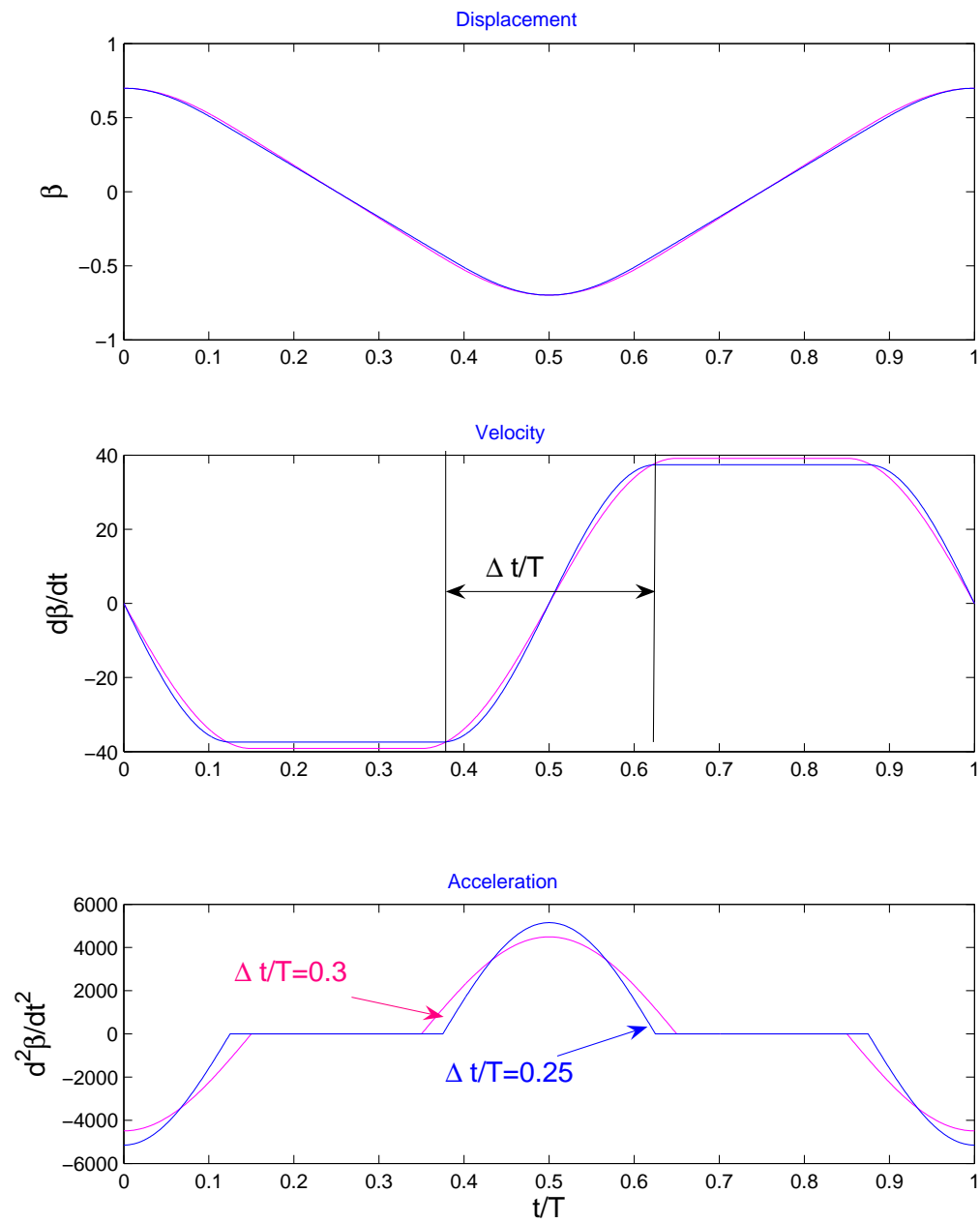


Figure 6.16: Input flap motion showing duration of acceleration

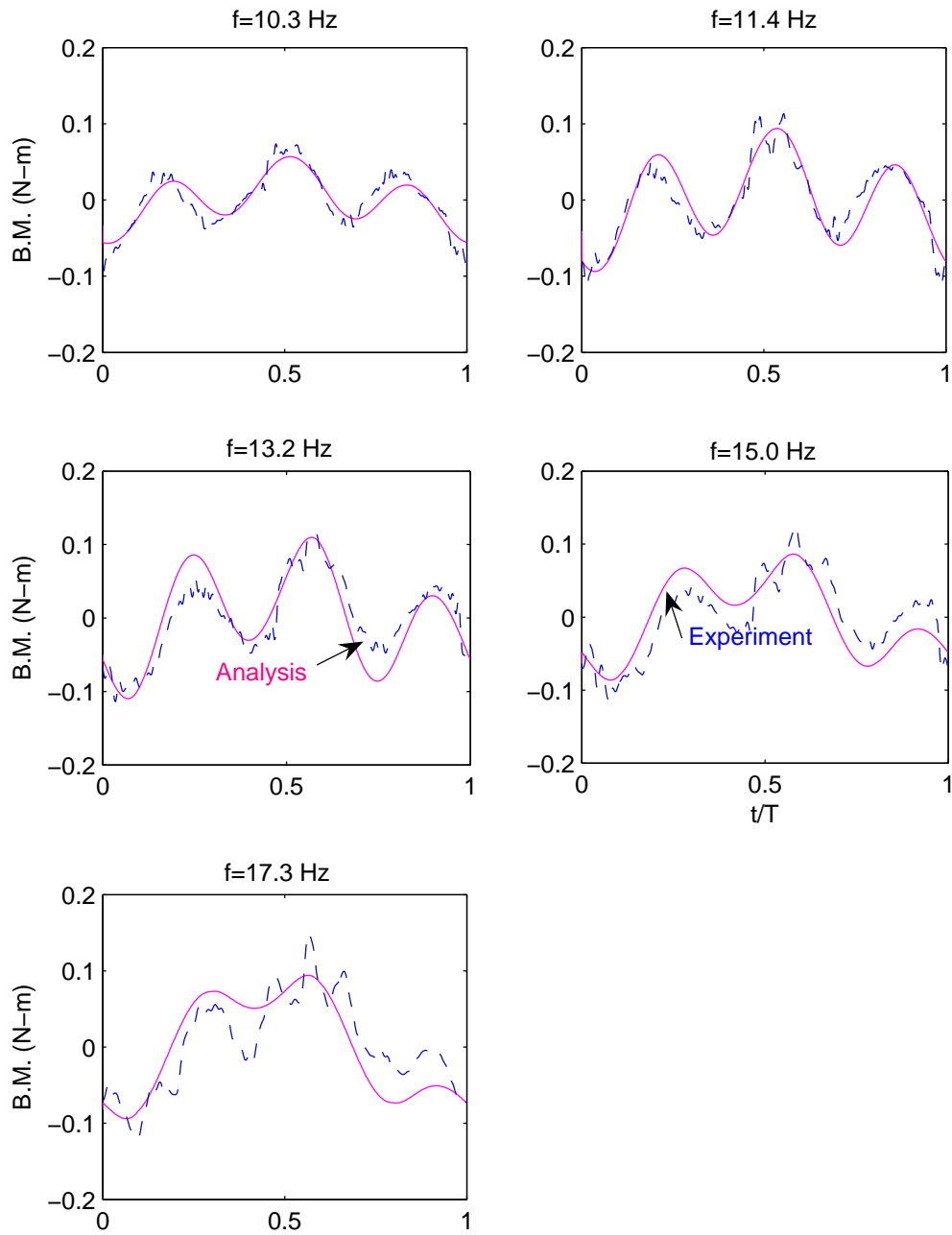


Figure 6.17: Comparison of measured and predicted bending moment for Wing III in pure flapping motion with  $\Delta t/T=0.3$ .

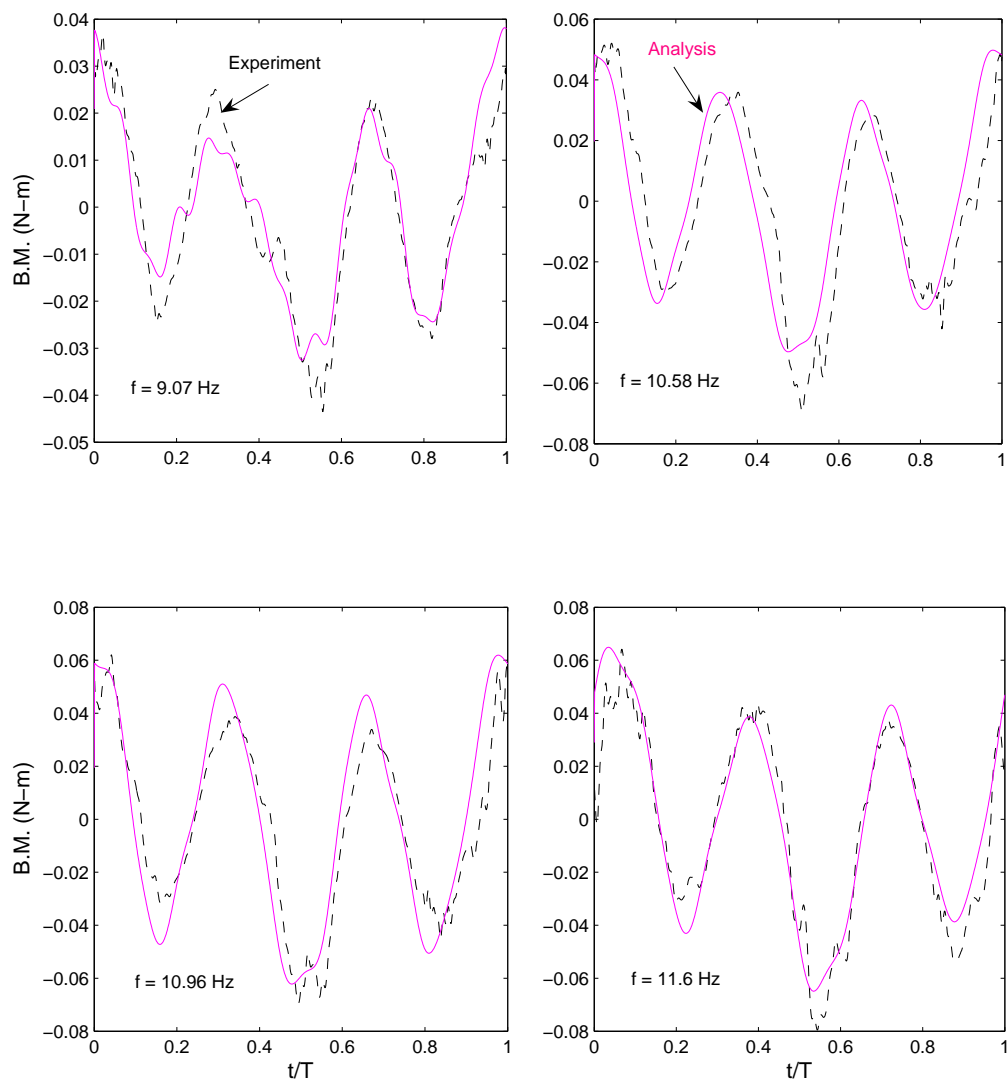


Figure 6.18: Improved bending moment prediction for Wing III undergoing combined flapping and pitching using  $\Delta t/T=0.3$

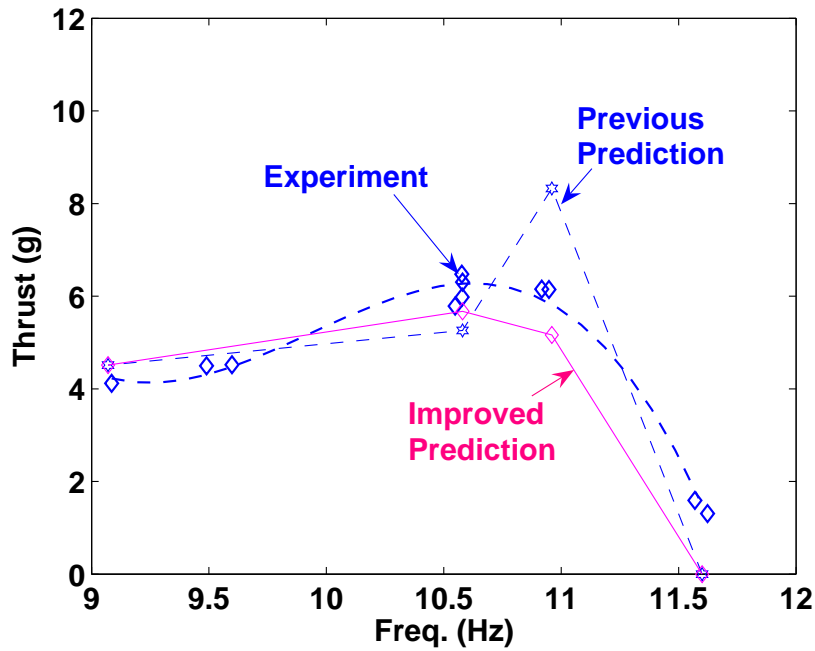


Figure 6.19: Improved thrust prediction (with  $\Delta t/T = 0.3$ ).

liquid medium . The blade element model requires 2D data. However, a CFD study on a two-dimensional wing has shown that the lift and drag coefficients measured on the 3D wing can be reproduced by a 2D analysis [110]. For this reason, the 3D data from the robofly experiments was used in the present study, based on the assumption that the lift and drag coefficients do not change appreciably in 2D flow.

## Aerodynamic center of pressure

In the experiments conducted on the flapping wings, it was assumed that the net aerodynamic force acts at the point defined by the second moment of area of the wing. This point was at a distance of 10.34 cm from the flapping axis. From the analytical predictions, the center of pressure of the airloads was found to be at

a distance of 9.52 cm and 11.03 cm from the flapping axis, for the rigid and elastic analyses, respectively. For the elastic case, this represents an error of 6.9 mm in the estimation of the location of the center of pressure. At maximum thrust, this error would lead to a 6.2% reduction in thrust.

## **Inflow model**

A uniform inflow model was used in the present study. However, the actual inflow in the experiments was not expected to be uniform. In order to investigate the effect of a change in the inflow model, a linear inflow model was used, in which, the inflow varied linearly from zero at the root to a maximum value at the tip. Figure 6.20 shows a comparison of the vertical force, obtained using this model, with the vertical force predicted by the uniform inflow model at a frequency of 10.58 Hz. With the linear inflow model, the higher inflow at the wing tip, caused the circulatory thrust to decrease marginally. This effect is more pronounced at a non-dimensional time between 0.2 and 0.4, when the wing is in translation. The average thrust reduced by 0.68 grams from 5.79 grams to 5.11 grams when the linear inflow model was used. However, even a linear inflow model may be an oversimplification of the actual inflow conditions in the experiment.

## **Effect of wing natural frequency**

A parametric study was carried out to investigate the effect of the first natural frequency of the wing on the analytical thrust prediction. Figure 6.21 shows the

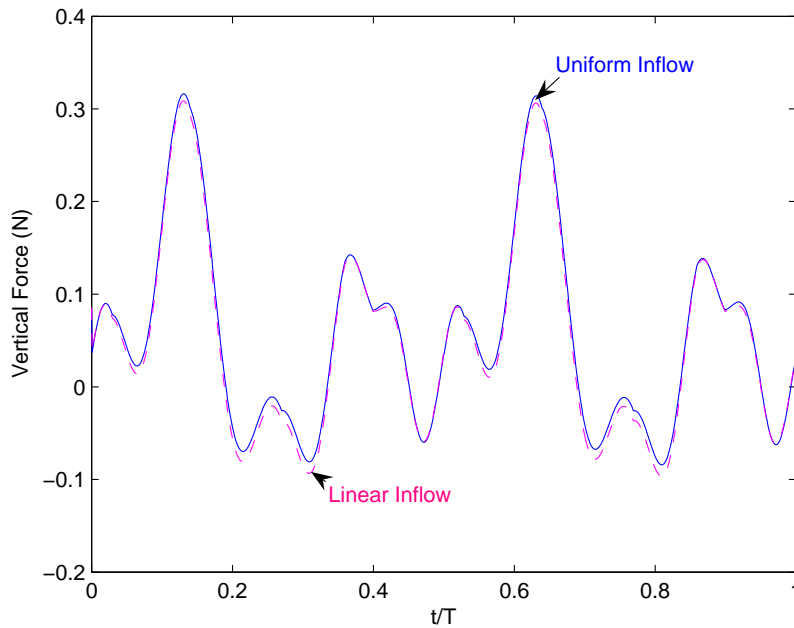


Figure 6.20: Effect of linear inflow model on vertical force at 10.58 Hz

variation of the thrust vs the ratio of the first natural frequency of the wing to the first natural frequency of the baseline wing (36.66 Hz). It is interesting to observe the large changes in wing thrust caused by a change in the wing natural frequency. For certain natural frequencies the thrust drop brought the shed wake close to the wing leading to no convergence. Also interesting is the fact that, at a natural frequency ratio of approximately 1.52, the wing is expected to generate a thrust greater than 8 grams.

## 6.5 Coupled Analysis

In order to investigate the effect of airloads on wing deformation, a loose coupling procedure was implemented. In this analysis, the wing deformations were first

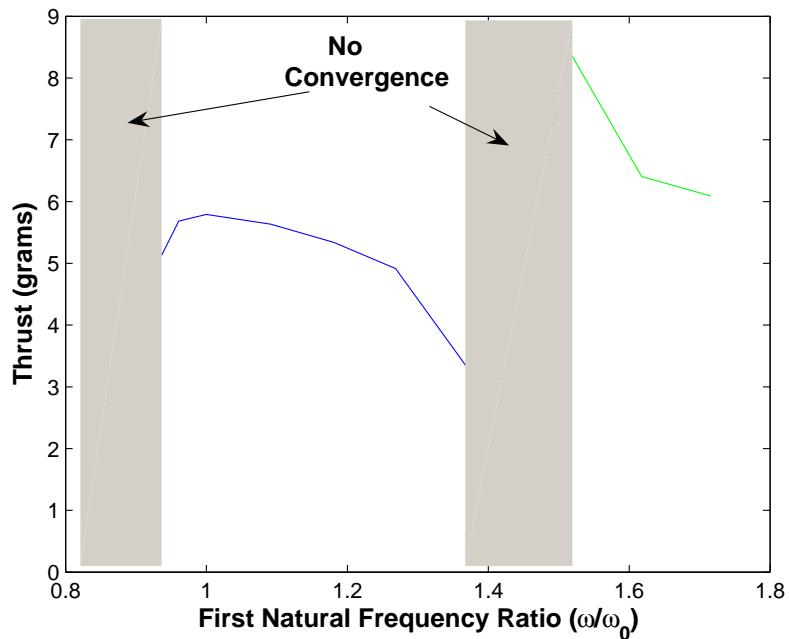


Figure 6.21: Effect of parametric variation of the first natural frequency of the wing at 10.58 Hz.

computed without the aerodynamic loads. Using these deformations, the airloads were computed. These airloads were then applied to the wing and its deformations were recomputed until the wing response converged (Fig. 6.22). It must be noted that the wing finite element grid points were used in the aerodynamic analysis as well. This simplified the coupling procedure to a great extent. Figure 6.23 shows a good correlation of the measured bending moments with those obtained using the coupled analysis. The comparison is not shown at the highest frequency (11.6 Hz) because, at this frequency, the aerodynamic forces do not converge.

Figure 6.24 shows the thrust computed using the coupled analysis at both, low and high frequencies. Good agreement was seen with experimental data, although there was a slight overprediction at low frequencies. Figure 6.25 shows a comparison

of the bending moment computed using the uncoupled and coupled analyses. These results show that, although the overall bending moment variation was governed by the inertial forces, the aerodynamic loads did effect this variation. Thus, for the wings used in this study, the aerodynamic forces cannot be neglected in the wing response computation, although they do not have a significant effect on the average thrust.

## 6.6 Summary

Data from the high frequency bio-inspired flapping mechanism was used to validate the structural analysis for the combined flapping and pitching motion of light-weight, Aluminum-Mylar wings. An accurate measurement of the flapping and pitching accelerations was essential for good agreement between experiment and analysis. These accelerations were provided as inputs to the analysis. However, only the flapping and pitch position data were available from the experiments. To overcome this problem, a Fourier series was fit to the measured motion, and, from this fit, the velocity and acceleration were approximated. Since the measured and approximate motions had significant variations from a smooth flapping motion, the analysis was also carried out with a smooth motion. At high frequencies, the predicted bending moment had significant errors. This discrepancy was resolved and a coupled analysis, with smooth motion input, was carried out with loose coupling between the structural and aerodynamic parts. Based on this analytical study, the following observations were made,

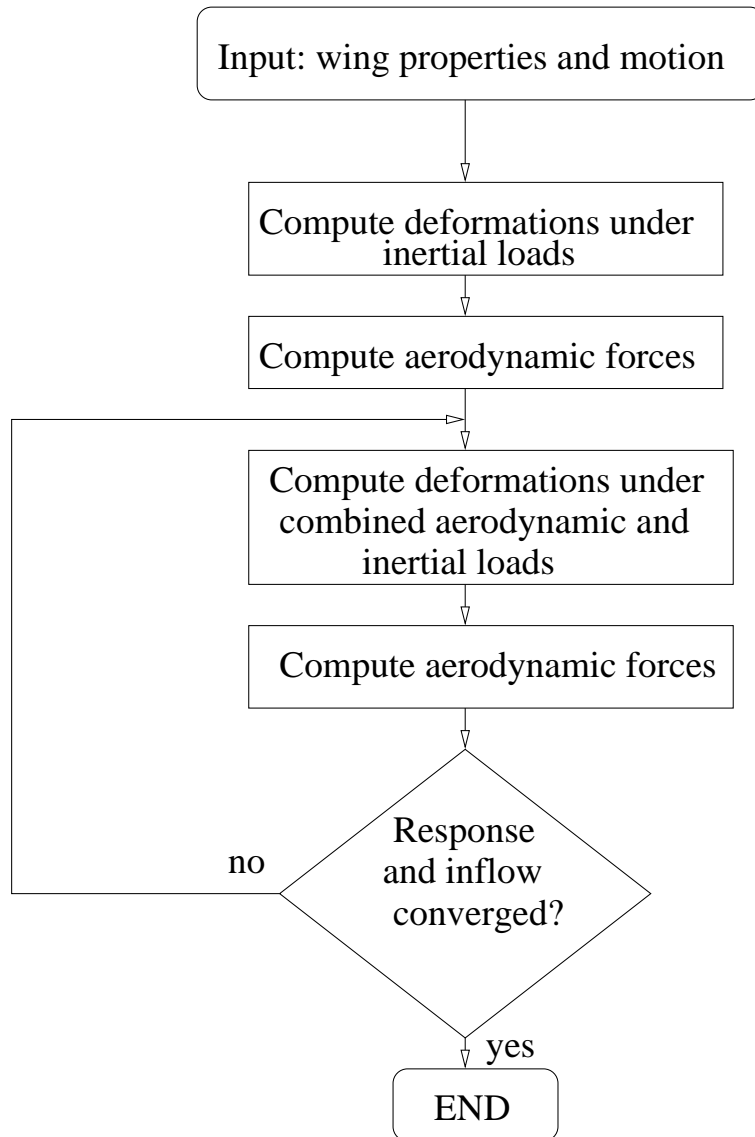


Figure 6.22: Loose coupling procedure.

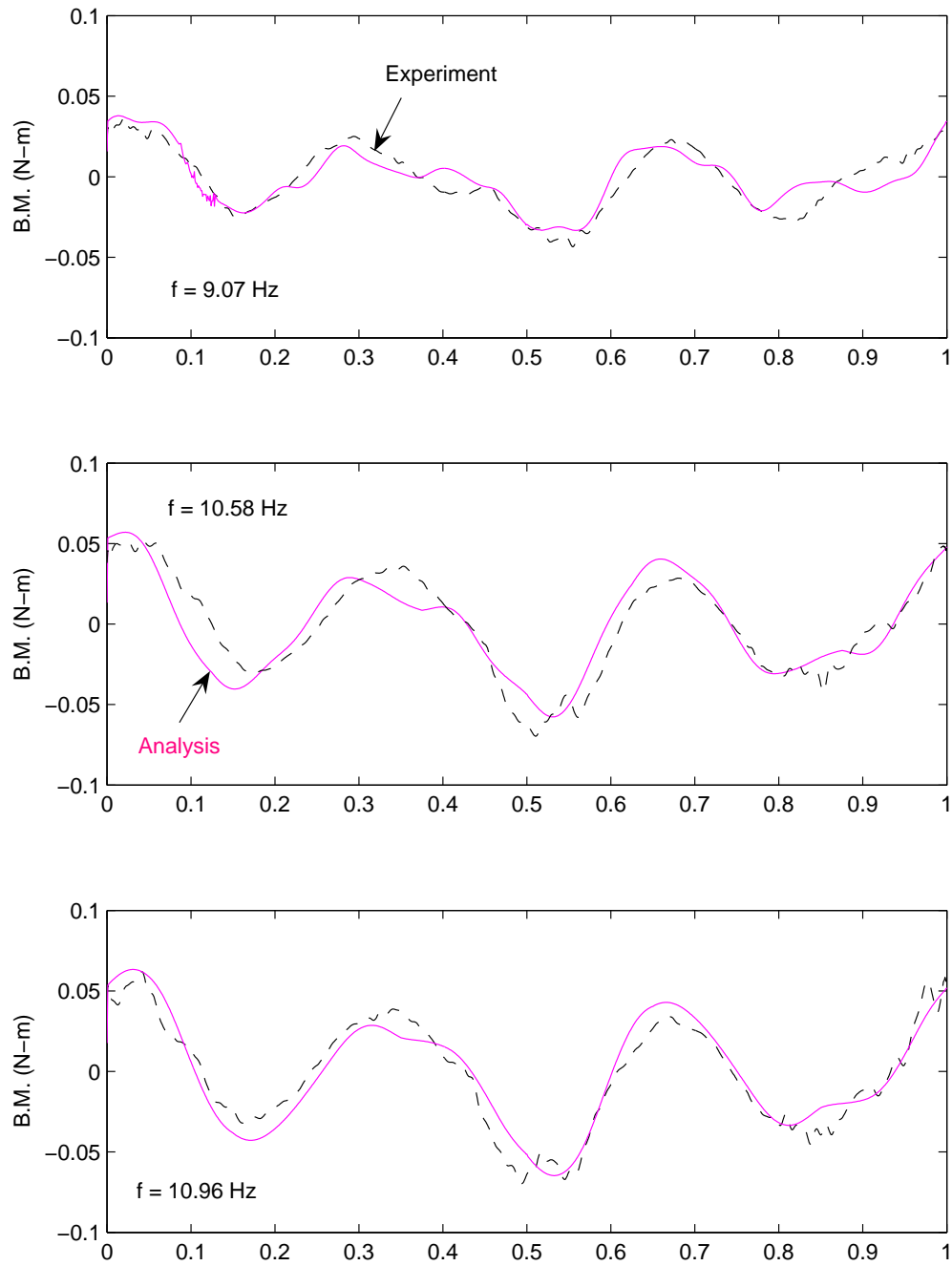


Figure 6.23: Bending moment prediction with coupled analysis for Wing III

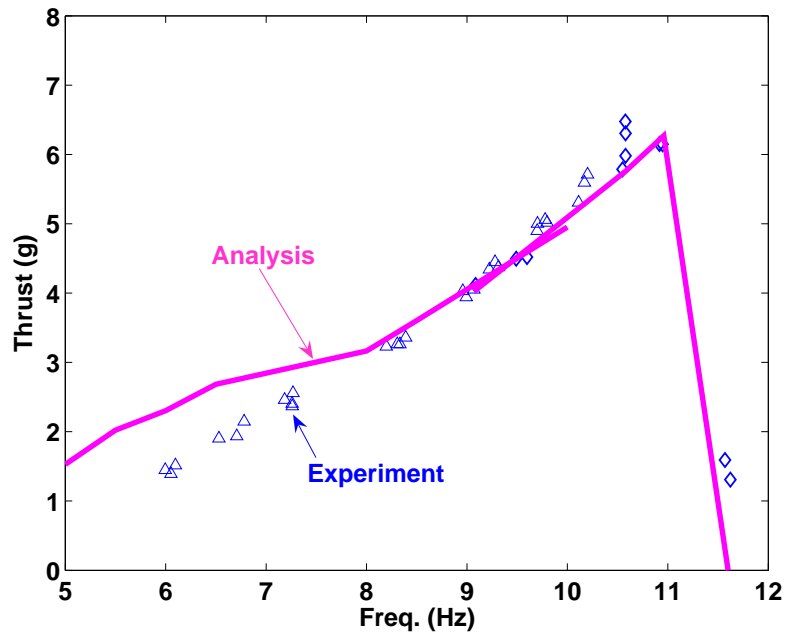


Figure 6.24: Thrust prediction with coupled analysis for Wing III

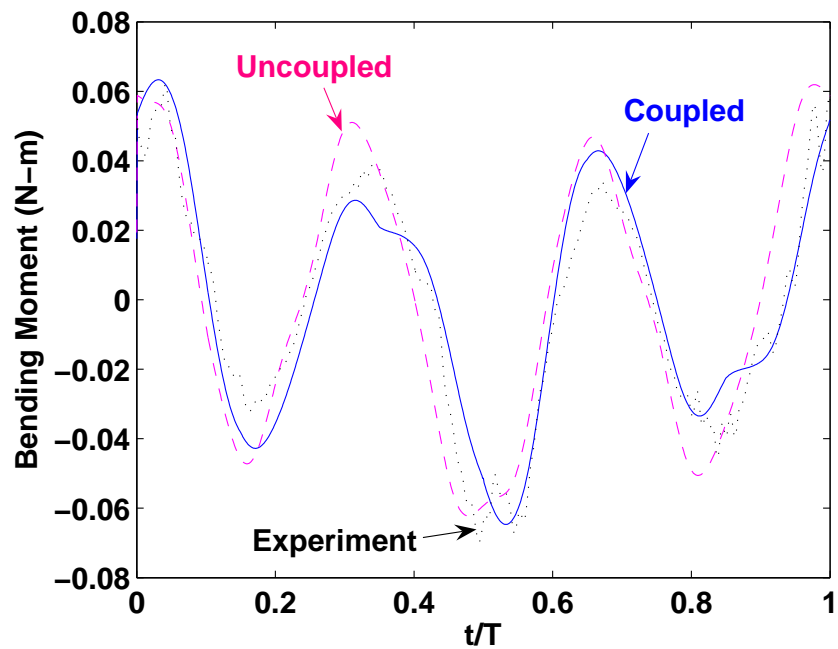


Figure 6.25: Comparison of bending moments calculated using coupled and uncoupled analyses

1. The predicted bending moment showed satisfactory correlation with experimental data, except at the highest frequencies. The errors in approximating the input accelerations caused a significant error.
2. The rigid wing analysis was unable to predict the drop in thrust at high frequencies. However, the elastic analysis predicted this drop, for both approximate and smooth motion inputs.
3. Wing elasticity led to a significant increase in the circulatory thrust because of the higher effective wing velocity. However, this increase was offset by a reduction in the thrust produced by non-circulatory forces. In fact, it is this reduction that caused the drop in thrust at high frequency.
4. At a high frequency, the large negative non-circulatory thrust caused by wing elasticity, led to convergence problems for the inflow. This was because a low thrust produced a low inflow velocity, which brought the strong shed wake in close proximity to the wing.
5. The analysis was also used to predict the thrust generated at pitch angles of  $30^\circ$  and  $45^\circ$  for two wings. One of these wings had a pitching axis at 20% (Wing III) chord while the other had a pitching axis located at 50% (Wing II) chord. The Experimental data showed that, unlike Wing III, an increase in wing pitch angle did not produce more thrust for Wing II. This effect was predicted by the analysis.
6. The bending moment error at a high frequency was found to be caused by the

duration of wing acceleration in a flapping cycle. With an improvement in bending moment prediction, the thrust prediction was also improved.

7. A coupled analysis did not have significant effect on the average thrust. However, the bending moment predictions were significantly altered. This shows that the aerodynamic loads cannot be neglected in computing the wing response.

## Chapter 7

# Concluding Remarks

This dissertation describes an experimental and analytical study conducted on a unique hover-capable, bio-inspired flapping mechanism. The mechanism was capable of producing the large amplitude flapping and pitching motions required for hover capability and it was operated at high frequencies in air. Because of the mechanical complexity involved in building such a mechanism, previous studies on hover capable flapping were conducted on scaled-up, slow-moving mechanisms that mimic insect wing kinematics in a liquid medium at very low Reynolds numbers ( $\sim 150$ ). In order to build a successful hover capable flapping wing MAV, the wings must be tested at the flapping frequencies, size range and Reynolds number typical of MAVs. There was no available experimental data on this type of flapping at MAV scales and flapping frequencies. The first part of this work attempts to address this gap.

Another issue is the analytical modeling of flapping flight. The complexity of the wing motion, low Reynolds numbers, an extremely unsteady flow field and wing aeroelasticity make this a difficult problem to tackle. However, analytical modeling is of utmost importance in the design of these MAVs to avoid designing by trial

and error. To achieve high flapping frequencies in air, the wings had to be light and flexible. This flexibility introduced aeroelastic effects which must be accounted for in the analysis. The second part of this study deals with the development and validation of an aeroelastic analysis for hover capable flapping wings.

## **7.1 Conclusions**

### **7.1.1 Experimental results**

The following conclusions were drawn from the experiments conducted on the flapping wing mechanism:

1. The inertial loads constituted the major portion of loads acting on the flapping wings tested on the mechanism. This had two consequences. First, this made it very difficult to obtain the time variations of the airloads. However, the average airloads could be measured by using a custom built load cell with highly sensitive piezo-resistive strain gauges. Second, any increase in the mass of the wing drastically reduced the maximum frequency attained with the mechanism.
2. For all the wings tested on the bio-inspired mechanism, the thrust dropped at high frequency.
3. The maximum thrust generated by bio-inspired flapping of a single wing was 6.5 grams. Hence, the all-up weight with two wings would be 13 grams. Existing flapping wing MAVs, which are based on ornithoptic flapping and lack

hover capability, are lighter than this mass. Hover capable insects and birds which fall within the MAV size range have a total mass which is less than 10 grams. This indicates the need for a re-evaluation of the 100 gram all-up weight requirement with respect to flapping wing MAVs. Perhaps the best example in nature is the Giant Hummingbird which can weigh more than 20 grams and has a wing-beat frequency of 17-20 Hz. This might be a better initial objective for an MAV based on hover-capable bio-inspired flapping.

4. The frequency limitation of the flapping mechanism could be alleviated by using a passive pitch mechanism. In this case, the wing was held vertical and flapped in a horizontal plane with pitch changes being caused passively by the aeroelastic forces acting on the wing. The pitch changes were facilitated by a torsion spring at the base of the wing. In this case, one wing was able to produce nearly 18 grams of thrust providing a 36 gram all-up weight. Keeping in view the mechanical challenges involved in building a bio-inspired mechanism, this configuration is perhaps the most promising in terms of getting an MAV to hover, at least in tethered mode. However, the problem of control needs to be addressed.

### **7.1.2 Aeroelastic Modeling**

From the validation of the structural and aerodynamic models, the following conclusions were drawn:

1. The input acceleration provided to the analysis was a key factor in obtaining

good correlation with experimental data. However, currently available MEMS accelerometers measure linear acceleration and not angular acceleration. Calculating the angular acceleration amplifies the measurement error for the linear acceleration.

2. Validation of the aerodynamic analysis with data for the Robofly showed that the ideal translatory lift coefficient, obtained from thin airfoil theory, was inadequate to capture the aerodynamic forces. The experimental lift coefficient improved predictions. However, non-circulatory forces introduced errors in the analysis.
3. At the beginning of each half-stroke, a force peak was observed in the analysis. This peak was primarily caused by non-circulatory forces. This force peak explained, at least in part, the force peak observed in the experiment. However, in Ref. 34 this peak was attributed to wake capture alone, based on the improper assumption that, for a flat stroke plane non-circulatory forces could not affect the vertical force.

The aeroelastic analysis was used to predict the airloads measured on the bio-inspired flapping wing mechanism:

1. The predicted bending moment showed satisfactory correlation with experimental data, except at the highest frequencies. The errors in approximating the input accelerations caused a significant error.
2. The rigid wing analysis was unable to predict the drop in thrust at high

frequency. However, the elastic analysis predicted this drop.

3. Wing elasticity led to a significant increase in the circulatory thrust because of the higher effective wing velocity. However, this increase was offset by a reduction in the thrust produced by non-circulatory forces. In fact, it is this reduction that caused the drop in thrust at high frequency. As the non-circulatory thrust dropped, the overall thrust and hence the inflow velocity, reduced. This brought the shed wake close to the wing, leading to large oscillations in the thrust and no convergence.
4. The bending moment error at a high frequency was found to be caused by the duration of wing acceleration in a flapping cycle. With an improvement in bending moment prediction, the thrust prediction was also improved.
5. A coupled analysis did not have significant effect on the average thrust. While the overall variation of the bending moment was adequately captured by the uncoupled analysis, the aerodynamic coupling introduced significant changes. This shows that the aerodynamic loads cannot be neglected to obtain the wing response accurately.

## 7.2 Important Contributions

The following are the major contributions of this research work:

1. Prior to this study there was no experimental data available for hover capable flapping wings at the Reynolds numbers and flapping frequencies relevant to

MAV development. This gap has been addressed to some extent by the present work.

2. The experimental challenges involved, such as, measurement of the small aerodynamic forces in the presence of large inertial loads, were addressed. Custom built force and motion transducers were used because of the need for small, sensitive and light-weight sensors.
3. Aeroelastic studies on wings undergoing large amplitude flapping and pitching motions, in the hover mode, were non-existent in literature. The development and validation of the aeroelastic analysis addressed this issue.
4. Wing aeroelasticity was found to be a major barrier in achieving high thrust from bio-inspired flapping. This underscores the importance of systematic structural and aeroelastic design of the wings.
5. A novel mechanism based on passive pitching of the wing, caused by aeroelastic forces, was also investigated. This type of flapping shows some promise for MAV development because of its mechanical simplicity and high thrust.

### **7.3 Recommendations for Future Work**

This dissertation describes a small step in the development of flapping wing MAVs which are still in their infancy. A considerable amount of work remains to be done before such MAVs are practically realized. The following are some directions along which further research can be carried out:

1. The aerodynamic model may be improved using an unsteady vortex lattice method. When coupled with the structural model, this analysis can be used to optimize the structural and aerodynamic design of the wing.
2. The structural model can be coupled with a CFD analysis to obtain greater accuracy in aerodynamic computations. The ultimate goal being a fluid structure interaction model with a non-linear, multi-body structural analysis and a CFD based aerodynamic analysis.
3. From an implementation standpoint, the design of the mechanism is the key issue. In order to achieve tethered flight a passive pitch mechanism might be the simplest mechanism. The stiffness of the torsion spring and the mass distribution of the wing may be optimized in order to obtain a wing motion that is as close to bio-inspired flapping as possible.
4. On the experimental side, the flapping wing mechanism can be used to study wings in forward flight and also under gusts. This will help in validating the above analyses under different flight conditions.
5. Ultimately, using the dragonfly as a model, wing-wing interactions may be studied using the analytical tools developed in order to see whether these interactions can be beneficial to the design of an MAV.

## Appendix A

### Finite Element Matrices

#### A.1 Shape function matrices

Bi-linear shape functions for in-plane deformations,

$$n_1 = \frac{1}{4}(1 - \xi)(1 - \eta) \quad (\text{A.1})$$

$$n_2 = \frac{1}{4}(1 + \xi)(1 - \eta) \quad (\text{A.2})$$

$$n_3 = \frac{1}{4}(1 + \xi)(1 + \eta) \quad (\text{A.3})$$

$$n_4 = \frac{1}{4}(1 - \xi)(1 + \eta) \quad (\text{A.4})$$

$$\{N_1\} = [n_1 \ n_2 \ n_3 \ n_4 \ \{0\}_{1 \times 20}] \quad (\text{A.5})$$

$$\{N_1\} = [\{0\}_{1 \times 4} \ n_1 \ n_2 \ n_3 \ n_4 \ \{0\}_{1 \times 16}] \quad (\text{A.6})$$

where,  $\xi = \frac{x}{a}$  and  $\eta = \frac{y}{b}$ .

$$\{N_3\} = \frac{1}{16a^3b^3} \left[ \begin{array}{c} \{0\}_{8 \times 1} \\ (y+2b)(-b+y)^2(2a+x)(a-x)^2 \\ (y+2b)(-b+y)^2(a+x)(a-x)^2a \\ (y+b)(-b+y)^2(2a+x)(a-x)^2b \\ (y+b)(-b+y)^2(a+x)(a-x)^2ab \\ (y+2b)(-b+y)^2(2a-x)(a+x)^2 \\ -(y+2b)(-b+y)^2(a-x)(a+x)^2a \\ (y+b)(-b+y)^2(2a-x)(a+x)^2b \\ -(y+b)(-b+y)^2(a-x)(a+x)^2ab \\ -(-2b+y)(y+b)^2(2a-x)(a+x)^2 \\ (-2b+y)(y+b)^2(a-x)(a+x)^2a \\ (-b+y)(y+b)^2(2a-x)(a+x)^2b \\ -(-b+y)(y+b)^2(a-x)(a+x)^2ab \\ -(-2b+y)(y+b)^2(2a+x)(a-x)^2 \\ -(-2b+y)(y+b)^2(a+x)(a-x)^2a \\ (-b+y)(y+b)^2(2a+x)(a-x)^2b \\ (-b+y)(y+b)^2(a+x)(a-x)^2ab \end{array} \right]^T \quad (\text{A.7})$$

## A.2 Dynamic stiffening matrices

$$\int_{-a}^{\bar{x}} [N_{3,x}]^T [N_{3,x}] dx = \frac{1}{3840a^6b^6}$$

$$\begin{bmatrix} 9C_1^2C_3^4C_6 & -\frac{3}{2}aC_1^2C_3^4C_7 & 9bC_1C_3^4C_4C_6 & -\frac{3}{2}abC_1C_3^4C_4C_7 \\ -9C_1^2C_3^4C_6 & \frac{3}{2}aC_1^2C_3^4C_9 & -9bC_1C_3^4C_4C_6 & \frac{3}{2}abC_1C_3^4C_4C_9 \\ 9C_3^2C_4^2C_6C_5 & -\frac{3}{2}aC_3^2C_4^2C_9C_5 & -9bC_1C_3^3C_4^2C_6 & \frac{3}{2}abC_1C_3^3C_4^2C_9 \\ -9C_3^2C_4^2C_6C_5 & \frac{3}{2}aC_3^2C_4^2C_7C_5 & 9bC_1C_3^3C_4^2C_6 & -\frac{3}{2}abC_1C_3^3C_4^2C_7 \end{bmatrix}$$

$$\begin{bmatrix} [-\frac{3}{2}aC_1^2C_3^4C_7 & a^2C_1^2C_3^4C_8 & -\frac{3}{2}abC_1C_3^4C_4C_7 & a^2bC_1C_3^4C_4C_8 \\ \frac{3}{2}aC_1^2C_3^4C_7 & -a^2C_1^2C_3^4C_{10} & \frac{3}{2}abC_1C_3^4C_4C_7 & -a^2bC_1C_3^4C_4C_{10} \\ -\frac{3}{2}aC_3^2C_4^2C_7C_5 & a^2C_3^2C_4^2C_{10}C_5 & \frac{3}{2}abC_1C_3^3C_4^2C_7 & -a^2bC_1C_3^3C_4^2C_{10} \\ \frac{3}{2}aC_3^2C_4^2C_7C_5 & -a^2C_3^2C_4^2C_8C_5 & -\frac{3}{2}abC_1C_3^3C_4^2C_7 & a^2bC_1C_3^3C_4^2C_8 \end{bmatrix}$$

$$\begin{bmatrix} [9bC_1C_3^4C_4C_6 & -\frac{3}{2}abC_1C_3^4C_4C_7 & 9b^2C_4^2C_3^4C_6 & -\frac{3}{2}ab^2C_4^2C_3^4C_7 \\ -9bC_1C_3^4C_4C_6 & \frac{3}{2}abC_1C_3^4C_4C_9 & -9b^2C_4^2C_3^4C_6 & \frac{3}{2}ab^2C_4^2C_3^4C_9 \\ 9bC_4^3C_3^2C_2C_6 & -\frac{3}{2}abC_4^3C_3^2C_2C_9 & -9b^2C_4^3C_3^3C_6 & \frac{3}{2}ab^2C_4^3C_3^3C_9 \\ -9bC_4^3C_3^2C_2C_6 & \frac{3}{2}abC_4^3C_3^2C_2C_7 & 9b^2C_4^3C_3^3C_6 & -\frac{3}{2}ab^2C_4^3C_3^3C_7 \end{bmatrix}$$

$$\begin{bmatrix} [-\frac{3}{2}abC_1C_3^4C_4C_7 & a^2bC_1C_3^4C_4C_8 & -\frac{3}{2}ab^2C_4^2C_3^4C_7 & a^2b^2C_4^2C_3^4C_8 \\ \frac{3}{2}abC_1C_3^4C_4C_7 & -a^2bC_1C_3^4C_4C_{10} & \frac{3}{2}ab^2C_4^2C_3^4C_7 & -a^2b^2C_4^2C_3^4C_{10} \\ -\frac{3}{2}abC_4^3C_3^2C_2C_7 & a^2bC_4^3C_3^2C_2C_{10} & \frac{3}{2}ab^2C_4^3C_3^3C_7 & -a^2b^2C_4^3C_3^3C_{10} \\ \frac{3}{2}abC_4^3C_3^2C_2C_7 & -a^2bC_4^3C_3^2C_2C_8 & -\frac{3}{2}ab^2C_4^3C_3^3C_7 & a^2b^2C_4^3C_3^3C_8 \end{bmatrix}$$

$$\begin{aligned}
& [-9 C_1^2 C_3^4 C_6 \quad \frac{3}{2} a C_1^2 C_3^4 C_7 \quad -9 b C_1 C_3^4 C_4 C_6 \quad \frac{3}{2} a b C_1 C_3^4 C_4 C_7 \\
& \quad 9 C_1^2 C_3^4 C_6 \quad -\frac{3}{2} a C_1^2 C_3^4 C_9 \quad 9 b C_1 C_3^4 C_4 C_6 \quad -\frac{3}{2} a b C_1 C_3^4 C_4 C_9 \\
& -9 C_3^2 C_4^2 C_6 C_5 \quad \frac{3}{2} a C_3^2 C_4^2 C_9 C_5 \quad 9 b C_1 C_3^3 C_4^2 C_6 \quad -\frac{3}{2} a b C_1 C_3^3 C_4^2 C_9 \\
& \quad 9 C_3^2 C_4^2 C_6 C_5 \quad -\frac{3}{2} a C_3^2 C_4^2 C_7 C_5 \quad -9 b C_1 C_3^3 C_4^2 C_6 \quad \frac{3}{2} a b C_1 C_3^3 C_4^2 C_7] \\
& [\frac{3}{2} a C_1^2 C_3^4 C_9 \quad -a^2 C_1^2 C_3^4 C_{10} \quad \frac{3}{2} a b C_1 C_3^4 C_4 C_9 \quad -a^2 b C_1 C_3^4 C_4 C_{10} \\
& -\frac{3}{2} a C_1^2 C_3^4 C_9 \quad a^2 C_1^2 C_3^4 C_{11} \quad -\frac{3}{2} a b C_1 C_3^4 C_4 C_9 \quad a^2 b C_1 C_3^4 C_4 C_{11} \\
& \frac{3}{2} a C_3^2 C_4^2 C_9 C_5 \quad -a^2 C_3^2 C_4^2 C_{11} C_5 \quad -\frac{3}{2} a b C_1 C_3^3 C_4^2 C_9 \quad a^2 b C_1 C_3^3 C_4^2 C_{11} \\
& -\frac{3}{2} a C_3^2 C_4^2 C_9 C_5 \quad a^2 C_3^2 C_4^2 C_{10} C_5 \quad \frac{3}{2} a b C_1 C_3^3 C_4^2 C_9 \quad -a^2 b C_1 C_3^3 C_4^2 C_{10}] \\
& [-9 b C_1 C_3^4 C_4 C_6 \quad \frac{3}{2} a b C_1 C_3^4 C_4 C_7 \quad -9 b^2 C_4^2 C_3^4 C_6 \quad \frac{3}{2} a b^2 C_4^2 C_3^4 C_7 \\
& \quad 9 b C_1 C_3^4 C_4 C_6 \quad -\frac{3}{2} a b C_1 C_3^4 C_4 C_9 \quad 9 b^2 C_4^2 C_3^4 C_6 \quad -\frac{3}{2} a b^2 C_4^2 C_3^4 C_9 \\
& -9 b C_4^3 C_3^2 C_2 C_6 \quad \frac{3}{2} a b C_4^3 C_3^2 C_2 C_9 \quad 9 b^2 C_4^3 C_3^3 C_6 \quad -\frac{3}{2} a b^2 C_4^3 C_3^3 C_9 \\
& \quad 9 b C_4^3 C_3^2 C_2 C_6 \quad -\frac{3}{2} a b C_4^3 C_3^2 C_2 C_7 \quad -9 b^2 C_4^3 C_3^3 C_6 \quad \frac{3}{2} a b^2 C_4^3 C_3^3 C_7] \\
& [\frac{3}{2} a b C_1 C_3^4 C_4 C_9 \quad -a^2 b C_1 C_3^4 C_4 C_{10} \quad \frac{3}{2} a b^2 C_4^2 C_3^4 C_9 \quad -a^2 b^2 C_4^2 C_3^4 C_{10} \\
& -\frac{3}{2} a b C_1 C_3^4 C_4 C_9 \quad a^2 b C_1 C_3^4 C_4 C_{11} \quad -\frac{3}{2} a b^2 C_4^2 C_3^4 C_9 \quad a^2 b^2 C_4^2 C_3^4 C_{11} \\
& \frac{3}{2} a b C_4^3 C_3^2 C_2 C_9 \quad -a^2 b C_4^3 C_3^2 C_2 C_{11} \quad -\frac{3}{2} a b^2 C_4^3 C_3^3 C_9 \quad a^2 b^2 C_4^3 C_3^3 C_{11} \\
& -\frac{3}{2} a b C_4^3 C_3^2 C_2 C_9 \quad a^2 b C_4^3 C_3^2 C_2 C_{10} \quad \frac{3}{2} a b^2 C_4^3 C_3^3 C_9 \quad -a^2 b^2 C_4^3 C_3^3 C_{10}] \\
& [9 C_3^2 C_4^2 C_6 C_5 \quad -\frac{3}{2} a C_3^2 C_4^2 C_7 C_5 \quad 9 b C_4^3 C_3^2 C_2 C_6 \quad -\frac{3}{2} a b C_4^3 C_3^2 C_2 C_7 \\
& -9 C_3^2 C_4^2 C_6 C_5 \quad \frac{3}{2} a C_3^2 C_4^2 C_9 C_5 \quad -9 b C_4^3 C_3^2 C_2 C_6 \quad \frac{3}{2} a b C_4^3 C_3^2 C_2 C_9 \\
& \quad 9 C_2^2 C_4^4 C_6 \quad -\frac{3}{2} a C_2^2 C_4^4 C_9 \quad -9 b C_3 C_4^4 C_2 C_6 \quad \frac{3}{2} a b C_2 C_4^4 C_3 C_9 \\
& -9 C_2^2 C_4^4 C_6 \quad \frac{3}{2} a C_2^2 C_4^4 C_7 \quad 9 b C_3 C_4^4 C_2 C_6 \quad -\frac{3}{2} a b C_3 C_4^4 C_2 C_7]
\end{aligned}$$

$$\begin{aligned}
& \left[ -\frac{3}{2} a C_3^2 C_4^2 C_9 C_5 \quad a^2 C_3^2 C_4^2 C_{10} C_5 \quad -\frac{3}{2} a b C_4^3 C_3^2 C_2 C_9 \quad a^2 b C_4^3 C_3^2 C_2 C_{10} \right. \\
& \quad \frac{3}{2} a C_3^2 C_4^2 C_9 C_5 \quad -a^2 C_3^2 C_4^2 C_{11} C_5 \quad \frac{3}{2} a b C_4^3 C_3^2 C_2 C_9 \quad -a^2 b C_4^3 C_3^2 C_2 C_{11} \\
& \quad -\frac{3}{2} a C_2^2 C_4^4 C_9 \quad a^2 C_2^2 C_4^4 C_{11} \quad \frac{3}{2} a b C_2 C_4^4 C_3 C_9 \quad -a^2 b C_2 C_4^4 C_3 C_{11} \\
& \quad \left. \frac{3}{2} a C_2^2 C_4^4 C_9 \quad -a^2 C_2^2 C_4^4 C_{10} \quad -\frac{3}{2} a b C_2 C_4^4 C_3 C_9 \quad a^2 b C_3 C_4^4 C_2 C_{10} \right]
\end{aligned}$$

$$\begin{aligned}
& \left[ -9 b C_1 C_3^3 C_4^2 C_6 \quad \frac{3}{2} a b C_1 C_3^3 C_4^2 C_7 \quad -9 b^2 C_4^3 C_3^3 C_6 \quad \frac{3}{2} a b^2 C_4^3 C_3^3 C_7 \right. \\
& \quad 9 b C_1 C_3^3 C_4^2 C_6 \quad -\frac{3}{2} a b C_1 C_3^3 C_4^2 C_9 \quad 9 b^2 C_4^3 C_3^3 C_6 \quad -\frac{3}{2} a b^2 C_4^3 C_3^3 C_9 \\
& \quad -9 b C_3 C_4^4 C_2 C_6 \quad \frac{3}{2} a b C_2 C_4^4 C_3 C_9 \quad 9 b^2 C_3^2 C_4^4 C_6 \quad -\frac{3}{2} a b^2 C_3^2 C_4^4 C_9 \\
& \quad \left. 9 b C_3 C_4^4 C_2 C_6 \quad -\frac{3}{2} a b C_3 C_4^4 C_2 C_7 \quad -9 b^2 C_3^2 C_4^4 C_6 \quad \frac{3}{2} a b^2 C_3^2 C_4^4 C_7 \right]
\end{aligned}$$

$$\begin{aligned}
& \left[ \frac{3}{2} a b C_1 C_3^3 C_4^2 C_9 \quad -a^2 b C_1 C_3^3 C_4^2 C_{10} \quad \frac{3}{2} a b^2 C_4^3 C_3^3 C_9 \quad -a^2 b^2 C_4^3 C_3^3 C_{10} \right. \\
& \quad -\frac{3}{2} a b C_1 C_3^3 C_4^2 C_9 \quad a^2 b C_1 C_3^3 C_4^2 C_{11} \quad -\frac{3}{2} a b^2 C_4^3 C_3^3 C_9 \quad a^2 b^2 C_4^3 C_3^3 C_{11} \\
& \quad \frac{3}{2} a b C_2 C_4^4 C_3 C_9 \quad -a^2 b C_2 C_4^4 C_3 C_{11} \quad -\frac{3}{2} a b^2 C_3^2 C_4^4 C_9 \quad a^2 b^2 C_3^2 C_4^4 C_{11} \\
& \quad \left. -\frac{3}{2} a b C_2 C_4^4 C_3 C_9 \quad a^2 b C_3 C_4^4 C_2 C_{10} \quad \frac{3}{2} a b^2 C_3^2 C_4^4 C_9 \quad -a^2 b^2 C_3^2 C_4^4 C_{10} \right]
\end{aligned}$$

$$\begin{aligned}
& \left[ -9 C_3^2 C_4^2 C_6 C_5 \quad \frac{3}{2} a C_3^2 C_4^2 C_7 C_5 \quad -9 b C_4^3 C_3^2 C_2 C_6 \quad \frac{3}{2} a b C_4^3 C_3^2 C_2 C_7 \right. \\
& \quad 9 C_3^2 C_4^2 C_6 C_5 \quad -\frac{3}{2} a C_3^2 C_4^2 C_9 C_5 \quad 9 b C_4^3 C_3^2 C_2 C_6 \quad -\frac{3}{2} a b C_4^3 C_3^2 C_2 C_9 \\
& \quad -9 C_2^2 C_4^4 C_6 \quad \frac{3}{2} a C_2^2 C_4^4 C_9 \quad 9 b C_3 C_4^4 C_2 C_6 \quad -\frac{3}{2} a b C_2 C_4^4 C_3 C_9 \\
& \quad \left. 9 C_2^2 C_4^4 C_6 \quad -\frac{3}{2} a C_2^2 C_4^4 C_7 \quad -9 b C_3 C_4^4 C_2 C_6 \quad \frac{3}{2} a b C_3 C_4^4 C_2 C_7 \right]
\end{aligned}$$

$$\begin{aligned}
& \left[ \frac{3}{2} a C_3^2 C_4^2 C_7 C_5 \quad -a^2 C_3^2 C_4^2 C_8 C_5 \quad \frac{3}{2} a b C_4^3 C_3^2 C_2 C_7 \quad -a^2 b C_4^3 C_3^2 C_2 C_8 \right. \\
& \quad -\frac{3}{2} a C_3^2 C_4^2 C_7 C_5 \quad a^2 C_3^2 C_4^2 C_{10} C_5 \quad -\frac{3}{2} a b C_4^3 C_3^2 C_2 C_7 \quad a^2 b C_4^3 C_3^2 C_2 C_{10} \\
& \quad \frac{3}{2} a C_2^2 C_4^4 C_7 \quad -a^2 C_2^2 C_4^4 C_{10} \quad -\frac{3}{2} a b C_3 C_4^4 C_2 C_7 \quad a^2 b C_3 C_4^4 C_2 C_{10} \\
& \quad \left. -\frac{3}{2} a C_2^2 C_4^4 C_7 \quad a^2 C_2^2 C_4^4 C_8 \quad \frac{3}{2} a b C_3 C_4^4 C_2 C_7 \quad -a^2 b C_2 C_4^4 C_3 C_8 \right]
\end{aligned}$$

$$\begin{aligned}
& [9bC_1 C_3^3 C_4^2 C_6 \quad -\frac{3}{2}abC_1 C_3^3 C_4^2 C_7 \quad 9b^2 C_4^3 C_3^3 C_6 \quad -\frac{3}{2}ab^2 C_4^3 C_3^3 C_7 \\
& -9bC_1 C_3^3 C_4^2 C_6 \quad \frac{3}{2}abC_1 C_3^3 C_4^2 C_9 \quad -9b^2 C_4^3 C_3^3 C_6 \quad \frac{3}{2}ab^2 C_4^3 C_3^3 C_9 \\
& 9bC_3 C_4^4 C_2 C_6 \quad -\frac{3}{2}abC_2 C_4^4 C_3 C_9 \quad -9b^2 C_3^2 C_4^4 C_6 \quad \frac{3}{2}ab^2 C_3^2 C_4^4 C_9 \\
& -9bC_3 C_4^4 C_2 C_6 \quad \frac{3}{2}abC_3 C_4^4 C_2 C_7 \quad 9b^2 C_3^2 C_4^4 C_6 \quad -\frac{3}{2}ab^2 C_3^2 C_4^4 C_7] \\
& [-\frac{3}{2}abC_1 C_3^3 C_4^2 C_7 \quad a^2bC_1 C_3^3 C_4^2 C_8 \quad -\frac{3}{2}ab^2 C_4^3 C_3^3 C_7 \quad a^2b^2 C_4^3 C_3^3 C_8 \\
& \frac{3}{2}abC_1 C_3^3 C_4^2 C_7 \quad -a^2bC_1 C_3^3 C_4^2 C_{10} \quad \frac{3}{2}ab^2 C_4^3 C_3^3 C_7 \quad -a^2b^2 C_4^3 C_3^3 C_{10} \\
& -\frac{3}{2}abC_3 C_4^4 C_2 C_7 \quad a^2bC_3 C_4^4 C_2 C_{10} \quad \frac{3}{2}ab^2 C_3^2 C_4^4 C_7 \quad -a^2b^2 C_3^2 C_4^4 C_{10} \\
& \frac{3}{2}abC_3 C_4^4 C_2 C_7 \quad -a^2bC_2 C_4^4 C_3 C_8 \quad -\frac{3}{2}ab^2 C_3^2 C_4^4 C_7 \quad a^2b^2 C_3^2 C_4^4 C_8]
\end{aligned} \tag{A.8}$$

where,

$$C_1 = y + 2b \tag{A.9}$$

$$C_2 = -2b + y \tag{A.10}$$

$$C_3 = -b + y \tag{A.11}$$

$$C_4 = y + b \tag{A.12}$$

$$C_5 = y^2 - 4b^2 \tag{A.13}$$

$$C_6 = 3\bar{x}^5 + 8a^5 - 10a^2\bar{x}^3 + 15a^4\bar{x} \tag{A.14}$$

$$C_7 = -18\bar{x}^5 + 7a^5 + 15a\bar{x}^4 + 40a^2\bar{x}^3 - 30a^3\bar{x}^2 - 30a^4\bar{x} \tag{A.15}$$

$$C_8 = 27\bar{x}^5 + 47a^5 - 45a\bar{x}^4 - 10a^2\bar{x}^3 + 30a^3\bar{x}^2 + 15a^4\bar{x} \tag{A.16}$$

$$C_9 = 18\bar{x}^5 + 23a^5 + 15a\bar{x}^4 - 40a^2\bar{x}^3 - 30a^3\bar{x}^2 + 30a^4\bar{x} \tag{A.17}$$

$$C_{10} = -27 \bar{x}^5 + 8 a^5 + 50 a^2 \bar{x}^3 - 15 a^4 \bar{x} \quad (\text{A.18})$$

$$C_{11} = 27 \bar{x}^5 + 17 a^5 + 45 a \bar{x}^4 - 10 a^2 \bar{x}^3 - 30 a^3 \bar{x}^2 + 15 a^4 \bar{x} \quad (\text{A.19})$$

$$\int_{-b}^{\bar{y}} [N_{3,y}]^T [N_{3,y}] dy = \frac{1}{3840 a^6 b^6}$$

$$\begin{aligned} & [9 D_1^2 D_4^4 D_7 \quad 9 a D_5 D_4^4 D_1 D_7 \quad -\frac{3}{2} b D_1^2 D_4^4 D_8 \quad -\frac{3}{2} a b D_5 D_4^4 D_1 D_8 \\ & 9 D_4^2 D_5^2 D_7 D_6 \quad -9 a D_4^3 D_5^2 D_1 D_7 \quad -\frac{3}{2} b D_4^2 D_5^2 D_8 D_6 \quad \frac{3}{2} a b D_4^3 D_5^2 D_1 D_8 \\ & -9 D_4^2 D_5^2 D_7 D_6 \quad 9 a D_4^3 D_5^2 D_1 D_7 \quad \frac{3}{2} b D_4^2 D_5^2 D_9 D_6 \quad -\frac{3}{2} a b D_4^3 D_5^2 D_1 D_9 \\ & -9 D_1^2 D_4^4 D_7 \quad -9 a D_5 D_4^4 D_1 D_7 \quad \frac{3}{2} b D_1^2 D_4^4 D_9 \quad \frac{3}{2} a b D_5 D_4^4 D_1 D_9] \\ & [9 a D_5 D_4^4 D_1 D_7 \quad 9 a^2 D_5^2 D_4^4 D_7 \quad -\frac{3}{2} a b D_5 D_4^4 D_1 D_8 \quad -\frac{3}{2} a^2 b D_5^2 D_4^4 D_8 \\ & 9 a D_3 D_5^3 D_4^2 D_7 \quad -9 a^2 D_4^3 D_5^3 D_7 \quad -\frac{3}{2} a b D_3 D_5^3 D_4^2 D_8 \quad \frac{3}{2} a^2 b D_4^3 D_5^3 D_8 \\ & -9 a D_3 D_5^3 D_4^2 D_7 \quad 9 a^2 D_4^3 D_5^3 D_7 \quad \frac{3}{2} a b D_3 D_5^3 D_4^2 D_9 \quad -\frac{3}{2} a^2 b D_4^3 D_5^3 D_9 \\ & -9 a D_5 D_4^4 D_1 D_7 \quad -9 a^2 D_5^2 D_4^4 D_7 \quad \frac{3}{2} a b D_5 D_4^4 D_1 D_9 \quad \frac{3}{2} a^2 b D_5^2 D_4^4 D_9] \\ & [-\frac{3}{2} b D_1^2 D_4^4 D_8 \quad -\frac{3}{2} a b D_5 D_4^4 D_1 D_8 \quad b^2 D_1^2 D_4^4 D_{12} \quad a b^2 D_5 D_4^4 D_1 D_{12} \\ & -\frac{3}{2} b D_4^2 D_5^2 D_8 D_6 \quad \frac{3}{2} a b D_4^3 D_5^2 D_1 D_8 \quad b^2 D_4^2 D_5^2 D_{12} D_6 \quad -a b^2 D_4^3 D_5^2 D_1 D_{12} \\ & \frac{3}{2} b D_4^2 D_5^2 D_8 D_6 \quad -\frac{3}{2} a b D_4^3 D_5^2 D_1 D_8 \quad -b^2 D_4^2 D_5^2 D_{11} D_6 \quad a b^2 D_4^3 D_5^2 D_1 D_{11} \\ & \frac{3}{2} b D_1^2 D_4^4 D_8 \quad \frac{3}{2} a b D_5 D_4^4 D_1 D_8 \quad -b^2 D_1^2 D_4^4 D_{11} \quad -a b^2 D_5 D_4^4 D_1 D_{11}] \\ & [-\frac{3}{2} a b D_5 D_4^4 D_1 D_8 \quad -\frac{3}{2} a^2 b D_5^2 D_4^4 D_8 \quad a b^2 D_5 D_4^4 D_1 D_{12} \quad a^2 b^2 D_5^2 D_4^4 D_{12} \\ & -\frac{3}{2} a b D_3 D_5^3 D_4^2 D_8 \quad \frac{3}{2} a^2 b D_4^3 D_5^3 D_8 \quad a b^2 D_5^3 D_4^2 D_3 D_{12} \quad -a^2 b^2 D_4^3 D_5^3 D_{12} \\ & \frac{3}{2} a b D_3 D_5^3 D_4^2 D_8 \quad -\frac{3}{2} a^2 b D_4^3 D_5^3 D_8 \quad -a b^2 D_5^3 D_4^2 D_3 D_{11} \quad a^2 b^2 D_4^3 D_5^3 D_{11} \\ & \frac{3}{2} a b D_5 D_4^4 D_1 D_8 \quad \frac{3}{2} a^2 b D_5^2 D_4^4 D_8 \quad -a b^2 D_5 D_4^4 D_1 D_{11} \quad -a^2 b^2 D_5^2 D_4^4 D_{11}] \end{aligned}$$

$$\begin{aligned}
& [9 D_4^2 D_5^2 D_7 D_6 \quad 9 a D_3 D_5^3 D_4^2 D_7 \quad -\frac{3}{2} b D_4^2 D_5^2 D_8 D_6 \quad -\frac{3}{2} a b D_3 D_5^3 D_4^2 D_8 \\
& \quad 9 D_3^2 D_5^4 D_7 \quad -9 a D_4 D_5^4 D_3 D_7 \quad -\frac{3}{2} b D_3^2 D_5^4 D_8 \quad \frac{3}{2} a b D_4 D_5^4 D_3 D_8 \\
& \quad -9 D_3^2 D_5^4 D_7 \quad 9 a D_4 D_5^4 D_3 D_7 \quad \frac{3}{2} b D_3^2 D_5^4 D_9 \quad -\frac{3}{2} a b D_4 D_5^4 D_3 D_9 \\
& -9 D_4^2 D_5^2 D_7 D_6 \quad -9 a D_3 D_5^3 D_4^2 D_7 \quad \frac{3}{2} b D_4^2 D_5^2 D_9 D_6 \quad \frac{3}{2} a b D_3 D_5^3 D_4^2 D_9]
\end{aligned}$$

$$\begin{aligned}
& [-9 a D_4^3 D_5^2 D_1 D_7 \quad -9 a^2 D_4^3 D_5^3 D_7 \quad \frac{3}{2} a b D_4^3 D_5^2 D_1 D_8 \quad \frac{3}{2} a^2 b D_4^3 D_5^3 D_8 \\
& \quad -9 a D_4 D_5^4 D_3 D_7 \quad 9 a^2 D_4^2 D_5^4 D_7 \quad \frac{3}{2} a b D_4 D_5^4 D_3 D_8 \quad -\frac{3}{2} a^2 b D_4^2 D_5^4 D_8 \\
& \quad 9 a D_4 D_5^4 D_3 D_7 \quad -9 a^2 D_4^2 D_5^4 D_7 \quad -\frac{3}{2} a b D_4 D_5^4 D_3 D_9 \quad \frac{3}{2} a^2 b D_4^2 D_5^4 D_9 \\
& \quad 9 a D_4^3 D_5^2 D_1 D_7 \quad 9 a^2 D_4^3 D_5^3 D_7 \quad -\frac{3}{2} a b D_4^3 D_5^2 D_1 D_9 \quad -\frac{3}{2} a^2 b D_4^3 D_5^3 D_9]
\end{aligned}$$

$$\begin{aligned}
& [-\frac{3}{2} b D_4^2 D_5^2 D_8 D_6 \quad -\frac{3}{2} a b D_3 D_5^3 D_4^2 D_8 \quad b^2 D_4^2 D_5^2 D_{12} D_6 \quad a b^2 D_5^3 D_4^2 D_3 D_{12} \\
& \quad -\frac{3}{2} b D_3^2 D_5^4 D_8 \quad \frac{3}{2} a b D_4 D_5^4 D_3 D_8 \quad b^2 D_3^2 D_5^4 D_{12} \quad -a b^2 D_4 D_5^4 D_3 D_{12} \\
& \quad \frac{3}{2} b D_3^2 D_5^4 D_8 \quad -\frac{3}{2} a b D_4 D_5^4 D_3 D_8 \quad -b^2 D_3^2 D_5^4 D_{11} \quad a b^2 D_4 D_5^4 D_3 D_{11} \\
& \quad \frac{3}{2} b D_4^2 D_5^2 D_8 D_6 \quad \frac{3}{2} a b D_3 D_5^3 D_4^2 D_8 \quad -b^2 D_4^2 D_5^2 D_{11} D_6 \quad -a b^2 D_5^3 D_4^2 D_3 D_{11}]
\end{aligned}$$

$$\begin{aligned}
& [\frac{3}{2} a b D_4^3 D_5^2 D_1 D_8 \quad \frac{3}{2} a^2 b D_4^3 D_5^3 D_8 \quad -a b^2 D_4^3 D_5^2 D_1 D_{12} \quad -a^2 b^2 D_4^3 D_5^3 D_{12} \\
& \quad \frac{3}{2} a b D_4 D_5^4 D_3 D_8 \quad -\frac{3}{2} a^2 b D_4^2 D_5^4 D_8 \quad -a b^2 D_4 D_5^4 D_3 D_{12} \quad a^2 b^2 D_4^2 D_5^4 D_{12} \\
& \quad -\frac{3}{2} a b D_4 D_5^4 D_3 D_8 \quad \frac{3}{2} a^2 b D_4^2 D_5^4 D_8 \quad a b^2 D_4 D_5^4 D_3 D_{11} \quad -a^2 b^2 D_4^2 D_5^4 D_{11} \\
& \quad -\frac{3}{2} a b D_4^3 D_5^2 D_1 D_8 \quad -\frac{3}{2} a^2 b D_4^3 D_5^3 D_8 \quad a b^2 D_4^3 D_5^2 D_1 D_{11} \quad a^2 b^2 D_4^3 D_5^3 D_{11}]
\end{aligned}$$

$$\begin{aligned}
& [-9 D_4^2 D_5^2 D_7 D_6 \quad -9 a D_3 D_5^3 D_4^2 D_7 \quad \frac{3}{2} b D_4^2 D_5^2 D_8 D_6 \quad \frac{3}{2} a b D_3 D_5^3 D_4^2 D_8 \\
& \quad -9 D_3^2 D_5^4 D_7 \quad 9 a D_4 D_5^4 D_3 D_7 \quad \frac{3}{2} b D_3^2 D_5^4 D_8 \quad -\frac{3}{2} a b D_4 D_5^4 D_3 D_8 \\
& \quad 9 D_3^2 D_5^4 D_7 \quad -9 a D_4 D_5^4 D_3 D_7 \quad -\frac{3}{2} b D_3^2 D_5^4 D_9 \quad \frac{3}{2} a b D_4 D_5^4 D_3 D_9 \\
& \quad 9 D_4^2 D_5^2 D_7 D_6 \quad 9 a D_3 D_5^3 D_4^2 D_7 \quad -\frac{3}{2} b D_4^2 D_5^2 D_9 D_6 \quad -\frac{3}{2} a b D_3 D_5^3 D_4^2 D_9]
\end{aligned}$$

$$\begin{aligned}
& [9aD_4^3D_5^2D_1D_7 \quad 9a^2D_4^3D_5^3D_7 \quad -\frac{3}{2}abD_4^3D_5^2D_1D_8 \quad -\frac{3}{2}a^2bD_4^3D_5^3D_8 \\
& \quad 9aD_4D_5^4D_3D_7 \quad -9a^2D_4^2D_5^4D_7 \quad -\frac{3}{2}abD_4D_5^4D_3D_8 \quad \frac{3}{2}a^2bD_4^2D_5^4D_8 \\
& \quad -9aD_4D_5^4D_3D_7 \quad 9a^2D_4^2D_5^4D_7 \quad \frac{3}{2}abD_4D_5^4D_3D_9 \quad -\frac{3}{2}a^2bD_4^2D_5^4D_9 \\
& \quad -9aD_4^3D_5^2D_1D_7 \quad -9a^2D_4^3D_5^3D_7 \quad \frac{3}{2}abD_4^3D_5^2D_1D_9 \quad \frac{3}{2}a^2bD_4^3D_5^3D_9] \\
& [\frac{3}{2}bD_4^2D_5^2D_9D_6 \quad \frac{3}{2}abD_3D_5^3D_4^2D_9 \quad -b^2D_4^2D_5^2D_{11}D_6 \quad -ab^2D_5^3D_4^2D_3D_{11} \\
& \quad \frac{3}{2}bD_3^2D_5^4D_9 \quad -\frac{3}{2}abD_4D_5^4D_3D_9 \quad -b^2D_3^2D_5^4D_{11} \quad ab^2D_4D_5^4D_3D_{11} \\
& \quad -\frac{3}{2}bD_3^2D_5^4D_9 \quad \frac{3}{2}abD_4D_5^4D_3D_9 \quad b^2D_3^2D_5^4D_{10} \quad -ab^2D_4D_5^4D_3D_{10} \\
& \quad -\frac{3}{2}bD_4^2D_5^2D_9D_6 \quad -\frac{3}{2}abD_3D_5^3D_4^2D_9 \quad b^2D_4^2D_5^2D_{10}D_6 \quad ab^2D_5^3D_4^2D_3D_{10}] \\
& [-\frac{3}{2}abD_4^3D_5^2D_1D_9 \quad -\frac{3}{2}a^2bD_4^3D_5^3D_9 \quad ab^2D_4^3D_5^2D_1D_{11} \quad a^2b^2D_4^3D_5^3D_{11} \\
& \quad -\frac{3}{2}abD_4D_5^4D_3D_9 \quad \frac{3}{2}a^2bD_4^2D_5^4D_9 \quad ab^2D_4D_5^4D_3D_{11} \quad -a^2b^2D_4^2D_5^4D_{11} \\
& \quad \frac{3}{2}abD_4D_5^4D_3D_9 \quad -\frac{3}{2}a^2bD_4^2D_5^4D_9 \quad -ab^2D_4D_5^4D_3D_{10} \quad a^2b^2D_4^2D_5^4D_{10} \\
& \quad \frac{3}{2}abD_4^3D_5^2D_1D_9 \quad \frac{3}{2}a^2bD_4^3D_5^3D_9 \quad -ab^2D_4^3D_5^2D_1D_{10} \quad -a^2b^2D_4^3D_5^3D_{10}] \\
& [-9D_1^2D_4^4D_7 \quad -9aD_5D_4^4D_1D_7 \quad \frac{3}{2}bD_1^2D_4^4D_8 \quad \frac{3}{2}abD_5D_4^4D_1D_8 \\
& \quad -9D_4^2D_5^2D_7D_6 \quad 9aD_4^3D_5^2D_1D_7 \quad \frac{3}{2}bD_4^2D_5^2D_8D_6 \quad -\frac{3}{2}abD_4^3D_5^2D_1D_8 \\
& \quad 9D_4^2D_5^2D_7D_6 \quad -9aD_4^3D_5^2D_1D_7 \quad -\frac{3}{2}bD_4^2D_5^2D_9D_6 \quad \frac{3}{2}abD_4^3D_5^2D_1D_9 \\
& \quad 9D_1^2D_4^4D_7 \quad 9aD_5D_4^4D_1D_7 \quad -\frac{3}{2}bD_1^2D_4^4D_9 \quad -\frac{3}{2}abD_5D_4^4D_1D_9] \\
& [-9aD_5D_4^4D_1D_7 \quad -9a^2D_5^2D_4^4D_7 \quad \frac{3}{2}abD_5D_4^4D_1D_8 \quad \frac{3}{2}a^2bD_5^2D_4^4D_8 \\
& \quad -9aD_3D_5^3D_4^2D_7 \quad 9a^2D_4^3D_5^3D_7 \quad \frac{3}{2}abD_3D_5^3D_4^2D_8 \quad -\frac{3}{2}a^2bD_4^3D_5^3D_8 \\
& \quad 9aD_3D_5^3D_4^2D_7 \quad -9a^2D_4^3D_5^3D_7 \quad -\frac{3}{2}abD_3D_5^3D_4^2D_9 \quad \frac{3}{2}a^2bD_4^3D_5^3D_9 \\
& \quad 9aD_5D_4^4D_1D_7 \quad 9a^2D_5^2D_4^4D_7 \quad -\frac{3}{2}abD_5D_4^4D_1D_9 \quad -\frac{3}{2}a^2bD_5^2D_4^4D_9]
\end{aligned}$$

$$\begin{aligned}
& \left[ \frac{3}{2} b D_1^2 D_4^4 D_9 \quad \frac{3}{2} a b D_5 D_4^4 D_1 D_9 \quad -b^2 D_1^2 D_4^4 D_{11} \quad -a b^2 D_5 D_4^4 D_1 D_{11} \right. \\
& \frac{3}{2} b D_4^2 D_5^2 D_9 D_6 \quad -\frac{3}{2} a b D_4^3 D_5^2 D_1 D_9 \quad -b^2 D_4^2 D_5^2 D_{11} D_6 \quad a b^2 D_4^3 D_5^2 D_1 D_{11} \\
& -\frac{3}{2} b D_4^2 D_5^2 D_9 D_6 \quad \frac{3}{2} a b D_4^3 D_5^2 D_1 D_9 \quad b^2 D_4^2 D_5^2 D_{10} D_6 \quad -a b^2 D_4^3 D_5^2 D_1 D_{10} \\
& \left. -\frac{3}{2} b D_1^2 D_4^4 D_9 \quad -\frac{3}{2} a b D_5 D_4^4 D_1 D_9 \quad b^2 D_1^2 D_4^4 D_{10} \quad a b^2 D_5 D_4^4 D_1 D_{10} \right] \\
& \\
& \left[ \frac{3}{2} a b D_5 D_4^4 D_1 D_9 \quad \frac{3}{2} a^2 b D_5^2 D_4^4 D_9 \quad -a b^2 D_5 D_4^4 D_1 D_{11} \quad -a^2 b^2 D_5^2 D_4^4 D_{11} \right. \\
& \frac{3}{2} a b D_3 D_5^3 D_4^2 D_9 \quad -\frac{3}{2} a^2 b D_4^3 D_5^3 D_9 \quad -a b^2 D_5^3 D_4^2 D_3 D_{11} \quad a^2 b^2 D_4^3 D_5^3 D_{11} \\
& -\frac{3}{2} a b D_3 D_5^3 D_4^2 D_9 \quad \frac{3}{2} a^2 b D_4^3 D_5^3 D_9 \quad a b^2 D_5^3 D_4^2 D_3 D_{10} \quad -a^2 b^2 D_4^3 D_5^3 D_{10} \\
& \left. -\frac{3}{2} a b D_5 D_4^4 D_1 D_9 \quad -\frac{3}{2} a^2 b D_5^2 D_4^4 D_9 \quad a b^2 D_5 D_4^4 D_1 D_{10} \quad a^2 b^2 D_5^2 D_4^4 D_{10} \right]
\end{aligned} \tag{A.20}$$

where,

$$D_1 = 2a + x \tag{A.21}$$

$$D_2 = x - 2a \tag{A.22}$$

$$D_3 = 2a - x \tag{A.23}$$

$$D_4 = a - x \tag{A.24}$$

$$D_5 = a + x \tag{A.25}$$

$$D_6 = 4a^2 - x^2 \tag{A.26}$$

$$D_7 = 3\bar{y}^5 + 8b^5 - 10b^2\bar{y}^3 + 15b^4\bar{y} \tag{A.27}$$

$$D_8 = -18\bar{y}^5 + 7b^5 + 15b\bar{y}^4 + 40b^2\bar{y}^3 - 30b^3\bar{y}^2 - 30b^4\bar{y} \tag{A.28}$$

$$D_9 = 18\bar{y}^5 + 23b^5 + 15b\bar{y}^4 - 40b^2\bar{y}^3 - 30b^3\bar{y}^2 + 30b^4\bar{y} \tag{A.29}$$

$$D_{10} = 27 \bar{y}^5 + 17 b^5 + 45 b \bar{y}^4 - 10 b^2 \bar{y}^3 - 30 b^3 \bar{y}^2 + 15 b^4 \bar{y} \quad (\text{A.30})$$

$$D_{11} = -27 \bar{y}^5 + 8 b^5 + 50 b^2 \bar{y}^3 - 15 b^4 \bar{y} \quad (\text{A.31})$$

$$D_{12} = 27 \bar{y}^5 + 47 b^5 - 45 b \bar{y}^4 - 10 b^2 \bar{y}^3 + 30 b^3 \bar{y}^2 + 15 b^4 \bar{y} \quad (\text{A.32})$$

## Appendix B

# Aerodynamic Expressions

### B.1 Non-circulatory force

The rigid part of the non-circulatory force is given by,

$$\begin{aligned}
 F_{nc}^{rigid} = \frac{1}{4} \rho c^2 \pi & \left( -3 \dot{V}_h \sin \theta - 3 V_h \cos \theta \frac{d\theta}{dt} - 3 \dot{V}_v \cos \theta \right. \\
 & \left. + 3 V_v \sin \theta \frac{d\theta}{dt} - 2 c \frac{d^2 \theta}{dt^2} + 3 a c \frac{d^2 \theta}{dt^2} \right) \quad (B.1)
 \end{aligned}$$

The elastic part of the non-circulatory force is given by,

$$\begin{aligned}
 F_{nc}^{elastic} = \frac{1}{4} \rho c^2 \sum_{p=1}^{N_m} & \left( -3 B_0^{\prime p} \dot{q}_p V_h \cos \theta - 3 B_0^p \ddot{q}_p \right. \\
 & -3 B_0^{\prime p} q_p \cos \theta \dot{V}_h + 3 B_0^{\prime p} q_p V_h \sin \theta \dot{\theta} + 3 B_0^{\prime p} q_p \dot{V}_v \sin \theta \\
 & +3 B_0^{\prime p} q_p V_v \cos \theta \dot{\theta} + 3 B_0^{\prime p} \dot{q}_p V_v \sin \theta + 2 B_1^p \ddot{q}_p \\
 & +2 B_1^{\prime p} q_p \cos \theta \dot{V}_h - 2 B_1^{\prime p} q_p V_h \sin \theta \dot{\theta} - 2 B_1^{\prime p} q_p \dot{V}_v \sin \theta \\
 & -2 B_1^{\prime p} q_p V_v \cos \theta \dot{\theta} + 2 B_1^{\prime p} \dot{q}_p V_h \cos \theta - 2 B_1^{\prime p} \dot{q}_p V_v \sin \theta \\
 & \left. + B_2^p \ddot{q}_p + B_2^{\prime p} q_p \cos \theta \dot{V}_h - B_2^{\prime p} q_p V_h \sin \theta \dot{\theta} - B_2^{\prime p} q_p \dot{V}_v \sin \theta \right)
 \end{aligned}$$

$$- B_2^{\prime p} q_p V_v \cos \theta \dot{\theta} + B_2^{\prime p} \dot{q}_p V_h \cos \theta - B_2^{\prime p} \dot{q}_p V_v \sin \theta \Big) \quad (\text{B.2})$$

## B.2 Circulation

$$\begin{aligned} \left( \frac{d\Gamma}{dt} \right)_{rigid} &= -\frac{1}{4}, \pi c \left( -4 \dot{V}_h \sin \theta - 4 V_h \cos \theta \dot{\theta} - 4 \dot{V}_v \cos \theta \right. \\ &\quad \left. + 4 V_v \sin \theta \dot{\theta} - 3 c \ddot{\theta} + 4 c \ddot{\theta} a \right) \end{aligned} \quad (\text{B.3})$$

$$\begin{aligned} \left( \frac{d\Gamma}{dt} \right)_{elastic} &= c \sum_{p=1}^{N_m} \left( -B_0^p \ddot{q}_p - B_0^{\prime p} \dot{q}_p V_h \cos \theta - B_0^{\prime p} q_p \dot{V}_h \cos \theta \right. \\ &\quad + B_0^{\prime p} q_p V_h \sin \theta \dot{\theta} + B_0^{\prime p} \dot{q}_p V_v \sin \theta + B_0^{\prime p} q_p \dot{V}_v \sin \theta \\ &\quad + B_0^{\prime p} q_p V_v(t) \cos \theta \dot{\theta} + B_1^p \ddot{q}_p + B_1^{\prime p} \dot{q}_p V_h \cos \theta \\ &\quad + B_1^{\prime p} q_p \dot{V}_h \cos \theta - B_1^{\prime p} q_p V_h \sin \theta \dot{\theta} - B_1^{\prime p} \dot{q}_p V_v \sin \theta \\ &\quad \left. - B_1^{\prime p} q_p \dot{V}_v \sin \theta - B_1^{\prime p} q_p V_v \cos \theta \dot{\theta} \right) \end{aligned} \quad (\text{B.4})$$

## BIBLIOGRAPHY

- [1] McMichael, J. M. and Francis, M. S., *Micro Air Vehicles - Toward a New Dimension in Flight*, Defence Advanced Research Projects Agency TTO Document, 1996.
- [2] Barret, C., "Aerobots and Hydrobots for Planetary Exploration," 38<sup>th</sup> AIAA Aerospace Sciences Meeting and Exhibit, Reno, Nevada, January 10-13 2000.
- [3] Tarascio, M. J. and Chopra, I., "Design and Development of a Thrust Augmented Entomopter : An Advanced Flapping Wing Micro Hovering Air Vehicle," *Proceedings of the 59<sup>th</sup> Annual Forum of the American Helicopter Society*, Phoenix, AZ, May 2003.
- [4] Grasmeyer, J. M. and Keennon, M. T., "Development of the Black Widow Micro Air Vehicle," 39<sup>th</sup> AIAA Aerospace Sciences Meeting and Exhibit, Reno, Nevada, January 8-11 2001.
- [5] Keennon, M. T. and Grasmeyer, J. M., "Development of the Black Widow and Microbat MAVs and a Vision of the Future of MAV Design," *AIAA/ICAS International Air and Space Symposium and Exposition: The Next 100 Years*, Dayton, Ohio, July 14-17 2003.
- [6] Gyllhem, D., Mohseni, K., Lawrence, D., and Geuzaine, P., "Numerical Simulation of Flow Around the Colorado Micro Aerial Vehicle," 35<sup>th</sup> AIAA Fluid Dynamics Conference and Exhibit, Toronto, Ontario, Canada, June 6-9 2005.
- [7] Ifju, P. G., Jenkins, D. A., Ettinger, S., Lian, Y., Shyy, W., and Waszak, M. R., "Flexible-Wing-Based Micro Air Vehicles," 40<sup>th</sup> AIAA Aerospace Sciences Meeting and Exhibit, Reno, Nevada, January 14-17 2002.
- [8] Petersen, B., Erath, B., Henry, K., Lyon, M., Walker, B., Powell, N., Fowkes, K., and Bowman, W. J., "Development of a Micro Air Vehicle for Maximum Endurance and Minimum Size," 41<sup>st</sup> AIAA Aerospace Sciences Meeting and Exhibit, Reno, Nevada, January 6-9 2003.
- [9] Brion, V., Aki, M., and Shkarayev, S., "Numerical Simulations of Low Reynolds Number Flows Around Micro Air Vehicles and Comparison against Wind Tunnel Data," 24<sup>th</sup> AIAA Applied Aerodynamics Conference, San Francisco, California, June 5-8 2006.
- [10] Lian, Y. and Shyy, W., "Numerical Simulations of Membrane Wing Aerodynamics for Micro Air Vehicle Applications," *Journal of Aircraft*, Vol. 42, No. 4, July-August 2005, pp. 865-873.
- [11] Stanford, B., Viieru, D., Albertani, R., Shyy, W., and Ifju, P., "A Numerical and Experimental Investigation of Flexible Micro Air Vehicle Wing Deformation," 44<sup>th</sup> AIAA Aerospace Sciences Meeting and Exhibit, Reno, Nevada, January 9-12 2006.

- [12] Viieru, D., Albertani, R., Shyy, W., and Ifju, P. G., “Effect of Tip Vortex on Wing Aerodynamics of Micro Air Vehicles,” *Journal of Aircraft*, Vol. 42, No. 6, November-December 2005, pp. 1530–1536.
- [13] Abdulrahim, M., Garcia, H., and Lind, R., “Analysis and estimation of the lift components of hovering insects,” *Journal of Aircraft*, Vol. 42, No. 1, January-February 2005, pp. 131–137.
- [14] Abdulrahim, M., Garcia, H., Ivey, G. F., and Lind, R., “Flight Testing A Micro Air Vehicle Using Morphing For Aeroservoelastic Control,” 45<sup>th</sup> *AIAA/ASME/ASCE/AHS/ASC SDM conference*, Palm Springs, California, April 19-22 2004.
- [15] DeLuca, A. M., Reeder, M. F., OL, M. V., Freeman, J., Bautista, I., and Simonich, M., “Experimental Investigation into the Aerodynamic Properties of a Flexible and Rigid Wing Micro Air Vehicle,” 24<sup>th</sup> *AIAA Aerodynamic Measurement Technology and Ground Testing Conference*, Portland, Oregon, June 28 - July 1 2004.
- [16] DeLuca, A. M., Reeder, M. F., Freeman, J., and OL, M. V., “Flexible and Rigid-Wing Micro Air Vehicle: Lift and Drag Comparison,” *Journal of Aircraft*, Vol. 43, No. 2, March-April 2006, pp. 572–575.
- [17] Garcia, H. M., Abdulrahim, M., and Lind, R., “Roll Control for a Micro Air Vehicle Using Active Wing Morphing,” *AIAA Guidance, Navigation and Control Conference and Exhibit*, Austin, Texas, August 11-14 2003.
- [18] Bohorquez, F. and Pines, D., “Hover Performance of Rotor Blades at Low Reynolds Numbers for Rotary Wing Micro Air Vehicles,” 2<sup>nd</sup> *AIAA “Unmanned Unlimited” Systems, Technologies and Operations Conference and Workshop*, San Diego, California, September 15-18 2003.
- [19] Bohorquez, F., Rankins, F., Baeder, J. D., and Pines, D., “Hover Performance of Rotor Blades at Low Reynolds Numbers for Rotary Wing Micro Air Vehicles. An Experimental and CFD Study,” 21<sup>st</sup> *Applied Aerodynamics Conference*, Orlando, Florida, June 23-26 2003.
- [20] Ramasamy, M., Leishman, J. G., and Lee, T. E., “Flow Field of a Rotating-Wing Micro Air Vehicle,” 62<sup>nd</sup> *Annual Forum of the American Helicopter Society*, Phoenix, AZ, May 9-11 2006.
- [21] Lakshminarayan, V. K., Bush, B. L., Duraisamy, K., and Baeder, J. D., “Computational Investigation of Micro Hovering Rotor Aerodynamics,” 24<sup>th</sup> *AIAA Applied Aerodynamics Conference*, San Francisco, California, June 5-8 2006.
- [22] Conroy, J. K., Samuel, P. D., and Pines, D. J., “Development of an MAV Control and Navigation System,” *Infotech@Aerospace*, Arlington, Virginia, September 26-29 2005.

- [23] Pines, D. J. and Bohorquez, F., “Challenges Facing Future Micro-Air-Vehicle Development,” *Journal of Aircraft*, Vol. 43, No. 2, March-April 2006, pp. 290–305.
- [24] Akle, B. J. and Leo, D. J., “Consideration of Ionic Polymer Materials as Flapping Mechanisms for Micro-Air Vehicles,” 44<sup>th</sup> *AIAA/ASME/ASCE/AHS/ASC SDM conference*, Norfolk, Virginia, April 7-10 2003.
- [25] Shyy, W., Berg, M., and Ljungqvist, D., “Flapping and Flexible Wings for Biological and Micro Air Vehicles,” *Progress in Aerospace Sciences*, Vol. 35, No. 5, July 1999, pp. 455–505.
- [26] Weis-fogh, T., “Quick Estimates of Flight Fitness in Hovering Animals, Including Novel Mechanisms for Lift Production,” *Journal of Experimental Biology*, Vol. 59, No. 1, 1973, pp. 169–230.
- [27] Ellington, C. P., “The Aerodynamics of Hovering Insect Flight,” *Philosophical Transactions of the Royal Society of London Series B*, Vol. 305, No. 1122, February 1984, pp. 1–181.
- [28] Willmott, A. P. and Ellington, C. P., “The Mechanics of Flight in the Hawkmoth *Manduca Sexta* I. Kinematics of Hovering and Forward Flight,” *Journal of Experimental Biology*, Vol. 200, 1997, pp. 2705–2722.
- [29] Altshuler, D. L. and Dudley, R., “Kinematics of Hovering Hummingbird Flight Along Simulated and Natural Elevational Gradients,” *Journal of Experimental Biology*, Vol. 206, 2003, pp. 3139–3147.
- [30] Wang, H., Zeng, L., Liu, H., and Yin, C., “Measuring Wing Kinematics, Flight Trajectory and Body Attitude During Forward Flight and Turning Maneuvers in Dragonflies,” *Journal of Experimental Biology*, Vol. 206, 2003, pp. 745–757.
- [31] Dickinson, M. H. and Götz, K. G., “Unsteady Aerodynamic Performance of Model Wings at Low Reynolds Numbers,” *Journal of Experimental Biology*, Vol. 174, 1993, pp. 45–64.
- [32] van den Berg, C. and Ellington, C. P., “The Vortex Wake of a ”Hovering” Model Hawkmoth,” *Philosophical Transactions: Biological Sciences*, Vol. 352, No. 1351, March 1997, pp. 317–328.
- [33] van den Berg, C. and Ellington, C. P., “The Three-Dimensional Leading-Edge Vortex of a ”Hovering” Model Hawkmoth,” *Philosophical Transactions: Biological Sciences*, Vol. 352, No. 1351, March 1997, pp. 329–340.
- [34] Dickinson, M. H., Lehmann, F., and Sane, S. P., “Wing Rotation and the Aerodynamic Basis of Insect Flight,” *Science*, Vol. 284, June 1999, pp. 1954–1960.

- [35] Willmott, A. P. and Ellington, C. P., “The Mechanics of Flight in the Hawkmoth *Manduca sexta* II. Aerodynamic Consequences of Kinematic and Morphological Variation,” *Journal of Experimental Biology*, Vol. 200, 1997, pp. 2723–2745.
- [36] Liu, T., “Comparative Scaling of Flapping- and Fixed-Wing Flyers,” *AIAA Journal*, Vol. 44, No. 1, January 2006, pp. 24–33.
- [37] Spedding, G. R., Rosen, M., and Hedenstrom, A., “A family of vortex wakes generated by a thrush nightingale in free flight in a wind tunnel over its entire natural range of flight speeds,” *Journal of Experimental Biology*, Vol. 206, 2003, pp. 2313–2344.
- [38] Usherwood, J. R., Hedrick, T. L., and Biewener, A. A., “The aerodynamics of avian take-off from direct pressure measurements in Canada geese (*Branta canadensis*),” *Journal of Experimental Biology*, Vol. 206, 2003, pp. 4051–4056.
- [39] Hedrick, T. L., Usherwood, J. R., and Biewener, A. A., “Wing inertia and whole-body acceleration: an analysis of instantaneous aerodynamic force production in cockatiels (*Nymphicus hollandicus*) flying across a range of speeds,” *Journal of Experimental Biology*, Vol. 207, 2004, pp. 1689–1702.
- [40] Usherwood, J. R., Hedrick, T. L., McGowan, C. P., and Biewener, A. A., “Dynamic pressure maps for wings and tails of pigeons in slow, flapping flight, and their energetic implications,” *Journal of Experimental Biology*, Vol. 208, 2005, pp. 355–369.
- [41] Srygley, R. B. and Thomas, A. L. R., “Unconventional Lift Generating Mechanisms in Free-Flying Butterflies,” *Nature*, Vol. 420, December 2002, pp. 660–664.
- [42] Thomas, A. L. R., Taylor, G. K., Srygley, R. B., Nudds, R. L., and Bomphrey, R. J., “Dragonfly flight: free-flight and tethered flow visualizations reveal a diverse array of unsteady lift-generating mechanisms, controlled primarily via angle of attack,” *Journal of Experimental Biology*, Vol. 207, 2004, pp. 4299–4323.
- [43] Bomphrey, R. J., Lawson, N. J., Harding, N. J., Taylor, G. K., and Thomas, A. L. R., “The aerodynamics of *Manduca sexta*: digital particle image velocimetry analysis of the leading-edge vortex,” *Journal of Experimental Biology*, Vol. 208, 2005, pp. 1079–1094.
- [44] Lehmann, F.-O. and Dickinson, M. H., “The production of elevated flight force compromises manoeuvrability in the fruit fly *Drosophila melanogaster*,” *Journal of Experimental Biology*, Vol. 204, 2001, pp. 627–635.
- [45] Dillon, M. E. and Dudley, R., “Allometry of maximum vertical force production during hovering flight of neotropical orchid bees (Apidae: Euglossini),” *Journal of Experimental Biology*, Vol. 207, 2004, pp. 417–425.

- [46] Song, F., Lee, K. L., Soh, A. K., Zhu, F., and Bai, Y. L., “Experimental studies of the material properties of the forewing of cicada (Homoptera, Cicadidae),” *Journal of Experimental Biology*, Vol. 207, 2004, pp. 3035–3042.
- [47] Combes, S. A. and Daniel, T. L., “Flexural stiffness in insect wings I. Scaling and the influence of wing venation,” *Journal of Experimental Biology*, Vol. 206, 2003, pp. 2979–2987.
- [48] Combes, S. A. and Daniel, T. L., “Flexural stiffness in insect wings II. Spatial distribution and dynamic wing bending,” *Journal of Experimental Biology*, Vol. 206, 2003, pp. 2989–2997.
- [49] Sane, S. P., “The Aerodynamics of Insect Flight,” *Journal of Experimental Biology*, Vol. 206, 2003, pp. 4191–4208.
- [50] Ellington, C. P. and Usherwood, J. R., “Lift and Drag Characteristics of Rotary and Flapping Wings,” *Fixed and Flapping Wing Aerodynamics for Micro Air Vehicle Applications*, edited by T. J. Mueller, Vol. 195 of *AIAA Progress in Aeronautics and Astronautics*, chap. 12, AIAA, 2001, pp. 231–248.
- [51] Birch, J. M., Dickson, W. B., and Dickinson, M. H., “Force production and flow structure of the leading edge vortex on flapping wings at high and low Reynolds numbers,” *Journal of Experimental Biology*, Vol. 207, 2004, pp. 1063–1072.
- [52] Ramasamy, M., Leishman, J. G., and Singh, B., “Wake structure diagnostics of a flapping wing MAV,” *International Powered Lift Conference*, Grapevine, Texas, October 2005.
- [53] Birch, J. M. and Dickinson, M. H., “The influence of wing wake interactions on the production of aerodynamic forces in flapping flight,” *Journal of Experimental Biology*, Vol. 206, 2003, pp. 2257–2272.
- [54] Sane, S. P. and Dickinson, M. H., “The Aerodynamic Effects of Wing Rotation and a Revised Quasi-Steady Model of Flapping Flight,” *Journal of Experimental Biology*, Vol. 205, 2002, pp. 1087–1096.
- [55] Maybury, W. J. and Lehmann, F.-O., “The fluid dynamics of flight control by kinematic phase lag variation between two robotic insect wings,” *Journal of Experimental Biology*, Vol. 207, 2004, pp. 4707–4726.
- [56] Lehmann, F.-O., Sane, S. P., and Dickinson, M., “The aerodynamic effects of wing-wing interaction in flapping insect wings,” *Journal of Experimental Biology*, Vol. 208, 2005, pp. 3075–3092.
- [57] Fearing, R. S., Chiang, K. H., Dickinson, M. H., Pick, D. L., Sitti, M., and Yan, J., “Wing Transmission for a Micromechanical Flying Insect,” *IEEE*

*International Conference on Robotics and Automation*, San Francisco, California, April 24-28 2000.

- [58] Yan, J., Avadhanula, S. A., Birch, J., Dickinson, M. H., Sitti, M., Su, T., and Fearing, R. S., “Wing Transmission for a Micromechanical Flying Insect,” *Journal of Micromechatronics*, Vol. 1, No. 3, 2002, pp. 221–237.
- [59] Sitti, M., Campolo, D., Yan, J., Fearing, R. S., Su, T., Taylor, D., and Sands, T. D., “Development of PZT and PZN-PT Based Unimorph Actuators for Micromechanical Flapping Mechanisms,” *IEEE International Conference on Robotics and Automation*, Seoul, Korea, May 21-26 2001.
- [60] Wood, R. J., Avadhanula, S., Menon, M., and Fearing, R. S., “Microrobotics Using Composite Materials: The Micromechanical Flying Insect Thorax,” *IEEE International Conference on Robotics and Automation*, Taipei, Taiwan, September 14-19 2003.
- [61] Schenato, L., Deng, X., and Sastry, S., “Flight Control System for a Micromechanical Flying Insect: Architecture and Implementation,” *IEEE International Conference on Robotics and Automation*, Seoul, Korea, May 21-26 2001.
- [62] Deng, X., Schenato, L., and Sastry, S., “Hovering Flight Control of a Micromechanical Flying Insect,” *40<sup>th</sup> IEEE Conference on Decision and Control*, Orlando, Florida, December 4-7 2001.
- [63] Deng, X., Schenato, L., and Sastry, S., “Model Identification and Attitude Control for a Micromechanical Flying Insect Including Thorax and Sensor Models,” *IEEE International Conference on Robotics and Automation*, Taipei, Taiwan, September 14-19 2003.
- [64] Wu, W. C., Wood, R. J., and Fearing, R. S., “Halteres for the Micromechanical Flying Insect,” *IEEE International Conference on Robotics and Automation*, Washington DC, May 11-15 2002.
- [65] Yan, J., Wood, R. J., Avadhanula, S., Sitti, M., and Fearing, R. S., “Towards Flapping Wing Control for a Micromechanical Flying Insect,” *IEEE International Conference on Robotics and Automation*, Seoul, Korea, May 21-26 2001.
- [66] Schenato, L., Wu, W. C., and Sastry, S., “Attitude Control for a Micromechanical Flying Insect via Sensor Output Feedback,” *IEEE Transactions on Robotics and Automation*, Vol. 20, No. 1, February 2004, pp. 93–106.
- [67] Wu, W.-C., Schenato, L., Wood, R. J., and Fearing, R. S., “Biomimetic Sensor Suite for Flight Control of a Micromechanical Flying Insect: Design and Experimental Results,” *IEEE International Conference on Robotics and Automation*, Taipei, Taiwan, September 14-19 2003.

- [68] Ho, S., Nassef, H., Pornsinsirak, N., Tai, Y.-C., and Ho, C.-M., “Unsteady aerodynamics and flow control for flapping wing flyers,” *Progress in Aerospace Sciences*, Vol. 39, No. 8, November 2003, pp. 635–681.
- [69] Heathcote, S., Martin, D., and Gursul, I., “Flexible Flapping Wing Propulsion at Zero Freestream Velocity,” *AIAA Journal*, Vol. 42, No. 11, November 2004, pp. 2196–2204.
- [70] Heathcote, S. and Gursul, I., “Flexible Flapping Airfoil Propulsion at Low Reynolds Numbers,” *43<sup>rd</sup> AIAA Aerospace Sciences Meeting and Exhibit*, Reno, Nevada, January 10-13 2005.
- [71] Heathcote, S., Wang, Z., and Gursul, I., “Effect of Spanwise Flexibility on Flapping Wing Propulsion,” *36<sup>rd</sup> AIAA Fluid Dynamics Conference and Exhibit*, San Francisco, California, June 5-8 2006.
- [72] Hong, Y. and Altman, A., “An Experimental Study on Lift Force Generation Resulting from Spanwise Flow in Flapping Wings,” *44<sup>th</sup> AIAA Aerospace Sciences Meeting and Exhibit*, Reno, Nevada, January 9-12 2006.
- [73] Beasley, B. and Chopra, I., “Planar and Nonplanar Membrane Wing Platform for the Design of a Flapping-Wing Micro Air Vehicle,” *Proceedings of the 62<sup>nd</sup> Annual Forum of the American Helicopter Society*, Phoenix, AZ, May 2006.
- [74] Jones, K. D. and Platzer, M. F., “An Experimental and Numerical Investigation of Flapping Wing Propulsion,” *37<sup>th</sup> AIAA Aerospace Sciences Meeting and Exhibit*, Reno, Nevada, January 11-14 1999.
- [75] Jones, K. D., Duggan, S. J., and Platzer, M. F., “Flapping-Wing Propulsion for a Micro Air Vehicle,” *39<sup>th</sup> AIAA Aerospace Sciences Meeting and Exhibit*, Reno, Nevada, January 8-11 2001.
- [76] Jones, K. D. and Platzer, M. F., “Bio-Inspired Design of Flapping Wing Micro Air Vehicles - An Engineer’s Perspective,” *44<sup>th</sup> AIAA Aerospace Sciences Meeting and Exhibit*, Reno, Nevada, January 9-12 2006.
- [77] DeLaurier, J. D., “An Aerodynamic Model for Flapping Wing Flight,” *Aeronautical Journal*, Vol. 97, April 1993, pp. 125–130.
- [78] Larijani, R. F. and DeLaurier, J. D., “A Nonlinear Aeroelastic Model for the Study of Flapping Wing Flight,” *Fixed and Flapping Wing Aerodynamics for Micro Air Vehicle Applications*, edited by T. J. Mueller, Vol. 195 of *AIAA Progress in Aeronautics and Astronautics*, chap. 18, AIAA, 2001, pp. 399–428.
- [79] Walker, J. A., “Rotational Lift: Something Different or More of the Same?” *Journal of Experimental Biology*, Vol. 205, 2002, pp. 3783–3792.

- [80] Żbikowski, R., “On aerodynamic modelling of an insect-like flapping wing in hover for micro air vehicles,” *Philosophical Transactions of the Royal Society London, Series A*, Vol. 360, January 2002, pp. 273–290.
- [81] Lan, C. E., “The Unsteady Quasi-Vortex-Lattice Method with Applications to Animal Propulsion,” *Journal of Fluid Mechanics*, Vol. 93, No. 4, 1979, pp. 747–765.
- [82] Fritz, T. E. and Long, L. N., “Object-Oriented Unsteady Vortex Lattice Method for Flapping Flight,” *Journal of Aircraft*, Vol. 41, No. 6, November–December 2004, pp. 1275–1290.
- [83] Vest, M. S. and Katz, J., “Unsteady Aerodynamic Model of Flapping Wings,” *AIAA Journal*, 1996.
- [84] Eldredge, J. D., “Efficient tools for the simulation of flapping wing flows,” *43<sup>rd</sup> AIAA Aerospace Sciences Meeting and Exhibit*, Reno, Nevada, January 10–13 2005.
- [85] Wang, Z. J., “Vortex Shedding and Frequency Selection in Flapping Flight,” *Journal of Fluid Mechanics*, Vol. 410, 2000, pp. 323–341.
- [86] Ramamurti, R. and Sandberg, W. C., “A Three-Dimensional Computational Study of the Aerodynamic Mechanisms of Insect Flight,” *Journal of Experimental Biology*, Vol. 205, 2002, pp. 1507–1518.
- [87] Wang, Z. J., “The Role of Drag in Insect Hovering,” *Journal of Experimental Biology*, Vol. 207, 2004, pp. 4147–4155.
- [88] Liu, H., Ellington, C. P., and Kawachi, K., “A Computational Fluid Dynamic Study of Hawkmoth Hovering,” *Journal of Experimental Biology*, Vol. 201, No. 4, 1998, pp. 461–477.
- [89] Sun, M. and Tang, J., “Unsteady Aerodynamic Force Generation by a Model Fruit Fly Wing in Flapping Motion,” *Journal of Experimental Biology*, Vol. 205, 2002, pp. 55–70.
- [90] Sun, M. and Tang, J., “Lift and Power Requirements of Hovering Flight in *Drosophila Virilis*,” *Journal of Experimental Biology*, Vol. 205, 2002, pp. 2413–2427.
- [91] Wu, J. H. and Sun, M., “Unsteady Aerodynamic Forces of a Flapping Wing,” *Journal of Experimental Biology*, Vol. 207, 2004, pp. 1137–1150.
- [92] Sun, M. and Wu, J. H., “Aerodynamic Force Generation and Power Requirements in Forward Flight in a Fruit Fly with Modeled Wing Motion,” *Journal of Experimental Biology*, Vol. 206, 2003, pp. 3065–3083.

- [93] Wootton, R. J., “The Mechanical Design of Insect Wings,” *Scientific American*, Vol. 263, November 1990, pp. 114–120.
- [94] Wootton, R. J., Herbert, R. C., Young, P. G., and Evans, K. E., “Approaches to the Structural Modeling of Insect Wings,” *Philosophical Transactions of the Royal Society of London Series B*, Vol. 358, August 2003, pp. 1577–1587.
- [95] Combes, S. A. and Daniel, T. L., “Into Thin Air: Contributions of Aerodynamic and Inertial-Elastic Forces to Wing Bending in the Hawkmoth *Maduca Sexta*,” *Journal of Experimental Biology*, Vol. 206, 2003, pp. 2999–3006.
- [96] Okamoto, M., Yasuda, K., and Azuma, A., “Aerodynamic Characteristics of the Wings and Body of a Dragonfly,” *Journal of Experimental Biology*, Vol. 199, 1996, pp. 281–294.
- [97] Raney, D. L. and Slominski, E. C., “Mechanization and Control Concepts for Biologically Inspired Micro Air Vehicles,” *Journal of Aircraft*, Vol. 41, No. 6, November-December 2004, pp. 1257–1265.
- [98] Banerjee, A. K. and Kane, T. R., “Dynamics of a plate in large overall motion,” *Journal of Applied Mechanics*, Vol. 56, No. 14, December 1989, pp. 887–892.
- [99] Banerjee, A. K. and Dickens, J. M., “Dynamics of an arbitrary flexible body in large rotation and translation,” *Journal of Guidance, Control and Dynamics*, Vol. 13, No. 2, March 1990, pp. 221–227.
- [100] Jinyang, L. and Jiazhen, H., “Geometric nonlinear formulation and discretization method for a rectangular plate undergoing large overall motions,” *Mechanics Research Communications*, Vol. 32, No. 5, September 2005, pp. 561–571.
- [101] Reddy, J. N., *Mechanics of laminated composite plates*, CRC press, 1997.
- [102] Polhamus, E. C., “A Concept of the Vortex Lift of Sharp Edge Delta Wings Based on a Leading-Edge Suction Analogy,” NASA TN D-3767, 1966.
- [103] Żbikowski, R., Pedersen, C. B., Ansari, S. A., and Galiński, C., “Flapping wing micro air vehicles,” Tech. Rep. DAPS/RZ/92/2003, Department of aerospace, power and sensors, The Royal Military College of Science, Cranfield University, November 2003.
- [104] Katz, J. and Plotkin, A., *Low-speed aerodynamics*, Cambridge University Press, 2001.
- [105] Polhamus, E. C., “Predictions of Vortex-Lift Characteristics by a Leading-Edge Suction Analogy,” *Journal of Aircraft*, Vol. 8, No. 4, April 1971, pp. 193–199.

- [106] Purvis, J. W., “Analytical Prediction of Vortex Lift,” *Journal of Aircraft*, Vol. 18, No. 4, April 1981, pp. 225–230.
- [107] Leishman, J. G., *Helicopter Aerodynamics*, Cambridge University Press, 2000.
- [108] Daniel, T. L. and Combes, S. A., “Flexible Wings and Fins: Bending by Inertial or Fluid Dynamic Forces?” *Integrative and Comparative Biology*, Vol. 42, 2002, pp. 1044–1049.
- [109] Nayfeh, A. H. and Mook, D. T., *Nonlinear Oscillations*, John Wiley and Sons Inc., 1995.
- [110] Wang, Z. J., Birch, J. M., and Dickinson, M. H., “Unsteady Forces and Flows in Low Reynolds Number Hovering Flight: Two-Dimensional Computations vs Robotic Wing Experiments,” *Journal of Experimental Biology*, Vol. 207, 2004, pp. 449–460.